

Doctoral thesis / *Dissertation*

for the doctoral degree / *zur Erlangung des Doktorgrads*

Doctor rerum naturalium (Dr. rer. nat.)

Correlation between Interface Energetics of Molecular Semiconductors and
Opto-Electronic Properties of Planar Organic Solar Cells

*Der Zusammenhang zwischen der Energetik molekularer Halbleitergrenzflächen und den
opto-elektronischen Eigenschaften planarer organischer Solarzellen*



Submitted by / *vorgelegt von*

Michael Brendel

from / *aus*

Lohr a. Main

Würzburg 2016

Submitted on / *Eingereicht am*: 11.11.2016

Stamp / *Stempel* Graduate School

Members of thesis committee / *Mitglieder des Promotionskomitees*

Chairperson / *Vorsitz*:

1. Reviewer and Examiner / *1. Gutachter und Prüfer*: Prof. Dr. Jens Pflaum

2. Reviewer and Examiner / *2. Gutachter und Prüfer*: Prof. Dr. Matthias Bode

3. Examiner / *3. Prüfer*: Prof. Dr. Bernd Engels

Additional Examiners / *weitere Prüfer*:

Day of thesis defense / *Tag des Promotionskolloquiums*:

Contents

1. Introduction	1
I. Physical Background	3
2. Organic Semiconductors	5
2.1. Intra- and Intermolecular Opto-Electronic Properties	5
2.1.1. Molecular Bonding Characteristics: The Delocalized π -Electron System	5
2.1.2. From Molecular to Solid State Properties	6
2.2. Electronic Transitions	7
2.3. Excitons	10
2.3.1. Types of Excitons	10
2.3.2. Exciton Transport in Organic Semiconductors	12
2.4. Charge Carrier Transport	14
3. Fundamentals of Organic Photovoltaic Cells (OPVCs)	19
3.1. Working Principle of OPVCs: The Donor/Acceptor (D/A) Heterojunction	20
3.2. Solar Cell Architectures	23
3.3. Current Density-Voltage ($j(V)$) Characteristics	24
II. Materials, Solar Cell Architecture and Experimental Methods	27
4. Materials for Organic Photovoltaic Devices	29
4.1. Electrode Materials	29
4.2. Hole Transport Materials	30
4.3. Organic Absorber Materials	31
4.3.1. Donor Compounds	31
4.3.2. Acceptor Compounds	35
4.4. Exciton Blocking Layer (EBL)	36
5. Sample Architecture and Fabrication	39
6. Experimental Techniques	41
6.1. <i>In-Situ</i> Opto-Electronic Device Characterization	41
6.1.1. Current Density-Voltage ($j(V)$) Characterization	41
6.1.2. External Quantum Efficiency (<i>EQE</i>)	41

6.2. Structural Investigation	42
6.2.1. X-Ray Diffraction (XRD)	42
6.2.2. Atomic Force Microscopy (AFM)	43
6.3. Optical Measurements	44
6.3.1. Steady State Absorption Spectroscopy	44
6.3.2. Spectrally Resolved Photoluminescence (PL)	44
6.3.3. Transient Absorption Spectroscopy (TAS)	45
6.4. Ultraviolet Photoelectron Spectroscopy (UPS)	47
III. Results and Discussion	51
7. Impact of Gradual Fluorination on the Properties of F_nZnPc/C_{60} Bilayer OPVCs	53
7.1. Tailored Modification of D/A Interface Energetics	53
7.2. $j(V)$ Characterization of F_nZnPc/C_{60} Bilayer Solar Cells	54
7.3. Thin Film Properties of F_nZnPc	56
7.4. Determination of F_nZnPc/C_{60} Interface Energetics by UPS	61
7.5. Correlation between F_nZnPc/C_{60} Interface Energetics and Device Characteristics	64
8. Correlating D/A Interface Energetics of F_nZnPc/C_{60} with Electronic Dynamics	71
8.1. TAS on F_nZnPc/C_{60} Heterostructures	71
8.2. Classification of the Transient Absorption Species	73
8.3. Charge Carrier Generation Mechanisms in the C_{60} Acceptor	77
9. Energy Cascades as a New Concept to Improve Charge Carrier Generation in OPV	83
9.1. Cascade Cells Based on Diketopyrrolopyrrole Derivatives (D1 - D3)	84
9.1.1. Structural Investigation of D1/D3/ C_{60} Cascade Cells by XRD and AFM	85
9.1.2. Opto-Electronic Characterization of D1/D3/ C_{60} Cascade Cells	86
9.1.3. Opto-Electronic Characterization of D1/D2/ C_{60} Cascade Cells	96
9.2. Application of Cascade Concept to DBP/ F_8ZnPc/C_{70} Solar Cells	97
10. Excitonic and Electronic Compatibility of Mixed $C_{60}:C_{70}$ Acceptor Layers	105
10.1. Fullerenes: Structure, Purification Costs and Technological Relevance in OPV . .	105
10.2. Thin Film Properties of the Molecular Semiconductors	107
10.3. Impact of Fullerene Composition Ratio on DIP/ $C_{60}:C_{70}$ Solar Cells	111
11. Summary	119
12. Zusammenfassung	125
List of Figures	133
List of Tables	135
Bibliography	137

1. Introduction

Since the discovery of electronic conductivity in doped polyacetylene in 1977, the field of organic electronics received considerable scientific and industrial attention. [1] Research on organic semiconductors stimulated applications in emergent technologies, such as organic field effect transistors, organic solar cells and organic light emitting diodes. [2-7] Outstandingly, the latter could be established in a variety of commercial products, for instance in high resolution displays. [8]

The advantages of organic semiconductors in comparison to their inorganic counterparts (e.g. Si or Ge) involve compatibility with established low-temperature and low-cost processing, allowing for large area deposition via printing or sublimation. [9] Moreover, the possibility of tailoring the opto-electronic properties by means of chemical modification is of paramount importance. Such a variation may encompass the substitution of functional groups of a molecular compound, yielding for example, a change of the electronic or optical band gap, a shift of absolute energy levels, or a variation of structural order within the thin film. [10,11] Organic semiconductors typically have high absorption coefficients in the range of $\alpha \approx 10^5 \frac{1}{cm}$. Hence, in organic photovoltaic applications, layer thicknesses of a few hundred nm are sufficient to absorb most of the incident light and therefore, little material consumption is required. [12] Accordingly, manufacturing of potentially light-weight electronic components, utilizing flexible foils as substrates, is possible.

Despite of these promising material characteristics, organic photovoltaics face distinct challenges to have a significant impact on the market, such as warranting long-term stability and solving up-scaling issues. [9,13] Today, power conversion efficiencies of organic solar cells exceed 13 %. [5] Yet, improving device efficiency is required to compete with established inorganic technologies such as for example solar cells based on polycrystalline silicon, yielding power conversion efficiencies of 14 - 18 %. [13,14]

Due to the low dielectric constants of organic semiconductors ($\epsilon_r = 3 - 4$), upon absorption of light, strongly Coulomb-bound electron-hole pairs are generated. [15] The working principle of organic photovoltaic cells (OPVCs) is based on the so-called donor/acceptor (D/A) heterojunction, comprised of two distinct molecular materials. This key functional building block provides the necessary driving force for splitting those bound electron-hole pairs. Accordingly, energetics at this common interface are of fundamental importance for device physics and, to a large extent determine macroscopic solar cell parameters. It is the scope of this work, to gain detailed understanding of the correlation between interface energetics of the molecular semiconductors and solar cell characteristics.

This thesis is divided into three parts. Starting with a discussion on the physical background in Part I, general aspects of organic semiconductors are elaborated. Based on this introduction, the working principle of an organic planar bilayer cell involving a donor/acceptor heterojunction is addressed. And finally, basics of solar cell characterization are demonstrated. In Part II, basic properties of the employed materials are presented and the utilized solar cell architecture is elucidated. In this context, the vacuum chamber system, used for solar cell preparation is illustrated, as well as the experimental techniques for sample characterization.

In Part III of this thesis, the experimental results are presented and discussed in detail. Aiming for a systematic variation of the D/A interface energetics, in Chapter 7 differently fluorinated zinc phthalocyanines $F_n\text{ZnPc}$ ($n = 0, 4, 8, 16$) are employed as donor compounds in planar bilayer solar cells in combination with the electron acceptor C_{60} . Upon fluorination, energy levels of the phthalocyanines are expected to be shifted towards lower energies. [16, 17] The actual energy level positions are tracked by thickness dependent photoelectron spectroscopy measurements on the respective D/A heterojunction, yielding in combination with complementary structural and opto-electronic investigations a detailed picture of the photoconversion processes occurring on microscopic length scales. In Chapter 8 the static picture of $F_n\text{ZnPc}/C_{60}$ interface energetics is extended by electronic dynamics. The time scale of exciton dissociation into free charge carriers is elucidated and recombination dynamics are investigated as a function of interface energetics by ultrafast transient absorption spectroscopy.

In the subsequent Chapter 9, the effect of implementing energetic staircases in planar solar cells is analyzed by means of their resulting performance. Following this approach, a thin interfacial layer is sandwiched between a planar D/A heterointerface. Importantly, energy levels of the interfacial layer are chosen to be intermediate to those of the D/A heterojunction. The potential of this concept will be explored with a special focus on the influence of the energy level alignment on the exciton dissociation into free charge carriers. Energetic cascades are established employing two different material combinations, aiming to demonstrate the universality of this conceptual approach.

Finally, in Chapter 10, the impact of a varying $C_{60}:C_{70}$ acceptor mixing ratio on the performance of organic solar cells is under investigation. Photoelectron spectroscopy measurements showed that the electronic structure of both fullerenes is very similar, but not identical. [18] These structurally and electronically similar compounds are utilized in an interlaced acceptor phase and the ramifications for excitonic and electronic transport are discussed. However, the motivation for these studies is not solely given by photo-physical implications, but also by reasons of technological relevance for OPVCs. Both fullerenes are generated simultaneously along with a small amount of higher mass fullerenes in common synthesis procedures. The individual material costs are determined by the purification process, i.e. by the separation of the molecular materials from each other. [18] Based on these investigations, a recommendation for refinement of raw fullerene mixtures is developed.

Part I.

Physical Background

2. Organic Semiconductors

In general, organic semiconductors are divided into polymers and molecular materials. The distinction between both carbon based classes is drawn according to their size. Macromolecular polymers may have a huge number of repeating units, resulting in spatial dimensions of up to a few hundred nm, whereas molecular materials are typically only a few nm in size. Therefore, molecular compounds are often referred to as “small molecules” in literature. [19] In this thesis, the focus is set on the investigation of organic photovoltaic cells (OPVCs) based on such small molecules.

2.1. Intra- and Intermolecular Opto-Electronic Properties

To understand the photo-physical properties of organic semiconductors, it is mandatory to elaborate the underlying electronic structure. Since semiconducting molecular crystals, polycrystalline or amorphous thin films are comprised of molecular subunits, this chapter starts with the molecular point of view, before addressing coupling between those subunits.

2.1.1. Molecular Bonding Characteristics: The Delocalized π -Electron System

The reason for the emergence of semiconducting behavior in polymers and molecular materials is their specific electronic motif - the so called conjugated π -system. Typically, it is characterized by alternating single and double bonds between neighboring carbon atoms, causing a delocalization of π -electrons. In such conjugated systems, carbon atoms hybridize in sp^2 -configuration, i.e. by mixing of the $2s$ - with $2p_x$ - and $2p_y$ -orbitals, three degenerate sp^2 -hybrid orbitals form. These orbitals enclose an angle of 120° with each other in a co-planar arrangement within the xy -plane. The remaining p_z -orbital is unaltered and oriented perpendicularly to this plane. When atoms combine to molecules, bonding and anti-bonding orbitals are formed. By overlapping of the wave functions of sp^2 -hybrid orbitals of neighboring carbon atoms, localized covalent σ -bondings arise, whereas overlapping of p_z -orbitals causes the formation of π -bonds. The latter, bridging the spatially interjacent σ -bonds, yield a delocalization of π -electrons. In case of benzene, the most prevalent building block of organic semiconductors, the electron density of the six π -electrons is delocalized above and below the planar molecule as schematically depicted in Figure 2.1 a). [20] Also other atoms but carbon can be part of a conjugated π -system, such as nitrogen or oxygen. In general, conjugation is maintained in case that contiguous atoms in the

compound contain an available p-orbital each. [21] As a consequence of the delocalized nature of π -conjugated systems, high electrical intramolecular conductivity can be obtained in organic semiconductors. [22]

Due to stronger overlap of the wave functions of sp^2 -hybrid orbitals, covalent σ -bondings cause a larger energetic splitting compared to π -bonds, as shown exemplarily for the energy levels of benzene in Figure 2.1 b). Therefore, typically π -orbitals represent highest occupied molecular orbitals (HOMO) in organic semiconductors, whereas π^* -orbitals constitute lowest unoccupied molecular orbitals (LUMO). Thus, usually $\pi \rightarrow \pi^*$ transitions determine the opto-electronic properties of organic semiconducting molecules. Extension of the π -electron system results in a reduction of the band gap, similarly to the picture of an increasing size of a quantum well. For anthracene composed of three linearly fused benzene rings, the main absorption peak is located at 2.58 eV, whereas for pentacene, with five conjugated benzene rings, the $\pi \rightarrow \pi^*$ transition maximum is obtained at 2.14 eV. [22] Hence, the modification of the conjugated π -electron system enables tailoring of molecular opto-electronic properties. Typically, $\pi \rightarrow \pi^*$ transitions occur in the energy range of 1.5 - 3 eV and thus, take place in the ultraviolet, visible and near-infrared spectral region. [15]

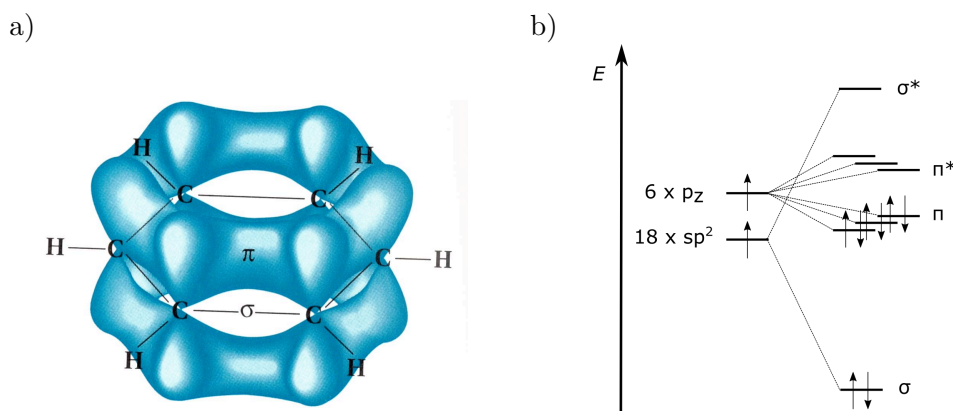


Figure 2.1.: a) Depiction of the delocalized π -electron system of benzene. [20] b) Illustration of the energy levels of benzene. Typically, $\pi \rightarrow \pi^*$ transitions determine the opto-electronic properties of organic semiconductors.

2.1.2. From Molecular to Solid State Properties

In contrast to intramolecular stability of polymers and molecular compounds, which is mainly determined by the covalent σ -bondings, intermolecular interaction in organic solids is governed by small range London dispersion forces. [15] London dispersion forces are counted among van-der-Waals forces and are based on fluctuating dipole moments of electrically neutral, unpolar molecules. Accordingly, these forces are to be considered extremely weak, with typical binding energies of 1 meV - 10 meV. For comparison, typical covalent bonds in inorganic crystals are orders of magnitude larger with 2 - 4 eV. [23] As a result, mechanical and thermodynamic properties of organic solids are inherently determined by these intermolecular London dispersion

forces. As a consequence, organic solids are much softer, have smaller dielectric constants ($\epsilon_r = 3 - 4$) and lower charge carrier mobilities (see Section 2.4), as well as lower sublimation enthalpies (usually ~ 100 kJ/mol), in comparison to their inorganic counterparts. [15] Due to the weak intermolecular forces, the electronic structure of an organic solid is almost unaltered in comparison to the electronic structure of the isolated molecules. [19] Hence, molecular opto-electronic properties are mainly conserved. Concomitantly, the formation of broad electronic bands, known from inorganic semiconductors, is not observed in organic single crystals or polycrystalline thin films. [24]

In Figure 2.2 the term scheme of an isolated molecule and a molecular crystal is illustrated. The electron affinity EA and the ionization potential IP of the molecule (index m) and the molecular crystal (index c) are indicated. The latter describes the energy difference between the HOMO and the vacuum level and former the energy difference between the LUMO and the vacuum level. Upon formation of a molecular crystal, IP_c and EA_c are modified by the polarization energies P_h and P_e with respect to the isolated molecule. This change can be attributed to the polarization of the dielectric surrounding, i.e. the neighboring molecules in the crystal stabilize a radical anion or cation. The energy difference between IP and EA denotes the electronic transport gap E_{gap} .

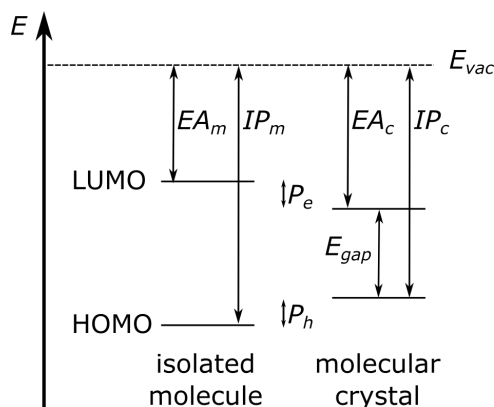


Figure 2.2.: Energy diagram of an isolated molecule and a molecular crystal. The term scheme includes the ionization potential IP and electron affinity EA of the molecule (index m) and the crystal (index c). Upon formation of the molecular crystal, IP_c and EA_c are stabilized by the polarization energies P_h and P_e with respect to the isolated molecule. The energy difference between IP_c and EA_c denotes the electronic band gap E_{gap} of the crystal. E_{vac} represents the vacuum energy.

2.2. Electronic Transitions

Transitions between electronic states of an organic semiconductor, such as excitation upon absorption of light, or radiative and non-radiative deactivation processes, are usually illustrated in a Jablonski diagram. [25] Such an energy scheme is depicted in Figure 2.3, including the ground state (S_0) and various excited states (S_1 , S_2 , T_1) of higher energy. Electronic states are

grouped horizontally according to their spin multiplicity into singlet (S: spin = 0) and triplet states (T: spin = 1). Due to dipole transition rules and the singlet character of the ground state, absorption of light typically promotes an electronic transition in the singlet branch. [22] The absorption probability is proportional to $\sqrt{\vec{p} \cdot \vec{E}}$. Here \vec{p} denotes the transition dipole moment and \vec{E} the electric field vector of the incident light. [23]

In general, providing a comprehensive description of the energy states of a molecule next to the electronic, also the vibrational and rotational excitations have to be considered. According to the Born-Oppenheimer approximation, these three components and hence their related energies can be separated, since the mass of the nuclei exceeds the mass of the electrons vastly and thus, electrons can be assumed to follow the motion of the nuclei instantaneously: [26]

$$E = E_{el} + E_{vib} + E_{rot}. \quad (2.1)$$

Here E_{el} , E_{vib} and E_{rot} denote the energies of the electronic, vibrational and rotational components of the respective molecular state. Though, all three components are to be considered for molecules in the gas phase and in solution, in case of organic solids, no rotational component can be observed due to the restricted degree of freedom.

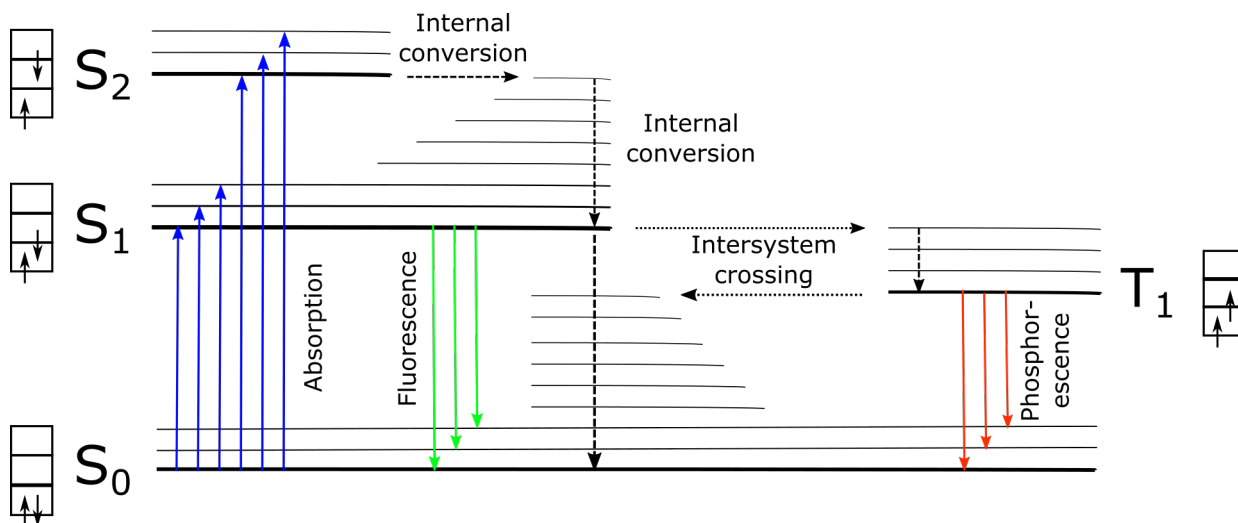


Figure 2.3.: Jablonski diagram illustrating the electronic singlet states (S_0 , S_1 , S_2 ,) and triplet state (T_1). Small arrows show the spin configuration of the electrons. Absorption as well as various deactivation processes (internal conversion, fluorescence and phosphorescence) are indicated. Intersystem crossing may occur due to weak spin-orbit coupling under a spin-flip. [25]

The intensity of emerging vibronic modes in absorption and photoluminescence spectra can be described by the Franck-Condon principle. [27–29] The principle is demonstrated on the basis of a potential energy diagram of a diatomic molecule in Figure 2.4. The energy scheme in the ground and first excited state is approximated utilizing Morse-like potentials. As a consequence

of deformation of the molecule upon excitation, the equilibrium position of the nuclei in S_1 is varied in comparison to that of S_0 , illustrated by the shift in the nuclear coordinate. In the term scheme, the vibrational energy levels of the ground and first excited state ($\nu = 0 - 4$ and $\nu' = 0 - 4$) are shown, as well as the corresponding vibrational wave functions.

Upon absorption, electronic transitions occur on an ultrafast time scale in the range of 10^{-15} s, and hence are much faster than the motion of the nuclei. Thus, absorption of a photon leads to a vertical electronic transition in the energy diagram, as shown in Figure 2.4. The Franck-Condon principle states that the probability for a specific vibrational transition to occur is proportional to the square of the overlap of the vibrational wave functions of the initial and the final state. For the given example depicted in Figure 2.4, the transition between the vibronic ground state of the electronic ground state (S_{0-0}) and the second vibronic energy level of the first excited state (S_{1-2}) is favored. Accordingly, a maximum is obtained for this transition in the absorption spectrum. The entirety of vibronic transitions belonging to an electronic state is called vibronic progression.

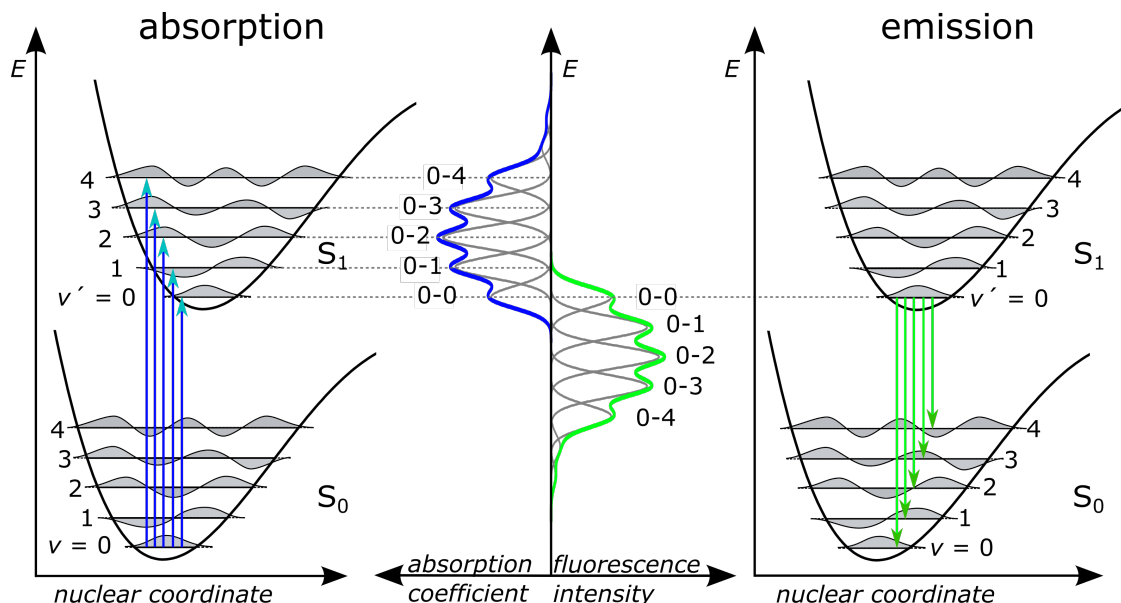


Figure 2.4.: Potential energy curves of the ground and first excited singlet state. The absorption and fluorescence intensity distribution can be explained according to the Franck-Condon principle. Adapted from [30].

In case, no chemical reaction or charge transfer occurs, an excited molecule relaxes back to its ground state. All excited states but S_1 and T_1 , have a very short life time. These states dissipate their excess energy into heat via vibronic sublevels under spin conservation as illustrated in Figure 2.3. The corresponding process is called internal conversion (IC) and takes place on an ultrashort time scale, ranging from sub-picoseconds to picoseconds. The lowest vibronically excited states S_{1-0} and T_{1-0} however, typically have life times of $10^{-12} - 10^{-8}$ s for S_{1-0} and $10^{-6} - 20$ s for T_{1-0} . [15] Radiative transitions $S_1 \rightarrow S_0$ and $T_1 \rightarrow S_0$ are called fluorescence and

phosphorescence, respectively. Due to the inherent deactivation times, radiative emission almost exclusively takes place from the lowest electronically and vibronically excited state of a given multiplicity (Kasha's rule). [31] As illustrated for the $S_1 \rightarrow S_0$ transition in Figure 2.4, emission takes place into the vibronic sublevels of the ground state and can also be described in the framework of the Franck-Condon principle.

Non-radiative transitions between the singlet and triplet system of a molecule are called intersystem crossing (ISC) and are reported to occur on a time scale on the order 10^{-8} - 10^{-3} s, depending on the position of the participating energy states and the strength of the spin orbit coupling. [32] Such transitions involve a spin-flip and therefore, are generally spin forbidden. However, due to weak coupling between electron spin and orbital angular momentum (spin-orbit coupling), ISC becomes partly allowed. Since spin-orbit coupling scales with the atomic number Z^4 , this process in particular becomes important with increasing number of heavy atoms, such as for instance Pt or Ir, which are frequently utilized in triplet emitters in organic light emitting diodes. [15, 22, 33]

2.3. Excitons

2.3.1. Types of Excitons

Excitons are Coulomb-bound electron-hole pairs, which can be generated in insulators or semiconductors. They can form upon absorption of light or by mutual capturing of free electrons and holes. [34] Excitons do not carry net charge and hence, are almost unaffected by the presence of an electric field. However, these quasi-particles with momentum $\vec{p} = \hbar\vec{k}$ can transport their inherent potential energy through solid states by diffusion. Here \hbar denotes the Planck constant and \vec{k} the wave vector. In order to generate excitons by absorption of light, at least the energy of the optical band gap E_{opt} has to be provided, which is determined by the energy difference of the electronic transport band gap E_{gap} (see Figure 2.2) and the exciton binding energy E_{bind} :

$$E_{opt} = E_{gap} - E_{bind}. \quad (2.2)$$

Excitons are classified into two different limiting cases, the so-called Frenkel and the Wannier-Mott exciton. These types of excitons are distinguished according to their electron-hole separation distance and related energy. [15] In conventional inorganic semiconductors, Wannier-Mott excitons form, which are delocalized over several constituents as depicted in Figure 2.5. [35, 36] Due to their high dielectric constants, electron-hole pairs are only weakly Coulomb-bound. For instance, in case of silicon ($\epsilon_r = 11.7$), Wannier-Mott excitons exhibit a binding energy of approx. 10 meV. Accordingly, the thermal energy at room temperature of 25 meV is sufficient to instantaneously dissociate those Wannier-Mott excitons within a p/n-junction into free charge carriers. [22]

In contrast, upon absorption of light in organic semiconductors, Frenkel excitons are generated. Owing to the weak intermolecular van der Waals forces, they are characterized by their small spatial dimensions with the wave function of a Frenkel exciton being predominantly located on a single molecule, as schematically depicted in Figure 2.5. Moreover, due to low dielectric constants of organic semiconductors ($\epsilon_r = 3 - 5$) Frenkel excitons are generally strongly Coulomb-bound. Typically, exciton binding energies are reported to range between 0.1 eV and 1.0 eV. [37,38] Thus, absorption of light in organic semiconductors, generally does not yield free charge carriers at room temperature, since the thermal energy is not sufficient to dissociate these Frenkel excitons into free electrons and holes.

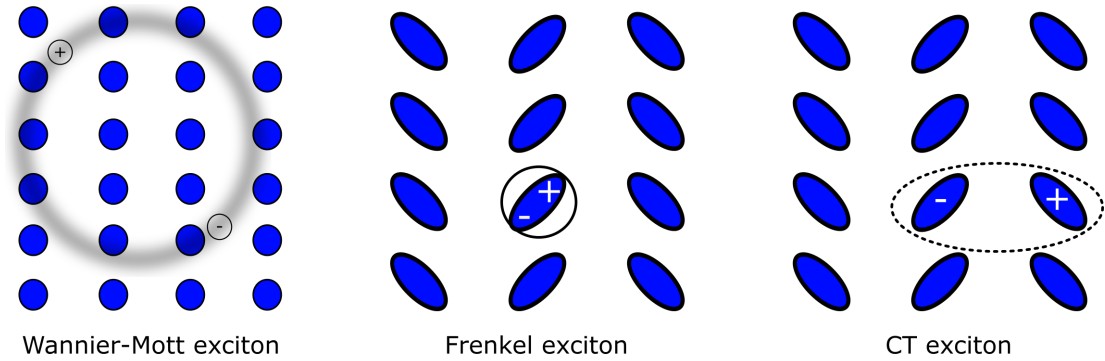


Figure 2.5.: Schematic depiction of different types of excitons: Wannier-Mott excitons are delocalized over several constituents of a solid state and are typically observed in inorganic semiconductors. In contrast, in organic semiconductors, predominantly Frenkel excitons form, which are localized on a single molecule. CT excitons are comprised of an electron-hole pair located on adjacent molecules. Adapted from [15].

In organic semiconductors, also charge-transfer (CT) excitons can form. As shown in Figure 2.5, a CT exciton is comprised of an electron-hole pair located on neighboring molecules. Hence, such excitons inherently feature a static electric dipole moment, polarizing their surrounding environment, which ultimately leads to screening of the charges. CT excitons can be generated in homo-nuclear layers. Optical characteristics of perylene-based compounds were found to be determined by a superposition of neutral Frenkel excitons and CT excitons on adjacent molecules. [39] The dimer structure in the unit cell yields an emission contribution from the associated excimer complex. [40] Moreover, optical characterization of the organic semiconductor diindenoperylene revealed a quantum mechanical superposition of Frenkel and CT excitonic states. [41] Furthermore, for plain fullerene C_{60} thin films the simultaneous formation of both exciton types is reported upon absorption. [42] However, in comparison to Frenkel excitons, the oscillator strength f of CT excitons is considered much weaker, for example $10^2 - 10^4$ times in case of anthracene in homo-nuclear molecules, generally yielding very weak optical excitation of CT excitons. [15]

CT excitons may also be generated at a heterointerface between two distinct organic materials. This process constitutes an important intermediate step in the generation of free charge carriers in organic photovoltaics (OPV). Hetero-CT excitons can either be generated upon absorption,

again at small oscillator strength, or due to diffusion of Frenkel excitons to such a heterointerface, accompanied by subsequent charge transfer across the heterojunction.

2.3.2. Exciton Transport in Organic Semiconductors

Excitons generated in organic semiconductors transfer their energy predominantly by diffusion based on incoherent hopping processes. [22, 43] The diffusion of excitons can be described by a differential equation of second order, taking into account the continuity equation in combination with Fick's first law:

$$\frac{\partial n(z, t)}{\partial t} = D \frac{\partial^2 n(z, t)}{\partial z^2} - \frac{n(z, t)}{\tau} + G(z, t). \quad (2.3)$$

Here $n(z, t)$ denotes the exciton concentration at position z at time t and accordingly, $n(z, t)/\tau$ represents a recombination term, with τ being the exciton life time. $G(z, t)$ is an exciton generation term. The first term on the right hand side of Equation 2.3 describes exciton motion caused by diffusion as a consequence of a gradient in the exciton density. Under steady-state conditions, as given in the opto-electronic experiments presented in this thesis utilizing continuous illumination, the time dependent term $\partial n(z, t)/\partial t$ becomes zero. The diffusion coefficient D connects the life time of an exciton with its average diffusion length L_D , which constitutes an important quantity for opto-electronic devices, as it represents the distance, an exciton can travel before recombination, i.e. before it gets lost: [44, 45]

$$L_D = \sqrt{D \cdot \tau}. \quad (2.4)$$

The diffusion coefficient is proportional to the sum of transfer rates of the individual exciton transport processes, namely cascade energy transfer, Förster resonant energy transfer and Dexter energy transfer which are described in more detail in the following. [46, 47]

Cascade Energy Transfer

Cascade energy transfer denotes a radiative energy transport mechanism caused by the decay of an exciton under emission of a photon (fluorescence or phosphorescence) and subsequent absorption of this photon by another molecule. Accordingly, this energy transport process is commonly called "reabsorption" and may occur on a length scale corresponding to the absorption depth of the material. A prerequisite for this process to occur is the overlap of the corresponding emission and absorption spectra of the participating molecules, as well as an appropriate alignment of the transition dipole moments. Triggering the energy transfer, exciton life time evidently is decisive for the reabsorption process. In state of the art organic solar cells, exciton life time exceeds the time necessary to promote other energy transfer processes, rendering cascade energy transfer negligible. [46, 48]

Förster Resonant Energy Transfer (FRET)

Diffusion of singlet excitons in organic semiconductors is predominantly described in terms of an incoherent Förster resonant energy transfer. [47, 49] Such an energy transfer is based on non-radiative dipole-dipole interaction between a donor and an acceptor molecule. The Förster resonant energy transfer rate k_F is given by:

$$k_F = \frac{1}{\tau_0} \left(\frac{R_0}{r} \right)^6. \quad (2.5)$$

Here, τ_0 represents the fluorescence life time of the singlet exciton, r is the distance between the donor and acceptor molecule and R_0 is the so-called Förster radius, which denotes the distance, at which the fluorescence probability equals the probability of the energy transfer. [47, 50] The Förster radius is dependent on the overlap of the normalized fluorescence spectrum of the donor $F_D(\lambda)$ and the normalized absorption cross section of the acceptor $\sigma_A(\lambda)$, as well as on the dipole orientation factor κ according to:

$$R_0^6 = \frac{9 \cdot \phi \cdot \kappa^2}{128\pi^5 \cdot n^4} \int \lambda^4 \cdot F_D(\lambda) \cdot \sigma_A(\lambda) d\lambda. \quad (2.6)$$

Here, n denotes the refractive index, ϕ photoluminescence efficiency and λ the wavelength. [50] Förster resonant energy transfer is reported to take place on length scales of $R_0 = 1 - 10$ nm and thus, exceeds intermolecular distances of approximately 1 nm by up to one order of magnitude. [51–53]

Dexter Energy Transfer

Short range multipole interaction and electron exchange is included in the framework of Dexter energy transfer. [54] As a consequence of the overlap of electron densities of an excited donor molecule and the ground state of an adjacent acceptor molecule, energy transfer takes place non-radiatively via electron exchange. The corresponding transfer rate $k_D(d)$ is given by: [22]

$$k_D(d) = K \cdot J \cdot \exp\left(-\frac{2d}{L}\right). \quad (2.7)$$

Here K refers to the orbital interaction, J represents the spectral overlap integral, normalized to the extinction coefficient of the molecule in the ground state. Additionally, L is the sum of the van-der-Waals radii of the donor and the acceptor and d their distance. As a consequence of the exponential dependence of the transfer rate, Dexter transfer is a short range energy transfer, occurring between neighboring molecules on a length scale of 0.1 - 1 nm. [46] Energy transfer in molecular triplet manifolds is considered to be mainly determined by Dexter energy transfer in case of singlet ground state systems. [49]

2.4. Charge Carrier Transport

Transport of charge carriers is of paramount importance for opto-electronic devices, such as organic light-emitting diodes, field-effect transistors or solar cells. In OPV, charge carriers have to be transferred from the D/A heterojunction to the electrodes before recombination takes place, in order to extract a macroscopic photocurrent. In contrast to excitons, free charge carriers are accelerated in presence of an electric field $F(\vec{x})$. The mobility of charge carriers $\underline{\mu}$ connects the electric field with the drift-velocity $\vec{\nu}_D(x)$ according to:

$$\vec{\nu}_D(x) = \underline{\mu} F(\vec{x}). \quad (2.8)$$

The electron current density $j_n(x)$ in an acceptor phase of a photovoltaic device is given by: [55]

$$j_n(x) = q \cdot n_n \cdot \underline{\mu}_n \vec{F}(x) + q \cdot D \nabla n_n(x). \quad (2.9)$$

$$D = \frac{k_B \cdot T}{q} \cdot \underline{\mu}_n. \quad (2.10)$$

Here q denotes the elementary charge, n_n the electron density, $\underline{\mu}_n$ the electron mobility, D the diffusion constant, k_B the Boltzmann constant and T the temperature. A corresponding equation exists for the hole current density $j_p(x)$ in the donor phase. The first summand in Equation 2.9 represents the drift contribution and the second summand the diffusion contribution to the electron current density. Due to distinct charge carrier density gradients in planar organic solar cells, the latter contribution is the dominant factor. [56]

As limiting cases, two different charge carrier transport mechanisms can be discerned, which show distinct characteristics with respect to mobility as a function of temperature and electric field. In the following, coherent band transport and transport via incoherent, thermally activated hopping will be discussed. In case of the former, transport is considered to be determined by quasi-free charge carriers, which are scattered by crystal defects or phonons.

Coherent Transport

Many organic crystals, for instance polyacene crystals such as anthracene or naphthalene, have been grown with excellent purity, containing only few defects or traps. [57] In such ultrapure molecular crystals, Bloch-states can form upon linear combination of the localized states, yielding a band structure in analogy to inorganic crystals. [15,58] In comparison to their covalently bound inorganic counterparts, these organic crystals feature a narrow bandwidth W of only a few hundred meV, as a consequence of the less pronounced intermolecular van-der-Waals interaction

(see section 2.1.2). Mobilities of 1 - 10 cm²/Vs at room temperature have been reported for such polyacene single crystals. [19] For coherent band transport to prevail, the mean scattering time τ of charge carriers has to exceed \hbar/W . [22]

$$\tau \gg \hbar/W. \quad (2.11)$$

For instance, for typical bandwidths of polyacene single crystals of 0.1 eV - 0.5 eV, the mean scattering time must be $> 10^{-15}$ s to allow for charge transport description by a coherent band model. [15] To enable coherent transport, delocalization of charge carriers must extend at least over a couple of unit cells, demanding for the mean free path of the charge carriers λ to be large in comparison to the lattice constant a_0 . [15] Scattering events of charge carriers with phonons are considered the limiting factor for the mobility μ in this approach. In turn, the occupation of phonon states increases as a function of temperature T and thus, the mobility for coherent band transport in general decreases with T according to:

$$\mu \propto T^{-n}. \quad (2.12)$$

The exponent n depends on the dominating scattering mechanism and the bandwidth. For example, for broad bands ($W \gg k_B T$) and scattering by acoustic phonons a value of $n = 3/2$ has been observed. [22] Only at very low temperatures these acoustic phonons are frozen out, resulting in a reverse temperature behavior of $\mu \propto T^{\frac{3}{2}}$, due to scattering from charged defects. [59] Complementary theoretical and experimental results revealed the conditions for coherent band transport to be fulfilled according to Equation 2.11, for example in ultrapure naphthalene single crystals within the (ab) plane for $T < 150$ K. [15,57] However, already at room temperature this is no more the case, even for many highly ordered crystals and thus, in that case charge transport is considered to be rather a mixture of coherent and incoherent processes. [22] The electronic transport in polycrystalline or amorphous thin films in turn, has to be described in terms of incoherent hopping. [15]

Incoherent Transport

In case of amorphous or polycrystalline organic thin films, the mean free path of charge carriers is smaller than the intermolecular distance (*vide supra*). Hence, the concept of band conduction is no longer valid. Instead, energetic states contributing to transport localize predominantly on the individual molecular sites. These energy levels are randomly distributed due to energetic and spatial disorder. [60] The former is due to the variation of the surrounding polarizability of the individual molecules, whereas the latter is caused by impurities, defects and grain boundaries, typically yielding a modulation in absolute energy values in the range of 10^{-1} - 10^{-2} eV. [61]

As a consequence, thermally activated incoherent hopping between these localized states appears to be the dominant transport mechanism and, in contrast to coherent transport, a different temperature dependence is observed, resulting in an enhanced mobility at higher temperatures. Such hopping transport usually yields mobilities orders of magnitude smaller in comparison to coherent transport in organic single crystals. Among highest mobilities reported, values are in the range of 10^{-3} cm²/Vs, but in many compounds mobilities are orders of magnitude lower. [15,19] Several different theoretical approaches have been proposed to describe thermally activated transport in disordered media. [59,62,63] Two of the most frequently utilized models will be discussed exemplarily in the following.

Gaussian Disorder Model (GDM)

A model incorporating energetic and spatial disorder was introduced for the first time by Bässler, describing transport of charges by their hopping in a regular array of discrete energetic sites. [60] In this model, the energy distribution of the localized states is represented by a Gaussian density of states $g(E)$, due to the statistical nature of disorder:

$$g(E) = \frac{1}{\sqrt{2\pi}\sigma} \cdot \exp\left(-\frac{E^2}{2\sigma^2}\right). \quad (2.13)$$

Here, σ denotes the width of the Gaussian distribution of states and E the energy difference relative to the center of the density of states. Such a Gaussian density of states is displayed in Figure 2.6. The hopping rates are considered to depend on the spatial distance and the energy difference between individual sites. This is accounted for in Miller-Abrahams hopping rates for charge carriers $\nu_{i \rightarrow j}$ from an initial occupied state i to a final unoccupied state j : [63,64]

$$\nu_{i \rightarrow j} = \nu_0 \cdot \exp(-2\gamma R_{ij}) \left\{ \begin{array}{ll} \exp\left(-\frac{E_j - E_i}{k_B T}\right) & \text{for } E_j > E_i \\ 1 & \text{for } E_j \leq E_i \end{array} \right\}. \quad (2.14)$$

The pre-factor ν_0 represents the attempt to escape frequency, γ the inverse localization length, R_{ij} denotes the distance between the two hopping sites, and $E_j - E_i$ their energy difference. The first exponential term in 2.14 describes tunneling of charge carriers. If the energy of the initial state E_i is lower than that of the final state E_j , thermal energy is necessary to induce a hopping event. This requirement is considered by the Boltzmann-factor in Equation 2.14. In contrast, energetic down-hill charge transfer is possible without restriction in case $E_i \geq E_j$.

Utilizing Miller-Abrahams hopping rates in combination with the energy distribution approximated by a Gaussian density of states in Monte Carlo simulations yields an equation describing the mobility in dependence of temperature T and electric field F : [63]

$$\mu(\sigma, \Sigma, T, F) = \mu_0 \exp \left[- \left(\frac{2\sigma}{3k_B T} \right)^2 \right] \exp \left[C \cdot \left\{ \left(\frac{\sigma}{k_B T} \right)^2 - \Sigma^2 \right\} \sqrt{F} \right]. \quad (2.15)$$

Here μ_0 represents the zero-field mobility, C an empirical constant and Σ an effective spatial disorder parameter. This description is known as the Gaussian Disorder Model (GDM) and treats charge carrier transport as a thermally activated tunneling process. In various experiments, the temperature dependence of transport was successfully reproduced by the GDM, rather than by an Arrhenius-type activation ($\mu \propto \exp(-\frac{E_A}{k_B T})$). [64–67] Moreover, 2.15 is predicting a Poole-Frenkel like field dependence with $\mu \propto \exp(\sqrt{F})$. However, in 2005 experimental results by Rubel et al. had shown charge carrier density dependent mobilities, not being explainable by the GDM model. [68] This requirement is met in the multiple trapping and release model.

Multiple Trapping and Release Model (MTRM)

The Multiple Trapping and Release Model (MTRM) is an extension of the GDM model introducing the concept of an effective transfer energy, known from inorganic semiconductors. [69,70] In this framework, excited charge carriers thermalize by hopping events to the lowest energetic site available for $T = 0$ K (see Figure 2.6, case I). At higher temperatures, charge carriers are thermally activated according to Equation 2.14. In the MTRM, hopping transport is described around the so-called transport energy E_{tr} , which represents the energy at which the probability of a charge carrier to thermalize to a lower energy and the probability for thermal excitation are equal. [71,72] Charge carriers occupying states below E_{tr} are considered immobile. In the MTRM the impact of such trap states, arising at lattice defects or impurities, on charge carrier motion is accounted for. Trapped charge carriers are released after a residence time τ_t by thermal excitation above the transport energy, as depicted in case II of Figure 2.6. A charge carrier located in a state higher in energy than E_{tr} is assumed to be delocalized and is described in the picture of band transport until another trapping event occurs after a time τ . This model has important implications for the description of transport in disordered media, e.g. for charge transfer to occur, an available state has to be in reach at a given temperature, otherwise the charge carrier is permanently trapped. Therefore, in the MTRM the ratio ϑ between the densities of free n_c and trapped charge carriers n_t can be defined as:

$$n = n_c + n_t = n_c \left(1 + \frac{1}{\vartheta} \right). \quad (2.16)$$

Here n denotes the total charge carrier density in the system. Upon increased charge carrier density, the difference between the Fermi-energy E_F and E_{tr} becomes smaller (see Figure 2.6),

yielding more available states for mobile charge carriers and thus, the effective mobility is enhanced. [73] The effective mobility μ_{eff} reads:

$$\mu_{eff}(T) = \mu_0(T) \left(1 + \frac{\tau_t}{\tau}\right)^{-1} = \mu_0(T) \left[1 + \frac{N_t}{N_0} \cdot \exp\left(\frac{E_t}{k_B T}\right)\right]. \quad (2.17)$$

Here μ_0 represents the defect-free mobility, N_t the trap density, N_0 the effective density of states and E_t the energy difference between the trap states and the transport energy. [74]

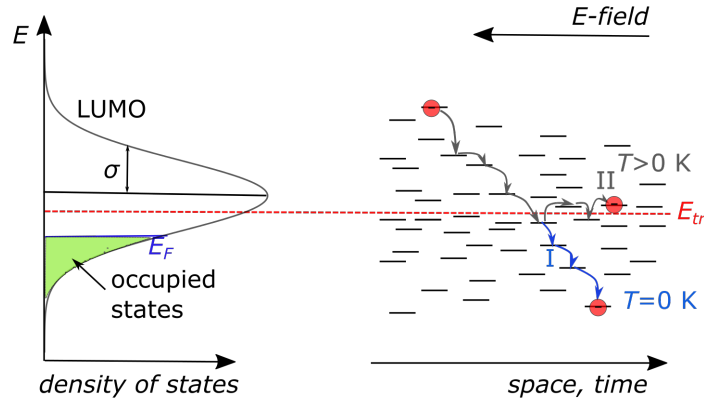


Figure 2.6.: In the Gaussian Disorder Model (GDM) a Gaussian distribution of the density of states is assumed. For $T = 0$ K (case I), an injected charge carrier relaxes by phonon-assisted tunneling to the lowest energetic state available, according to 2.14. At higher temperatures (case II), an equilibrium between relaxation and thermally induced activation occurs. In the Multiple Trapping and Release Mode (MTRM) the energy, around which the equilibrium occurs is called the transport energy E_{tr} . After [72].

3. Fundamentals of Organic Photovoltaic Cells (OPVCs)

The characteristic properties of organic semiconductors, illustrated in the previous chapter, distinctly determine the device architecture, as well as the functional principle of organic photovoltaic cells. Due to the high absorption coefficients of organic semiconductors ($\alpha \approx 10^5 \frac{1}{cm}$), absorber layer thicknesses in the range of a few hundred nm are sufficient to absorb a large amount of the incident light. [12] Hence, little material consumption is required for the production of OPVCs, utilizing established preparation processes. In case of polymers, processing can be carried out wet-chemically by spin coating or doctor blading. In contrast, small molecular compounds are predominantly deposited via sublimation under vacuum conditions, but also solution processes gaining more and more interest, enabling light weight and flexible devices. Upon absorption of light in conventional inorganic photovoltaic devices, such as silicon solar cells, the generated Wannier-Mott excitons are split into free charge carriers at a p/n junction at room temperature. In contrast, absorption by organic semiconductors under these conditions leads to the generation of strongly Coulomb-bound Frenkel excitons. Early organic photovoltaic cells were comprised of a single absorber layer, sandwiched between two electrodes of different work function. In such Schottky-cells, excitons are separated due to the electric field, established by the Schottky-barrier at the absorber/electrode interface. However, the dissociation process has a rather low efficiency due to high recombination losses at the electrode and the loss of charge carriers of opposite sign upon their travel to the counter electrode. Utilizing a single chlorophyll absorber layer, Tang achieved a power conversion efficiency of the order of 10^{-3} % in 1975. [58] Another thorough investigation of a Schottky-junction, comprised of a merocyanine absorber layer, was carried out by Ghosh, including a comprehensive theoretical model to elucidate the photovoltaic behavior of Schottky-junctions. [75]

In 1986, Tang achieved a quantum leap in terms of exciton dissociation efficiency by the introduction of a second absorber layer, forming a so-called donor/acceptor (D/A) heterojunction configuration. The photo-active region of this planar bilayer solar cell was comprised of a metal phthalocyanine in combination with a perylene derivative. [58] Today, such a D/A heterojunction is still at the heart of “any state of the art” organic photovoltaic cell. [8, 76]

Therefore, the working principle of OPVCs, comprising a D/A heterojunction, will be discussed exemplarily for a planar bilayer architecture in the following, covering the important steps in the photon to current conversion. Subsequently, alternatives to the planar bilayer design will briefly

be presented and finally, this chapter ends with a discussion of the key parameters deduced from the characteristic current density-voltage $j(V)$ curves.

3.1. Working Principle of OPVCs: The Donor/Acceptor (D/A) Heterojunction

In general, a D/A heterojunction is comprised of two distinct semiconducting materials forming a common interface. The material featuring higher frontier orbital energies is called the electron donor, whereas the other compound is denoted the electron acceptor. In planar bilayer solar cells, donor and acceptor layers are stacked on top of each other and the D/A heterojunction is sandwiched between two electrodes, as schematically displayed in the energy diagram in Figure 3.1. The work function difference of the anode Φ_A and cathode Φ_C is referred to as the built-in potential eV_{bi} , creating an intrinsic electric field.

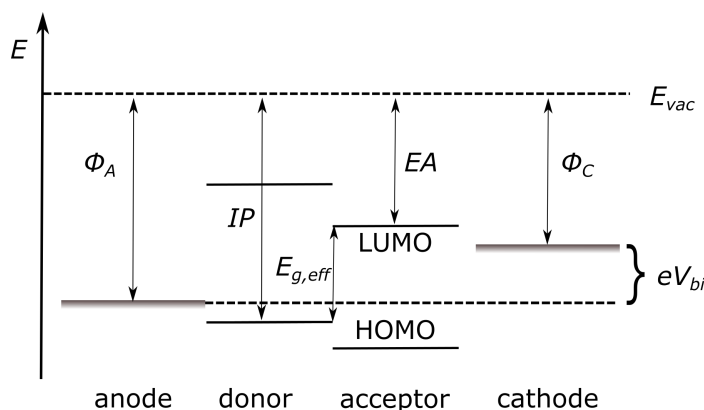


Figure 3.1.: Energy diagram of a planar bilayer solar cell, comprising a D/A heterojunction sandwiched between two electrodes. The absorber materials differ in their frontier orbital energies, yielding an energetic drop at the common interface to drive exciton dissociation. IP and EA represent the ionization potential and the electron affinity of the donor and acceptor material, respectively, determining the effective band gap $E_{g,eff}$ at the interface. The energy difference of the work functions of the electrodes generates the built-in potential eV_{bi} . For sake of simplicity the vacuum level E_{vac} is assumed to be constant.

The energy necessary to induce dissociation of strongly Coulomb-bound excitons into free charge carriers is provided at the donor/acceptor heterointerface. The relevant steps of photon to current conversion are shown for a planar bilayer solar cell in Figure 3.2 under short circuit conditions. As a consequence, the work functions of the electrodes are equilibrated, forcing a band bending in the organic layers. The processes will be discussed for an initial excitation of the donor material. A description of the photoconversion upon absorption in the acceptor material proceeds analogously.

Steps of Photon to Current Conversion

a) Absorption of a photon, exceeding the energy of the optical band gap E_{opt} of the donor, creates a strongly Coulomb-bound exciton with an exciton binding energy of typically 0.1 - 1.0 eV. [38] The optical band gap equals the energy difference between the transport band gap E_{gap} and the exciton binding energy E_{bind} .¹

b) Photogenerated excitons are transported across the absorber layer by diffusion. The exciton diffusion length is a critical quantity for exciton transport, as it constitutes the distance, the exciton can travel before recombination occurs. [45] Hence, L_d determines whether the exciton can reach the potentially dissociating D/A acceptor interface. Exciton diffusion lengths of organic semiconductors are typically in the range of nanometers to a few tens of nanometers, ultimately limiting the layer thickness for light harvesting. [49]

c) In case an exciton reaches the D/A interface during its lifetime, it can dissociate, if it is energetically favorable for the electron of the donor to undergo a charge transfer into the LUMO of the acceptor, generating a CT exciton, which also is referred to as bound polaron pair. [12] Veldman et al. reported on a required energetic offset of at least 0.1 eV to induce CT formation. [77] For various material combinations, charge transfer is reported to occur on an ultrashort time scale within 10^{-14} to 10^{-13} s. [42, 78] Hence, exciton dissociation occurs much faster than competing deactivation processes (see Section 2.2), rendering this process typically very efficient, often with almost unity efficiency. [78, 79]

d) Subsequent to CT formation, separation of the Coulomb-bound geminate pair, is still required to gain free charge carriers. If this process does not proceed within the life time of the CT state, geminate recombination occurs. [43, 80] Due to the increased electron-hole distance of the CT state, the exciton binding energy is decreased compared to the initial Frenkel exciton. As a consequence of the energetic offset at the D/A interface, the CT state formed often possesses excess energy, which is referred to as “hot CT-exciton state”, allowing for larger separation distances, at which the electron is considered to be thermalized with respect to its initial state in the acceptor. If the distance between the charge carrier pair exceeds the Coulomb capture radius, dissociated free charge carriers are generated. [62, 81]

e) After exciton dissociation, charge carrier transport is mainly driven by a diffusion current due to the gradient in charge carrier density at the D/A heterojunction (see Equation 2.9). Moreover, there is a drift current contribution as a consequence of the internal electric field. The internal electric field is created by the work function difference of the electrodes and, as

1

- It is common practice to draw the bound electron hole pair, with the electron state $E_{bind}/2$ below the LUMO and the hole $E_{bind}/2$ above the HOMO energy (see Figure 3.2). However, it is to be noted that this illustration does not accurately describe the real energetic picture, since the excitonic state is a neutral two-particle state, whereas HOMO and LUMO energies are determined for charged single particle states.

the case may be, by a modification of the electric field due to charge carrier accumulation zones within the device.

f) Finally, charge carriers are extracted at the respective electrodes, generating a macroscopic photocurrent in the outer circuit. By the choice of electrode materials, potential contact barriers can be adjusted to support efficient extraction of charge carriers.

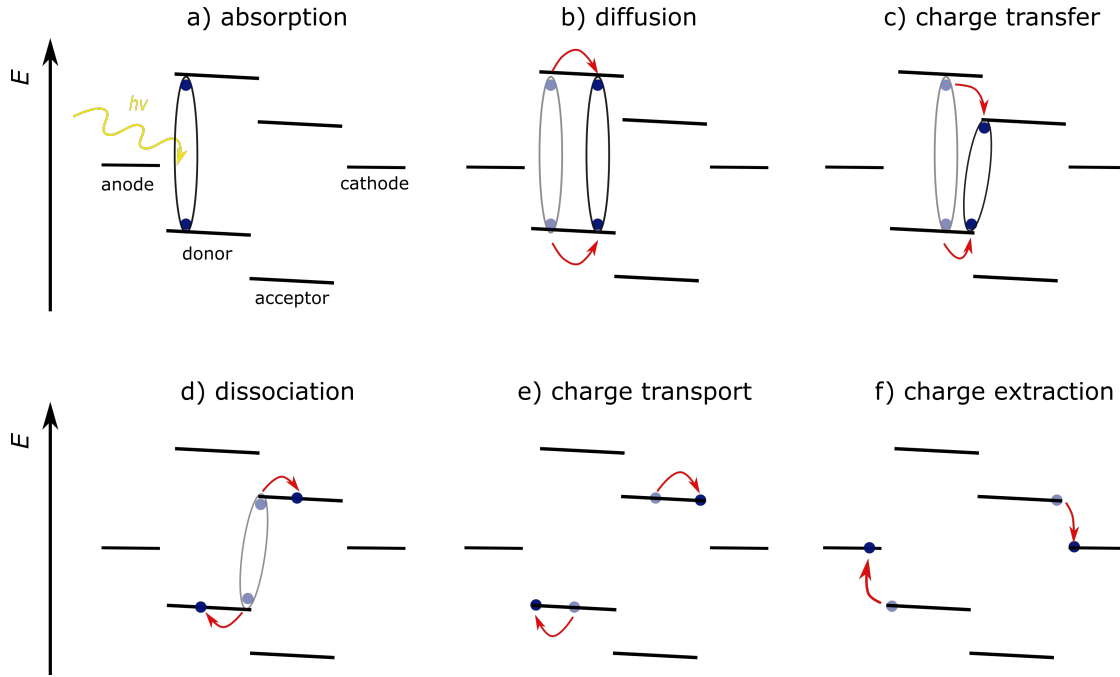


Figure 3.2.: Step by step illustration of the processes involved in photoconversion by a planar D/A heterojunction solar cell: a) Absorption of a photon, generating a strongly Coulomb-bound exciton in the donor. b) Exciton motion across the thin film, caused by diffusion. c) Charge transfer of an electron from the LUMO of the donor to the LUMO of the acceptor induced by the potential drop at the D/A interface. d) Separation of bound CT exciton into free charge carriers. e) Transport of charge carriers across the photo-active layers. f) Charge extraction at the electrodes.

In particular, a fully comprehensive picture of the steps c) and d) is not yet available. The role of excess energy in the course of the CT dissociation is still controversially debated. Ohkita et al. showed a similar CT formation yield, for an excess energy of 0.6 - 1.0 eV, but the dissociation efficiency varied by two orders of magnitude, increasing with the energy offset at the interface. [79] This indicates excess energy to be a crucial parameter for CT exciton dissociation. However, a related study by Clarke et al. demonstrated high CT dissociation yield for an energy offset < 0.2 eV. [43] Aiming to qualitatively assess the dissociation of excitons into free charge carriers at the D/A interface, CT formation and dissociation into free charge carriers can be considered as a combined step in a simplified approach. As an approximation, a dissociation into fully separated charge carriers is assumed possible in case the energy offset at the D/A interface is larger than the binding energy of the initial Frenkel exciton. [12]

The external quantum efficiency ($EQE(\lambda)$) of an organic solar cell denotes the number of extracted charge carrier pairs divided by the number of incident photons spectrally resolved. This quantity is expressed by the product of the respective efficiencies of the processes a) - f) described above:

$$EQE(\lambda) = \eta_{Abs}(\lambda) \cdot \eta_{Diff} \cdot \eta_{CT} \cdot \eta_{CC}. \quad (3.1)$$

Here $\eta_{Abs}(\lambda)$ represents the spectrally resolved absorption efficiency and η_{Diff} the efficiency of exciton diffusion to the D/A interface. Charge transfer and dissociation into free charge carriers are summarized together in the efficiency η_{CT} , just as the processes of charge transport and extraction in the charge carrier collection efficiency η_{CC} .

3.2. Solar Cell Architectures

Since the introduction of the first planar bilayer cells with a power conversion efficiency of approx. 1% in the 1990s (*vide supra*), solar cell efficiencies have been improved continuously, today exceeding 13 %. [8] In part, this increase can be attributed to the implementation of amended absorber materials but also to advanced device architectures, such as the bulk-heterojunction (BHJ) or multi-junction design. [76,82] Accounting for generally low exciton diffusion lengths in organic semiconductors, the BHJ concept is based on an interpenetrating D/A network. This is experimentally realized by co-evaporation of the molecular compounds or by solution processing in case of polymers. [83–85] Due to the interpenetrating character of the photo-active region the probability of photo-generated excitons to reach a dissociating D/A interface is strongly enhanced. [86] In multi-junction devices two or more individual solar cells are stacked on top of each other, typically in a serial connection, employing a recombination layer sandwiched between the individual sub-cells. Availing such device design, the resulting voltage is determined by the sum of the individual-sub cells. [87] Those stacked sub-cells often feature different optical gaps with respect to each other. Therefore, a combination of complementary absorber materials can be utilized to cover a broad spectral range. [88]

Also, striving for widening the spectral absorption range, a further development of the initial planar heterojunction lately attracted attention. In so-called cascade solar cells, one or several additional absorber layers are implemented such that an energy cascade is established at the D/A junction, which supports energy or charge carrier transfer across the multilayer stack. [89–91] In such a three layer stack, the interlayer between donor and acceptor may enable exciton dissociation at both interfaces, yielding larger photocurrents. Besides extending the absorption range, photocurrent enhancement in cascade solar cells has widely been associated with reduced recombination losses. [4,91,92] Following this approach a remarkable power conversion efficiency of 8.4 % for a fullerene-free three layer stack could be achieved. [4] Instead of explicitly aiming for increased absorption, cascade energy level alignment employing thin interfacial layers in the sub-monolayer thickness range has proven to remarkably increase the photocurrent output of

organic solar cells. Heidel et al. attributed an increase of the short circuit current density by approx. a factor of two to a destabilization of hetero-CT states by an additional intermediate molecular layer. [93]

3.3. Current Density-Voltage ($j(V)$) Characteristics

In Section 3.1, a planar bilayer cell was described under short circuit conditions, under which the solar cell generates the maximum photocurrent density. However, in an actual device under operating conditions, the current density is decreased, depending on the internal resistance of the cell and the resistance of the load. This electrical behavior can be accounted for by measuring the current density-voltage $j(V)$ characteristics of the solar cell, i.e. an external voltage is applied to the cell and the corresponding current density is measured. Such a $j(V)$ characteristics is exemplarily shown in Figure 3.3 in the dark and under illumination. Without illumination, the $j(V)$ curve ideally follows a diode characteristics, showing rectifying behavior. Under illumination, an additional current density contribution j_{ph} is obtained due to the photo-generated charge carriers. The diode characteristics can be described by the Shockley-Equation:

$$j(V) = j_s \cdot \exp \left[\left(\frac{e \cdot V}{n \cdot k_B \cdot T} \right) - 1 \right] - j_{ph}. \quad (3.2)$$

Here j_{ph} denotes the current density under illumination, j_s the saturated dark current density, e represents the elementary charge, V the voltage, n the ideality factor, k_B the Boltzmann constant and T the temperature. Describing a real solar cell with active area A , parasitic parallel R_p and series resistances R_s have to be considered. [94]

$$j(V) = j_s \cdot \exp \left[\left(\frac{e \cdot (V - j(V) \cdot R_s \cdot A)}{n \cdot k_B \cdot T} \right) - 1 \right] - j_{ph} + \frac{U - j(U) \cdot R_s \cdot A}{R_p}. \quad (3.3)$$

A decreased parallel resistance may occur due to partial shortening of the photo-active layers upon electrode deposition. The series resistance for example depends on the bulk conductivity of the photo-active layers and the electrodes, but also on the contact resistances of all interfaces being present in the device. [95]

Important parameters that can be derived from the $j(V)$ characteristics under illumination are the short circuit current density j_{sc} , in case no external voltage is applied, and the open circuit voltage V_{oc} , at which the net current becomes zero.

The maximum achievable open circuit voltage of an organic solar cell is limited by the maximum quasi-Fermi-level splitting: [56]

$$eV_{oc\ max} = (E_{Fn} - E_{Fp})_{max}. \quad (3.4)$$

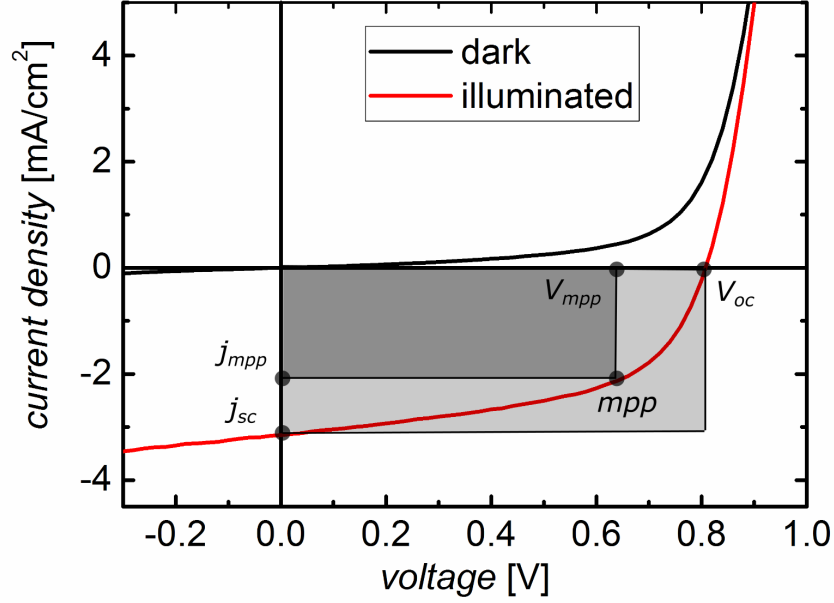


Figure 3.3.: $j(V)$ characteristics in the dark (black line) and under illumination (red line). Indicated are the short circuit current density j_{sc} and the open circuit voltage V_{oc} . j_{mpp} and V_{mpp} describe the current density and voltage, respectively, at the maximum power point mpp .

Here E_{Fn} and E_{Fp} represent the quasi-Fermi levels of electrons in the acceptor and holes in the donor material, respectively. Hence, as a first approximation, V_{oc} depends linearly on the energy difference between the HOMO of the donor and the LUMO of the acceptor, i.e. the so-called effective band gap, $E_{g,eff}$ (see Figure 3.1). Considering the effective doping of the absorber layers after exciton dissociation into free charge carriers, the open circuit voltage can be expressed as: [96]

$$e \cdot V_{oc} = E_{g,eff} + k_B \cdot T \cdot \ln \left(\frac{n_n \cdot n_p}{N_{LUMO\ acceptor} \cdot N_{HOMO\ donor}} \right).$$

Or in shorthand:

$$e \cdot V_{oc} = E_{g,eff} - \Delta. \quad (3.5)$$

Here k_B represents the Boltzmann constant, T the temperature, $n_n/N_{LUMO\ acceptor}$ and $n_p/N_{HOMO\ donor}$ the charge carrier doping concentrations of the acceptor and the donor layer, respectively. The loss term Δ in Equation 3.5 is reported to be 0.3 - 0.8 eV under standard illumination conditions (AM 1.5G) for various donor/acceptor material combinations and is attributed to radiative and non-radiative recombination losses. [4, 97–100]

The fourth quadrant of the $j(V)$ characteristics, i.e. the voltage range between 0 V and V_{oc} , describes the power generated by the solar cell. For voltages above $> V_{oc}$ charge carriers are injected into the device and the solar cell is operated like an organic light emitting diode. The power density, at which the product of the current density and the voltage reaches a maximum value in the fourth quadrant, represents the maximum power point mpp . The corresponding current density is denoted j_{mpp} and the voltage V_{mpp} . The fill factor is the ratio of the power density at the maximum power point and the maximum power density achievable (both power densities are illustrated by the two grey boxes in Figure 3.3):

$$FF = \frac{V_{mpp} \cdot j_{mpp}}{V_{oc} \cdot j_{sc}} . \quad (3.6)$$

Accordingly, the fill factor represents the “squareness” of the $j(V)$ curve. Low mobility of the photo-active materials, recombination losses, as well as parasitic parallel and series resistances are known to reduce the fill factor. [95] Hence, in general, this quantity represents a sensitive indicator on the transport properties of the device, however in a very complex manner.

The overall power conversion efficiency of a solar cell η is defined as the ratio of the power density at the maximum power point and the power density of the incident light P_L and hence, depends linearly on FF , V_{oc} and j_{sc} :

$$\eta = \frac{V_{mpp} \cdot j_{mpp}}{P_L} = FF \cdot \frac{V_{oc} \cdot j_{sc}}{P_L} . \quad (3.7)$$

Part II.

Materials, Solar Cell Architecture and Experimental Methods

4. Materials for Organic Photovoltaic Devices

In this chapter, the compounds utilized for organic photovoltaic cells are presented, starting with the electrode materials. Afterwards, compounds are introduced step by step, according to their appearance in the photovoltaic stack. The presentation of the hole conducting materials is followed by the demonstration of the respective donor and acceptor molecules. Finally, the employed exciton blocking material is introduced. Some of the photo-active materials, such as the fluorinated zinc phthalocyanines are only briefly introduced, since a detailed discussion of the photo-physical properties is subject of Part III of this thesis. Purification of the molecular semiconductors was carried-out by S. Hirschmann at the 3rd Physics Institute, University of Stuttgart.

4.1. Electrode Materials

Indium Tin Oxide (ITO)

The bottom anode, employed in photovoltaic devices, is comprised of indium tin oxide. The metal oxide consists of approx. 90 % indium (III) oxide (In_2O_3) and approx. 10 % of tin (IV) oxide (SnO_2). It is commonly used in organic electronics due to its unique opto-electronic properties. For instance, for layer thicknesses of approx. 100 nm, as utilized in this thesis, ITO has a high transparency of up to 90 % in the UV/VIS range. Moreover, the sheet resistance is typically small with $14.2 \Omega/\square$. [30] The work function is reported to range between 3.8 eV and 4.4 eV, depending on the chemical stoichiometry at the surface. [101–103] ITO was prepared by Dr. S. Höhla, Institute for Large Area Microelectronics, University of Stuttgart.

Silver (Ag)

For the metallic back contact silver is used. Ag has a conductivity of $6 \cdot 10^5 \text{ S/cm}$. [104] The density of Ag is 10.49 g/cm^3 and the sublimation temperature is approx. $960 \text{ }^\circ\text{C}$, allowing for deposition from a tungsten boat in vacuum. [105] The thickness of the Ag cathode is chosen 60 nm, yielding an opaque top contact. As a consequence, incident light is reflected at this back contact, thereby enhancing the absorption in the organic absorber layers. The work function of Ag depends on the surface morphology of its crystalline structure. Deposited on organic

compounds, Ag typically adopts a polycrystalline morphology with a work function of about 4.3 eV. [106, 107]

4.2. Hole Transport Materials

An extraction barrier caused by an energetic mismatch at the electrode/organic interface can lead to electronic transport limitations, resulting in deterioration of the macroscopic photovoltaic parameters. [108, 109] To avoid this issue, hole transport materials are implemented between the anode/organic interface of organic photovoltaic cells to enable transport via an energy ladder.

Poly(3,4-ethylenedioxythiophene):Poly-Styrenesulfonate (PEDOT:PSS)

In organic electronics the most frequently used hole transport material is the polymer mixture poly(3,4-ethylenedioxythiophene):poly-styrenesulfonate (PEDOT:PSS). Since PEDOT:PSS is an aqueous dispersion, layer deposition can be carried-out wet-chemically at room temperature for instance via spin-casting or doctor blading, warranting homogeneous film formation. The photo-physical properties rendering PEDOT:PSS an attractive material to apply in opto-electronic devices are its high transparency in the visible and its moderately high vertical conductivity of approx. 10 S/cm. [110] Additionally, in literature PEDOT:PSS is reported to smoothen the ITO anode, hence reducing shortcuts in the cell. [45] In this thesis, the polymeric PEDOT:PSS dispersion Clevios P VL AP 4083 is utilized, purchased from Heraeus. Its work function of 5.2 eV is higher compared to that of ITO and thus, closer in energy with respect to the HOMO level of the donor materials, therefore facilitating hole extraction as desired. [111]

Molybdenum Oxide (MoO₃)

Transition metal oxides (TMOs) have been shown suited candidates to replace PEDOT:PSS as hole transport materials in opto-electronic devices. [112–114] The motivation for this replacement is given by the aim to increase long term stability. For the utilization of PEDOT:PSS detrimental reactions with the ITO electrode have been reported. Since PEDOT:PSS is an aqueous dispersion, degradation of subsequently deposited organic layers and electrodes due to residual humidity has been observed. [109] Moreover, the work function of PEDOT:PSS is very sensitive to the residual water content and with it to the exact preparation conditions, impeding reproducibility. [115] In this thesis, instead of PEDOT:PSS, alternatively the TMO molybdenum oxide (MoO₃, purchased from MaTeck GmbH) is applied, covering the ITO anode. In contrast to other TMOs such as V₂O₅ or WO₃, molybdenum oxide features a comparably low sublimation temperature, allowing for deposition from a Knudsen cell under vacuum conditions at ~ 400 °C. In comparison to PEDOT:PSS, the conductivity is distinctly smaller, however MoO₃ yields a much higher work function of 6.9 eV. Thus, implementation of a thin MoO₃ interlayer

allows to enhance the work function of the anode considerably. [109] With respect to organic photovoltaics, this possibility is beneficial, in particular, when utilizing donor materials with high ionization potential, as is the case, for instance, for perfluorinated zinc phthalocyanines (see Section 7.4).

MoO₃ is reported to have a very large ionization potential of 9.7 eV, thus excluding hole extraction from an organic donor material to occur via valence band states of the TMO. Instead, due to the n-type character of MoO₃, with the conduction band close to the Fermi level, hole collection is expected to take place by a recombination process of photo-generated holes of the donor and electrons of the conduction band of MoO₃. This means in effect, the TMO layer acts as a charge recombination layer rather than an extraction layer. [109]

4.3. Organic Absorber Materials

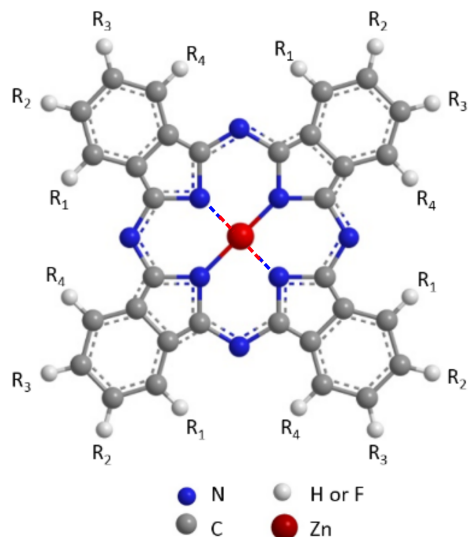
4.3.1. Donor Compounds

Phthalocyanines (Pcs)

Phthalocyanines are macrocyclic compounds, comprised of four benzo-pyrrole groups which are connected via nitrogen bridges. The original dye, with the chemical structure C₃₂H₁₈N₈, was synthesized for the first time in 1907 by Braun and Tcherniac. [62] It was twenty years later, when Diesbach and von der Weid created the first metal phthalocyanine (MPc), introducing a copper atom in the central cavity of the macrocycle by substitution of two hydrogen groups. Since that time, more than 70 different phthalocyanines have been synthesized by solely changing this central atom. [116] This replacement allows for a slight variation of the chemical and electronic properties, whereas the structural characteristics are mainly unchanged. [117–119] Besides, substitution of hydrogen atoms in the ligand by electron withdrawing or pushing functional groups enables additional variability of the electronic and photo-physical properties. [16, 120]

The conjugated π -electron system of MPcs consists of 18 π -electrons and typically leads to distinct absorption in the red part of the visible, hence causing an intense blue color of the compounds. Phthalocyanine derivatives are presumed to make up 25 % of the worldwide artificial pigment production, being commonly used for example in inks and paints. [117, 121] Moreover, MPcs are applied in opto-electronics, for instance in organic thin film transistors of liquid crystal display devices or as photoconductors in laser printers. [122, 123] Moreover, their polycrystalline structure, their high p-conductivity and high extinction coefficient render MPc's an attractive material class for OPV, yielding remarkable power conversion efficiencies. For example, a tandem solar cell employing a ZnPc derivative as absorber layer in one of the sub-cells is reported with an efficiency of 6.5 %. [88]

In this work, differently fluorinated zinc phthalocyanines ($F_n\text{ZnPc}$, $n = 0, 4, 8, 16$) are utilized as donor molecules. The detailed ligand configurations and the molecular masses of the respective phthalocyanines are illustrated in Figure 4.1.



formula	M_{mol} [g/mol]	R ₁	R ₂	R ₃	R ₄
ZnPc (C ₃₂ H ₁₆ N ₈ Zn)	577.91	H	H	H	H
F ₄ ZnPc (C ₃₂ F ₄ H ₁₂ N ₈ Zn)	649.87	H	H	H	F
F ₈ ZnPc (C ₃₂ F ₈ H ₈ N ₈ Zn)	721.84	H	F	F	H
F ₁₆ ZnPc (C ₃₂ F ₁₆ N ₈ Zn)	865.76	F	F	F	F

Figure 4.1.: Illustration of the ligand configuration of the employed $F_n\text{ZnPcs}$ ($n = 0, 4, 8, 16$) and summary of the corresponding molecular masses M_{mol} .

The exciton diffusion length of about 15 nm was deduced from photovoltaic measurements. [124] The electron and hole mobility in thin film applications is reported in the range of 10^{-2} cm²/Vs. [125] On weakly interacting substrates, such as glass or ITO/MoO₃ as employed in this thesis, ZnPc typically adopts the so-called α -crystal structure (see Chapter 7), with an almost upright standing orientation of the entities. [126] For this crystal phase a HOMO energy of 4.8 eV was reported by photoelectron spectroscopy measurements. [16, 17, 127] The optical band gap E_{opt} of the α -phase amounts to 1.5 eV and the transport gap E_{gap} is reported 2.1 eV, resulting in an exciton binding energy of about 0.6 eV. [128] Upon fluorination, energy levels are expected to be gradually shifted towards lower energies, whereas the bandgap remains almost unaffected. [11] The energetic staircase-behavior of the HOMO and LUMO levels was qualitatively confirmed by semi-empirical calculations, though absolute values differed slightly from those experimentally determined. [11, 129]

The donor compounds ZnPc and F₁₆ZnPc (purchased from Sigma-Aldrich), F₄ZnPc (received from BASF) and F₈ZnPc (Creaphys), were purified twice by thermal gradient sublimation.

Diketopyrrolopyrrole (DPP) Derivatives

Diketopyrrolopyrrole pigments were reported for the first time in 1974 by Farnum. [130] Various derivatives of the initial compound have been synthesized since then, finding their way to numerous applications, such as inks, paints and plastics. [131–133] Due to their high fluorescent yield and chemical stability, DPP derivatives have been used in organic light emitting diodes, as well as in other fields of opto-electronics, for instance in organic thin film transistors or chemosensors. [92, 134] Recently, also the potential of DPP pigments as absorber materials in organic photovoltaic cells has been elucidated. [131, 135] Chemical modifications to the DPP core allow for tailoring the photo-physical properties, influencing for example the packing motif or frontier orbital energies. [131]

For this work, different DPP derivatives D1 - D3 were synthesized by Dr. Christian Müller at the Department of Applied Functional Polymers – Macromolecular Chemistry I, University of Bayreuth. The compounds differ in their outer aryl group, in which either a phenyl ring or pyridine ring was employed, as illustrated in Figure 4.2. The molecular weight of D1 ($C_{58}H_{80}N_2O_2S_2$) is 901.40 g/mol, of D2 and D3 ($C_{56}H_{80}N_4O_2S_2$) 905.39 g/mol, respectively and the density amounts to 1.6 g/cm³. The chemical modification applied is geared towards a specific adjustment of the HOMO and LUMO levels without changing the chemical structure or dipole moment significantly. Due to an expected energy level shift for D2 and D3 with respect to D1, these diketopyrrolopyrroles are tested in energetic staircases of D1/D2(D3)/C₆₀ cascade solar cells, as elucidated in Chapter 9. The synthesized compounds all have high thermal stability up to 400 °C, enabling vacuum deposition by thermal evaporation without degradation at a temperature of 215 °C. [136]

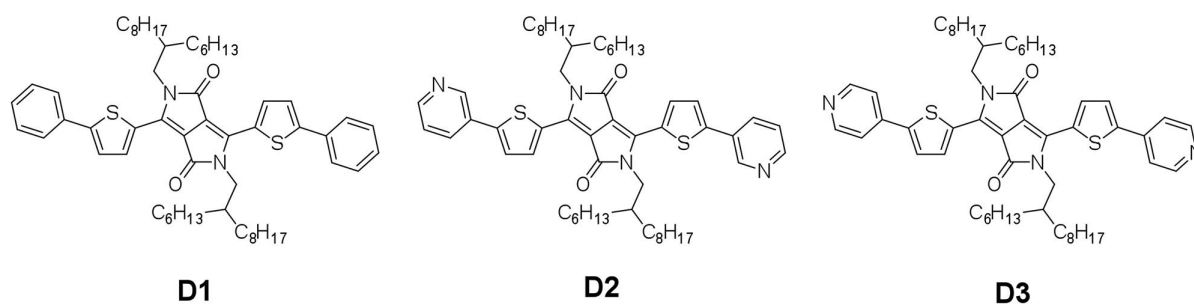


Figure 4.2.: Structure of the diketopyrrolopyrrole derivatives D1 - D3.

Diindenoperylene (DIP)

The planar donor molecule diindenoperylene (DIP, $C_{32}H_{16}$) is a polycyclic aromatic hydrocarbon comprised of a central perylene core with two indeno-groups attached. The chemical structure of DIP is depicted in Figure 4.3. The spatial dimensions of the molecule were approximated on the basis of the "Cambridge Crystallographic Database" to be 18.4 Å × 7 Å. [137] DIP has a

molecular weight of 400.47 g/mol and a density of 1.35 g/cm³. Due to its high thermal stability, deposition under vacuum conditions at a sublimation temperature of approx. 330 °C yields thin films without degradation or polymerization of the organic compound. [138, 139]

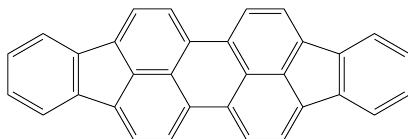


Figure 4.3.: Illustration of the chemical structure of the donor compound DIP.

In thin film applications, DIP molecules typically form a polycrystalline order, featuring in general two different molecular orientations with respect to the substrate: The λ -phase is characterized by a parallel alignment of the molecular plane with respect to the substrate, whereas in the σ -phase, molecules adopt an almost upright standing orientation with a tilt angle of approx. 17° with respect to the substrate normal. [140–142] On weakly-interacting substrates such as glass or ITO/PEDOT:PSS, as utilized in this thesis, typically the σ -phase is observed at room temperature. The high structural out-of-plane order of DIP thin films enables long range exciton transport with exciton diffusion length of up to 100 nm. [143] Yet this quantity is still under debate. [49, 144] Besides, an almost ambipolar transport was confirmed along the c' -direction by time-of-flight measurements, which corresponds to the charge carrier transport direction in solar cells, yielding a relatively high electron mobility of $\mu_e = 0.02$ cm²/Vs and a hole mobility of $\mu_h = 0.003$ cm²/Vs at room temperature. [145] The optical band gap E_{opt} of the σ -phase is 2.2 eV, thus optical transitions occur in the VIS (S1 transition) and UV (S2 transition) spectral region. The ionization energy was determined to be 5.8 eV and the electron affinity 3.1 eV, resulting in a transport gap E_{gap} of 2.7 eV. [141] Accordingly, the exciton binding energy is estimated 0.5 eV. DIP was synthesized and purified twice by gradient sublimation.

Tetraphenyldibenzoperiflanthene (DBP)

The DIP derivative tetraphenyldibenzoperiflanthene was utilized as donor material in this thesis. In comparison to DIP, the planar core of the molecule is extended by a single benzene ring at each side. Moreover, four additional phenyl rings, attached to the core, cause a steric hindrance for crystallization, resulting in an amorphous thin film phase upon deposition. The chemical structure of DBP is displayed in Figure 4.4. The density of DBP is 1.35 g/cm³ and the sublimation temperature is 370 °C in vacuum.

Just like in case of DIP, the transition dipole moment is aligned along the long axis of the molecule. In contrast to the standing-upright configuration of DIP molecules in the σ -phase, the amorphous character of DBP yields a preferential orientation of the molecules lying flat on the substrate, as confirmed by ellipsometry measurements. [146] Thus, with illumination being incident vertically on the sample, the absorption of DBP thin films is strongly enhanced, in comparison to DIP. An exciton diffusion length of 16 nm was observed in photoluminescence

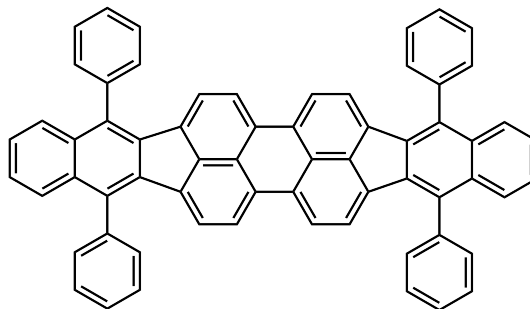


Figure 4.4.: Structure of the donor material DBP.

quenching measurements. [147] The hole mobility of DBP was determined to be $\mu_h = 10^{-4} - 10^{-3} \text{ cm}^2/\text{Vs}$ [148] Finally, HOMO and LUMO energy levels of DBP are reported to be very similar in comparison to DIP. [149]

4.3.2. Acceptor Compounds

Fullerene C₆₀

As acceptor material for organic photovoltaic devices, the buckminsterfullerene C₆₀ is employed in this thesis. It is comprised of 12 carbon pentagons and 20 hexagons, forming a closed cage molecule, as illustrated in Figure 4.5. C₆₀ features a diameter of 7.1 Å and crystallizes in a face centered cubic structure at room temperature. [150,151] Yet, in organic thin film applications, typically an amorphous morphology is observed. The molecular weight of C₆₀ is 720.64 g/mol, yielding a density of 1.65 g/cm³. Due to its thermal stability, the buckminsterfullerene is suitable for vacuum deposition, at a sublimation temperature of $\sim 350 \text{ }^\circ\text{C}$ under UHV conditions. [152] For the exciton diffusion length of C₆₀, deduced from photoluminescence quenching measurements, different values are reported, ranging between 8 nm and 40 nm. [45,153] Being the most frequently used acceptor material in organic photovoltaics, C₆₀ has a high electron mobility of approx. $1 \text{ cm}^2/\text{Vs}$, as concluded from field effect transistor measurements at room temperature. [45] The HOMO energy is located at 6.4 eV and the band gap is 2.0 eV. [154] In combination with a variety of donor materials, the high electron affinity of C₆₀ enables efficient exciton dissociation at the D/A hetero-interface. C₆₀ was purchased from CreaPhys (purity > 99.95 %) and was purified twice by gradient sublimation.

Fullerene C₇₀

The fullerene C₇₀ consists of 12 pentagons and 25 hexagons and is also depicted in Figure 4.5. C₇₀ features a molecular weight of 840.77 g/mol and a density of 1.7 g/cm³. Due to the higher mass of C₇₀ in comparison to C₆₀, a slightly higher sublimation temperature of 460 °C results. [152] However, as a consequence of the similar chemical structure of C₆₀ and C₇₀,

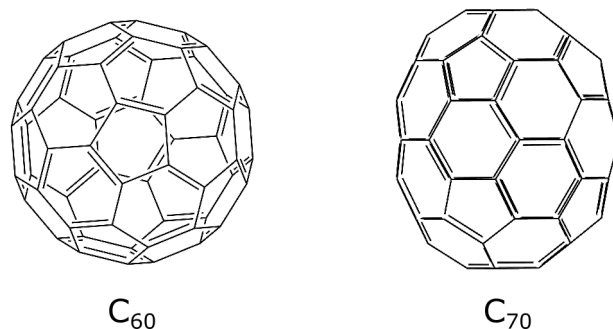


Figure 4.5.: Chemical structure of the employed fullerene acceptor molecules C₆₀ and C₇₀.

their general electronic properties almost resemble each other, i.e. frontier orbital energies are reported to be almost identical. [18] C₇₀ was purchased from Solaris Chem Inc. (purity > 99%) and was utilized without further purification.

4.4. Exciton Blocking Layer (EBL)

Bathophenanthroline (BPhen)

Applying metal electrodes in direct contact with organic absorber materials, in general leads to annihilation of photo-generated excitons. This so-called quenching proceeds via the formation of mirror charges and dipoles at the metal interface. [155] Besides, a high density of trap states at the metal/organic interface can cause radiationless recombination of excitons. [106] In order to spatially separate the metal top contact from the photo-active absorber materials, warranting a minimization of exciton quenching by the metal contact, so-called exciton blocking materials are typically utilized in organic photovoltaics. In this thesis, the EBL bathophenanthroline (C₂₄H₁₆N₂) is employed. The chemical structure is displayed in Figure 4.6. Bathophenanthroline has a molecular weight of 332.40 g/mol and a density of 1.24 g/cm³. The sublimation temperature under ultra high vacuum conditions is 220°C.

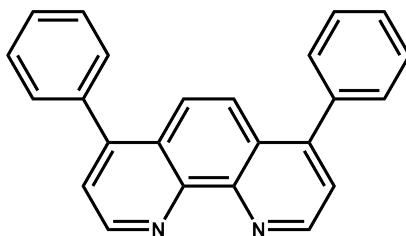


Figure 4.6.: Chemical structure of the exciton blocking material BPhen.

BPhen possesses a large band gap of 3.5 eV, yielding no parasitic absorption in the visible spectral range. Thus, BPhen can be used as an optical spacer between organic absorber layers and the metal top contact. The HOMO and LUMO energies of BPhen are positioned at 6.4

eV and 2.9 eV, respectively. [156] When applied in combination with the most commonly used acceptor materials C₆₀ and C₇₀, the HOMO energies of these materials are almost identical, however, the EBL has a distinctly larger band gap, thus hampering exciton transfer from the acceptor phase to the metal electrode. The extraction of free charge carriers was illustrated to take place via metal induced trap states generated and located energetically below the LUMO level of BPhen, upon metal deposition. [157] BPhen was purchased from Sigma-Aldrich and utilized without further purification.

5. Sample Architecture and Fabrication

In this thesis predominantly planar bilayer cells are under investigation. The schematic architecture is displayed in Figure 5.1. The heterojunction is established by deposition of a planar donor and acceptor absorber layer on top of each other. Moreover, so-called cascade solar cells are under study, in which an energetic staircase is established by introducing an additional thin interfacial layer between donor and acceptor.

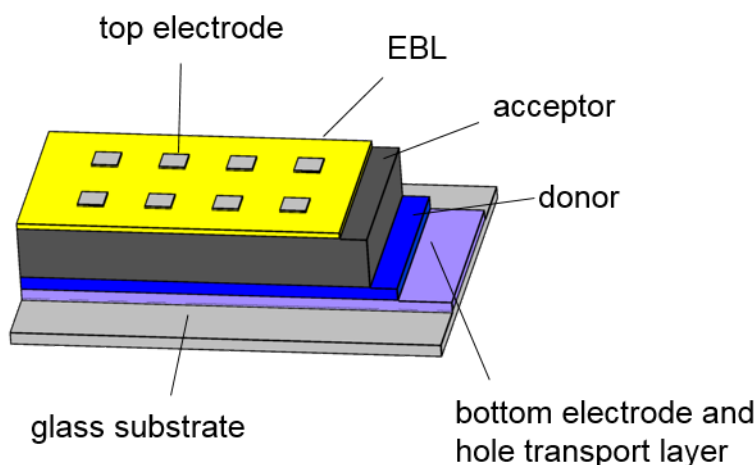


Figure 5.1.: Schematic architecture of a planar bilayer cell.

The glass substrates utilized for sample preparation are $32 \times 24 \text{ mm}^2$ in size. A 100 nm thick ITO layer was sputtered at the Institute for Large Area Microelectronics at the University of Stuttgart by Dr. Steffen Höhla. Lithographic patterning yields ITO stripes of $32 \times 14 \text{ mm}^2$ centered on the respective glass substrates. The ITO bare edge region is used to contact the silver top electrode. Substrates are sonicated in acetone and isopropanol for 15 minutes each. Afterwards, the hole conduction layer PEDOT:PSS is spin-coated under ambient conditions at 3000 rotations per minute, resulting in a layer thickness of approx. 50 nm. Subsequently, the specimen is heated for 20 minutes on a hot plate at $120 \text{ }^\circ\text{C}$ to get rid of residual humidity, prior to loading it to the vacuum chamber. The vacuum chamber used for solar cell preparation, is schematically depicted in Figure 5.2. Alternatively, instead of PEDOT:PSS, a MoO_3 hole transport layer, is employed. In that case, the metal oxide layer is evaporated from a tungsten boat in the ultra high vacuum chamber system.

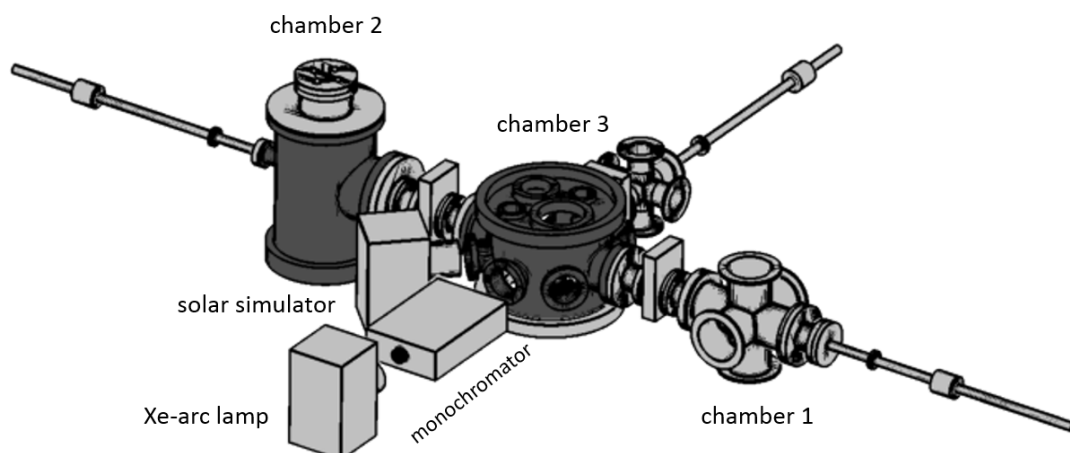


Figure 5.2.: Schematic illustration of the vacuum chamber system used for sample preparation. Samples are loaded into the vacuum chamber system via load-lock chamber 1. In addition, metal and metal oxide layers are processed in this chamber. In chamber 2 the organic semiconductors are deposited, whereas in chamber 3 organic solar cells are characterized *in-situ*. Illumination is carried-out with a solar simulator in case of $j(V)$ characterization. For EQE measurements, light from a Xe-arc lamp is guided onto the sample through a monochromator.

This experimental setup consists of three separable vacuum-chambers, each operated with an oil-free membrane pump and a turbo pump at a base pressure of $\leq 10^{-7}$ mbar. Samples are loaded into the vacuum via load-lock chamber 1 and are transferred between the chambers by means of three transfer rods.

Organic photo-active materials, as well as the exciton blocking layer are sublimed from seven separate Knudsen cells by resistive heating in chamber 2. Each of these evaporation cells, as well as the substrate itself, can be covered by a shutter system, allowing to adjust sublimation rates prior to the actual deposition process. This is in particular crucial in case of simultaneous co-evaporation of two different materials. During evaporation the substrate is fixed on a copper stage warranting reliable substrate position. During deposition of the organic semiconductors the substrate temperature can be varied between 80 K and 450 K. The sublimed layer thickness is controlled with the help of a quartz crystal microbalance and the tooling factor for each Knudsen cell is determined independently by X-Ray reflectometry. Top silver electrodes are processed in chamber 1 in order to avoid cross contamination by the organic materials. The deposition takes places through a circular shadow mask with 1 mm radius, ultimately defining the active solar cell area. Within one preparation process 14 solar cells are generated simultaneously. For the *in-situ* determination of the solar cell parameters, organic photovoltaic cells are transferred to vacuum chamber 3.

6. Experimental Techniques

6.1. *In-Situ* Opto-Electronic Device Characterization

Subsequent to sample preparation, solar cell parameters are determined *in-situ* without breaking the vacuum at a base pressure of $\leq 10^{-7}$ mbar. A battery-driven multiplexer allows for automatized, consecutive measurement of the opto-electronic device characteristics of all 14 solar cells prepared on a single substrate. Triggering a Keithley source measure unit 236, the current-voltage measurements are conducted by a LabView program.

6.1.1. Current Density-Voltage ($j(V)$) Characterization

Steady-state $j(V)$ characteristics in the dark and under illumination are measured for voltages between -0.5 V and 1.5 V at a step width of 0.01 V. Illumination is carried-out, employing a 300 W LOT Oriel LS0306 solar simulator with the irradiance calibrated to 1 sun at AM1.5 G (100 mW/cm²). The intensity is corrected for mismatch. [158]

6.1.2. External Quantum Efficiency (EQE)

The measurement of the spectrally resolved photocurrent density $j_{ph}(\lambda)$ is performed to determine the external quantum efficiency $EQE(\lambda)$, which is defined as the ratio of extracted electron-hole pairs and the number of incident photons (see also Section 3.1):

$$EQE(\lambda) = \frac{j_{ph}(\lambda)/q}{P_{light}(\lambda)/h\nu}. \quad (6.1)$$

Here $P_{light}(\lambda)$ denotes the incident light intensity. Light from a Xe-arc lamp (Osram 150 W/4Suprasil) is directed into a 260 Cornerstone monochromator from Newport and is spectrally split with a grid line (line density: 1200 mm⁻¹) and subsequently, is guided onto the solar cells in the vacuum chamber via mirror optics. EQE measurements are performed without background illumination at low average light intensity of 10⁻² mW/cm², corresponding to 10⁻⁴ suns under standard AM1.5G illumination, in order to avoid pronounced space charging effects, affecting the current density. For the different positions on the substrate the incident illumination intensity varies and thus, has to be determined. This is realized with the help of a reference Si

diode featuring a known *EQE* characteristic. Spectrally resolved photocurrent measurements are recorded in the wavelength range between 400 nm and 900 nm in step sizes of 1 nm at a current noise level in the range of 10^{-11} A.

6.2. Structural Investigation

6.2.1. X-Ray Diffraction (XRD)

By means of X-ray diffraction, the structure of a crystalline or polycrystalline material can be investigated at atomic length scales, providing insight into a variety of morphological properties, such as the crystal structure, layer thickness or roughness of a sample. At this point, only the basic principles necessary for data interpretation are introduced. For a broad overview of the experimental details, reference to literature is given. [159,160]

XRD is based on coherent scattering of X-rays at periodic spatial variations of the electron density, for example at lattice planes of a crystal, upon multiple reflections at the interfaces of a stacked layer system of different refractive indices. In this thesis, XRD measurements are carried-out using a XRD 3003 T/T thin film reflectometer from GE Sensing & Inspection Technologies in Bragg-Brentano geometry. In this configuration, the X-Ray source is oriented with respect to the surface of the sample at an angle θ , whereas the detector is positioned at the angle 2θ with respect to the incident X-ray beam. That is why an experiment, carried-out in Bragg-Brentano geometry, is commonly called a θ - 2θ -scan. In such an experiment, solely electron density variations caused by lattice planes perpendicular to the surface normal are detectable. For constructive interference to occur, the Bragg condition has to be fulfilled, meaning that the change in path length by the crystal planes has to correspond to an integer multiple n of the wavelength λ of the X-ray beam:

$$2 \cdot d \cdot \sin(\theta) = n \cdot \lambda. \quad (6.2)$$

Here d denotes the lattice spacing. Instead of showing X-ray diffraction spectra as a function of θ , for reasons of better comparability, it is common practice to utilize the momentum transfer q_z along the surface normal, rendering the diffractogram independent of the wavelength of the employed X-ray source:

$$q_z = \frac{4\pi}{\lambda} \cdot \sin(\theta). \quad (6.3)$$

X-Ray diffraction can be described in analogy to diffraction by an optical grating, yielding the emergence of alternating intensity maxima and minima, so-called Laue oscillations. However, in case of rough interfaces or in case of a too large layer thickness, only the main maximum is

to be resolved. Provided that no Laue oscillations are detectable in the diffraction spectra, the crystallite height h can be calculated according to the modified Scherrer equation: [161]

$$h = 2 \cdot \sqrt{\frac{\ln(2)}{\pi}} \cdot \frac{\lambda}{\cos\left(\frac{2\theta}{2}\right) \cdot \sqrt{(\Delta\Theta)^2 - b^2}}. \quad (6.4)$$

Here $\Delta\Theta$ represents the full-width-at-half-maximum of the Bragg peak and b is the instrumental broadening of the diffractometer, which amounts to 0.07° for the setup used in this study. An employed monochromator allows to use solely the wavelength of the $Cu K_\alpha$ line ($\lambda = 1.5418 \text{ \AA}$) in the diffractometer.

6.2.2. Atomic Force Microscopy (AFM)

Atomic force microscopy is a scanning probe technique allowing to monitor the topography of a sample on the nanometer scale. [162] Hence, in contrast to X-Ray diffraction, which yields integral information about the crystalline structure and the roughness of a sample, AFM measurements reveal the local surface morphology. Thus, this experimental method gives complementary insight, for instance into the root mean square roughness σ or the lateral domain size of a film.

The key functional unit of an atomic force microscope is comprised of a sharp nanoscopic tip, attached to a cantilever. The working principle relies on the deflection of this cantilever as a consequence of attractive and repulsive forces between the tip and the investigated specimen surface. Attractive Van-der-Waals and capillary forces are superimposed with repulsive forces when scanning the sample in close proximity. Repulsive forces are caused due to the Pauli exclusion principle and Coulomb repulsion between the incomplete electrostatic screening of the positive nuclear charges of the tip and the sample in close proximity. Usually, the mechanical deflection is optically tracked by focusing a laser beam onto the backside of the cantilever and detecting the reflected laser light by a 4-quadrant laser diode.

For AFM measurements, a Dimension Icon from Veeco is utilized in tapping mode. In this operational mode, with the help of a piezo element, the cantilever is driven to oscillate near its resonance frequency with a constant amplitude. The tips (RFESP resonance frequency: 70 - 90 kHz) utilized in the AFM measurements were purchased from Veeco. When approaching the surface, interactions described above between tip and sample surface cause a damping of the oscillation amplitude. This change is the parameter regulated by a feedback loop to adjust the height of the cantilever, in order to restore the initial cantilever oscillation amplitude. Accordingly, the auxiliary voltage necessary for the height adjustment is a direct measure of the local height and thus, of the topography of the sample. Generally, tapping mode is in wide use in the field of soft-matter sciences, since the force and hence, the possibility of irreversibly damaging

the sample surface is strongly reduced in comparison to contact mode. The resulting data are analyzed using the freeware Gwyddion. [163]

6.3. Optical Measurements

6.3.1. Steady State Absorption Spectroscopy

Optical absorption spectra were determined from transmission and reflection measurements according to:

$$A = 1 - T - R. \quad (6.5)$$

Here, A represents the absorption, T the transmission and R the reflection, respectively. For a sample of layer thickness d , the Beer-Lambert law describes the substance-specific exponential attenuation of the incident light intensity I_0 , passing through the sample and thus, allowing to assign its spectral dependent absorption coefficient $\alpha(\lambda)$ by

$$\alpha(\lambda) = -\ln\left(\frac{I(d)}{I_0}\right)/d. \quad (6.6)$$

The ratio of the intensities $\frac{I(d)}{I_0}$ is the transmission of the sample. UV/VIS steady state absorption spectroscopy measurements were carried-out under ambient conditions in the wavelength range between 300 nm and 900 nm at a resolution of 1 nm, using a Jasco V-650 UV/VIS spectrometer.

6.3.2. Spectrally Resolved Photoluminescence (PL)

After photo-excitation of an organic semiconductor, excitons can recombine radiatively under emission of photons or non-radiatively (see also chapter 2.2). Radiative transitions are monitored in photoluminescence measurements enabling for example an evaluation of the ability of a D/A interface to dissociate excitons.

In this thesis photoluminescence measurements were carried-out utilizing a continuous wave (cw) solid state laser with an excitation wavelength of 532 nm, purchased from Laser2000. The excitation power density is continuously adjustable between 0.3 mW/cm² and 50 mW/cm². Alternatively, a laser diode with a central excitation wavelength of 630 nm was employed. Measurements are conducted under ambient conditions without encapsulation of the samples. The photoluminescence is recorded with an Acton SP-2558 spectrometer connected to a Pixis100BR_eXcelon CCD-camera, both purchased from Princeton Instruments. The CCD-camera offers a quantum efficiency of at least 90 % in the spectral wavelength range between 420 nm and 900 nm.

6.3.3. Transient Absorption Spectroscopy (TAS)

Upon light absorption in organic semiconductors, the decay of singlet excitons typically takes places on sub-picosecond to nanosecond time scales. [92] The temporal investigation of such deactivation processes requires an experimental method with femtosecond time resolution. Ultrafast transient absorption spectroscopy constitutes such a technique, which allows for the examination of inter- and intra-molecular dynamics, i.e. processes involving for instance, an energy or charge transfer can be monitored on the corresponding time scales.

Transient absorption spectroscopy falls in the category of pump-probe-spectroscopy techniques. The working mechanism is based on detecting the change in absorption of a photo-excited molecules in solution or solid state as a function of time and wavelength and is schematically depicted in Figure 6.1.

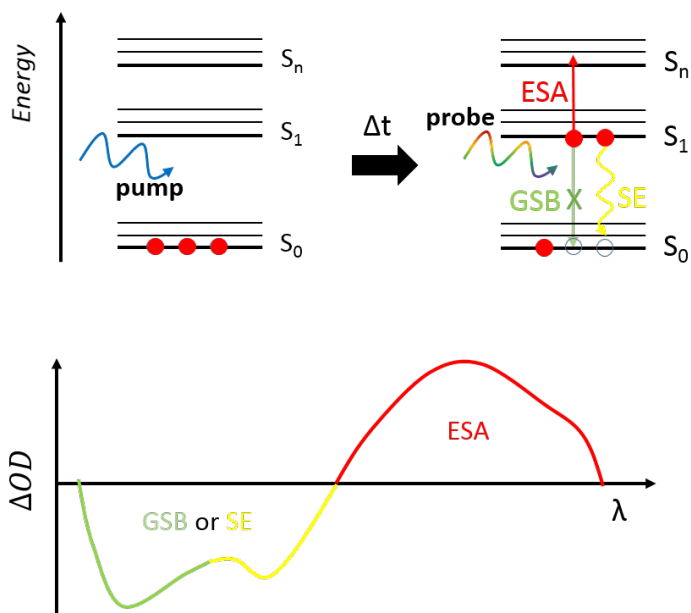


Figure 6.1.: Working principle of transient absorption spectroscopy (top) and related transient spectrum (bottom). Here, ESA denotes excited state absorption, GSB ground state bleaching and SE stimulated emission.

The quantity to be analyzed is the change in optical density $\Delta OD(\lambda, \Delta t)$:

$$\Delta OD(\lambda, \Delta t) = \log \left(\frac{I_0(\lambda)}{I(\lambda, \Delta t)} \right). \quad (6.7)$$

Here, $I_0(\lambda)$ and $I(\lambda, \Delta t)$ represent the transmitted intensities of the probe beam, measured for the non-excited and excited sample, respectively, and λ and Δt are the wavelength and the time delay between pump and probe pulse. Photo-excitation is realized by a laser source providing ultrashort monochromatic pulses. After a defined time delay, a second pulse impinges on the sample and probes the density of the initially photo-excited states and their evolution in the

specimen. A transient spectrum may feature three different contributions, which are illustrated schematically in Figure 6.1:

1. Excited state absorption (ESA): Photo-activated molecules might be excited to higher-lying energy levels by the probe beam. According to Equation 6.7, such a transition induced by the probe appears as positive change in optical density and is called excited state absorption. ESA of both, excitons and free charge carriers may be monitored in a transient absorption spectroscopy experiment.
2. Ground state bleaching (GSB): Photo-excitation of a sample by the pump pulse generates molecules residing in an excited state. Accordingly, the ground state population is depleted and hence, upon probing the sample in a wavelength range of an electronic transition, more light is transmitted through the sample and a negative $\Delta OD(\lambda, t)$ value is obtained.
3. Stimulated emission (SE): The probe beam provides a photon to cause a stimulated relaxation of the S_1 into the S_0 state. Effectively, this fluorescence signal appears as negative change in optical density in the transient spectrum.

Carrying-out transient absorption spectroscopy measurement for various time delays, gives access to the dynamics of the above mentioned processes and their energetics.

The transient absorption spectroscopy measurements, presented in this thesis were performed at the Laser Research Institute (LRI) at the University of Stellenbosch, South Africa under the supervision of Prof. Heinrich Schworer. The experimental setup is schematically depicted in Figure 6.2.

A femtosecond laser source (CPA2101, ClarkMXR) is operated as a chirped pulse amplifier (CPA), utilizing a femtosecond oscillator in combination with a Ti:sapphire amplifier. A central wavelength of 775 nm is provided with a pulse duration of approximately 150 fs and a repetition rate of 1 kHz. A 50:50 beam splitter divides the fundamental laser beam into two distinct pathways. Along the first path (path 1 in Figure 6.2), the laser beam is directed towards a non-linear optical parametric amplifier (NOPA), which allows to select the intended wavelength between 480 nm and 700 nm. For details on non-linear parametric amplification reference to the literature is given. [165] Before directing this pump beam onto the sample, the pulse is compressed by a two-prism compressor to less than 50 fs. [164] On pathway two (path 2 in Figure 6.2), the probe pulse is realized by directing the fundamental laser beam onto a white light generating (WLG) yttrium aluminum garnet (YAG) crystal. The temporal resolution of the probe beam by using such a crystal is approx. 150 fs, resulting in an overall temporal resolution of the TAS experiment of less than 200 fs. Alternatively, the probe beam may be generated in a second NOPA, yielding after signal compression again a time resolution of approx. 50 fs. Thus, a temporal resolution of the experiment of less than 100 fs is feasible. However, in this configuration only a narrow spectral range can be probed.

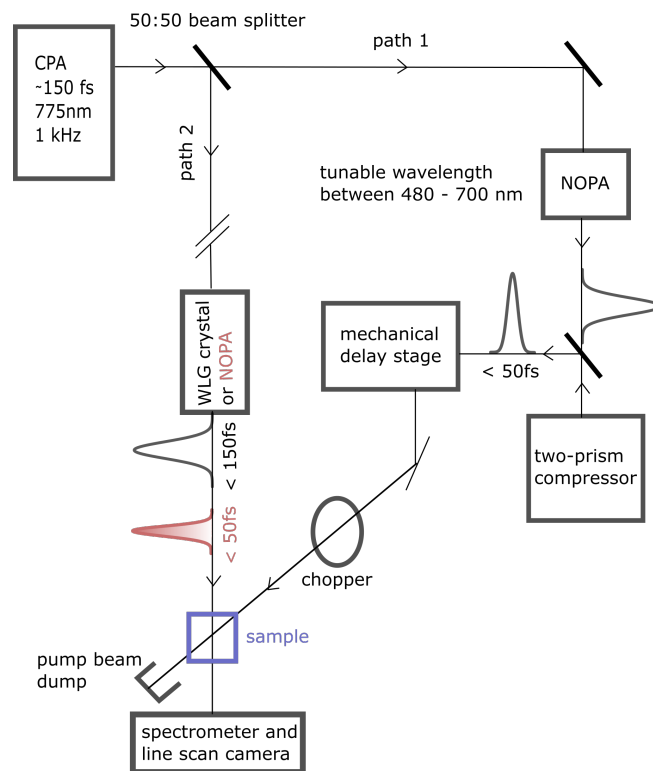


Figure 6.2.: Schematic demonstration of the TAS setup, according to [164].

The temporal delay between pump and probe pulse is adjusted via a mechanical delay stage and covers a temporal delay of up to 600 ps. As shown in Figure 6.2, the delay stage is positioned in pathway one since the pump beam is much more stable in comparison to the generated white light supercontinuum. Additionally, a chopper is introduced in pathway one with a frequency of 0.5 kHz in order to block every second pump pulse. Pump and probe beam are spatially overlaid on the sample by means of a pin hole. The temporal overlap is realized by ensuring the path lengths of pump and probe pulse to be equally long. The spectrally resolved change in optical density is accessible by measuring the transmitted intensities of the probe beam, with and without pumping the sample before (see Equation 6.7), with a line scan camera in combination with a spectrometer. For each time step, transient absorption spectra are averaged over 6000 measurements.

6.4. Ultraviolet Photoelectron Spectroscopy (UPS)

Photoelectron spectroscopy (PES) is an experimental technique employing X-ray (XPS) or ultraviolet (UPS) radiation in order to promote electron emission from the near surface region of an investigated sample. The method is in particular suited for analyzing the chemical and electronic structure of surfaces and interfaces. [166] The working principle of PES is based on the photoelectric effect. In general, the photoemission process is considered to take place in three steps: Firstly, absorption of light yields excitation of electrons. Secondly, electrons are

transferred to the surface of the sample and finally, the emission of these electrons into the vacuum occurs. [167,168]

Utilizing UV light in ultraviolet photoelectron spectroscopy measurements, the employed energy $h\nu$ is only sufficient to enable photoemission from the valence band region of a material. To gain insight into the kinetic energy distribution of photo-emitted electrons and thus, in the density of states constituting the valence band, they are sent through an energy analyzer. Since the analyzer is in electrical contact with the sample their Fermi-levels are equilibrated. Figure 6.3 illustrates the relevant energy levels of a semiconducting sample and of the analyzer determining the photoemission process. Considering the kinetic energy distribution E_{kin} , the binding energy E_B with respect to the Fermi-edge E_F reads: [166,169]

$$E_B = h\nu - E_{kin} - \Phi_{spec}. \quad (6.8)$$

Equation 6.8 illustrates that the binding energy of the emitted electrons does not depend on the work function of the sample Φ_{sample} but on the work function of the spectrometer Φ_{spec} .

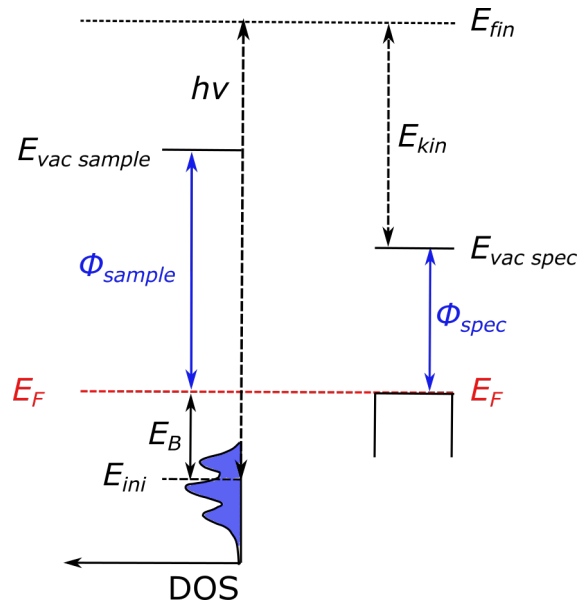


Figure 6.3.: Illustration of the relevant energy levels of the sample (index *sample*) and the spectrometer (index *spec*) in photoelectron spectroscopy measurements. Φ represents the work function and E_{vac} the vacuum energy. The kinetic energy is represented by E_{kin} . Since the analyzer and the semiconducting sample are in electrical contact, their Fermi-levels E_F are equilibrated. E_B denotes the binding energy with respect to E_F . E_{ini} and E_{fin} indicate the initial and final state of the photo-emitted electron. After [169,170].

The HOMO energy of a sample can be deduced from the onset at low binding energy, which corresponds to the electrons of highest kinetic energy photo-emitted from the sample. The work function Φ_{sample} is calculated from the secondary electron cutoff (SECO). In this case, the photoelectrons of lowest kinetic energy are tracked. In order to separate those electrons barely

ejected from the sample from secondary electrons generated upon impacting the analyzer, an auxiliary accelerating voltage is applied.

In situ UPS measurements provide insight into the electronic structure of a sample, or to be more precise and accounting for the short mean-free-path of the photo-electrons, of the sample surface. For instance, a change of work function at organic/organic or metal/organic interfaces can be monitored. Such a variation in the vacuum level corresponds to the formation of an effective interfacial dipole Δ . Besides, thickness dependent photoemission experiments trace band bending effects. These information are crucial for a correlation of microscopic interface energetics to the macroscopic opto-electronic performance of thin film devices. However, the electronic effects described are sensitive to various parameters, such as preparation conditions, the choice of substrate or molecular orientation. [127, 171, 172] *Vice versa* this means, that a combination of literature values can only yield a rough estimate of the energetic positions of the participating levels. Hence, for a distinct material combination it is mandatory to determine the real energy levels by PES measurements. [99, 170]

The determination of energy levels from spectra of the binding energy is carried-out according to the peak-onset method. [173] UPS measurements were performed at the photon source Bessy II in Berlin at the end-station SurIcat (Surface Investigation and Catalysis). The UHV chamber was kept at a base pressure of $< 2 \cdot 10^{-9}$ mbar. Spectra were recorded with a high resolution electron spectrometer Scienta SES 10 and at a photon energy of 35 eV. The measurements were performed in collaboration with the AG Prof. Koch at Humboldt-University.

Part III.

Results and Discussion

7. Impact of Gradual Fluorination on the Properties of $F_n\text{ZnPc}/\text{C}_{60}$ Bilayer OPVCs

7.1. Tailored Modification of D/A Interface Energetics

The D/A heterojunction is the crucial functional building block of any “state of the art” organic solar cell. At this interface, the energetic offset of the frontier orbital energies between donor and acceptor drives the dissociation of the photo-generated, strongly Coulomb-bound excitons into free charge carriers, a prerequisite for photocurrent generation (see Section 3.1). Besides, interface energetics at the D/A heterojunction is associated with the open circuit voltage. The energy difference between the HOMO of the donor and the LUMO of the acceptor, the so-called effective band gap $E_{g,eff}$, determines the upper limit for the maximum quasi-Fermi level splitting and thus, for V_{oc} , according to Equation 3.5.

To gain fundamental insight into the correlation between D/A interface energetics and macroscopic solar cell parameters, tailoring of energy levels by chemical modification of the absorber materials is a powerful approach. In this regard, phthalocyanines are a promising class of compounds, due to versatile options for their modification, such as the substitution of hydrogen atoms in the ligand or the implementation of different metal atoms in the central cavity of the molecules (see Section 4.3.1). [126,174]

In this study, differently fluorinated zinc phthalocyanines $F_n\text{ZnPc}$ ($n = 0, 4, 8, 16$) are deliberately chosen as donor materials in combination with the electron acceptor C_{60} . Energy levels of the former are expected to be gradually shifted towards lower energies upon fluorination. [16,17] Concomitantly, the bandgap of the respective phthalocyanine is anticipated to remain almost unaffected allowing for a systematic variation of the D/A interface energetics dependent on the degree of fluorination however, without changing the absorption characteristics. [11] The ligand configuration of the respective fluorinated zinc phthalocyanines is displayed in Section 4.3.1, Figure 4.1. Correlated multi-reference *ab-initio* calculations revealed a beneficial electronic configuration for the donor ZnPc in comparison to other metal phthalocyanines MPcs ($M = \text{Cu}, \text{Ni}, \text{Fe}$), i.e. for all MPcs mentioned but ZnPc , intrinsic intermediate gap states exist in the band gap of the $\pi \rightarrow \pi^*$ transition. These intermediate gap states are associated with non-radiative recombination losses. Due to these electronic characteristics, superior device performance of ZnPc based planar-heterojunction solar cells was reported with respect to the other MPcs mentioned, rendering the former first choice as a starting compound for chemical modification. [126,129]

In this chapter, the impact of gradual fluorination on the optical and structural properties of $F_n\text{ZnPc}$ thin films and opto-electronic characteristics of $F_n\text{ZnPc}/\text{C}_{60}$ ($n = 0, 4, 8, 16$) bilayer cells is investigated. The photovoltaic parameters are correlated with interface energetics, assessed by complementary UPS measurements. The results of this chapter are published in *Advanced Functional Materials*. [175]

7.2. $j(V)$ Characterization of $F_n\text{ZnPc}/\text{C}_{60}$ Bilayer Solar Cells

In order to investigate the effect of successive fluorination on the macroscopic device performance, $F_n\text{ZnPc}/\text{C}_{60}$ bilayer solar cells were prepared by vacuum sublimation. The following layer sequence was chosen:

ITO/MoO₃(5 nm)/ $F_n\text{ZnPc}$ (30 nm)/ C_{60} (35 nm)/BPhen(5 nm)/Ag .

The corresponding $j(V)$ characteristics under AM1.5G standard illumination conditions are displayed in Figure 7.1 and the photovoltaic parameters are summarized in Figure 7.2. Moreover, exemplarily the dark $j(V)$ characteristics of two bilayer cells are displayed as dotted lines in Figure 7.1, showing typical diode characteristics with rectifying behavior. Upon illumination, an additional current density contribution is obtained as a consequence of the photo-generated charge carriers. In the first quadrant, the respective $j(V)$ characteristics in the dark and under illumination converge, as expected (see Section 3.3).

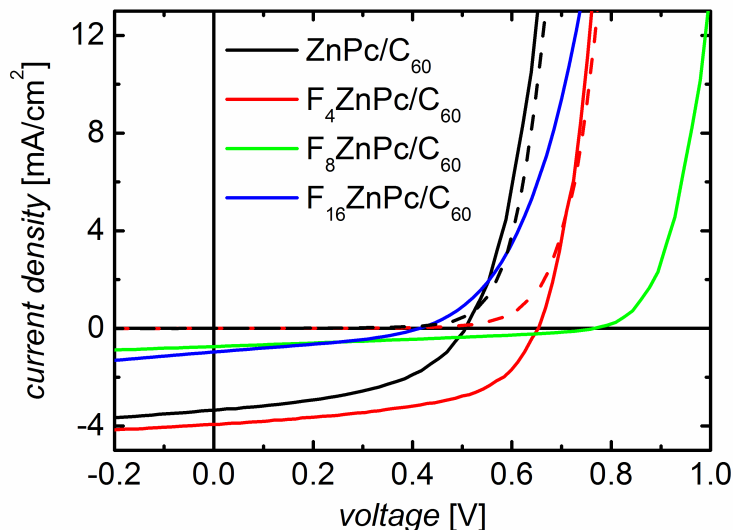


Figure 7.1.: $j(V)$ characteristics of $F_n\text{ZnPc}/\text{C}_{60}$ solar cells under AM1.5G standard illumination conditions. Additionally, dotted lines represent the corresponding $j(V)$ characteristics of two exemplary bilayer cells in the dark.

Since fluorination was considered to shift frontier energy levels to lower values, hence affecting the D/A heterojunction energetics, a severe impact on V_{oc} was expected. For ZnPc/C₆₀ solar cells an open circuit voltage of 0.51 V is measured, which concurs with the results of other groups. [124, 176] In case of F₄ZnPc/C₆₀ based devices the open circuit voltage is increased to 0.65 V. Similar results of up to 0.68 V were achieved in literature for bulk-heterojunction architecture. [176] A further improvement of this quantity is detected for F₈ZnPc/C₆₀ solar cells, yielding a 50 % increase in comparison to unsubstituted devices based on ZnPc/C₆₀. Photovoltaic investigations for this material combination have been reported for the first time in this study. [175] Considering different published photoelectron spectroscopy measurements, the remarkable increase of the open circuit voltage can qualitatively be assigned to an augmented effective band gap. By plain combination of HOMO and LUMO energies reported in literature, the effective band gap was calculated assuming vacuum level alignment between the different D/A interfaces. [99, 177, 178] Thereby, the expected open circuit voltage for all devices was ascertained according to Equation 3.5, using $\Delta = 0.5$ eV. The calculated data is indicated by the red symbols in the bottom graph of Figure 7.2. Evidently, the actual gain in V_{oc} for F₈ZnPc/C₆₀ observed in the $j(V)$ characterization is considerably smaller than the predicted increase according to Equation 3.5. For bilayer devices based on the perfluorinated homologue F₁₆ZnPc the open circuit voltage is even reduced to 0.41 V despite the expected larger effective band gap and with it, larger open circuit voltage.

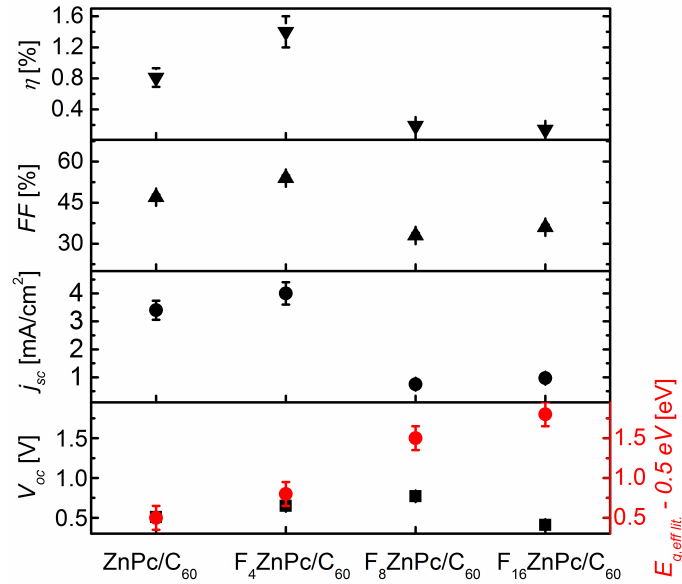


Figure 7.2.: Solar cell parameters of F_nZnPc/C₆₀ photovoltaic devices. For the calculation of the effective band gap $E_{g,eff,lit.}$ literature values were taken as reference, assuming vacuum level alignment. [99, 177, 178]

Distinct variations of the short circuit current densities are confirmed upon incremental fluorination. The reference material combination ZnPc/C₆₀ yields a short circuit current density

of 3.4 mA/cm². The largest j_{sc} of 4.0 mA/cm² is obtained for F₄ZnPc/C₆₀ bilayers, which constitutes an increase of almost 20 % in comparison to ZnPc/C₆₀. Upon further fluorination however, the short circuit current density is reduced to 0.77 mA/cm² and 0.98 mA/cm² in F₈ZnPc/C₆₀ and F₁₆ZnPc/C₆₀ based devices, respectively. Thus, the solar cells comprised of differently fluorinated phthalocyanines yield a discrepancy in j_{sc} of up to a factor of five.

For ZnPc/C₆₀ photovoltaic cells a FF of 47 % was obtained. In comparison to these reference devices, improved transport properties for F₄ZnPc/C₆₀ bilayer cells are evinced by a fill factor of 55 %. Upon further fluorination however, this quantity drops to 33 % for F₈ZnPc/C₆₀ and to 36 % for F₁₆ZnPc/C₆₀ devices, respectively. The phenomenological quantity markedly determining the resulting fill factors upon fluorination is the variation of the series resistance R_s (see Section 3.3). The series resistance of a solar cell is determined under open circuit conditions and the parallel resistance under short circuit conditions. As summarized in Table 7.1, the macroscopic series resistances for F₈ZnPc/C₆₀ and F₁₆ZnPc/C₆₀ thin film devices is one order of magnitude higher in comparison to bilayer cells based on ZnPc/C₆₀ and F₄ZnPc/C₆₀. In contrast, the parallel resistances vary only slightly by approx. a factor of two.

	ZnPc	F ₄ ZnPc	F ₈ ZnPc	F ₁₆ ZnPc
series resistance R_s [Ωcm^2]	31	22	250	150
parallel resistance R_p [Ωcm^2]	900	600	1400	600

Table 7.1.: Series and parallel resistances of F_nZnPc/C₆₀ solar cells.

Finally, as a key criterion for the overall solar cell performance, the power conversion efficiency η was calculated. The efficiency of 0.81 % for the reference ZnPc/C₆₀ bilayer cell coincides with values reported in literature. [179] The best performance is obtained for the material combination F₄ZnPc/C₆₀ with a power conversion efficiency of 1.4 %. In contrast, further fluorination results in a decrease of η to 0.19 % and 0.14 % for F₈ZnPc/C₆₀ and F₁₆ZnPc/C₆₀ bilayer devices, respectively.

After this preliminary overview of the impact of fluorination on the $j(V)$ characteristics, the physical origins of the observed variations will be elucidated step by step in this chapter by means of complementary measurements, aiming for a comprehensive picture of the contributing processes on microscopic length scales. For that purpose, the focus is initially set on the investigation of the optical and structural thin film properties of the fluorinated zinc phthalocyanines.

7.3. Thin Film Properties of F_nZnPc

Optical Investigations

The first step in photon to current conversion in photovoltaics is the absorption of incident light. In order to assign a potential change of the absorption characteristics of F_nZnPc upon

fluorination to the generated photocurrent in $F_n\text{ZnPc}/\text{C}_{60}$ solar cells (see section 7.2), 40 nm thick phthalocyanine thin films were evaporated on glass substrates and investigated by UV/Vis spectroscopy. The resulting absorption coefficients are displayed in Figure 7.3. Additionally, the upper graph shows the absorption coefficient of the acceptor C_{60} .

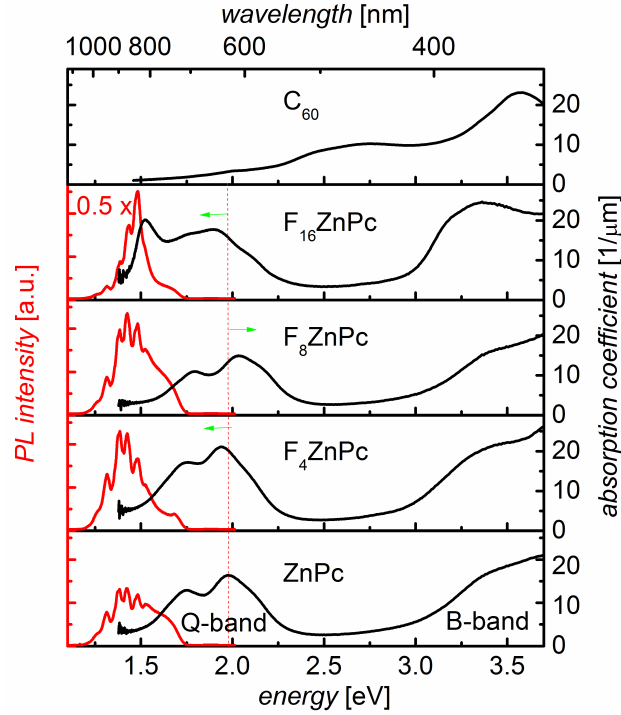


Figure 7.3.: Absorption coefficients and photoluminescence spectra of differently fluorinated zinc phthalocyanine $F_n\text{ZnPc}$ ($n = 0, 4, 8, 16$) thin films. The top graph shows the absorption coefficient of the acceptor C_{60} .

Evidently, all $F_n\text{ZnPc}$ thin films absorb in two broad but structured bands in an almost complementary spectral region with respect to the acceptor C_{60} . The absorption coefficients of ZnPc , $F_4\text{ZnPc}$ and $F_8\text{ZnPc}$ are remarkably similar, confirming the conservation of the relative frontier orbital energies as well as of the general packing motif upon fluorination. The absorption band appearing between 1.5 eV and 2.25 eV is the so-called Q-band and has been assigned to an a_{1u} to e_g transition. [128] This Q-band has a characteristic doublet, which is attributed to Davydov-splitting with absorption peaks located between 1.75 eV and 1.79 eV and at higher energies between 1.94 eV and 2.04 eV. [180] Davydov-splitting refers to the splitting of bands to lift the energy degeneracy caused by the presence of two or more translational invariant molecular entities in the unit cell. [15] The spectral features described are typical for the so-called α -crystal structure of crystalline metal phthalocyanine thin films. [11, 128, 176, 181] This assertion will be elucidated in more detail in the morphological investigation below. Moreover, the second absorption band with an onset at 3.0 eV and a maximum at 3.4 eV is the so-called B-band which corresponds to the Soret- or γ -band in porphyrins.

Despite the overall similarity of the absorption features, slight differences are detected for the different $F_n\text{ZnPc}$ thin films, namely a variation of the Q-band doublet peak positions, as indicated by green arrows in Figure 7.3. For example, with reference to unsubstituted ZnPc , the Q-band absorption maximum of $F_4\text{ZnPc}$ is slightly red-shifted by 30 meV, whereas for $F_8\text{ZnPc}$ a blue-shift of 50 meV appears. Moreover, the energy difference between peak positions of the Q-band doublet, which corresponds to a change of Davydov-splitting, is altered slightly. Despite their small amplitudes, the observed energy shifts render reproducible in the photovoltaic device characterization, as will be demonstrated by external quantum efficiency measurements in Section 7.5 and can be attributed to slight modifications of the relative transition dipole alignment and the intermolecular coupling upon fluorination.

In contrast to its homologues, UV/Vis absorption data of perfluorinated $F_{16}\text{ZnPc}$ yield a characteristically different spectral pattern, resulting in considerably broadened Q- and B-band absorption. Beside a strong peak at 1.91 eV and a weaker absorption shoulder at 1.71 eV, resembling the Davydov-splitting of the previously discussed compounds, an additional intense peak in the near-infrared spectral region appears at 1.54 eV. This characteristically different absorption behavior of perfluorinated $F_{16}\text{ZnPc}$ speaks in favor of a change of intermolecular coupling, compared to the other phthalocyanines under study, giving first evidence for the occurrence of a different crystal structure. Thin films comprised of the related molecule $F_{16}\text{CuPc}$ are known to crystallize in two different packings, the so-called β -bilayer and the β -phase crystal structure. The β -bilayer phase contains one molecule in a rectangular unit cell and crystallizes with molecules standing upright in a face-on configuration along the (ab)-plane, whereas for the β -phase, the stacking within the (ab)-plane shows a herringbone arrangement with two molecules in an oblique unit cell. [182] As a result of the different packings, both crystal structures show distinct absorption characteristics associated with absorption peaks at 1.54 eV for the β -phase polymorph and at 1.91 eV and 1.71 eV for the β -bilayer phase. [174] The occurrence of absorption peaks at identical energetic positions speaks in favor of the existence of a similar polymorph in $F_{16}\text{ZnPc}$ and $F_{16}\text{CuPc}$.

The complementary photoluminescence (PL) spectra of $F_n\text{ZnPc}$ thin films were measured additionally, utilizing a laser diode with an excitation wavelength of 635 nm. The corresponding spectra are illustrated in 7.3. Evidently, broad PL bands appear between 1.20 eV and 1.75 eV and can be related to fluorescence originating from the Q-band. [183] The modulation of the PL intensity in all $F_n\text{ZnPc}$ thin films is attributed to optical etaloning of the CCD camera. Next to the similarity of absorption features discussed above, the shapes of the PL spectra of ZnPc , $F_4\text{ZnPc}$, and $F_8\text{ZnPc}$ closely resemble each other. The emission maxima located at 1.42 eV result in Stokes-shifts of $2600 - 2800 \text{ cm}^{-1}$ (0.32 - 0.35 eV). Again, a change in the optical properties is detected for the perfluorinated homologue $F_{16}\text{ZnPc}$. Especially the PL peak intensity at 1.48 eV appears to be exceptionally high and the related Stokes-shift is reduced to 380 cm^{-1} (0.047 eV). Despite spectrally broader absorption of $F_{16}\text{ZnPc}$, the width of the PL emission-band renders almost identical to that of the other $F_n\text{ZnPc}$ s. This observation can be rationalized by the fact that according to Kasha's rule, emission always occurs from the energetically lowest

lying, dipole-allowed excited state which is expected to refer to the energetically lowest lying Davydov-component in $F_{16}ZnPc$ crystalline thin films (see Section 2.2).

In regard of the only minor modifications of optical characteristics of F_nZnPc thin films presented in this section, the evident discrepancies between the photovoltaic characteristics of the corresponding F_nZnPc/C_{60} bilayer cells (see section 7.2), in particular with regard to the generated photocurrents, are not allegeable. On the contrary, for differently fluorinated F_nZnPc s the first step in photon to current conversion, i.e. the absorption of incident light, is expected to proceed in a similar manner.

Structural Investigations

As excitonic and electronic transport properties of an organic thin film are closely related to its microstructure, the impact of gradual fluorination of F_nZnPc thin films on the morphology was analyzed by X-ray diffraction measurements in Bragg-Brentano geometry (see Section 6.2.1). The corresponding diffraction spectra are displayed in Figure 7.4. These spectra refer to the momentum transfer q_z along the surface normal and hence, probe the out-of-plane crystallinity, corresponding to the direction of charge carrier and exciton transport in F_nZnPc/C_{60} solar cells.

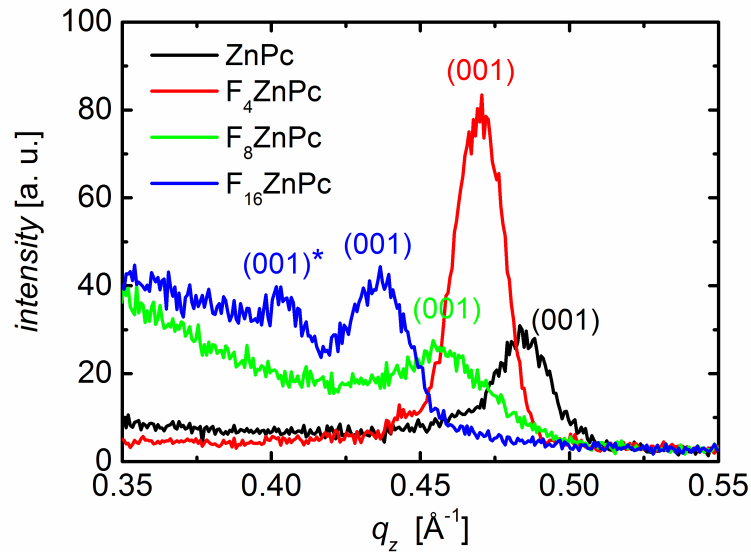


Figure 7.4.: X-ray diffraction measurements in Bragg-Brentano geometry of F_nZnPc thin films.

For all F_nZnPc thin films under study a polycrystalline structure could be confirmed. The indicated Bragg peak at $q_z = 0.48 \text{\AA}^{-1}$ for unsubstituted ZnPc was assigned to the (001) diffraction of the α -crystal phase and corresponds to a lattice spacing of 13.0\AA . [126, 174, 184] In this configuration ZnPc molecules adopt an almost upright standing orientation. Upon fluorination, the (001) Bragg peak of the associated α -phase is continuously shifted towards smaller values, thus resulting in an increased lattice spacing ($d_{F_4ZnPc} = 13.4 \text{\AA}$, $d_{F_8ZnPc} = 14.0 \text{\AA}$,

$d_{F_{16}ZnPc} = 14.4 \text{ \AA}$) as illustrated in the upper graph of Figure 7.5. Due to the overall bigger van-der-Waals radii of the fluorinated compounds, the repulsion between adjacent phthalocyanine molecules is leading to an increasing upright-standing alignment and thus, to an increase of the lattice spacing perpendicularly to the substrate upon fluorination. Additionally, this stronger Coulomb repulsion may alter the subtle balance between the substrate–molecule interaction and the intermolecular packing energy. This can result in a different tilt angle with respect to the substrate normal and therefore, in the observed changes of the out-of-plane lattice spacing. Similar lattice spacings were reported by Meiss et al. for ZnPc and F_4ZnPc thin films grown on ITO. [176] Moreover, for co-evaporated thin films of the related molecules CuPc and $F_{16}CuPc$ on ITO/PEDOT:PSS substrates the out-of-plane lattice spacing was linearly increased as a function of the content of the latter at room temperature. [185, 186]

Evidently, for $F_{16}ZnPc$ another Bragg Peak appears at $q_z = 0.41 \text{ \AA}^{-1}$ in the diffraction spectrum in Figure 7.4, confirming the presence of a second crystal structure. The corresponding lattice spacing for the supposed (001)* diffraction peak accounts to $d_{F_{16}ZnPc^*} = 15.6 \text{ \AA}$. Results associated with this $F_{16}ZnPc$ polymorph are indicated by red symbols in Figure 7.5. Accordingly, in this phase $F_{16}ZnPc$ molecules adopt an alignment with a smaller tilt angle with respect to the surface normal. For the related molecule $F_{16}CuPc$ on SiO_2 substrates, two co-existing crystal structures are reported in literature, as mentioned above, called β -bilayer and the β -phase. [174, 182, 187] For the former, a (001) layer spacing of 14.1 \AA was observed, whereas for the latter also an increased lattice spacing between 14.3 and 14.9 \AA was confirmed. [182, 188]

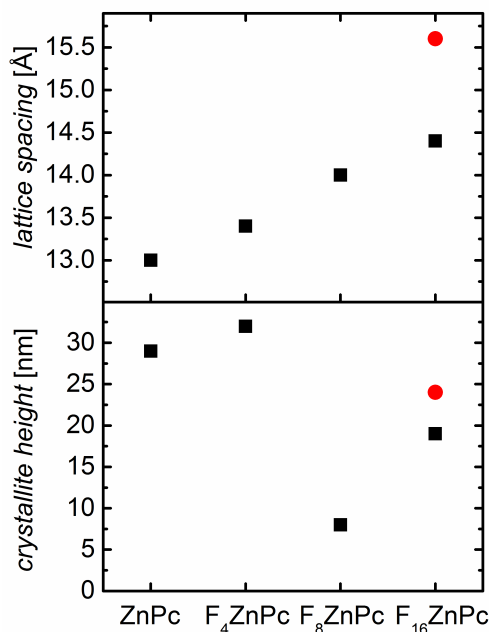


Figure 7.5.: Lattice spacings (upper graph) and crystallite heights (lower graph) of F_nZnPc thin films. The red dots represent the data of the $F_{16}ZnPc$ polymorph (see Figure 7.4).

For the application of organic semiconductors in opto-electronic devices such as organic solar cells or organic light emitting diodes, sufficiently good transport properties are imperative. A correlation between transport properties of excitons as well as of free charge carriers and the degree of crystallinity of the organic thin films has been established in literature for many different organic compounds. [49, 189, 190] Hence, the crystallite height h along the transport direction is considered to be a measure for this correlation and was calculated according to the Scherrer-Equation 6.4. The crystallite heights for differently fluorinated thin films are summarized in Figure 7.5. Evidently, a strong influence of fluorination on the crystallite height is confirmed. For ZnPc and F₄ZnPc thin films, crystallites spread as far as 80 % of the nominal film thickness, illustrating the high degree of long range order. In contrast, the texture of F₈ZnPc and F₁₆ZnPc is markedly distorted, resulting in smaller crystalline domains extending only to 20 % and 50 % of the total film thickness, respectively. Therefore, the more distorted structure of F₈ZnPc and F₁₆ZnPc thin films may be the reason for the obtained higher series resistances in the corresponding photovoltaic devices (see Table 7.1) and for the smaller fill factors and short circuit current densities (see Figure 7.2). Remarkably, similar crystallite heights are observed for the two F₁₆ZnPc phases which, moreover add up to the total film thickness of 40 nm. This hints at the fact that the two polymorphs grow mainly on-top of each other, which has a strong impact for the F₁₆ZnPc film thicknesses chosen for thin film organic electronics. [175] In general, the growth behavior of metal phthalocyanine thin films is sensitive to the preparation conditions. [182] In particular, the substrate temperature during deposition has a crucial influence on the crystalline structure of the respective phthalocyanine thin film. It is to be noted, that XRD measurements were carried-out on samples with the substrate kept at room temperature during deposition, i.e. under processing conditions striven for in the production of potential opto-electronic devices.

7.4. Determination of F_nZnPc/C₆₀ Interface Energetics by UPS

The energetics at the donor/acceptor interface are crucial for the macroscopic solar cell performance. [97, 99] However, the values obtained for the open circuit voltage in Section 7.2 could not be explained with the help of the empirically found Equation 3.5 and under the simple assumption of combining literature values of relevant energy levels of the photo-active materials (see Figure 7.2 bottom graph). Therefore, UPS measurements were carried-out to reveal the actual energy level positions present in the photovoltaic bilayer cells. To resemble the device architecture of the photovoltaic cells, thickness-dependent UPS investigations were conducted on F_nZnPc/C₆₀ bilayers, thermally deposited onto ITO/MoO₃ substrates. In Figure 7.6 the valence band (VB) spectra and the secondary electron cut-off (SECO) at the respective final layer thicknesses of an ITO/MoO₃(5 nm)/ZnPc(30 nm)/C₆₀(35 nm) stack are displayed exemplarily. The energy levels were determined according to the onset method (see Section 6.4). LUMO energies and CB energies were determined by adding the electronic transport band gap to the respective HOMO or VB energies. [173]

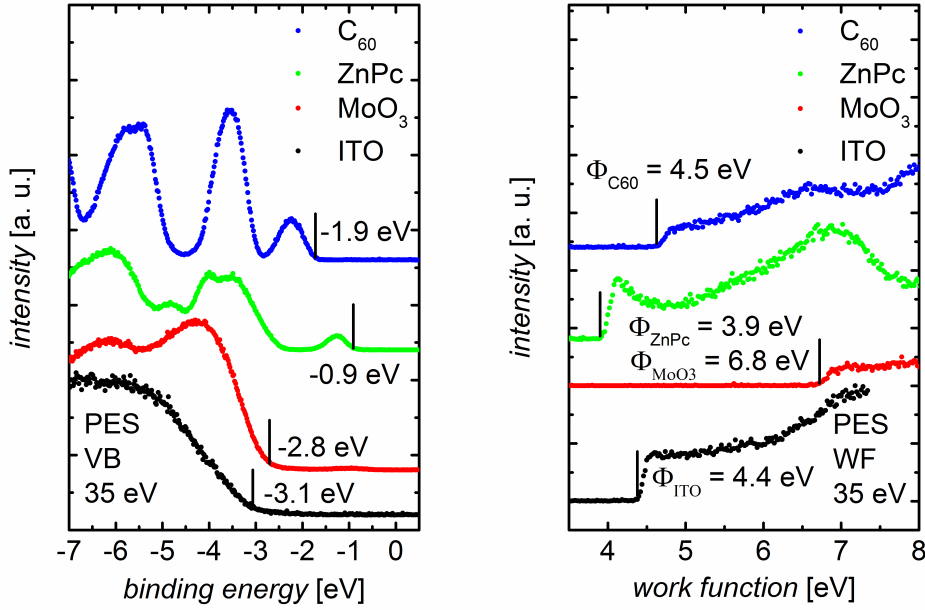


Figure 7.6.: Valence band and work function spectra at respective final layer thicknesses of the ZnPc/C₆₀ heterojunction on ITO/MoO₃.

The band alignments of all four F_nZnPc/C₆₀ heterostructures, deduced from the UPS measurements, are summarized in Figure 7.7. For all samples under study, identical energy levels of the bottom electrode and the MoO₃ hole conduction layer could be confirmed, wherefore these energy levels are only exemplarily shown for the ZnPc/C₆₀ heterojunction. The obtained work function of 4.4 eV for ITO is in perfect agreement with values reported in literature. [103, 109] All F_nZnPc donor layers are forced into a strong Fermi-level pinning, since the ionization energy with respect to the vacuum level of the respective phthalocyanine exceeds the work function of MoO₃. Concomitantly, charge carrier transfer across this interface takes place causing a positive charge accumulation in the phthalocyanine layers until a thermodynamic equilibrium is established. However, the pinning is not sustained across the total thickness of the respective phthalocyanine thin film. Instead, with increasing phthalocyanine layer thickness band bending sets in to shift the HOMO level away from the Fermi-level.

At the final layer thickness of 30 nm, the energy difference between the HOMO and the Fermi-energy amounts to 0.9 eV for ZnPc and 1.0 eV for F₄ZnPc. When depositing C₆₀ on top, the HOMOs of these phthalocyanines bend upward and an electron transfer from the respective phthalocyanine across the interface to the fullerene takes place, leading to a negative charge accumulation at the boundary as schematically depicted in Figure 7.7. This charge transfer occurs since the electron affinity of the fullerene exceeds the Fermi-energy of the respective phthalocyanine for both ZnPc/C₆₀ and F₄ZnPc/C₆₀. Accordingly, a pinning of the LUMO of C₆₀ to the Fermi-level is observed. The electric field at the interface generated by the negative

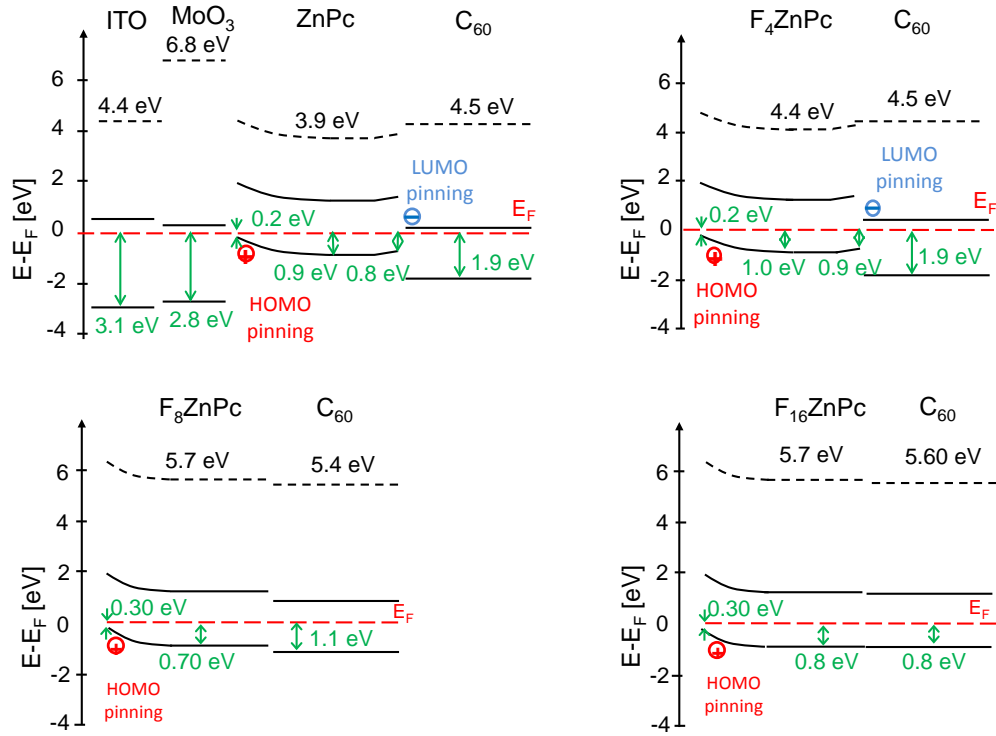


Figure 7.7.: Band schemes of $F_n\text{ZnPc}/\text{C}_{60}$ heterojunctions. The LUMO energies of the photoactive materials were calculated by adding the electronic transport gap to the HOMO energies ($E_{gap\text{ZnPc}} = 2.1\text{ eV}$ and $E_{gap\text{C}_{60}} = 2.0\text{ eV}$). [173]

charges located in C_{60} and the positive charges in the $F_n\text{ZnPc}$ layer causes the energy levels of the latter to bend upward by 0.1 eV.

After final deposition of C_{60} on top of ZnPc , a shift of the secondary electron cut-off (see work function scan in Figure 7.6) of 0.6 eV is observed, i.e. a vacuum level mismatch between donor and acceptor appears. Such an abrupt vacuum level shift between two organic layers is equivalent to the occurrence of an interfacial dipole at their common interface.

Upon increasing degree of fluorination, frontier orbital energies are successively shifted towards lower energies with respect to the vacuum level, as indicated in Figure 7.8. This cascade-like energy level shift was qualitatively anticipated by semi-empirical calculations and previous photoelectron spectroscopy measurements on partly fluorinated $F_n\text{ZnPcs}$ and $F_n\text{CuPcs}$. [11, 16, 177] However, a comprehensive study of all four compounds, implemented in a real optoelectronic layer sequence, was not reported yet. Finally, the absolute energy level shift upon perfluorination in $F_{16}\text{ZnPc}$ accounts to 1.7 eV yielding a HOMO energy with respect to the vacuum level of 6.5 eV. Despite this successive shift of energy levels with respect to the vacuum level upon increasing fluorination, the position of the HOMO energies at the final layer thickness of 30 nm is only slightly varied between -0.7 eV and -0.9 eV with respect to the Fermi-energy, as indicated in Figure 7.8.

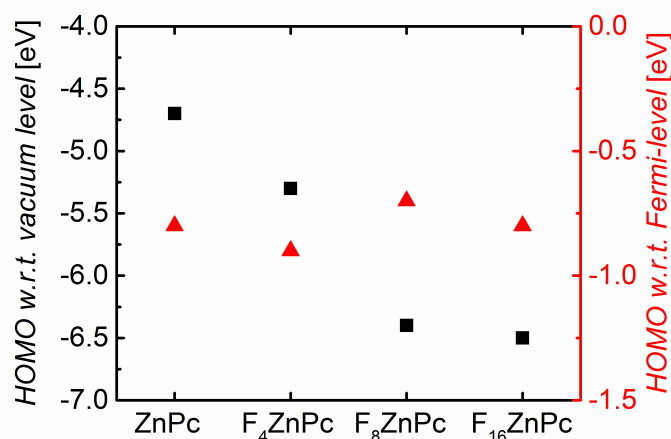


Figure 7.8.: HOMO energies of $F_n\text{ZnPc}$ s at the D/A interface with respect to the vacuum level and the Fermi-level, respectively.

For the heterostructures based on highly fluorinated zinc phthalocyanines, i.e. $F_8\text{ZnPc}/\text{C}_{60}$ and $F_{16}\text{ZnPc}/\text{C}_{60}$, no LUMO level pinning of the C_{60} layer is detected. Instead, vacuum level alignment between the respective donor and the C_{60} acceptor is observed. The presence and absence of this C_{60} LUMO pinning to the Fermi-level evidently constitutes a decisive factor for the D/A interface energetics and thus for the efficiency of the photon-to-charge conversion. This model system is a vivid example for the complex interplay of microscopic electronic effects, resulting from the energetic modification of the D/A interface constituents at otherwise structurally similar boundaries. With this total set of data, the determination of the real energetic offsets at the D/A heterojunctions is possible. In the final section of this chapter these energetic offsets will be correlated to the photocurrent contributions by the individual molecular layers in *EQE* measurements and to the initially discussed $j(V)$ characteristics (see section 7.1).

7.5. Correlation between $F_n\text{ZnPc}/\text{C}_{60}$ Interface Energetics and Device Characteristics

Spectrally resolved photocurrents of $F_n\text{ZnPc}/\text{C}_{60}$ bilayer cells were determined enabling the calculation of the external quantum efficiencies according to Equation 6.1. The corresponding results are displayed in Figure 7.9 a). With the knowledge of the respective absorption coefficients of the molecular constituents, shown in Figure 7.3, it becomes apparent, that both photo-active materials yield a photocurrent contribution in all bilayer cells under study. Between 400 nm and 550 nm the *EQE* is primarily assigned to the fullerene acceptor layer, whereas at higher wavelengths, the *EQE* is attributed to the phthalocyanine donor material. In accordance with the absorption coefficients of ZnPc , $F_4\text{ZnPc}$ and $F_8\text{ZnPc}$ in Figure 7.3, two distinct maxima centered at 630 nm and 700 nm are detected. Remarkably, the same spectral shifts of the latter

two with respect to the former one can be confirmed in the EQE measurement. Moreover, in agreement with the absorption coefficient of the perfluorinated $F_{16}ZnPc$ thin film, an additional peak at 815 nm is detected in the NIR spectral region for the $F_{16}ZnPc/C_{60}$ bilayer solar cell.

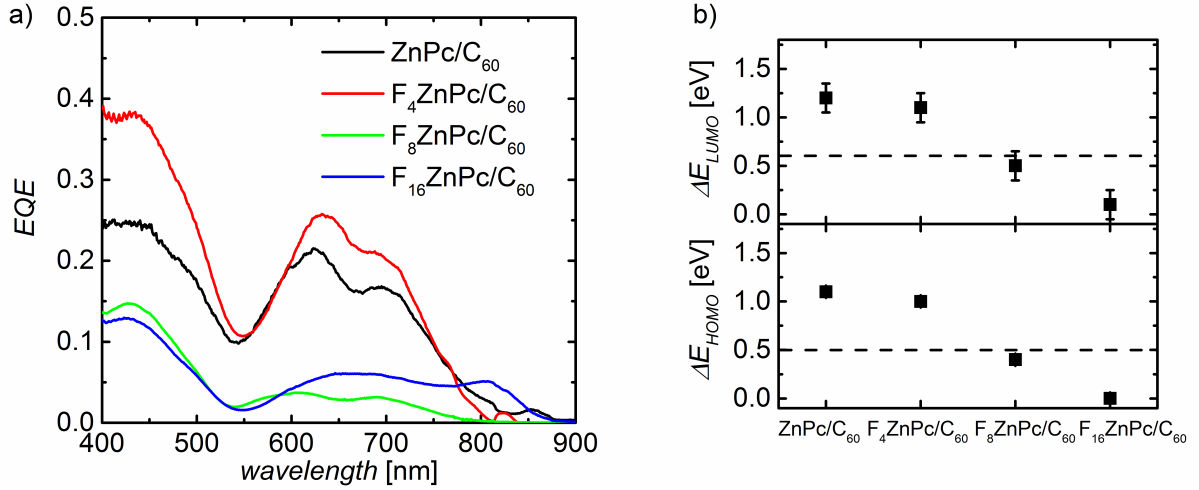


Figure 7.9.: a) External quantum efficiency of F_nZnPc/C_{60} solar cells and b) energetic offsets at the respective donor/acceptor interface. Dotted lines represent the expected exciton binding energies. [128, 191, 192]

Although both semiconductors contribute to the EQE in all bilayer solar cell configurations, absolute values vary distinctly for the four different heterostructures. Striving for a deeper understanding of this discrepancy, the relevant energetic positions of frontier orbitals at the D/A interface have to be taken into account. The upper graph of Figure 7.9 b) shows the energy difference ΔE_{LUMO} between the respective F_nZnPc and the C_{60} LUMO level. This energetic offset is supposed to drive the dissociation of excitons created in the respective phthalocyanine layer into free charge carriers, under the assumption that the offset exceeds the exciton binding energy (see Section 3.1). Likewise, the bottom graph illustrates the energy difference ΔE_{HOMO} between the HOMO energies of the donor and acceptor materials, considered to be decisive for dissociation of excitons generated in the fullerene phase into free charge carriers. Additionally, the dotted lines in Figure 7.9 b) indicate the anticipated exciton binding energies of $E_{bind\ ZnPc} = 0.6$ eV in the phthalocyanine phase (upper graph) and of $E_{bind\ C_{60}} = 0.5$ eV for the fullerene acceptor (lower graph), necessary to overcome for exciton dissociation. [128, 191, 192]

Obviously, the highest EQE values over the whole spectral range are obtained for the bilayer cells based on $ZnPc/C_{60}$ and F_4ZnPc/C_{60} . In both cases, the energetic offsets at the interface ΔE_{LUMO} and ΔE_{HOMO} exceed the required exciton binding energy, as illustrated in Figure 7.9 b), rendering a separation into free charge carriers highly efficient. Large crystallites being present in F_4ZnPc thin films (see Figure 7.5) support both improved excitonic and electronic transport, resulting in a distinctly increased EQE by 25 % of bilayer cells based on this compound in comparison to $ZnPc/C_{60}$ reference devices. [49, 189, 190] For F_8ZnPc/C_{60} bilayer solar cells the energetic offsets at the D/A interface are in the range of the required exciton binding energies.

Accordingly, a dissociation into free charge carriers may be energetically limited. Concomitantly, considering the higher degree of disorder in F_8ZnPc thin films a distinct EQE decrease in the spectral absorption range of both the donor and acceptor compound is obtained. Finally, as illustrated in Figure 7.9, for $F_{16}ZnPc/C_{60}$ based devices there is no excess energy available at the D/A interface to drive exciton separation. However, clearly a photovoltaic response is obtained over the whole spectral absorption range, hence raising the question about the functional principle of these devices. Therefore, it is imperative to verify first of all, whether the $F_{16}ZnPc/C_{60}$ interface can be considered photo-active, i.e. if it enables exciton dissociation in general.

For that purpose, comparative spectrally resolved photoluminescence (PL) measurements were carried-out on ITO/ MoO_3/F_nZnPc thin films and ITO/ $MoO_3/F_nZnPc/C_{60}$ heterostructures, comprising the additional fullerene acceptor layer. Utilizing a cw-laser source with an excitation wavelength of 532 nm, the upper graph in Figure 7.10 a) illustrates the impact of this additional C_{60} layer on the spectrally resolved PL in case of F_4ZnPc based samples. The PL of the fullerene layer is considered to be very weak, because radiative transitions are dipole forbidden due to symmetry considerations. [18] Nevertheless, this weak PL contribution was taken into account for background correction by using a polynomial fit of second order.

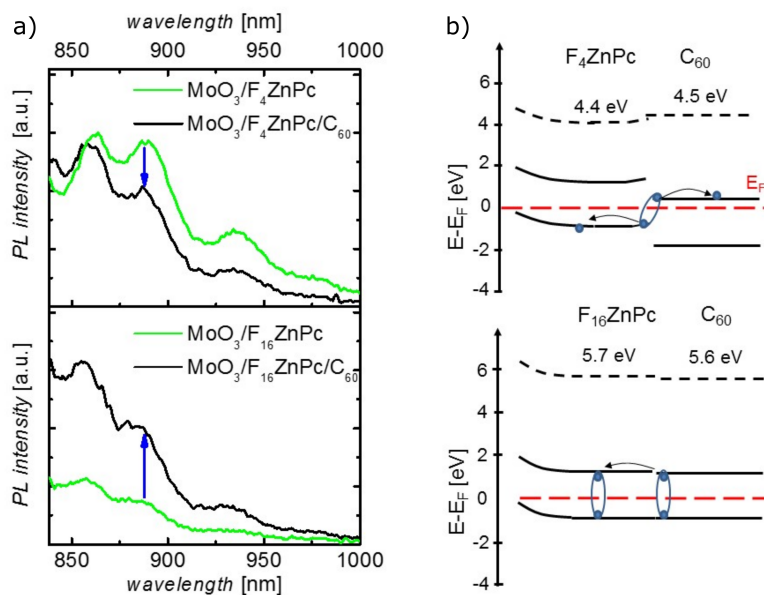


Figure 7.10.: a) Spectrally resolved photoluminescence of ITO/ MoO_3/F_nZnPc thin films and the corresponding heterostructures comprising the additional C_{60} acceptor layer. b) At a conventional D/A heterojunction, such as constituted in F_4ZnPc/C_{60} , excitons become dissociated into free charge carriers. Instead, in $F_{16}ZnPc/C_{60}$ heterostructures the almost identical energetic positions of the frontier orbitals prevent an efficient exciton separation, but allow for energy transfer from the fullerene to the phthalocyanine layer.

Evidently, the presence of the C_{60} acceptor layer results in a distinct quenching contribution of the photoluminescence. This finding is intuitively expected for a conventional D/A heterojunction, yielding efficient exciton dissociation at the D/A interface and hence, reducing the number of radiatively decaying excitons in F_4ZnPc . This photo-physical behavior was also obtained for heterostructures based on $ZnPc$ and F_8ZnPc (not shown).

In contrast, the photoluminescence of samples based on $F_{16}ZnPc$ are affected fundamentally different, i.e. the implementation of the additional C_{60} fullerene layer causes an increase of the PL of $F_{16}ZnPc$ (see Figure 7.10 a) lower graph). Accordingly, instead of becoming dissociated at the common interface, excitons created in C_{60} are transferred as a whole to the $F_{16}ZnPc$ layer, as schematically depicted in the bottom graph of Figure 7.10 b). This energy transfer is assumed possible due to the specific energy level alignment at the D/A interface, comprising almost no energetic offsets. [175] Hence, the $F_{16}ZnPc/C_{60}$ interface is proven photo-inactive, not allowing for an efficient dissociation of excitons generated in C_{60} . This is also considered to be true for the dissociation of excitons generated in $F_{16}ZnPc$, since the energetic offset at the D/A interface and the required exciton binding energy are comparable under these conditions. The photovoltaic response obtained from the phthalocyanine layer is anticipated to originate from a dissociation of excitons at the MoO_3 interface via a charge recombination mechanism (see Section 4.2), since a separation of excitons at transition metal oxide/organic interfaces is reported possible in literature. [109, 193] In general, such a phthalocyanine photocurrent contribution is also existent in the other solar cells under study, but is considered less pronounced in comparison to that originating from the immediate dissociation at the D/A interface. The fullerene contribution to the *EQE* is more eclectic. Partly, excitons created in C_{60} are transferred to the phthalocyanine layer and subsequently, may be dissociated at the MoO_3 interface. However, assuming this to be the dominant mechanism for dissociation of excitons generated in C_{60} , it seems surprising that the *EQE* of $F_{16}ZnPc$ based solar cells is only marginally smaller in the spectral absorption range of the fullerene (see Figure 7.9) compared to that of F_8ZnPc/C_{60} solar cells. This speaks in favor of the existence of an additional mechanism for fullerene photocurrent generation. This hypothesis will be elucidated in more detail in the next Chapter 8.

Since the $F_{16}ZnPc/C_{60}$ interface was proven to be photo-inactive, i.e. not enabling exciton dissociation, those devices are suggested to behave like Schottky-cells in which C_{60} acts as sensitizer and charge carrier transport layer. [175] In literature, the working principle of identical solar cells was assigned to a charge carrier generation mechanism caused by an exciton recombination process at the $F_{16}ZnPc/C_{60}$ interface. Zhang et al. concluded on the recombination of holes from C_{60} excitons and electrons of $F_{16}ZnPc$ to generate free charge carriers. [193] However, the spectrally resolved photoluminescence measurements in this study yield no indication for the presence of such a process.

The hypothesis that $F_{16}ZnPc/C_{60}$ bilayers act like Schottky-cells is corroborated by the results of the $j(V)$ characterization in Section 7.2. For this material combination, an open circuit voltage of 0.41 V is obtained. Photoelectron spectroscopy measurements in Section 7.4 revealed

an effective band gap energy of 2.0 eV. According to Equation 3.5, a loss term of $\Delta = 1.59$ eV is ascertained (see Table 7.2). This quantity clearly is incompatible with values of Δ ranging between 0.3 eV and 0.8 eV for common D/A heterojunctions illustrating that the $F_{16}ZnPc/C_{60}$ interface is not determining the open circuit voltage. [4, 97–100] Rather, the work function of the electrodes is considered decisive for V_{oc} . This assumption is in agreement with varying open circuit voltages reported in literature for $F_{16}ZnPc/C_{60}$ bilayer cells, depending on the choice of electrode materials. [175, 193, 194]

heterojunction	$E_{g,eff}$ [eV]	$e \cdot V_{oc}$ [eV]	$\Delta = E_{g,eff} - e \cdot V_{oc}$ [eV]
ZnPc/ C_{60}	0.9	0.51	0.39
F_4ZnPc/C_{60}	1.0	0.65	0.35
F_8ZnPc/C_{60}	1.6	0.77	0.83
$F_{16}ZnPc/C_{60}$	2.0	0.41	1.59

Table 7.2.: Summary of the effective band gap $E_{g,eff}$, open circuit voltage V_{oc} , and loss term Δ according to Equation 3.5 for solar cells based on differently fluorinated zinc phthalocyanines.

The V_{oc} increase for F_4ZnPc/C_{60} and F_8ZnPc/C_{60} with respect to $ZnPc/C_{60}$ based devices can be attributed to an enhanced effective band gap. As indicated in Table 7.2, the loss term Δ for $ZnPc/C_{60}$ and F_4ZnPc/C_{60} bilayer solar cells is very similar and in general, can be considered small in comparison to other bilayer solar cells reported in literature. [4, 99, 100] In contrast, for F_8ZnPc/C_{60} photovoltaic cells, the loss term of 0.83 eV is considerably increased. With the utmost probability, due to the insufficient energetic offsets ΔE_{HOMO} and ΔE_{LUMO} at the D/A interface, exciton dissociation is efficiently impeded leading to enhanced recombination losses and accordingly, to an increased loss term.

Conclusion

In this chapter, the effect of successive fluorination on the photo-physical properties of F_nZnPc thin films and F_nZnPc/C_{60} ($n = 0, 4, 8, 16$) planar bilayer solar cells was under investigation. Whereas absorption coefficients of F_nZnPc thin films were proven to be mainly unaffected, photoelectron spectroscopy measurements revealed a systematic shift of frontier orbital energies towards lower energies upon fluorination. In comparison to unsubstituted $ZnPc$, energy levels of the perfluorinated $F_{16}ZnPc$ homologue are lowered by 1.7 eV with respect to the vacuum level. Complex electronic effects at the interface emerge by the deposition of the acceptor material C_{60} on top of the respective phthalocyanine layer, e.g. yielding for $ZnPc/C_{60}$ and F_4ZnPc/C_{60} a pinning of the C_{60} LUMO to the Fermi-energy. Additionally, formation of interfacial dipoles is observed at these D/A interfaces. Thus, assuming a common vacuum level between both photo-active materials, as frequently done in literature, is *a priori* not justified in such organic opto-electronic devices. In contrast, for bilayers containing F_nZnPc donor layers with a higher degree of fluorination, pinning of the C_{60} LUMO and the formation of an interfacial dipole at

the respective D/A interface are not detected. Evidently, the occurrence and absence of this Fermi-level pinning distinctly affects the D/A interface energetics and thus, the corresponding macroscopic solar cell performance. For instance, in comparison to ZnPc/C₆₀ reference cells an increase of the open circuit voltage by approx. 30 % and 50 % was obtained for bilayer devices based on F₄ZnPc/C₆₀ and F₈ZnPc/C₆₀, respectively. This increase was qualitatively attributed to an enhanced quasi Fermi-level splitting at the D/A interface. In this context, the doubled loss term of $\Delta = 0.8$ eV for F₈ZnPc/C₆₀ in comparison to ZnPc/C₆₀ and F₄ZnPc/C₆₀ bilayer cells was attributed to enhanced recombination losses.

This interpretation is corroborated by *EQE* measurements. In ZnPc/C₆₀ and F₄ZnPc/C₆₀ devices the energetic offsets ΔE_{HOMO} and ΔE_{LUMO} at the respective D/A interface exceed the exciton binding energies, rendering exciton dissociation into free charge carriers highly efficient. In contrast, for F₈ZnPc/C₆₀ solar cells those energetic offsets are in the same range as the exciton binding energies, thus preventing exciton dissociation and *vice versa* leading to enhanced recombination losses. Ultimately, the power conversion efficiency of F₄ZnPc/C₆₀ based devices is increased by more than 70 % with reference to ZnPc/C₆₀ bilayer cells, whereas for F₈ZnPc/C₆₀ η is decreased by almost 80 %.

Finally, upon perfluorination there is no energetic driving force left in F₁₆ZnPc/C₆₀ devices to separate excitons generated in either the donor or the acceptor material. However, a clear photovoltaic response was detected in the *EQE* measurements. Spectrally resolved PL studies revealed that the working principle of these devices is fundamentally different. The F₁₆ZnPc/C₆₀ interface was proven photo-inactive, not enabling exciton dissociation. Instead, at least a partial Förster resonant energy transfer from C₆₀ to F₁₆ZnPc molecules is approved. Excitons are presumably dissociated at MoO₃/F₁₆ZnPc interface. However, a comparison of the photocurrent contribution of the fullerene phase in F₁₆ZnPc/C₆₀ versus F₈ZnPc/C₆₀ indicated an additional exciton dissociation mechanism, which will be elucidated in the next chapter.

This systematic study highlights the fundamental significance of the D/A interface energetics in organic planar bilayer cells and the possibilities to deliberately change these energetics by chemical modification. Nevertheless, it is a subtle interplay between morphology and electronic effects that determines the quasi Fermi-level splitting at the D/A interface and thus V_{oc} and that provides the optimum driving force for exciton separation to achieve high photocurrent densities and thus power conversion efficiencies.

8. Correlating D/A Interface Energetics of $F_n\text{ZnPc}/\text{C}_{60}$ with Electronic Dynamics

The contributions of the individual molecular components of $F_n\text{ZnPc}/\text{C}_{60}$ ($n = 0, 4, 8, 16$) bilayer photovoltaic cells to the generated photocurrent densities varied considerably as evinced in the previous Chapter 7. The main factor causing this variation was qualitatively assigned to the modification of D/A interface energetics, ultimately governing exciton dissociation into free charge carriers. Up to now, little experimental work has been reported in literature on the underlying exciton dissociation and charge carrier recombination dynamics. This is in particular true for small molecule based organic solar cells of stacked layer design. In this chapter, the static picture of $F_n\text{ZnPc}/\text{C}_{60}$ interface energetics is complemented by involving electronic dynamics, accessed by means of ultrafast transient absorption spectroscopy (TAS) measurements. Not only the time scale of exciton separation and charge carrier recombination of one of the most prominent small molecule material combinations $\text{ZnPc}/\text{C}_{60}$ is under investigation, but also the impact of the D/A interface energetics of $F_n\text{ZnPc}/\text{C}_{60}$ bilayers on the electronic dynamics is established.

The presented studies were-carried out at the University of Stellenbosch in South Africa under the supervision of Prof. Heinrich Schworer during a scholarship provided by the German Academic Exchange Service (DAAD).

8.1. TAS on $F_n\text{ZnPc}/\text{C}_{60}$ Heterostructures

In order to resemble the device design of the bilayer solar cells studied so far, heterostructures of the following stack architecture were prepared for TAS measurements:

ITO/MoO₃(5 nm)/ $F_n\text{ZnPc}$ (30 nm)/ C_{60} (35 nm) $n = 0, 4, 8, 16$.

Additionally, a 35 nm thick neat C_{60} reference film evaporated on glass was characterized. The TAS measurements were carried-out for time delays of up to 500 ps at room temperature without encapsulation of the samples, since no changes of the electronic dynamics were reported under ambient conditions for neither ZnPc nor C_{60} . [42] By means of a non-linear optical parametric amplifier (NOPA), the pump pulse was either adjusted to 480 nm, i.e. the pump pulse only excites fullerene molecules, or to 700 nm resulting in absorption solely by the respective $F_n\text{ZnPc}$ layers (see steady state absorption spectra in Figure 7.3). The intensity of the pump pulse was

set to 125 mW/cm^2 . The probe pulse was generated either by utilizing a white light (WL) generating YAG-crystal or by the use of a second NOPA to probe a specific wavelength range. The duration of a pulse generated by the NOPA is less than 50 fs, and for a WL pulse it is approx. 150 fs. Thus, for a NOPA pump - WL probe experiment the time resolution is better than 200 fs, whereas for a NOPA pump - NOPA probe experiment a time resolution better than 100 fs is obtained. The results shown in this chapter were attained using NOPA pump - WL probe settings, unless specified otherwise.

In Figure 8.1 the transient absorption spectra of the $F_n\text{ZnPc}/\text{C}_{60}$ heterostructures and the neat C_{60} thin film are displayed for time delays of up to 20 ps in the NIR spectral region using a pump wavelength of 480 nm. For all heterostructures and the C_{60} reference sample, broad excited state absorption (ESA) bands, corresponding to positive ΔmOD values (see Section 6.3.3), are observed in the NIR. The maxima of the ESA are centered at 1050 nm, only for the $F_{16}\text{ZnPc}/\text{C}_{60}$ heterojunction a slight red-shift to 1130 nm is detected.

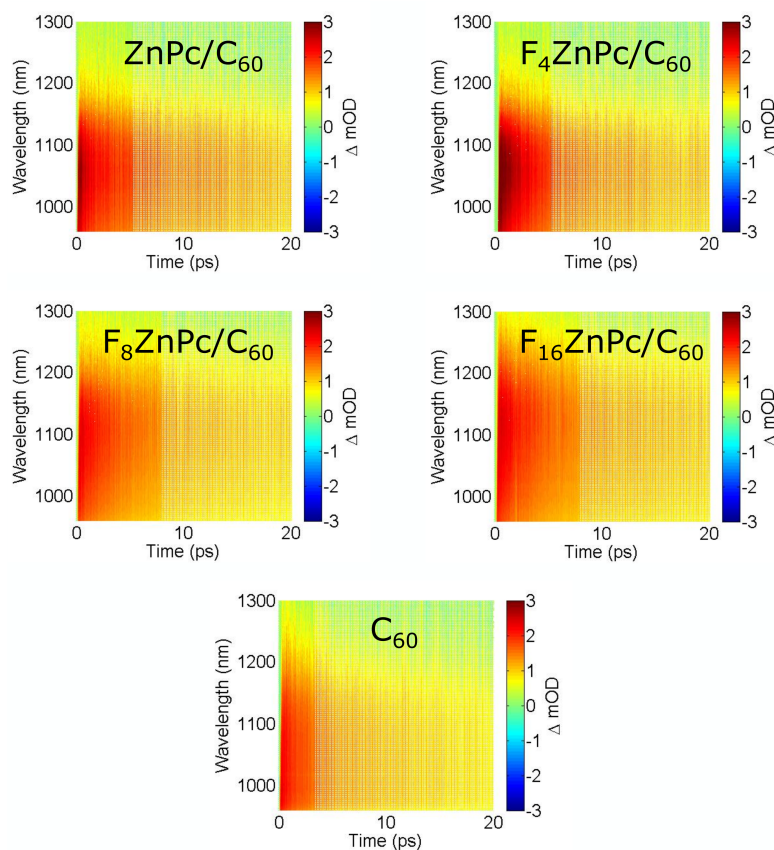


Figure 8.1.: Transient absorption spectra of $F_n\text{ZnPc}/\text{C}_{60}$ heterostructures and a neat C_{60} thin film in the near-infrared spectral region, utilizing a pump wavelength of 480 nm.

NOPA pump (480 nm) - NOPA probe (1050 nm) measurements were performed to conclude on the time scales of the emergence of the transient species. The corresponding results are shown in Figure 8.2. For the sake of clarity, only measurements on two $F_n\text{ZnPc}/\text{C}_{60}$ heterostructures and the C_{60} thin film are shown. Notably, the rise of the ESA signals occurs on ultrashort time

scales within 100 - 150 fs for all samples, thus being at the limit of the instrumental response of the employed TAS setup.

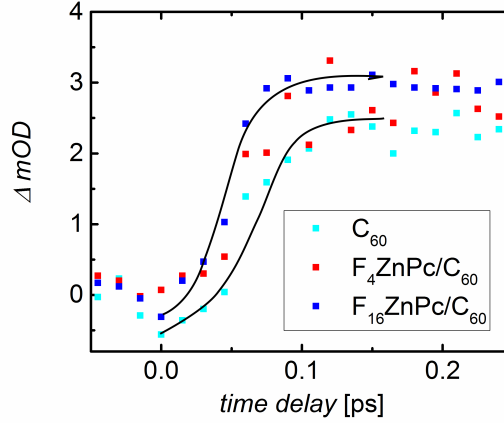


Figure 8.2.: NOPA pump (480 nm) - NOPA probe (1050 nm) experiments to conclude on the dynamics of the emergence of the ESA signal. For the sake of clarity, only the measurements on $F_{16}ZnPc/C_{60}$ and F_4ZnPc/C_{60} heterostructures as well as on the C_{60} film are shown. Black lines represent guides to the eye. The ESA signals arise on ultrashort time scales limited by the instrumental response function of the setup.

8.2. Classification of the Transient Absorption Species

In order to correlate interface energetics with electronic or excitonic dynamics, a classification of the observed absorption species is mandatory. In a first step, absolute ΔmOD values of the heterostructures are compared to those of the C_{60} thin film. In Figure 8.3 transient absorption spectra of the F_nZnPc/C_{60} heterojunctions and the C_{60} reference layer are shown at different time delays ranging between 0.3 ps and 400 ps. Obviously, for all samples under study, just after the ultrafast initial rise, a continuous decay of the ESA signal with time is observed, reflecting the recombination dynamics. Generally, higher ΔmOD values are obtained for all bilayer stacks with reference to those of the bare C_{60} sample, yielding clear evidence that these ESA signals are not merely originating from an excitonic species. If the signal had been originating solely from C_{60} excitons, a reverse behavior would have been expected, as the presence of the dissociating D/A interfaces would rather result in a reduction of the excited state population by quenching.

In a second step, relating the transient spectra of the bilayers to the *EQE* data in Figure 7.9, a remarkable qualitative agreement between the amplitude of the ΔmOD values and the respective C_{60} contribution to the *EQE* is attested. This correlation distinctly speaks in favor of generated free charge carriers being, at least, in part responsible for the the origin of ESA signals observed in the transient absorption spectra. This deduction is corroborated by literature, attributing the ESA bands centered at 1050 nm to negatively charged C_{60}^- fullerene molecules. [195–197] This means that for D/A heterostructures yielding the strongest ESA signals associated with

C_{60}^- , consistently the largest fullerene contributions to the photocurrent were detected in the *EQE* measurements on the corresponding solar cells.

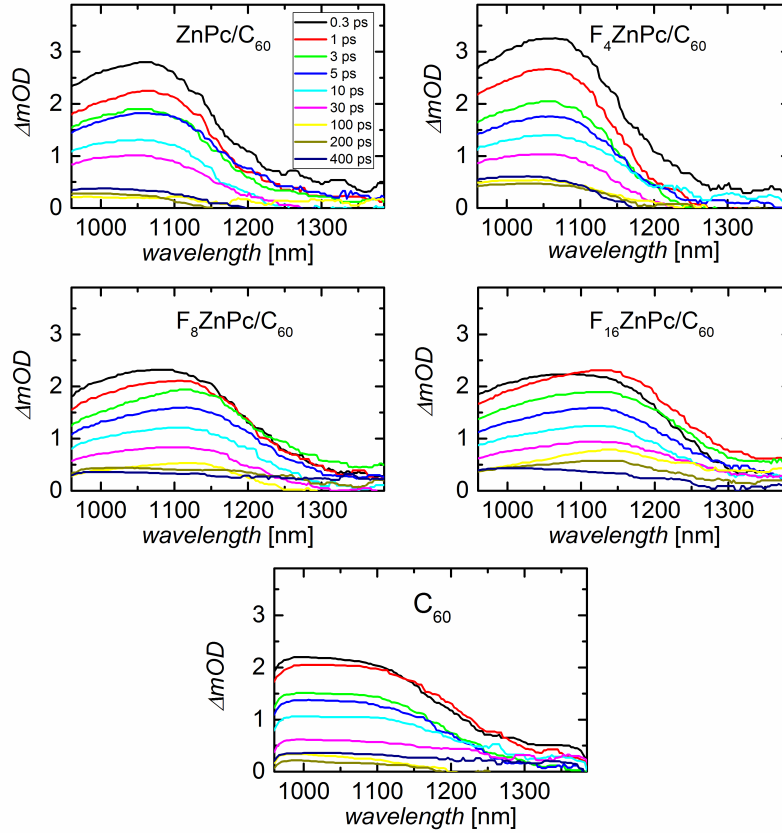


Figure 8.3.: Transient absorption spectra of $F_n\text{ZnPc}/C_{60}$ heterostructures at different time delays between 0.3 ps and 400 ps. Additionally, the bottom graph shows transient absorption spectra of a neat C_{60} reference thin film evaporated on a glass substrate.

Concerning this relation it has to be noted, that comparing absolute ΔmOD values of different TAS experiments with each other, care must be taken due to the sensitivity of the setup on the respective experimental conditions, in particular the laser alignment of the pump and probe pulse and the stability of the laser source. However, the presented measurements were performed without changing the spectral and temporal overlap and after warranting identical pump intensity for all experiments, allowing for a comparison of the absolute data.

After concluding that negatively charged fullerene molecules are contributing to the ESA band in the NIR spectral region in $F_n\text{ZnPc}/C_{60}$ heterojunctions, the possible contribution by an excitonic species to the signal is still imperative to consider aiming for a disentanglement of the different recombination processes, such as recombination of the initially created exciton or non geminate recombination of separated charge carriers and for a quantification of their respective magnitudes.

In order to address this issue, lineouts were extracted from the transient spectra at 1050 nm for time delays of up to 500 ps. For all samples, the transient data could be fitted with the help of a biexponential decay function of the following form:

$$y = y_0 + A_1 \cdot \exp\left(\frac{-t}{\tau_1}\right) + A_2 \cdot \exp\left(\frac{-t}{\tau_2}\right). \quad (8.1)$$

For the sake of clarity, the corresponding fits are displayed in Figure 8.4 only for time delays of up to 55 ps.

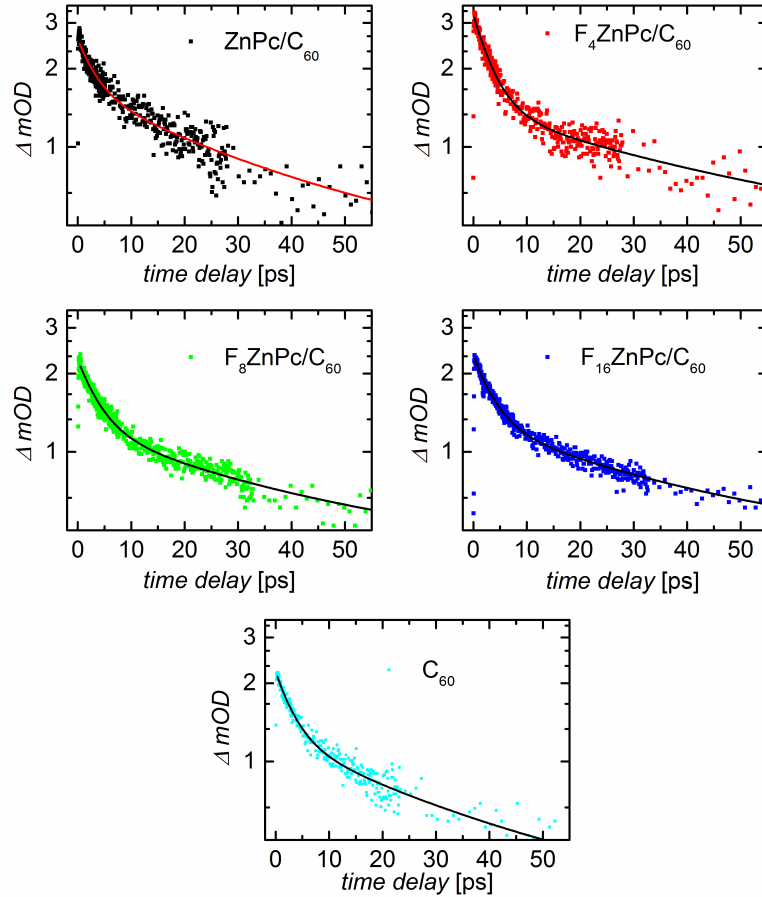


Figure 8.4.: Biexponential fits of the ESA signals at 1050 nm of $F_n\text{ZnPc}/\text{C}_{60}$ heterostructures and a C_{60} reference film.

The decay constants τ_1 and τ_2 , the corresponding amplitudes A_1 and A_2 , their ratio A_1/A_2 , as well as the offset y_0 are summarized in Table 8.1. For all $F_n\text{ZnPc}/\text{C}_{60}$ heterostructures and the neat C_{60} thin film virtually identical decay constants are obtained, indicating that the nature of the decay processes is likely to be identical in all samples under study. Additionally, a minor long lived ESA signal exceeding the monitored maximum time delay of 500 ps is observed, as indicated by the remaining offset y_0 . For all samples, the first decay channel is dominant yielding time constants τ_1 in the range of 3.8 ± 0.5 ps. For the second exponential decay time constants

τ_2 of 37 ± 10 ps are obtained. Moreover, the ratio of the amplitudes A_1/A_2 is almost constant, demonstrating the relative weighting of both decay processes to be independent at the chosen pump intensity. Taking into account the obvious impact of interface energetics on the absolute ΔmOD values clearly indicates C_{60}^- to be the dominant origin of the detected ESA signals. If one of the two decay processes had been directly related to an excitonic C_{60} species, this would have become manifested in a change of the amplitude ratio for the different samples or in a variation of the respective time constants τ_1 and τ_2 .

	τ_1 [ps]	A_1	τ_2 [ps]	A_2	y_o	A_1/A_2
ZnPc/ C_{60}	3.5	1.9	35	1.4	0.36	1.4
F ₄ ZnPc/ C_{60}	3.6	1.9	40	0.99	0.39	1.9
F ₈ ZnPc/ C_{60}	4.0	1.5	38	0.87	0.40	1.7
F ₁₆ ZnPc/ C_{60}	3.8	1.6	38	0.90	0.42	1.8
C_{60} thin film	3.5	1.4	36	0.98	0.26	1.4

Table 8.1.: Parameters extracted from the biexponential fits of the ESA decay at 1050 nm of F_nZnPc/ C_{60} heterostructures and the C_{60} reference film according to equation 8.1.

This conclusion is corroborated by additional TAS measurements on the ZnPc/ C_{60} heterojunction using an altered pump wavelength of 700 nm, i.e. initially exciting only the ZnPc donor molecules by the pump pulse (see Figure 7.3). Both series, utilizing either excitation of the acceptor or the donor by the selected pump wavelength, are contrasted in Figure 8.5.

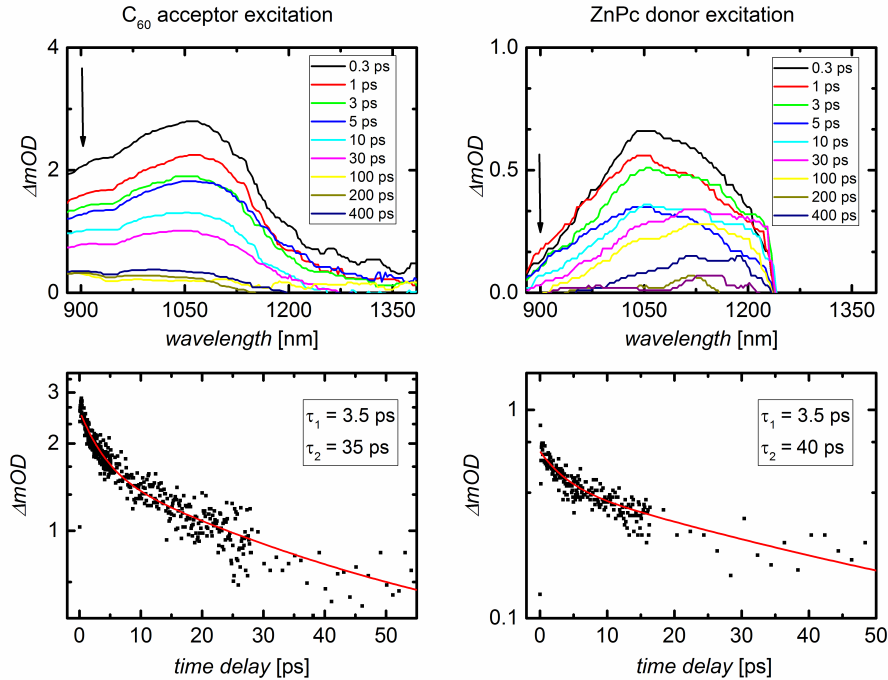


Figure 8.5.: Upper row: ZnPc/ C_{60} TA spectra at different time delays utilizing different pump wavelengths. By using a pump wavelength of 480 nm solely the fullerene acceptor is excited, whereas for 700 nm only the donor material ZnPc is excited. Bottom row: Biexponential fits of the ESA maxima at 1050 nm according to equation 8.1.

Upon excitation at a pump wavelength of 700 nm, distinct ESA signals are observed with the maximum centered again at 1050 nm. This signal cannot arise due to ESA of C₆₀ excitons as no ESA absorption signal is obtained for the C₆₀ thin film (not shown). Instead, excitons are generated in ZnPc and become dissociated at the D/A interface into free charge carriers. Thus, the emergence of the ESA can be attributed to ultrafast transfer of electrons from the phthalocyanine donor to the fullerene acceptor phase upon dissociation at the donor/acceptor interface. The ESA maximum was fitted utilizing the biexponential decay function 8.1. The obtained decay constants and the ratio of the amplitudes A_1/A_2 are very similar compared to the experiment using a pump wavelength of 480 nm, i.e. solely exciting the C₆₀ acceptor molecules, as shown in Table 8.2.

	τ_1 [ps]	A_1	τ_2 [ps]	A_2	y_o	A_1/A_2
ZnPc/C ₆₀ (acceptor excitation at 480 nm)	3.5	1.9	35	1.4	0.36	1.4
ZnPc/C ₆₀ (donor excitation at 700 nm)	3.5	0.60	40	0.41	0.062	1.5

Table 8.2.: Fit parameters of the biexponential fits of the ESA signals at 1050 nm, according to equation 8.1, for ZnPc/C₆₀ either exciting only the acceptor or donor.

This result confirms that in both experiments, exciting either the donor or the acceptor material of the ZnPc/C₆₀ bilayer, the same C₆₀⁻ species leads to the observed ESA feature in the transient spectra. After assigning the ESA signals at 1050 nm and its ultrafast emergence in Figure 8.2 to the generation of C₆₀⁻, it can be concluded that C₆₀ excitons, as well as ZnPc excitons, are separated into charge carriers within 150 fs. This result is in good agreement with the time scales reported for exciton dissociation in photovoltaic devices in both planar as well as bulk-heterojunction configuration. [92,198,199]

8.3. Charge Carrier Generation Mechanisms in the C₆₀ Acceptor

The occurrence of similar ESA characteristics for all F_nZnPc/C₆₀ heterostructures and the neat C₆₀ thin film illustrates the existence of free charge carriers in the fullerene phase not only after dissociation at the heterojunction of the bilayer structures, but importantly, also in the bare fullerene thin film upon excitation at 480 nm, even though no dissociating D/A interface is present. In contrast, transient absorption spectroscopy measurements on the C₆₀ thin film utilizing a pump wavelength of 700 nm (1.97 eV) do not yield free charge carriers (not shown). The optically driven charge carrier generation within an organic semiconductor originates from autoionization and subsequent dissociation of homo-CT excitons caused by excess energy. For this process to occur, an excitation to a high-lying Franck-Condon state is mandatory, from which a charge transfer to a neighboring C₆₀ molecule can take place. [22,200] The chosen pump wavelength of 480 nm (2.58 eV) corresponds to an excitation energy of about 0.6 eV above the absorption edge of the S₁ transition (corresponding energy 1.97 eV), thus providing enough excess energy for a charge transfer to a neighboring molecule to be possible. Afterwards, the CT state may dissociate driven by the available excess energy of the hot CT state or by a

temperature activated step into free charge carriers or recombine geminately. [42, 201] A study by Köhler et al. on the prevalent π -conjugated polymer MEH-PPV showed, that not only the energy of the initially excited state is crucial for the efficiency of dissociation, but also the wave function character of the primary electronic excited state. Quantum chemical calculations revealed the high dissociation yield of high-lying Franck-Condon states to be associated with the CT character of the former. [202] Autoionization was reported to occur in C_{60} and fullerene derivatives at excitation wavelengths below 530 nm (2.34 eV). [42, 203, 204] Jeong et al. reported on autoionization of C_{60} bulk excitons to contribute to the photocurrent in CuPc/ C_{60} bilayer devices. [205]

As a consequence of the virtually identical decay parameters of the different $F_n\text{ZnPc}/C_{60}$ bilayers in Table 8.1, it can be concluded, that subsequent to exciton dissociation, charge carrier recombination dynamics are unaffected by the variation of the D/A interface energetics. Additionally, the fact that similar decay constants of the ESA signal are obtained also for the C_{60} thin film indicates that recombination of charge carriers occurs in a similar manner in the C_{60} thin film and the acceptor layers of the heterostructures. This in turn leads to the implication, that recombination of charge carriers is not particularly dominant at the D/A interface region but takes places uniformly across the entire C_{60} layer. An exact assignment of the observed decay constants to microscopic processes occurring in the investigated bilayers and single layers is intricate and, in part, will remain speculative. However, it has to be stated, that recombination on these time scales seems not to be governed by bimolecular recombination processes, since the related time constants could be proven to be independent of the incident pump fluence (not shown). The motion of electrons in the fullerene phase is considered to be predominantly determined by diffusion (see Section 2.4). Taking into account an electron mobility of C_{60} of $\mu_{C_{60}} = 1 \text{ cm}^2/\text{Vs}$ (see Section 4.3.2), the diffusion coefficient can be calculated according to the Einstein-relation in Equation 2.10 and accounts to $D = 2.6 \cdot 10^{-6} \text{ m}^2/\text{s}$. The decay constants τ_1 and τ_2 can be correlated with an associated diffusion length of the electrons within the respective $F_n\text{ZnPc}/C_{60}$ heterostructure and the C_{60} thin film assuming a one-dimensional diffusive motion:

$$L_D = \sqrt{D \cdot \tau}.$$

For the first decay constant $\tau_1 = 3.8 \text{ ps}$ the diffusion length L_{D1} accounts to 3 nm, corresponding to a length scale of molecular distances. Hence, this decay channel is attributed to trap states located inside the band gap of C_{60} . There is no significant impact of a varying charge carrier density in the fullerene phase on the decay constants and the relative amplitudes A_1/A_2 detectable (see Table 8.1) suggesting that a saturation of the first decay channel, e.g. by trap filling, is not given in these experiments. This indicates that the second recombination channel is only accessible in a specific region of the samples to be reached by the diffusion of the charge carriers. The second decay constant $\tau_2 = 37 \text{ ps}$ corresponds to a diffusion length L_{D2} of approximately 10 nm. This quantity is on a length scale regime of the C_{60} film thickness. Hence,

this decay constant is proposed to be associated with trap states at the C₆₀/air surface, possibly introduced by a change of the surrounding polarizability of the C₆₀ molecules at this interface in comparison to the bulk.

Comparing the spectral shape of the ESA in Figure 8.5 for different pump wavelengths, one striking discrepancy at around 900 nm appears to be evident. For a pump wavelength of 480 nm a distinct side band is observed centered at 900 nm, whereas this spectral feature is missing entirely in the measurements using a pump wavelength of 700 nm, which is indicated by black arrows in Figure 8.5. In literature, the ESA at 890 to 900 nm is attributed to positively charged fullerene molecules C₆₀⁺. [79] Accordingly, in case autoionization and dissociation of CT excitons takes place within the C₆₀ layer, which is assumed for a pump wavelength of 480 nm, the associated excited state absorption signals should occur simultaneously. In contrast, for the experiment utilizing a pump wavelength of 700 nm only the ESA signature of C₆₀⁻ is observed due to the injection of electrons from the ZnPc donor to the fullerene acceptor. For the neat C₆₀ thin film no transient species is observed in the NIR spectral region using a pump wavelength of 700 nm (not shown).

For a pump wavelength of 700 nm the overall ΔmOD values are markedly smaller compared to the experiments employing a pump wavelength of 480 nm. This observation might be explained by a change of the spatial overlap between pump and probe pulse as discussed above. Moreover, the absence of autoionization in case of a pump wavelength of 700 nm generally results in smaller ΔmOD values.

Considering the occurrence of autoionization and subsequent dissociation of C₆₀ CT excitons upon illumination, the transient spectra in Figure 8.3 are examined in more detail. Apparently, the shape of the ESA bands and the absolute ΔmOD values of the F₁₆ZnPc/C₆₀ heterostructure are strikingly similar compared to the C₆₀ thin film. Given these results and taking into account that the F₁₆ZnPc/C₆₀ interface was proven to be photo-inactive due to the lack of energetic offset between the phthalocyanine and the fullerene (see Figure 7.10), the conclusion can be drawn that autoionization followed by separation of the CT excitons is the dominant charge carrier generation mechanism, as schematically depicted in Figure 8.6. Thus, it is deduced that this process renders the main contribution to the C₆₀ photocurrent in F₁₆ZnPc/C₆₀ bilayer cells. The dominance of this process in the photocurrent generation by the fullerene phase seems to be confirmed for F₈ZnPc/C₆₀ photovoltaic devices (compare spectra in Figure 8.3). Although in these bilayer cells the D/A interface was verified photo-active in general, its dissociation efficiency is strongly limited, since the energetic offset at the D/A interface is of the same range as the exciton binding energy.

As illustrated schematically in Figure 8.6, in ZnPc/C₆₀ and F₄ZnPc/C₆₀ bilayer cells, this autoionization process likewise contributes to the generation of free charge carriers and with it, to the macroscopic photocurrent monitored in the *EQE* measurements. But as concluded from the TAS measurements in combination with the *EQE* data, the exciton dissociation at the D/A interface is more efficient in comparison to the intrinsic C₆₀ dissociation mechanism.

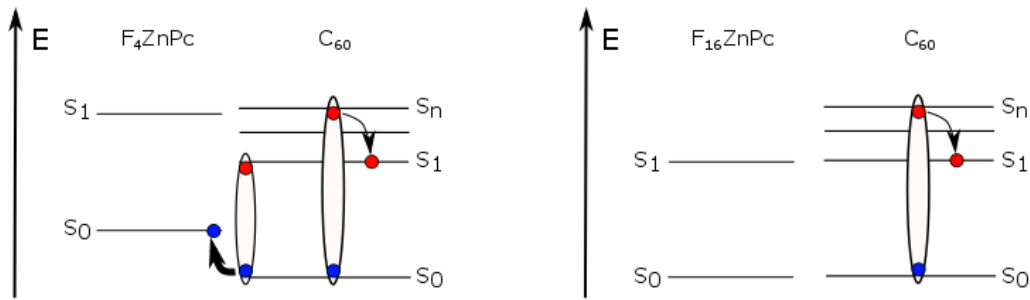


Figure 8.6.: Illustration of the relevant exciton dissociation mechanisms leading to free charge carriers in C_{60} for the F_nZnPc/C_{60} heterostructures under study. In a D/A bilayer heterostructure, such as F_4ZnPc/C_{60} , in which the energetic offset at the interface exceeds the exciton binding energy, exciton dissociation is predominantly driven by this D/A interface. Additionally, charge generation takes place distant from this interface in the C_{60} bulk as a consequence of autoionization and subsequent dissociation of CT excitons. In $F_{16}ZnPc/C_{60}$ heterostructures the common interface is photo-inactive, i.e. the main contribution to the spectral photocurrent originates from autoionization and subsequent CT exciton dissociation in the acceptor phase.

Under the assumption that the EQE at a wavelength of 480 nm in $F_{16}ZnPc/C_{60}$ bilayer cells solely originates from autoionization and subsequent dissociation into free charge carriers and that the efficiency of this charge carrier generation mechanism is similar in all F_nZnPc/C_{60} devices, the additional impact of the respective D/A interface on the EQE can be estimated. According to this approach, in $ZnPc/C_{60}$ and F_4ZnPc/C_{60} based devices 60 % and 75 % of the total photocurrent, respectively, can be attributed to the dissociating D/A heterojunction at a wavelength of 480 nm. This means that geminate recombination of C_{60} excitons is lowered in the presence of the dissociating D/A interface in case of $ZnPc/C_{60}$ and F_4ZnPc/C_{60} devices. However, after separation into free charge carriers, recombination dynamics are proven to be unaffected by the respective D/A interface energetics in all F_nZnPc/C_{60} bilayers on the time scales investigated.

Conclusion

In this chapter, the static view of interface energetics was complemented by the exciton and charge carrier dynamics in F_nZnPc/C_{60} bilayers by means of ultrafast transient absorption spectroscopy measurements, yielding a comprehensive understanding of the processes occurring on microscopic length scales. For F_nZnPc/C_{60} bilayers and a neat C_{60} reference film, broad ESA bands centered at 1050 nm were detected. These signals were assigned to negatively charged fullerene molecules C_{60}^- and arise on an ultrashort time scale within 150 fs.

A distinct impact of F_nZnPc/C_{60} interface energetics on the absolute ΔmOD values was illustrated. Evidently, an energetic offset at the D/A interface exceeding the exciton binding energy

results in a higher density of electrons in the C_{60} phase. The improved exciton separation at the D/A interface was attributed to reduced exciton recombination losses. These results are in good qualitative agreement with the fullerene contribution to the EQE of the bilayer solar cells as discussed in Chapter 7. In all samples under study, autoionization and subsequent dissociation of CT excitons was observed as a potential charge generation mechanism, which occurs across the acceptor layer and is intrinsic to the bulk fullerene. Probably, this exciton dissociation mechanism is also accountable for the considerable photocurrent densities observed in Schottky-cells based on C_{60} in literature. [206] Comparison of the ESA signals of the C_{60} reference thin film and the F_8ZnPc/C_{60} and the $F_{16}ZnPc/C_{60}$ heterostructures showed, that autoionization and subsequent generation of free charge carriers mainly determines the fullerene EQE contribution at a reference wavelength of 480 nm in the corresponding bilayer cells. Assuming a similar autoionization contribution to the EQE in all bilayer solar cells, allows to evaluate the additional impact by the respective exciton dissociating D/A heterojunction on the C_{60} photocurrent generation. In case of $ZnPc/C_{60}$ (F_4ZnPc/C_{60}) bilayer cells, approximately 60 % (75 %) of the generated photocurrent is due to dissociation of excitons at the D/A interface and 40 % (25 %) originates by exciton splitting as a consequence of autoionization.

Once exciton splitting had taken place either across the D/A interface or inside the C_{60} bulk, recombination dynamics are unaffected by the D/A interface energetics. This outcome reveals that non-geminate recombination of charge carriers is not particularly located at the D/A interface, but takes place uniformly across the acceptor layer. Two recombination related time constants are determined for F_nZnPc/C_{60} bilayers and the C_{60} reference film. The decay constant τ_1 was found to 3.8 ± 0.5 ps and was tentatively attributed to trap assisted recombination within the band gap of the C_{60} layer, whereas τ_2 was estimated to 37 ± 10 ps and was assigned to recombination at trap states at the C_{60} /air boundary.

9. Energy Cascades as a New Concept to Improve Charge Carrier Generation in OPV

The implementation of energetically tailored intermediate molecular layers at a planar D/A heterointerface allows for the construction of an energetic staircase, aiming for improved exciton dissociation efficiency and thereby, for larger photocurrents in OPV devices. The applicability of this generic concept is illustrated in this chapter, investigating two material combinations of technological relevance.

In the first place, three chemically different low molecular weight diketopyrrolopyrroles (D1 - D3) were synthesized to provide compounds with a distinct energy level gradation. Exploiting this energy level modification, energetic staircases are realized by embedding these diketopyrrolopyrroles in a planar layer architecture, employing fullerene C₆₀ as acceptor. For instance, inserting a sub-monolayer thick D3 interlayer at the heterojunction between D1 and C₆₀ a doubling of overall j_{sc} is obtained with respect to neat D1/C₆₀-bilayer cells. *EQE* measurements reveal that this enhancement can mainly be attributed to an improved photocurrent contribution by the fullerene acceptor phase. The increase is associated with a destabilization of strongly Coulomb-bound hetero-CT states at the interlayer interface, thus reducing geminate recombination losses. Synthesis of diketopyrrolopyrroles and their characterization by cyclic voltammetry (CV) was carried-out by Dr. Christian Müller, Applied Functional Polymers – Macromolecular Chemistry I, University of Bayreuth. Cascade solar cell preparation and opto-electronic as well as structural investigations were performed by the author. The results of this section were published in *Advanced Energy Materials*. [136]

In the second case, the universality of cascade energy level alignment is illustrated by transferring this concept to an, *a priori*, more efficient material combination. As described in Section 7.4, the position of frontier energy levels of fluorinated zinc phthalocyanines are reliably controlled by the degree of fluorination. By the prudent choice of F₈ZnPc as interlayer material, sandwiched between a DBP donor and a C₇₀ acceptor layer, a three layer cascade structure is established. Upon employing a sub-monolayer thick interlayer in DBP/F₈ZnPc/C₇₀ cascade cells, a remarkable efficiency improvement to 3.7 % is demonstrated, in comparison to 2.2 % obtained for plain DBP/C₇₀ bilayer photovoltaic devices. Cascade solar cells based on DBP/F₈ZnPc/C₆₀ were prepared and characterized with the support of Jana Wulf and Philipp Groppe both members of our workgroup.

9.1. Cascade Cells Based on Diketopyrrolopyrrole Derivatives (D1 - D3)

For the results presented in the first part of this chapter, small molecule diketopyrrolopyrrole derivatives D1, D2, and D3 were synthesized for the application in three-layer cascade cells by our collaboration partners at the University of Bayreuth. Aiming for a defined energy gradation with keeping the central structural motif of the molecules fixed as well as their dipole moments and the surface energies, the terminal aryl groups of the DPP compounds were modified. The chemical structures of the employed compounds are depicted in the insets of Figure 9.1. For experimental details on the synthesis, reference to the literature is given. [136, 207] A slight variation of the π -electron system is achieved by substituting final phenyl groups by pyridine rings. The implementation of a specific substitution pattern, *viz.* the introduction of the pyridine groups in para- or meta-position, in these experiments is crucial since it allows for fine tuning the frontier energy level alignment. For generic para-pyridine substitution in D3, energy levels are shifted by 160 meV towards lower energies in comparison to D1 comprising phenyl end groups. This energy level shift was tracked by cyclic voltammetry (CV) measurements carried-out by Dr. Christian Müller, Applied Functional Polymers – Macromolecular Chemistry I, University of Bayreuth. The resulting energy levels are displayed in Figure 9.1.

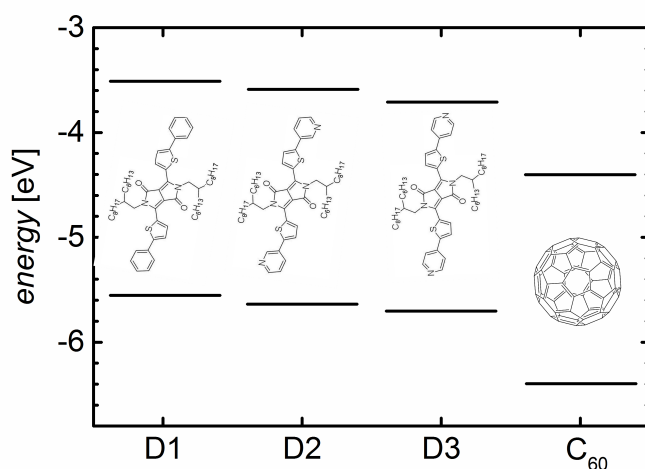


Figure 9.1.: HOMO and LUMO energies of diketopyrrolopyrroles (D1 -D3) accessed by cyclic voltammetry (CV). For reference the respective energy levels of the acceptor C₆₀ are displayed, which were determined by UPS measurements in section 7.4. The insets show the chemical structures of the molecular semiconductors.

Upon substitution of the phenyl ring in D1, energy levels are slightly shifted towards lower energies by 80 meV in D2 and 160 meV in D3, respectively, whereas the electronic band gap remains unchanged. Therefore, in order to establish cascade energy level alignment, D2 and D3 are suitable candidates for interlayer formation between D1 and C₆₀. In the following, the

focus is particularly set to D1/D3/C₆₀ cascade cells yielding a higher energetic offset at the D/A interface compared to D1/D2/C₆₀ solar cells.

For the first time, a donor molecule and its modified derivative were utilized to create an energetic staircase in combination with the acceptor C₆₀. The thickness dependent effects of the thin interlayer on the opto-electronic device parameters of cascade cells were investigated using the following stack architecture:

ITO/MoO₃(50 Å)/D1(200 Å)/D2 or D3(x Å)/C₆₀(800 Å) .

Additionally, bilayer reference cells were characterized comprising donor and acceptor layers of same thicknesses as for the cascade cells. It has to be mentioned that the stack architecture of the reference bilayer cells was not optimized for achieving highest power conversion efficiencies possible, but rather to avoid shortening of contacts while at the same time a sufficiently good performance is guaranteed.

9.1.1. Structural Investigation of D1/D3/C₆₀ Cascade Cells by XRD and AFM

Before addressing the thickness dependent effects of the D3 interlayer on the opto-electronic cell characteristics, the focus is on the structural investigation of photovoltaic devices. Aiming to analyze the structural properties of the photo-active materials, X-ray diffraction measurements were conducted in Bragg-Brentano geometry. Figure 9.2 shows the diffraction spectra of a selected cascade solar cell and two reference bilayer cells.

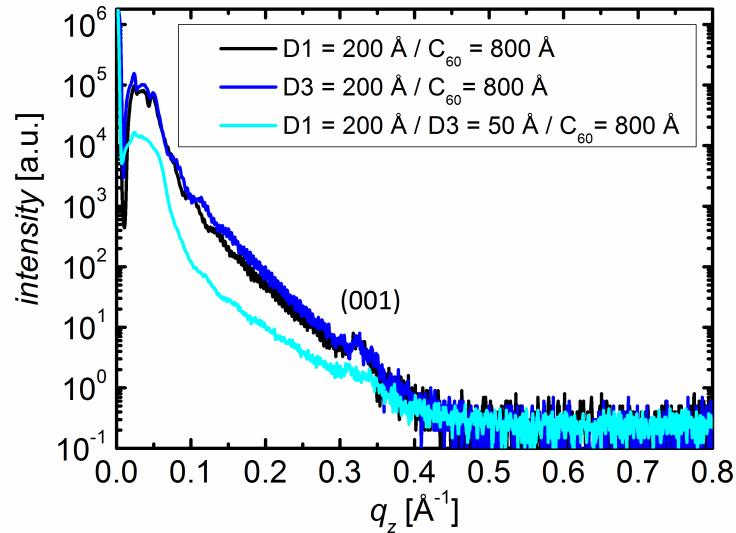


Figure 9.2.: X-ray diffraction pattern of a selected cascade solar cell and the two corresponding bilayer cells. Measurements were carried-out in Bragg-Brentano geometry, thus probing the out-of-plane crystallinity.

For reference cells D1/C₆₀ and D3/C₆₀ diffraction peaks are clearly observed at $q_z = 0.32 \text{ \AA}^{-1}$, which are attributed to the first order (001) diffraction peak of the respective diketopyrrolopyrroles. Accordingly, these peaks correspond to a lattice spacing of 19.3 Å. This value for the out-of-plane lattice constant is crucial, when assessing effective coverage by the respective interlayer. In addition, a representative X-ray diffraction spectrum is shown for a cascade solar cell comprising an interlayer thickness of 50 Å. Evidently, a similar Bragg peak is observed at $q_z = 0.32 \text{ \AA}^{-1}$. Diketopyrrolopyrrole molecules D1 and D3 have a very similar structural motif (see Figure 4.2). Additionally, the growth modes on ITO/MoO₃ substrates appear to be identical, leading to the assumption, that D3 interlayer molecules adopt the molecular orientation of the underlying D1 layer in cascade devices. The molecular dimension along the alkyl-chains amounts to approx. 24 Å. Accordingly, a standing orientation of the respective diketopyrrolopyrrole molecules is assumed with a tilt angle of approx. 36° with respect to the substrate normal. For all bilayer cells and cascade cells no indication for a crystalline C₆₀ fraction was observed. Therefore, the thickness dependent effects on the opto-electronic device characteristics in cascade solar cell can be ascribed to a variation of recombination processes occurring in the cascade region as a consequence of its energy level alignment.

In order to conclude on the coverage of the D1 underlayer upon D3 interlayer deposition, complementary atomic force microscopy measurements on ITO/MoO₃/D1 samples were performed. The AFM scan reveals a smooth and featureless topography with a root mean square roughness of $\sigma_{D1} = 11 \text{ \AA}$ (not shown). Small laterally isolated islands with a maximum height of approx. 30 nm exist. Taking into account the obtained σ_{D1} roughness with respect to the out-of-plane lattice spacing of $d_{D3} = 19.3 \text{ \AA}$, a completely closed D3 interlayer cannot occur for interlayer thicknesses below 20 Å. However, for the maximum employed D3 interlayer thickness of 50 Å it can be assumed that almost full coverage of the D1 underlayer is achieved.

9.1.2. Opto-Electronic Characterization of D1/D3/C₆₀ Cascade Cells

To analyze the effects associated with the insertion of D3 interlayers of varying thickness on the photovoltaic parameters of D1/D3/C₆₀ cascade cells, $j(V)$ characterization was carried-out under standard illumination conditions. Selected $j(V)$ curves of cascade cells are displayed in Figure 9.3 together with that of the corresponding bilayer solar cell D1/C₆₀. In order to compare device performance, photovoltaic parameters of cascade solar cells were normalized with respect to those of D1/C₆₀ bilayer cells. The corresponding results are summarized in Figure 9.4. Moreover, D3/C₆₀ bilayer cells were prepared to judge on the general photovoltaic behavior of this heterojunction with respect to devices based on D1/C₆₀. The characterization of D1/D2/C₆₀ cascade photovoltaic cells comprising a smaller energetic offset between the diketopyrrolopyrroles is addressed at the end of this section.

Solar cell parameters of D1/D3/C₆₀ cascade cells are distinctly varied as a function of interlayer thickness. In particular, remarkable changes of the short circuit current density are obtained.

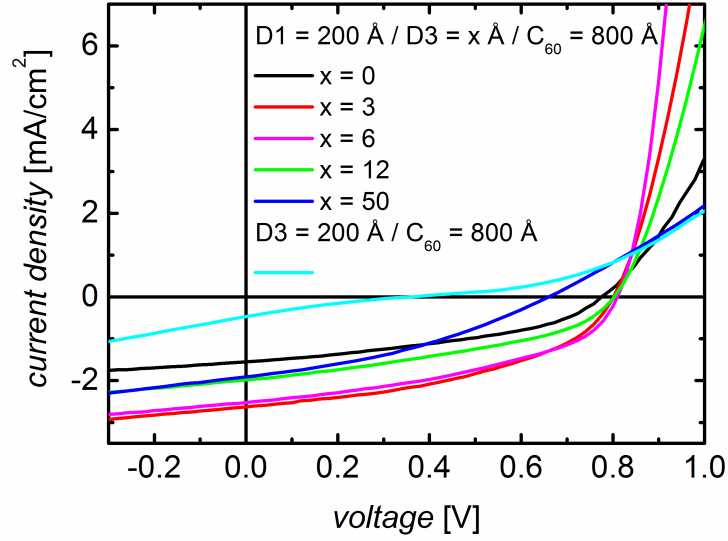


Figure 9.3.: $j(V)$ characteristics of D1/D3/C₆₀ cascade solar cells, employing various D3 interlayer thicknesses. For comparison D1/C₆₀ and D3/C₆₀ bilayer reference solar cells are displayed.

For thin D3 interlayers of 3 Å and 6 Å thickness, j_{sc} is enhanced by 80 % to 2.5 mA/cm² in comparison to the corresponding neat bilayer cells with 1.4 mA/cm². For these D3 interlayer thicknesses a full coverage of the underlying D1 layer cannot be assumed, since the out-of-plane lattice spacing was determined to be $d_{D3} = 19.3$ Å. For interlayer thicknesses above 6 Å, the raise in j_{sc} decreases, but even for cascade cells comprising interlayer thicknesses of 12 - 50 Å the short circuit current densities still exceed those of the bilayer reference devices by 30 - 40 %. In section 9.1.1 no changes in morphology of the C₆₀ acceptor layer were detected upon implementation of the D3 interfacial layer in the D1/C₆₀ bilayer cells. Thus, the observed variations of j_{sc} as a function of the D3 interlayer thickness cannot be attributed morphological origins.

UV/Vis measurements on cascade structures as well as reference bilayers were performed in order to verify changes in spectral absorption as a consequence of the insertion of the respective D3 interlayer. Note that optical studies were carried-out on heterostructures, lacking the Ag top electrode to achieve a better signal to noise ratio. Selected absorption measurements are displayed in Figure 9.5. The absorption between 400 nm and 550 nm is again attributed to the fullerene acceptor layer (see Section 7.5), whereas between 550 nm and 680 nm absorption originates from the respective diketopyrrolopyrroles. [136] It becomes evident that the diketopyrrolopyrrole absorption maximum of D3/C₆₀ bilayers is slightly blue-shifted with respect to the D1 based structures. This spectral shift will be shown reproducible in the course of the *EQE* measurements. Obviously, even for the maximum interlayer thickness of 50 Å utilized in this study, the absorption is only slightly altered, compared to D1/C₆₀ bilayer cells. This outcome clearly illustrates that the drastic j_{sc} increase of the cascade solar cells cannot predominantly be assigned to a distinct change of absorption. Instead, the increase is attributed to reduced

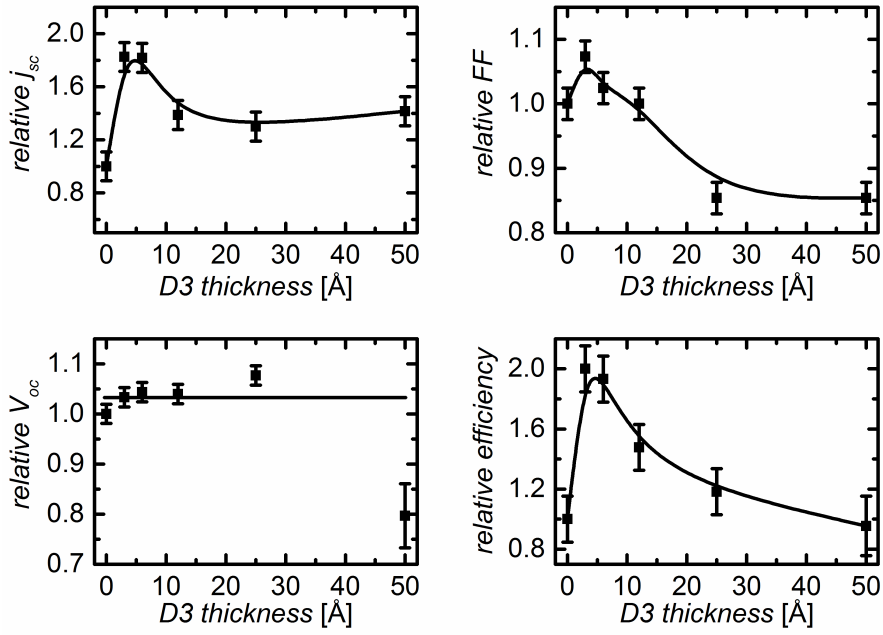


Figure 9.4.: Normalized photovoltaic parameters of D1/D3/C₆₀ cascade solar cells. Scaling was carried-out with respect to the bilayer solar cells, lacking the thin interfacial D3 layer. Solid lines represent guides to the eye.

geminate recombination of excitons at the D/A interface. Remarkably, the short circuit current density enhancement is strongest for intermediate D3 layers in the sub-monolayer thickness range. Apparently, in the cascade energy level scheme D3 molecules act as exciton dissociation sites, resulting in high charge carrier generation yields. This assumption is supported by the general increase of the photocurrent in cascade cells comprising a D3 interlayer thicknesses of up to 25 Å at all biases between -0.5 V and V_{oc} .

Reduced recombination losses manifest themselves in improved transport properties as confirmed by increased fill factors of 44 ± 1 % upon implementation of thin D3 interfacial layers of 3 Å and 6 Å thickness in D1/D3/C₆₀ cascade cells. In comparison, D1/C₆₀ bilayer cells feature a fill factor 41 ± 1 %. Whereas the parallel resistances R_p (determined at $V = 0$ V) remain almost unaffected upon insertion of sub-monolayer thick D3 interlayers, the series resistances R_s are clearly reduced in this thickness regime (see Figure 9.6). The series resistance in organic photovoltaics is comprised of a number of different contributions such as the bulk resistances of the photo-active layers, the bulk resistances of the electrodes as well as contact resistances of all existing interfaces. [95] The cascade energy level design employing thin interfacial layers in the sub-monolayer thickness range facilitates exciton dissociation, thereby reducing the contact resistance of the D1/C₆₀ interface, which results in smaller R_s and, *vice versa*, in higher fill factors. Upon further increase of the interlayer thickness, the fill factor drops to 35 % for 25 Å and 50 Å intermediate layer thickness. This decrease can be understood considering the $j(V)$ characteristics of D3/C₆₀ reference cells. From the combination of a small fill factor of only 20 % and a reduced j_{sc} of 0.49 mA/cm², inferences can be drawn, that transport properties

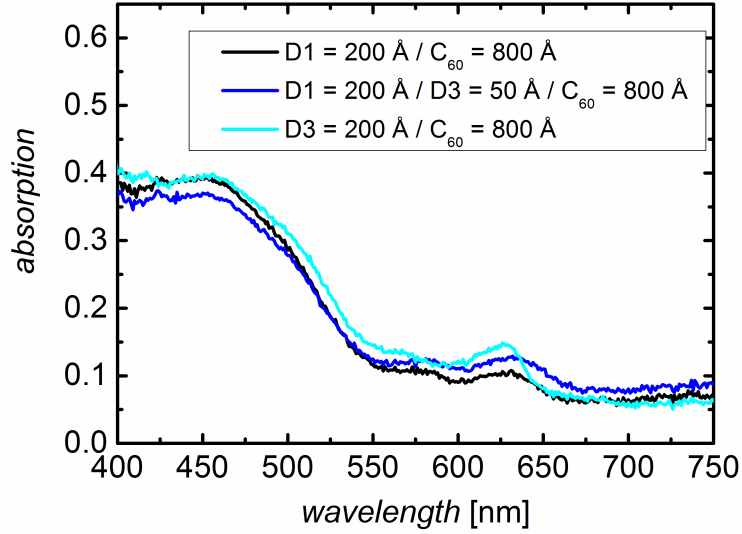


Figure 9.5.: Spectral absorption of a selected cascade solar cell and reference bilayer cells. It has to be noted that optical absorption was determined on plain heterostructures without Ag top electrode. Due to back reflection of incident light at the top contact of the solar cells, external quantum efficiencies can exceed the observed spectral absorption as illustrated in Figure 9.7.

are distinctly limited in these OPVCs. This conclusion is corroborated by the occurrence of a so-called S-shape. Such kinks around V_{oc} are associated with the appearance of space charges occurring in an organic solar cell as a consequence of extraction barriers or transport-induced charge carrier imbalances. [154,208] By organic field effect transistor measurements on D3 thin films a hole mobility of $\mu_h = 3 \times 10^{-4} \text{ cm}^2\text{V}^{-1}\text{s}^{-1}$ was obtained, constituting a reduction with respect to D1 by an order of magnitude ($\mu_h = 5 \times 10^{-3} \text{ cm}^2\text{V}^{-1}\text{s}^{-1}$). For experimental details reference to the literature is given. [136] Accordingly, due to transport limitations of D3 thin films, R_s is expected to be distinctly enhanced for interlayer thicknesses of 25 Å and 50 Å, resulting in small fill factors. Thus, with the introduction of the D3 interlayers there is a trade-off between reduced recombination losses as a consequence of the energetic staircase, slightly increased absorption, and transport limitations.

The open circuit voltage remains almost unchanged as a function of D3 interlayer thicknesses up to 25 Å, yielding only a slight monotonous enhancement by 30 meV to 0.82 V. V_{oc} is associated with the energy of the bound CT state at the dissociating interface. [93] Energy levels of D3 are shifted towards lower energies by 160 meV in comparison to D1. Therefore, upon increasing coverage of the D1 underlayer with D3, successively an increasing number of these high energy CT states at the D3/C₆₀ interface determine V_{oc} . Thus, the monotonous increase of V_{oc} is in good qualitative agreement with the CV data. Cascade cells comprising a 50 Å thick D3 interlayer yield reduced open circuit voltages of 0.66 V. Due to an expected d_{D3} lattice spacing of 19.3 Å in combination with a smooth D1 underlayer, featuring a root mean square roughness

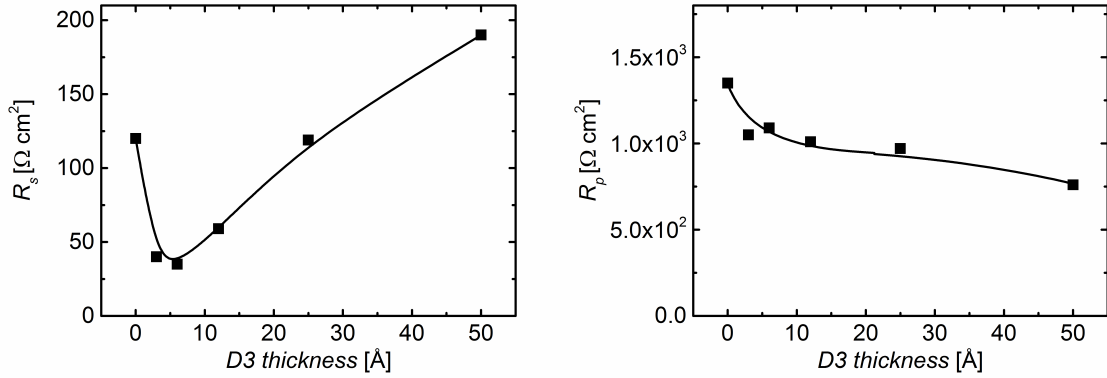


Figure 9.6.: Series and parallel resistances of D1/D3/C₆₀ cascade solar cells and D1/C₆₀ reference OPVCs. Solid lines represent guides to the eye.

of only $\sigma_{D1} = 11 \text{ \AA}$, the formation of closed D3 monolayers can be expected in this case. With this, the general transport limitations of D3 come into effect as evinced by the increased series resistance (see Figure 9.6) and additionally, the D3/C₆₀ interface becomes increasingly important for the overall device properties and performance. As a consequence, solar cell characteristics remarkably converge with those of the D3/C₆₀ bilayer cell for voltages $> 0.7 \text{ V}$, and a decrease in open circuit voltage is obtained.

Finally, as the key criterion to judge on the photovoltaic performance, the power conversion efficiencies were determined and evaluated for cascade solar cells as well as reference bilayer cells. As a consequence of the remarkable increase of j_{sc} , for thin interfacial D3 layers of 3 \AA and 6 \AA thickness the power conversion efficiency could be doubled to 0.88%. Yet, for larger interlayer thicknesses the power conversion efficiencies dropped and for solar cells utilizing D3 interlayers of 50 \AA thickness, the power conversion efficiency is approximately equal or even smaller than that of D1/C₆₀ reference cells because of the emerging transport limitations.

In order to correlate the j_{sc} increase upon insertion of the D3 interlayers to the photocurrent contributions of the molecular components, spectrally resolved *EQE* measurements were carried-out. The corresponding data are displayed in Figure 9.7. In agreement with the UV/Vis optical characterization in Figure 9.5, the respective shape of *EQE* spectra resembles that of the absorption spectra. For D1/C₆₀ reference devices, both donor and acceptor material contribute to the macroscopic photocurrent. Roughly, between 400 nm and 550 nm the photocurrent contribution to the *EQE* is mainly assigned to the fullerene. In this wavelength range only a minor absorption peak at 420 nm can be attributed to D1. [136] For higher wavelength above 550 nm two *EQE* peaks can be assigned to the donor D1 at 585 nm and 635 nm in agreement with the absorption data. The energy spacing between these peaks amounts to 170 meV, a value typically observed for the progression of the vibronic breathing-mode. [41]

Apparently, *EQE* values do not directly resemble the absorption behavior of the plain heterostructures shown in Figure 9.5, for instance for D1/D3(50 Å)/C₆₀ cascade cells at 635 nm.

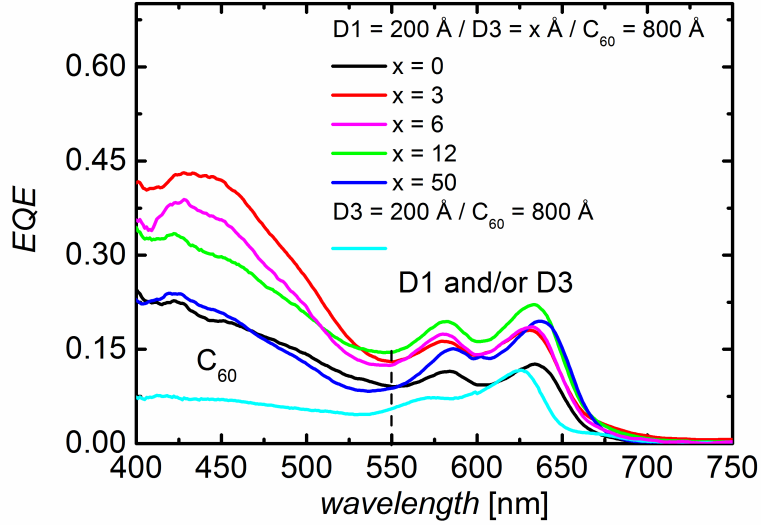


Figure 9.7.: *EQE* measurements of D1/D3/C₆₀ cascade photovoltaic devices, comprising varying D3 interlayer thicknesses. For reference, D1/C₆₀ and D3/C₆₀ bilayer cells are shown.

In contrast to the heterostructures, the photovoltaic cells comprise an Ag back contact. This top electrode reflects most of the non-absorbed light back into the photo-active layers, enabling an effectively doubled optical path for absorption. Therefore, absorption of solar cells exceeds the absorption of plain heterostructure and hence, *EQE* values can overcome the absorption reported in Figure 9.5. In accordance with the strongly enhanced photocurrents observed in the $j(V)$ characterization, for the implementation of a 3 Å thick D3 interlayer, the *EQE* is distinctly increased over the whole spectral absorption range. In particular, the *EQE* associated with the C₆₀ acceptor phase is strongly enhanced. To illustrate this effect, the *EQE* of the D1/D3(3 Å)/C₆₀ cell at 450 nm, where the fullerene contributes exclusively, was normalized to the *EQE* of the corresponding bilayer devices (see Figure 9.8). Evidently, the fullerene contribution for this particular wavelength is enhanced by more than a factor of two. Upon increasing the interlayer thickness, the C₆₀ contribution drops continuously. Finally, for a D3 interlayer thickness of 50 Å the *EQE* spectra of the cascade solar cell and the corresponding bilayer device almost converge in the whole spectral range of the fullerene absorption.

The initial enhancement for thin intermediate D3 layers is ascribed to reduced geminate recombination losses, caused by the particular energy level alignment. The facilitated dissociation of excitons is a consequence of the energetic staircase as schematically illustrated in Figure 9.9. After photo-generation, excitons in the acceptor material C₆₀ diffuse to the interlayer interface. This is where they form CT states that are still Coulomb-bound. The second interface D1/D3 in close proximity is suggested to destabilize these CT states, supporting charge carrier separation by the energetic staircase. Hence, the three layer cascade is proposed to destabilize C₆₀ excitons into CT states that are subsequently dissociated into free charge carriers in the donor and acceptor phase. Clearly, charge carrier generation proceeding via exciton dissociation at

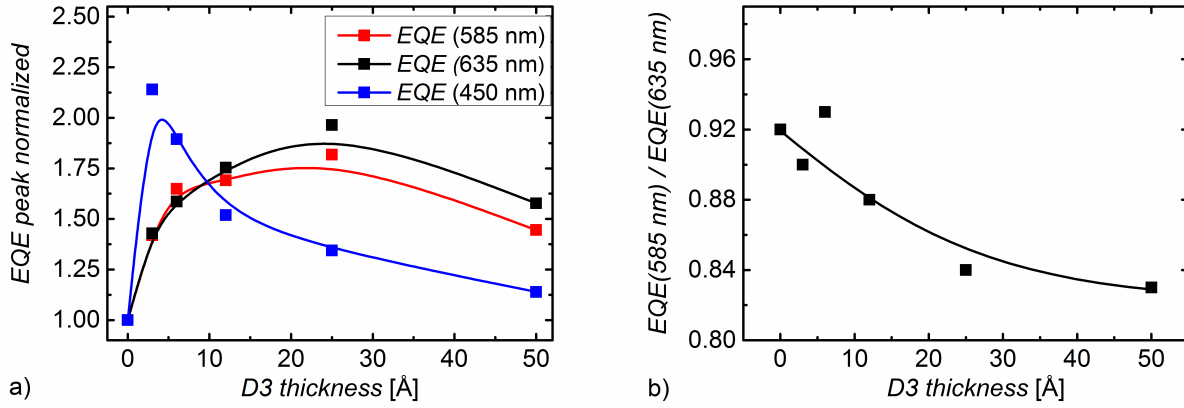


Figure 9.8.: a) Relative *EQE* at three different wavelengths for cascade cells normalized to D1/C₆₀ bilayer devices as a function of interlayer thickness. The *EQE* at 450 nm is associated with the fullerene photocurrent, whereas at 585 nm and 635 nm the *EQE* is assigned to a photocurrent originating from the diketopyrrolopyrroles. b) Ratio of *EQE* peaks at 585 nm and 635 nm as a function of interlayer thickness. The decreasing ratio with increasing interlayer thickness indicates an additional photocurrent contribution due to the D3 interlayer. Solid lines represent guides to the eye.

these stacked interlayer boundaries can be considered significantly more efficient than for the plain D1/C₆₀ interface. This separation mechanism may be accompanied by hole delocalization effects via a wave function spread-out across the D1/D3 interface into the donor phase, as schematically indicated in Figure 9.9 by the shaded area. Excited state delocalization was shown to have a crucial impact on the charge carrier generation yield by effectively reducing the Coulomb-binding energy. [209] Such delocalization effects are associated with structural order. The polycrystalline character of the D1 donor layer was illustrated in X-ray diffraction measurements in Figure 9.2, hence supporting the assumption that delocalization plays a significant role for the exciton into free charge carrier conversion in these samples.

Upon further increase of the interlayer thickness, the gain in the fullerene contribution continuously decreases. Finally, in the wavelength range of the fullerene absorption the *EQE* spectra resemble each other for cascade solar cells comprising 50 Å thick D3 interlayers and D1/C₆₀ bilayer cells. This observation can be rationalized considering the data of the morphological investigation (see section 9.1.1). For a lattice spacing of $d_{D3} = 19.3$ Å and the smooth D1 underlayer featuring a root mean square roughness of $\sigma_{D1} = 11$ Å, the formation of closed intermediate D3 layers can be assumed. As illustrated in Figure 9.9, after generation of CT states at the D3/C₆₀ interface the second interface D1/D3 can be considered to be spatially separated on molecular length scales. Therefore, the cascade energy level alignment is limited in supporting free charge carrier generation. Instead, the D3/C₆₀ interface predominantly determines the photovoltaic properties, i.e. the dissociation of excitons originally generated in the fullerene phase. Additionally, the associated hole delocalization is not expected to be spread across the

D1/D3 interface but rather to be confined in the interlayer phase (see Figure 9.9). The model is supported by the *EQE* data of the D3/C₆₀ bilayer device. The fullerene contribution in those solar cells is significantly decreased by approx. 60 %, whereas in the spectral region of the diketopyrrolopyrrole absorption the *EQE* is influenced less by this interface.

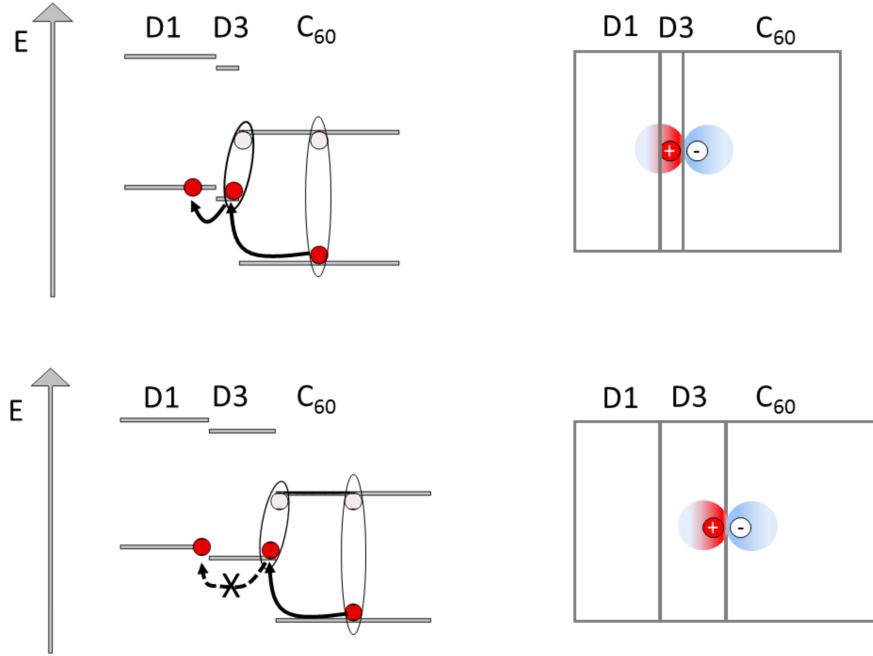


Figure 9.9.: Left side: Illustration of energy level alignments and exciton dissociation mechanisms in D1/D3/C₆₀ cells comprising thin (upper row) and thick interlayers (lower row). Right side: Associated spreading-out of the wave function across the D1/D3 interface (upper row) facilitates exciton dissociation. Hole delocalization is restricted to the D3 interlayer (lower row), limiting the support of exciton dissociation. Diffuse shading represents the charge carrier delocalization schematically.

Moreover, distinct enhancements of the *EQE* in the spectral range of the diketopyrrolopyrroles were detected as a function of interlayer thickness. As illustrated by the relative *EQE* peaks associated with the diketopyrrolopyrroles (585 nm and 635 nm) in Figure 9.8, this enhancement follows a different trend in comparison to the photocurrent increase associated with the fullerene phase (450 nm). A monotonous rise up to 25 Å interlayer thickness is evinced, for which the *EQE* is increased by up to 70 - 80 %. Excitons generated in D1 are not assumed to be dissociated at the D1/D3 interface, since the energetic offset of approx. 160 meV should be insufficient for exciton splitting. [38,210] However, the formation of hetero-CT states at the D1/D3 interface is anticipated, which may be destabilized by the cascade alignment. Additionally, coupling between D1 and C₆₀ is presumed, in particular for very thin only fragmentally closed interlayers. This coupling, reaching across the intermediate layer may spatially separate CT excitons, rendering their dissociation more efficient due to reduced Coulomb-attraction. By the *EQE* measurements on the respective bilayer solar cells the plain D1/C₆₀ interface was confirmed to dissociate excitons generated in D1. For an interlayer thickness of 50 Å the normalized *EQE* gain drops to approx. 50 %. Probably, electronic coupling between D1 and C₆₀ is considerably

reduced as well as the destabilization of CT excitons at the D1/D3 junction due to the formation of closed D3 layers of sufficient thickness as discussed above. In this case, transport limitations due to low charge carrier mobility of D3 hinder the efficient extraction of charges. Nevertheless, the *EQE* at 50 Å D3 interlayer thickness in this spectral range is still 50 % higher compared to neat bilayer cells.

A contribution to consider when evaluating the *EQE* in this spectral region is the increased absorption due to the introduction of the additional D3 layer. This contribution is continuously enhanced upon increasing the interlayer thickness as can be rationalized by the *EQE* behavior of D3/C₆₀ reference cells. In those cells, the diketopyrrolopyrrole *EQE* peak at smaller wavelength is less pronounced in comparison to that at higher wavelength. For increasing intermediate layer thicknesses in cascade solar cells the ratio of these peaks centered at 585 nm and 635 nm is progressively reduced as shown in Figure 9.8 b). Since both diketopyrrolopyrroles absorb in this spectral range, a discrimination and a clear assignment of the respective contributions is not easily accessible, but the change in peak ratio can qualitatively be accounted for an additional photocurrent contribution by the D3 interlayer.

Aiming for a deeper understanding of the photocurrent origins by the diketopyrrolopyrroles, additional spectrally resolved photoluminescence measurements were carried-out. In Figure 9.10 the PL spectra of four selected solar cells are displayed.

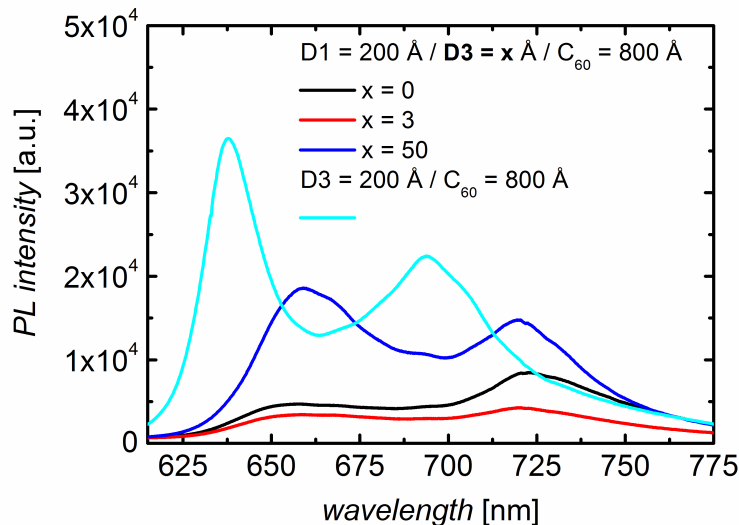


Figure 9.10.: Spectrally resolved photoluminescence of cascade solar cells and the corresponding bilayer cells.

The samples were excited utilizing a continuous wave laser with a central wavelength of 532 nm, keeping the excitation intensity constant at 6 mW/cm². Broad but structured PL bands are detected between 625 nm and 775 nm and can be attributed to radiative decay of the respective first excited state S₁ of the diketopyrrolopyrroles D1 and D3. The photoluminescence of C₆₀ is considered negligible because radiative transitions are dipole forbidden and accordingly, are

weak. [211] For D1/C₆₀ bilayer cells, photoluminescence peaks are observed at 655 nm and 720 nm, again corresponding to an energy spacing of 170 meV (see *EQE* measurements in Figure 9.7) and hence, are attributed to the vibronic progression.

The PL of D1/D3/C₆₀ cascade solar cells, comprising a thin interfacial layer of 3 Å, is considerably reduced in comparison to D1/C₆₀ reference devices. This observation is in accordance with the previous opto-electronic device characterization by *EQE* and *j(V)* studies. In those cascade solar cells improved exciton dissociation into free charge carriers was proven and accordingly, a quenching of the photoluminescence of D1 excitons is observed. For reference devices based on D3/C₆₀ a spectral shift of the PL peaks to 630 nm and 690 nm is obvious. A similar spectral shift was obtained in the *EQE* measurements with respect to D1/C₆₀ bilayer cells. Generally, for D3/C₆₀ solar cells strongly pronounced PL bands are obtained, revealing higher radiative recombination losses compared to D1/C₆₀ and hence, explaining the smaller photocurrent in these photovoltaic devices. Despite the energetic staircase and the increased diketopyrrolopyrrole contribution illustrated in Figure 9.7, cascade cells comprising an interlayer thickness of 50 Å yield a distinctly pronounced PL in comparison to D1/C₆₀ bilayer solar cells. In this case, the interlayer is assumed entirely closed and accordingly, dissociation of excitons created in D1 is strongly limited since the energetic offset at the D1/D3 interface is not assumed sufficient for exciton dissociation and the potentially separating C₆₀ interface is separated on nanometer length scale. Therefore, in those cascade cells the number of excitons created in the D1 phase to decay radiatively is increased. In these devices employing a 50 Å thick interlayer, the PL signature of D3 is almost missing entirely, indicating that excitons created in this intermediate layer probably become dissociated very efficiently at the confining interfaces during their lifetime. Only a small contribution at 690 nm can be identified, which is attributed to fluorescence originating from this intermediate layer. Additionally, it is noted that Förster resonant energy transfer is possible between diketopyrrolopyrroles since the absorption spectrum of D1 and the emission spectrum of D3 overlap considerably (see Figure 9.5 and Figure 9.10). Subsequent to such a resonant energy transfer, exciton dissociation into free charge carriers may take place at the fullerene interface.

9.1.3. Opto-Electronic Characterization of D1/D2/C₆₀ Cascade Cells

In the following Section, the focus lies on cascade devices comprising a smaller energetic offset between the donor material and the intermediate layer. This was realized by utilizing the diketopyrrolopyrrole D2 as an interlayer material instead of D3. As illustrated in Figure 9.1, the meta-pyridine substitution in D2 results in an energy level shift of only 80 meV with respect to the donor material D1. For comparison the energy level shift in D3 is twice as large with 160 meV. Figure 9.11 shows the *EQE* for D1/D2/C₆₀ solar cells in comparison to already discussed D1/D3/C₆₀ cascade cells and D1/C₆₀ reference devices.

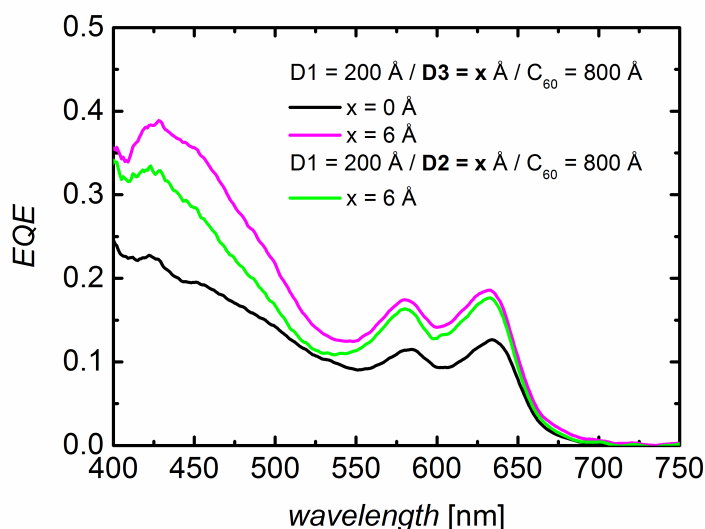


Figure 9.11.: *EQE* of D1/D2/C₆₀ and D1/D3/C₆₀ cascade solar cells and D1/C₆₀ bilayer cells.

The *EQE* is enhanced over the whole spectral absorption range for employing a 6 Å thick intermediate layer of D2. Evidently, for the *EQE* in the spectral absorption range of the diketopyrrolopyrroles between 550 nm and 670 nm, similar results are obtained for cascade solar cells utilizing a 6 Å thick intermediate layer of D2 and D3, respectively. Hence, this improvement is ascribed to the mechanisms already discussed in the previous Section 9.1.2. Compared to the cascade solar cells utilizing interfacial layers of D3, the fullerene contribution in the spectral range between 400 nm and 550 nm is slightly decreased in D1/D2/C₆₀ layered cells. This observation is ascribed to the modified energetics of the interlayer compound. Excitons generated in the fullerene phase are expected to form hetero-CT states at the D2/C₆₀ interface. Due to the smaller energetic offset at the D1/D2 interface with respect to D1/D3, the destabilization of these CT states is less efficient and so is the generation of free charge carriers. This interpretation is corroborated by the $j(V)$ characteristics displayed in Figure 9.12.

The obtained j_{sc} for D1/D2/C₆₀ solar cells exceeds the values observed for the bilayer solar cell by 35 %, but is smaller compared to D1/D3/C₆₀ cascade solar cells featuring a bigger energetic

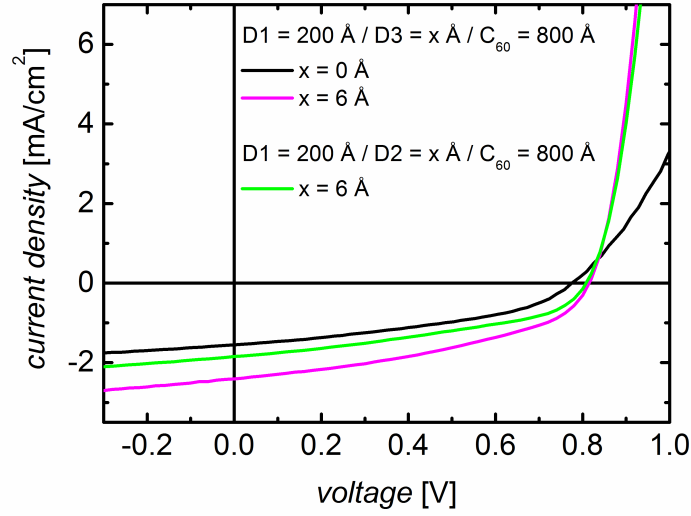


Figure 9.12.: Comparison of $j(V)$ characteristics of D1/D2/C₆₀ and D1/D3/C₆₀ cascade solar cells. The energetic offset between diketopyrrolopyrroles is smaller in case of the former. Additionally, the corresponding D1/C₆₀ reference device is included.

offset at the interface. Noteworthy, other solar cell parameters, such as V_{oc} or FF of cascade solar cells employing D2 and D3 are almost identical (see Table 9.1).

solar cell structure	j_{sc} [mA/cm ²]	V_{oc} [V]	FF [%]	η [%]
D1/C ₆₀	1.37 ± 0.14	0.78 ± 0.01	41 ± 1	0.44 ± 0.06
D1/D2/C ₆₀	1.85 ± 0.19	0.81 ± 0.01	42 ± 1	0.60 ± 0.09
D1/D3/C ₆₀	2.49 ± 0.25	0.82 ± 0.01	42 ± 1	0.85 ± 0.1

Table 9.1.: Photovoltaic parameters for D1/D2/C₆₀ and D1/D3/C₆₀ cascade solar cells and D1/C₆₀ bilayer devices.

In summary, these results illustrate the remarkable impact of inserting energetically tuned intermediate layers at a donor/acceptor heterojunction and the sensitivity of the overall device performance on the interface energetics, effecting the fundamental processes occurring during photo-conversion on microscopic length scales.

9.2. Application of Cascade Concept to DBP/F₈ZnPc/C₇₀ Solar Cells

After the general proof-of-concept, cascade energy level alignment is applied to a more efficient material combination. The donor DBP is chosen in combination with the acceptor C₇₀, since this material combination has been shown highly efficient in planar-heterojunction configuration yielding efficiencies of up to 2.8 %. [212,213] In order to establish cascade energy level alignment, the choice of a suited interlayer material is crucial. As elaborated in the course of this thesis,

the use of fluorinated zinc phthalocyanines offers an eligible option, due to the feasibility of modifying their energy level positions as a function of the degree of fluorination (see Chapter 7). Moreover, good transport properties were confirmed, promising the implementation of thicker interlayers comprised of several $F_n\text{ZnPc}$ monolayers without significant limitation of charge carrier transport. Taking into account the energy levels of DBP and C_{70} reported in literature, the mandatory choice to establish staircase energy level alignment finally went in favor of $F_8\text{ZnPc}$. The expected energy level alignment is displayed in Figure 9.13. [175, 212] The chemical structures of the employed semiconductors are shown in the insets of Figure 9.13. Cascade solar cells were comprised of the following layer sequence:

ITO/PEDOT:PSS/DBP(100 Å)/ $F_8\text{ZnPc}$ (x Å)/ C_{70} (400 Å)/BPhen(100 Å)/Ag .

To evaluate the functionality of the energetic staircase, morphological properties of the photo-active layers are important to consider, as discussed above. AFM measurement on an ITO/PEDOT:PSS/DBP thin film revealed smooth and featureless morphology yielding a root mean square roughness of $\sigma_{DBP} = 15 \text{ \AA}$ (not shown). [214] Moreover, the lattice spacing of $F_8\text{ZnPc}$ thin films was determined $d_{F_8\text{ZnPc}} = 14.0 \text{ \AA}$ in Chapter 7.

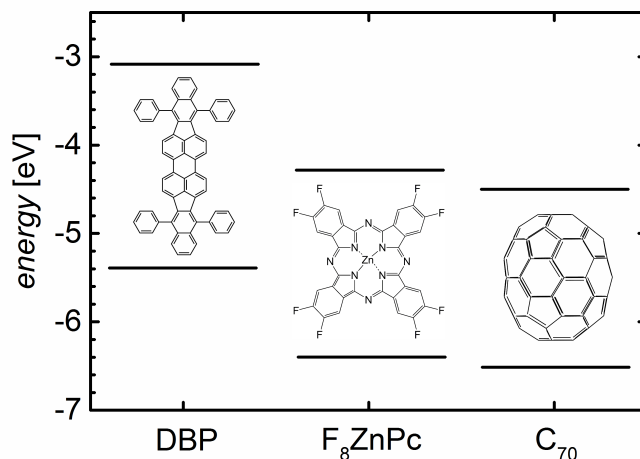


Figure 9.13.: Expected energy level alignment of the photo-active materials in DBP/ $F_8\text{ZnPc}$ / C_{70} cascade solar cells. Insets show the chemical structures of the organic semiconductors.

The impact of the insertion of an $F_8\text{ZnPc}$ interfacial layer on the photovoltaic parameters was analyzed as a function of thickness. The corresponding $j(V)$ characteristics are shown in Figure 9.14. As the cascade energy level alignment was demonstrated to have a strong impact on the exciton dissociation efficiency and therefore, on j_{sc} , this quantity is addressed at first. Evidently, upon implementation of $F_8\text{ZnPc}$ interlayers again a remarkable enhancement of j_{sc} is observed. The maximum increase is obtained for a interlayer thickness of 5 \AA , resulting in a j_{sc} enhancement by 40% compared to bilayer reference devices, yielding a short circuit current density of

6.8 mA/cm². For thicker interlayers, j_{sc} values drop linearly, hinting at an Ohmic effect. Even for an intermediate layer thickness of 100 Å, j_{sc} of the cascade cell still excels that of the neat bilayer cell by 20 %. The overall increase is attributed to the destabilization of hetero-CT states at the D/A interface, being in good qualitative agreement with the data reported on D1/D3/C₆₀ cascade cells. However, the attenuation of the gain in j_{sc} upon increasing interlayer thickness is obviously changed, comparing the two different material combinations. This discrepancy will be elucidated in more detail in the course of the *EQE* measurements below.

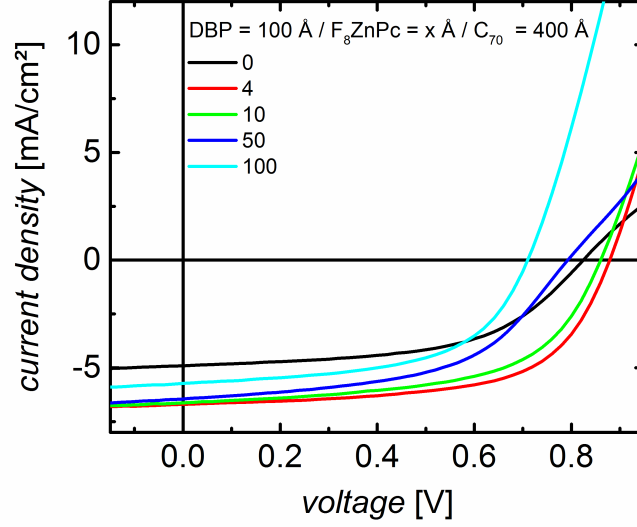


Figure 9.14.: $j(V)$ characteristics of DBP/ F_8ZnPc / C_{70} cascade solar cells and DBP/ C_{70} reference bilayer cells.

After demonstrating the distinct increase of j_{sc} in cascade solar cells in comparison to neat bilayer devices, an approximation of the maximum achievable short circuit current density $j_{sc max}$ for the chosen layer thicknesses of the molecular semiconductors is carried-out, in order to judge on the potential for further improvement of the overall photocurrent generation efficiency within these stacks. On the idealized situation that all photo-generated excitons get dissociated into free charge carriers and are subsequently extracted at the electrodes, i.e. that no recombination losses occur within the solar cell, the maximum achievable short circuit current density $j_{sc max}$ can be calculated (compare Section 6.1.2):

$$j_{sc max} = \int \frac{A(\lambda) \cdot P_{AM1.5G}(\lambda) \cdot q \cdot \lambda}{h \cdot c} d\lambda. \quad (9.1)$$

Here $A(\lambda)$ denotes the spectrally resolved absorption of the molecular semiconductors, $P_{AM1.5G}(\lambda)$ the solar spectrum, q the elementary charge, λ the wavelength, h the Planck constant, c the speed of light. For the exemplary cascade solar cell featuring an intermediate layer thickness of 5 Å, the calculated maximum achievable short circuit current density amounts to $j_{sc max} = 12.5$ mA/cm², whereas the real macroscopic j_{sc} amounts to 6.8 mA/cm². Thus, for this solar cell

configuration approximately 55 % of all photo-generated excitons contribute to the photocurrent under short circuit conditions.

Evidently, transport properties across the energy staircase are distinctly improved as manifested in the enhanced FF for thin F_8ZnPc interfacial layers of up to 10 Å, (see Figure 9.15). For instance, for a 4 Å thick F_8ZnPc layer the fill factor is increased to 62 % in comparison to 54 % obtained for the bilayer reference cells. The reasons for this improvement were addressed in detail for cascade solar cells based on D1/D3/ C_{60} in the previous section. Upon increasing the interlayer thickness further, the FF drops, but even for interlayer thicknesses of 50 Å and 100 Å the observed fill factors are still comparable to that of the bilayer reference device. At this point, a clear discrepancy has to be noticed in comparison to D1/D3/ C_{60} cascade solar cells, for which transport properties were significantly limited by the formation of space charges in this thickness regime of several monolayers. Evaluating the two cascade architectures, D1/D3/ C_{60} and DBP/ F_8ZnPc / C_{70} , the interlayer material utilized in the latter turns out to yield superior transport properties.

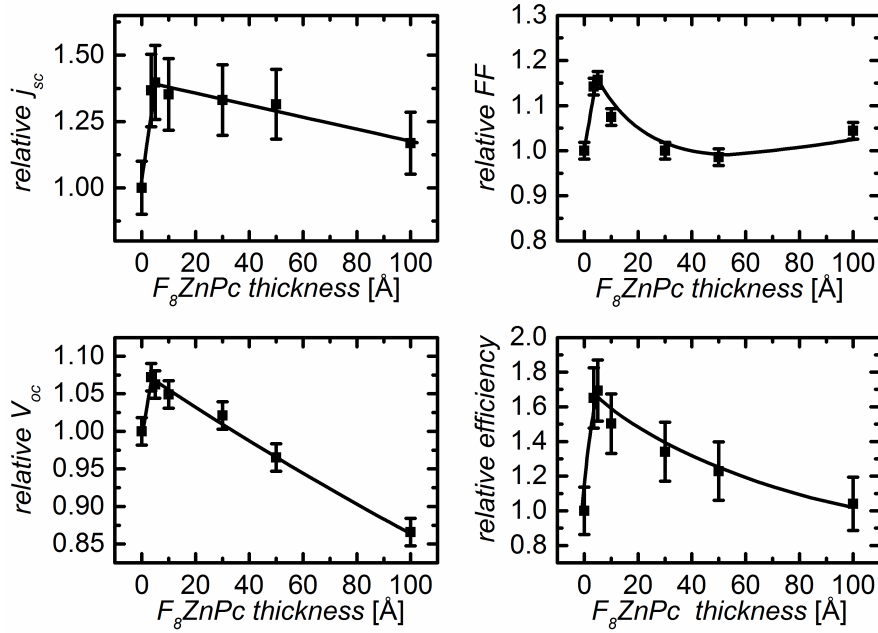


Figure 9.15.: Normalized photovoltaic parameters of DBP/ F_8ZnPc / C_{70} cascade devices for different interlayer thickness. Scaling was carried-out with respect to the DBP/ C_{70} bilayer solar cell. Solid lines represent guides to the eye.

Moreover, in accordance with reduced recombination losses a slight increase of V_{oc} is detected for thin interlayers. For a 4 Å thick intermediate F_8ZnPc layer the open circuit voltage amounts to $V_{oc} = 0.87$ V. This gain in voltage drops upon increasing the interlayer thickness and finally, for a 100 Å thick interlayer V_{oc} is reduced to 0.71 V. For such a solar cell configuration, the DBP/ F_8ZnPc and F_8ZnPc / C_{70} heterojunction are supposed to operate independently and as such, the two heterojunctions of the cascade structure are considered to be connected in parallel. As a consequence, the macroscopic V_{oc} of such a device is determined by the smaller open

circuit voltage of the two spatially separated heterojunctions. [215] In this case, the F_8ZnPc/C_{70} interface would limit V_{oc} , as the related material combination F_8ZnPc/C_{60} yielded a comparable open circuit voltage (see Section 7.2). The decisive energy levels, which determine V_{oc} , of C_{60} and C_{70} are virtually the same. [18]

Finally, the beneficial impact of the implementation of F_8ZnPc interlayers on the individual solar cell parameters leads to a remarkable improvement of the power conversion efficiency. For instance, for an F_8ZnPc interlayer thickness in the sub-monolayer range between 4 Å to 10 Å the power conversion efficiency is enhanced by 50 - 70 % (see Figure 9.15), demonstrating the capability of this functional design concept to improve device parameters of established planar heterojunctions. The maximum power conversion efficiency of 3.7 % obtained for an interlayer thickness of 5 Å is among the best reported in literature so far for planar solar cells utilizing thin interfacial dissociation layers.

The lower graph of Figure 9.16 shows the *EQE* of $DBP/F_8ZnPc/C_{70}$ cascade solar cells and the corresponding DBP/C_{70} bilayer cells. Additionally, in the upper graph the absorption coefficients of the molecular components are displayed.

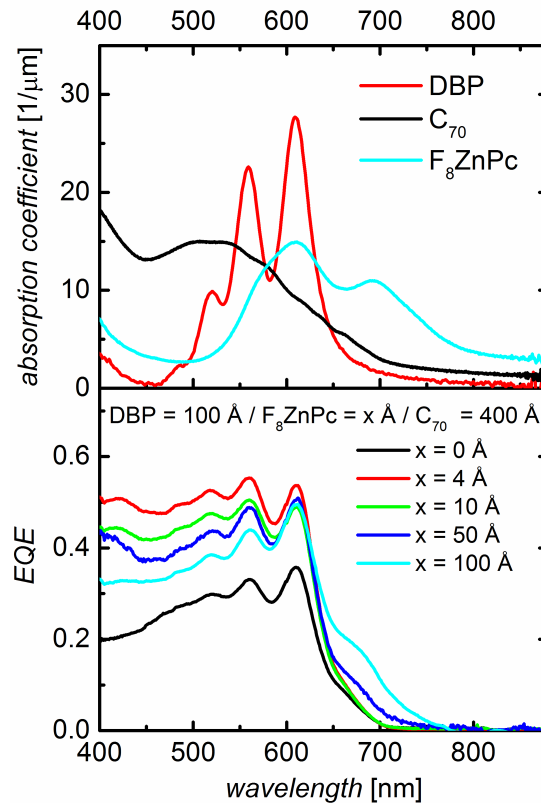


Figure 9.16.: Upper graph: Absorption coefficients of the photo-active materials. Lower graph: *EQE* of $DBP/F_8ZnPc/C_{70}$ cascade solar cells and DBP/C_{70} bilayer devices.

For the neat DBP thin film three distinct absorption peaks are observed at 517 nm, 559 nm and 611 nm. The energy spacing of 0.18 eV between these peaks is associated with the vibronic

progression. [41] The existence of this donor related photocurrent contribution is clearly verified in the *EQE* measurements on DBP/C₇₀ bilayer solar cells. Also the C₇₀ acceptor yields a clear photocurrent contribution, as evinced exemplarily for a wavelength of 450 nm.

Upon insertion of a 5 Å thick F₈ZnPc intermediate layer sandwiched between the DBP/C₇₀ heterojunction, the *EQE* is increased over the whole spectral absorption range in comparison to bilayer reference cells. Particularly, the fullerene contribution is enhanced by more than a factor of 2, as demonstrated in Figure 9.17. Excitons created in the fullerene phase can form hetero-CT states at the F₈ZnPc/C₇₀ interface. Due to the staircase energy level alignment and the close proximity of the second interface, these CT states are effectively destabilized. Increasing the interlayer thickness further, the gain continuously decreases, but even for an interlayer thickness of 100 Å the C₇₀ contribution is still enhanced by 50 %. Therefore, it can be rationalized that for macroscopic interlayers comprising several monolayers, such as the 50 Å and 100 Å thick F₈ZnPc layers, the common interface between phthalocyanine and fullerene enables efficient exciton dissociation.

For the D1/D3/C₆₀ and DBP/F₈ZnPc/C₇₀ cascade cells analyzed in this chapter, there is an important difference concerning the respective energetic position of the interlayer with respect to the donor and acceptor material. In D1/D3/C₆₀ cascade cells, the interlayer features an energetic offset of approx. 700 meV with respect to the acceptor, whereas in DBP/F₈ZnPc/C₇₀ cells this energetic offset amounts to approx. 150 meV. Nevertheless, for both material combinations a substantial increase of the fullerene acceptor contribution to the photocurrent could be established in cascade cells, demonstrating the universality of this conceptual approach to improve exciton dissociation.

The DBP photocurrent contribution to the *EQE* cannot be separated precisely from that of the fullerene fraction, because the donor absorption spectrum is superimposed to that of the acceptor. However, a qualitative increase is also confirmed for the DBP photocurrent implementing F₈ZnPc intermediate layers in comparison to the respective bilayer solar cells. In the spectral range of strong DBP absorption, i.e. in particular between 560 nm and 610 nm, the *EQE* is enhanced by 55 % to 70 % for the insertion of a 4 Å thick interlayer. Upon increasing interlayer thickness, the *EQE* gain only slightly diminishes despite the fact, that the fullerene contribution was shown to decrease much steeper in Figure 9.17. This illustrates that the relative DBP contribution to the *EQE* is enhanced upon increasing interlayer thickness. This trend was also observed for the donor material in D1/D3/C₆₀ cascade solar cells. It has to be noted, that interference effects may play an important role, in particular for the DBP donor layer, since the introduction of an additional interlayer between the donor and acceptor shifts the position of the maximum E-field amplitude within the stack.

Finally, for 50 Å and 100 Å thick intermediate F₈ZnPc layers, a clearly discernable *EQE* contribution by the phthalocyanine is obtained as indicated by the shoulder in absorption at 675 nm, suggesting the ability of at least one of the organic/organic interfaces to dissociate excitons created in the phthalocyanine layer.

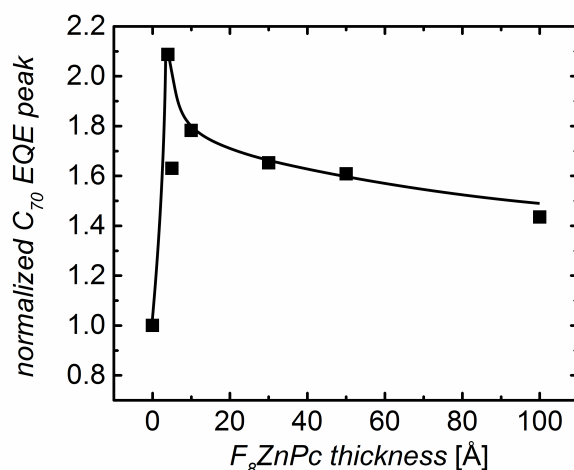


Figure 9.17.: Normalized EQE peak at an excitation wavelength of 450 nm, corresponding to the C_{70} fullerene contribution, as a function of interlayer thickness. Normalization was performed with respect to the DBP/ C_{70} bilayer solar cell. The solid line represents a guide to the eye.

Conclusion

In this chapter the impact of establishing cascade energy level alignment in tri-layer solar cells was under investigation. Such energetic staircases were realized for two different material combinations by introducing thin interfacial layers between the respective donor/acceptor heterojunction. The first material combination was based on diketopyrrolopyrroles, which differed in their energy levels by approx. 160 meV due to the chemical substitution of phenyl end groups (D1) by para-pyridines (D3). In D1/D3/ C_{60} cascade solar cells employing thicknesses in the sub-monolayer range, a remarkable increase of the short circuit current density was obtained by almost a factor of two in comparison to neat D1/ C_{60} bilayer cells. This increase was attributed to an improved destabilization of hetero-CT states at the D3/ C_{60} interface, rendering the generation of free charge carriers more efficient. The fact that interlayer thicknesses in the sub-monolayer range operated most efficiently reveals that interlayer molecules act as dissociation sites, without imposing severe constraints on the charge transport across the cascade.

The cascade concept was transferred to the well-established, high performing small molecule material combination DBP/ C_{70} by introducing interlayers of fluorinated zinc phthalocyanine F_8ZnPc at this D/A heterojunction, causing a significant improvement of all solar cell parameters. This translates into a power conversion efficiency of 3.7 % for an interlayer thickness of 5 Å, in comparison to 2.2 % for the corresponding DBP/ C_{70} bilayer devices. For organic cascade solar cells employing thin molecular interfacial layers this is among the best results reported in literature up to now. [92, 93]

Comparing both cascade structures it becomes evident, that energy levels of the respective interlayers have to differ relative to those of the donor and acceptor material. Nevertheless, the gain in photocurrent by the molecular donor and acceptor component is comparable for the two different cascade structures investigated, as evinced by the *EQE* measurement, illustrating the universality of this concept. This study highlights the crucial role of interface energetics on the separation of excitons into free charge carriers and demonstrates the possibility of intentionally targeting recombination losses by the implementation of an additional single layer, *viz.* an additional processing step in the preparation of planar heterojunction organic solar cells.

10. Excitonic and Electronic Compatibility of Mixed C₆₀:C₇₀ Acceptor Layers

10.1. Fullerenes: Structure, Purification Costs and Technological Relevance in OPV

Fullerenes are carbon based, closed cage molecules. Owing to Euler's theorem, fullerenes are formed by exactly 12 pentagons and an arbitrary number of hexagonal faces, i.e. the smallest fullerene possible is C₂₀, consisting of solely 12 pentagonal faces. [18] However, such a structure comprising adjacent pentagons is energetically unfavorable, because it yields a high local curvature and with it, a high strain on the fullerene cage. The trend of preferential formation of fullerenes with pentagons at all sites being adjacent to hexagonal faces is called the isolated pentagon rule. [216,217] The smallest compounds to fulfill this requirement are C₆₀ and C₇₀.

Fullerenes are generated from carbon rich vapors, e.g. by resistive heating of carbon rods or an electric discharge between graphite electrodes in He atmosphere. In these common synthesis procedures, predominantly C₆₀ and C₇₀ are created at a ratio of 3:1 enclosed in a carbon rich soot. [218] This raw fullerene blend also includes 1 - 3 % of higher mass fullerenes such as C₇₆, C₇₈ and C₈₂, satisfying the above-mentioned isolated pentagon rule. Due to the different molecular masses of the individual fullerenes, their sublimation temperatures vary (see Section 4.3.2). Accordingly, a separation is for example possible by gradient sublimation, rendering C₆₀ easiest to be isolated from higher order fullerenes, with potential impurities being mainly comprised of C₇₀. [219]

In most organic photovoltaic cells, either C₆₀ or C₇₀ is utilized as acceptor material. This is due to the isotropically closed-packed structure of the molecules in thin films, the high electron mobility of up to 1 Vs/cm² and the high electron affinity, respectively (see Section 4.3.2). [45,220] Those fullerenes, employed in opto-electronic applications, are generally highly purified, leading to the fact that the overall fullerene material costs are mainly determined by this purification process. To date, refinement of C₆₀ at a chemical purity of 99.9 % instead of 99.5 %, already results in a price disparity of approximately a factor of two. Isolating higher mass fullerenes is even more cost-intensive. The purification costs for C₇₀, having a purity grade > 99 %, are already one order of magnitude higher compared to those of refined C₆₀ at a purity degree of 99.5 % and two orders of magnitude higher with respect to raw fullerene blends.

With regard to the optical properties, C_{70} by its slight spherical distortion yields a distinctly higher absorption coefficient in comparison to C_{60} . Thus, the implementation of C_{70} as an acceptor layer generally translates into superior photocurrents in photovoltaic applications compared to C_{60} , in bulk-heterojunction as well as planar-heterojunction architectures. [221, 222] This tendency is also observed for solar cells based on the related fullerene derivatives [6,6]-phenyl-C-71-butyric acid methyl ester ($PC_{70}BM$) and [6,6]-phenyl-C-61-butyric acid methyl ester ($PC_{60}BM$). [223–225] A side-chain attached to these fullerene derivatives facilitates solubility in commonly used organic solvents such as toluene or chlorobenzene and hence, enables liquid processing.

A recent study by Popescu et al., applying blends of these two electron acceptors in combination with the donor poly(3-hexylthiophen-2,5-diyl) (P3HT) questions the necessity of utilizing only highly-refined fullerenes, because identical device performance was obtained for a widely varying composition range of $PC_{60}BM:PC_{70}BM$ blends. [226] This result was rather unexpected because thin film absorption differs significantly for both fullerenes and energy levels were reported very similar, but not identical. [18, 101, 227] However, electron paramagnetic resonance measurements indeed revealed a common electron affinity for such $PC_{60}BM:PC_{70}BM$ blends. [228] Accordingly, no preferential formation of the anionic state of either fullerene derivative was observed, i.e. no preferred trapping of electrons on either molecular compound was obtained. As a consequence thereof, the authors suggested the use of so-called technical grade PCBM, containing a mixture of $PC_{60}BM$ and $PC_{70}BM$, for bulk-heterojunction fabrication, since such a fullerene blend is much cheaper to produce. [226, 228]

In this chapter, the scope of research is extended to blends of archetypical fullerene molecules C_{60} and C_{70} , which are the most commonly used compounds in small molecule organic photovoltaics. The two structurally and energetically very similar materials are tested in an interlaced acceptor phase and the consequences for excitonic and electronic transport are elucidated. Next to photo-physical implications, also the technical relevance of purification is discussed in this chapter and from a cost-related point of view, a recommendation for refinement is given. To this end, highly purified fullerenes C_{60} (Creaphys: purity > 99.95 %) and C_{70} (Solaris Chem. Inc.: purity > 99 %) were employed at various mixing ratios as co-evaporated acceptor phases and in combination with the prototypical donor material DIP. The following solar cell architecture was utilized:

ITO/PEDOT:PSS/DIP(30 nm)/ $C_{60}:C_{70}$ (35 nm)/BPhen(5 nm)/Ag .

This sequence includes the corresponding bilayer solar cells DIP/ C_{60} and DIP/ C_{70} for reference. Additionally, in Section 10.3 solar cells based on an acceptor phase comprising a raw fullerene mixture (Ionic Liquids Technologies GmbH: 75 % of C_{60} and 25 % of C_{70} and 1 - 3 % of higher mass fullerenes) were tested, in order to verify the impact of higher order fullerenes on the photovoltaic characteristics. Photovoltaic devices were prepared together with Johannes Mahr.

10.2. Thin Film Properties of the Molecular Semiconductors

Opto-electronic properties of photovoltaic devices are closely linked to the microscopic morphology of the photo-active layers. Therefore, structural properties were investigated by atomic force microscopy. The photo-active layers were evaporated on ITO/PEDOT:PSS covered glass substrates to resemble the solar cell geometry. The morphologies of neat bilayer heterostructures DIP/C₆₀ and DIP/C₇₀, were compared to DIP/C₆₀:C₇₀ heterojunctions, consisting of an inter-laced acceptor phase. A variation of the microstructure may result in different coverages of the respective acceptor phase by the subsequent BPhen exciton blocking layer within the cells. The coverage of the acceptor by BPhen is a crucial factor in terms of extraction of charge carriers by the top-grown cathode (see Section 4.4). Besides, BPhen prevents detrimental effects associated with the deposition of the Ag top-electrode, such a partial shortening. [157]

Figure 10.1 shows the obtained AFM images of a 30 nm thick DIP thin film (a) and of the investigated DIP/C₆₀:C₇₀ heterostructures (b - d). The AFM image of the bare PEDOT:PSS hole transporting layer is omitted, since it showed a smooth and featureless surface, yielding a root mean square roughness of $\sigma_{PEDOT:PSS} < 1$ nm. The topography of the DIP donor layer features a distinct island (Voolmer-Weber) growth mode. [229] Accordingly, a rough surface with $\sigma_{DIP} = 4.9$ nm is obtained. The island shaped crystallites yield lateral dimensions of 50 - 100 nm in diameter.

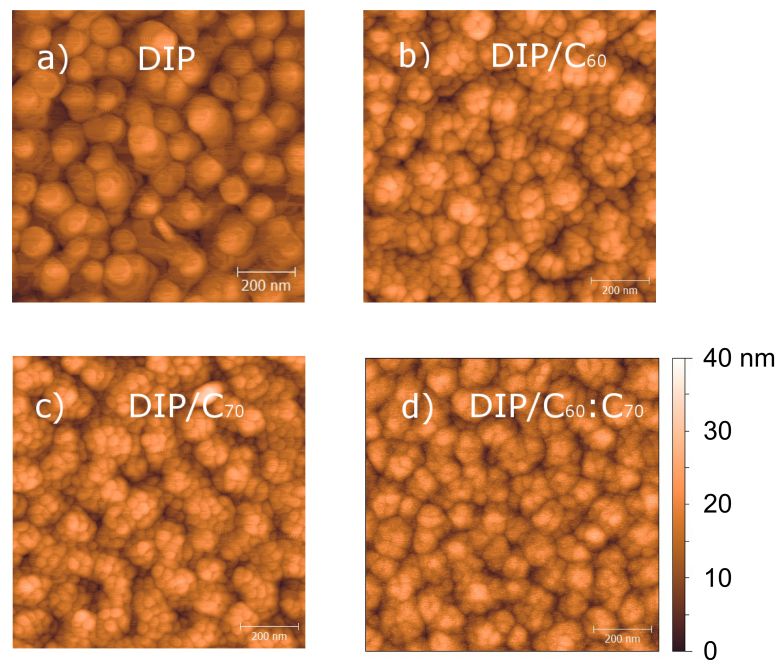


Figure 10.1.: AFM images of a) a neat DIP thin film and b) - d) DIP/C₆₀:C₇₀ heterostructures.

Evidently, upon evaporation of a 35 nm thick C₆₀ layer on top of the donor material, fullerene molecules adopt the morphology of the underlying DIP layer. Fine-grained, almost spherically shaped fullerene domains are formed atop the donor islands, hence yielding a correlated rough-

ness of $\sigma_{DIP/C_{60}} = 5.0$ nm. Since the closed cage structural motif of C_{70} and C_{60} molecules is very similar, so is the topography of DIP/C_{60} and DIP/C_{70} (compare Figure 10.1 b) and c)). This observation is corroborated by an almost unaffected roughness of $\sigma_{DIP/C_{70}} = 5.1$ nm. For the same reason, this similarity is also observed for the microscopic topography of co-evaporated fullerene phases in the $DIP/C_{60}:C_{70}$ (1:1) heterostructure in Figure 10.1 d). A corresponding roughness of $\sigma_{DIP/C_{60}:C_{70}} = 5.0$ nm is detected.

The overall morphological similarity of all fullerene phases under investigation, i.e. DIP/C_{60} , DIP/C_{70} and $DIP/C_{60}:C_{70}$, allows to exclude changes in the electrical losses associated with a variation of the BPhen blocking layer coverage for the different heterostructures (*vide supra*). Moreover, the heterostructures were analyzed by X-ray diffraction measurements. No crystalline texture of the top-grown fullerene fraction could be observed. Hence, variations in opto-electronic behavior can be mainly attributed to the material inherent properties of the respective fullerene phase.

In order to correlate effects by the varying acceptor mixing ratio to the performance of the corresponding photovoltaic devices it is obligatory to analyze the absorption of the molecular components beforehand. Therefore, organic thin films comprised of neat C_{60} , C_{70} as well as the raw fullerene mixture were evaporated on glass substrates and were investigated by UV/Vis spectroscopy. The respective absorption coefficients were determined according to Equation 6.6 and are displayed in Figure 10.2. For the sake of completeness, the absorption coefficient of the donor material DIP is also shown.

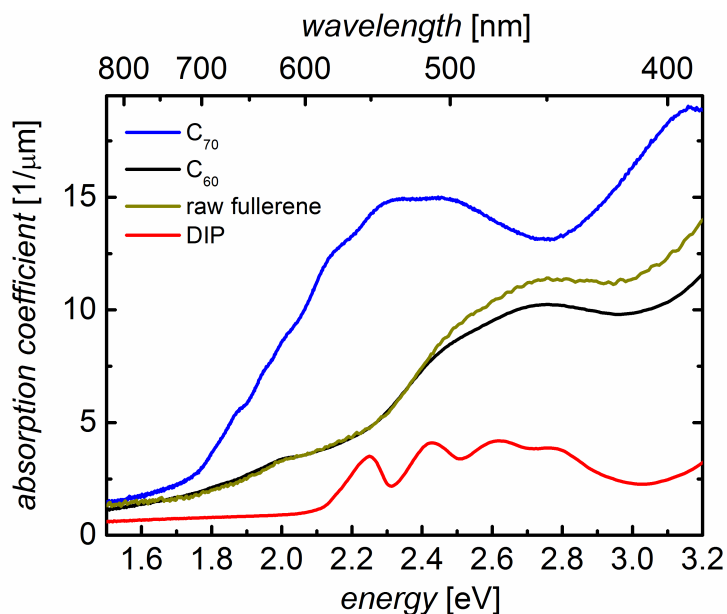


Figure 10.2.: Absorption coefficients of the donor DIP and the acceptor compounds C_{60} , C_{70} and the raw fullerene mixture.

The absorption onset of the buckminsterfullerene C_{60} is observed at 1.7 eV. Around this absorption threshold, optical transitions are very weak, because electric dipole transitions are forbidden

due to symmetry considerations. [230] Moving away from the absorption threshold towards increasing energy, the absorption coefficient becomes larger. The absorption peak at 2.7 eV is attributed to dipole allowed electronic transitions between HOMO-1 \rightarrow LUMO and HOMO \rightarrow LUMO+1 states. [123] As fullerenes generally comprise a closed cage motif their fundamental electronic structures qualitatively resemble one another. Accordingly, electronic transitions and therewith, optical absorption of C₆₀ and C₇₀ is similar. The absorption edge of C₇₀ is slightly red-shifted due to the extended π -electron system. In particular, near the absorption edge the absorption coefficient of C₇₀ distinctly exceeds that of C₆₀. This is due to the lower symmetry of the former. The absorption coefficient of the raw fullerene mixture is strikingly similar to that of C₆₀ concerning spectral shape and absolute values. The raw fullerene mixture was specified to be comprised of a C₆₀:C₇₀ blend ratio of 3:1 including additionally 1 - 3 % of higher mass fullerenes by mass spectrometry (not shown). However, the optical data of the corresponding thin film appear to be solely determined by the absorption of C₆₀. Due to the different molecular masses of the contained fullerenes their sublimation temperatures vary considerably (see Section 4.3.2) and thus, it can be concluded that vacuum sublimation of the raw fullerene mixture yields thin films predominantly comprised of C₆₀.

The absorption onset of the HOMO \rightarrow LUMO transition of the DIP donor material is observed at 2.1 eV. The local absorption maximum at 2.25 eV is clearly associated with vibronic progression of the breathing mode equidistantly separated in energy by 0.18 ± 0.01 eV. [41] The spectral absorption is correlated to the so-called σ -crystal structure of DIP, for which the molecules adopt an almost upright standing position with respect to the substrate surface (see Section 4.3.1). [141] The dipole moment \vec{p} of the S₀ \rightarrow S₁ transition is oriented along the long molecular axis of DIP. In turn, this results in weak coupling of the E -field vector \vec{E} of the incident light to this transition dipole moment, since the absorption probability is proportional to $\sqrt{\vec{p} \cdot \vec{E}}$. Hence, the overall absorption of the transition S₀ \rightarrow S₁ is weak in the σ -crystal structure. Although excellent transport properties were reported in literature for DIP/C₆₀ bilayer cells, yielding fill factors higher than 70 %, the weak absorption in the visible spectral range constitutes a limiting factor for the application of DIP in crystalline bilayer solar cells. [154, 174] However, for this particular study the constraint is not considered detrimental, as the respective fullerene phase is anticipated to provide the dominant contribution to the generated photocurrent, thus enabling to verify the impact of the respective fullerene phase on the photovoltaic parameters directly. Aiming to illustrate the role of the fullerene phase in photocurrent generation, the spectrally resolved absorption coefficients were weighted with the solar spectrum at AM1.5G, considering the respective layer thickness of the donor and acceptor material. [158] Under this simplified approach, i.e. without consideration of interference effects and recombination losses, the fullerene contribution is expected to yield approximately 70 % of the total generated photocurrent in DIP/C₆₀ solar cells. Due to the stronger absorption of C₇₀, the photocurrent of DIP/C₇₀ is anticipated 80 % larger in comparison to DIP/C₆₀.

Photoemission and inverse photoemission experiments on C₆₀ and C₇₀ thin films revealed remarkable similarities of both fullerenes with respect to the density of states and also to the

absolute HOMO and LUMO energies with respect to the Fermi-level. However, minor differences are reported, i.e. the band gap of C_{70} is supposed to be slightly decreased by several tens of meV in comparison to C_{60} . [18] This observation was in good qualitative agreement with theoretical calculations. [231] Due to these slight differences in frontier energy positions, it has to be verified if this energetic disparity translates into enhanced trapping of excitons on either fullerene phase in case of interlaced $C_{60}:C_{70}$ blends. For that purpose, spectrally resolved photoluminescence measurements were carried-out on C_{60} , C_{70} as well as $C_{60}:C_{70}$ thin films evaporated on glass substrates. The corresponding PL spectra, using a 532 nm cw-laser for excitation are shown in Figure 10.3.

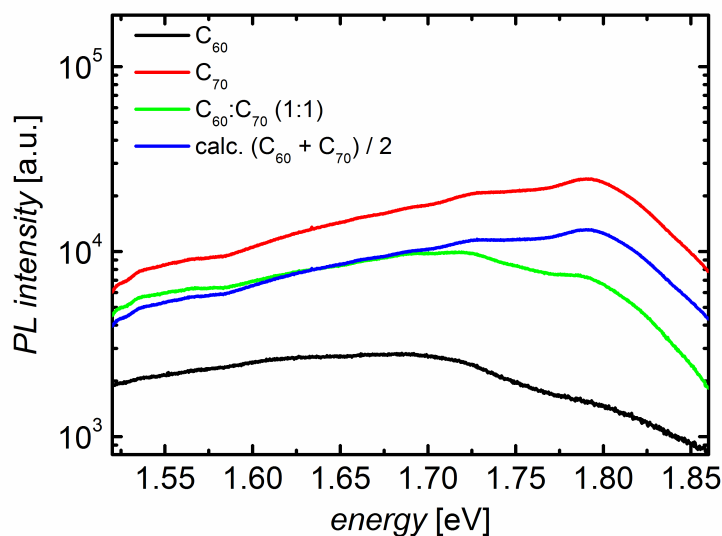


Figure 10.3.: Spectrally resolved photoluminescence intensity utilizing a 532 nm cw-laser with an incident intensity of 1.5 mW/cm^2 for excitation. Samples were comprised of 35 nm C_{60} , C_{70} and $C_{60}:C_{70}$ thin films. Additionally, the sum of half of the PL of both plain C_{60} and C_{70} thin films was calculated.

Broad PL bands are observed between 1.50 eV and 1.85 eV for C_{60} and C_{70} thin films. Evidently, the PL of the higher mass fullerene C_{70} exceeds the fluorescence of C_{60} by approximately one order of magnitude. For the co-evaporated $C_{60}:C_{70}$ (1:1) blend, a PL signal is obtained, which is intermediate to that of both plain fullerene thin films.

Averaging the PL intensity of neat C_{60} and C_{70} thin films with respect to the nominal 50:50 stoichiometric mixing ratio of the blended sample, i.e. calculating the arithmetic mean $(\text{PL}_{C_{60}} + \text{PL}_{C_{70}})/2$, yields a PL signal (blue curve), which is quite similar in spectral shape and absolute intensities compared to the PL signal of co-evaporated $C_{60}:C_{70}$ (1:1) thin films (green curve), for energies up to 1.7 eV. However, towards higher energies an evident mismatch is obtained rendering the calculated PL higher than the experimentally observed PL of the co-evaporated sample. Apparently, this discrepancy is most pronounced around 1.79 eV, i.e. in an energy regime in which the PL signal is predominantly determined by the fluorescence of C_{70} . As-

suming the existence of an efficient Förster-type energy transfer between both fullerene entities, excited state populations are expected to equilibrate over time, since such an energy transfer is anticipated to be faster than the competing radiative decay of excitons. [195] Furthermore, these exciton populations on either fullerene phase instantaneously after photo-excitation are determined by the respective absorption coefficient. For the utilized excitation wavelength of 532 nm the absorption coefficient of C₇₀ ($\alpha_{C_{70}} = 14.3 \frac{1}{\mu m}$) exceeds that of C₆₀ ($\alpha_{C_{60}} = 6.0 \frac{1}{\mu m}$) by almost a factor of 2.5 (see Figure 10.2). Hence, qualitatively an energy transfer from C₇₀ to C₆₀ is expected to take place subsequent to the initial absorption process. By this effect, the number of excitons on weakly photoluminescent C₆₀ molecules is increased and *vice versa*, the population of excited C₇₀ molecules with a comparably strong PL is decreased. Therefore, the smaller PL of co-evaporated C₆₀:C₇₀ (1:1) thin films in comparison to the calculated mean PL = $(PL_{C_{60}} + PL_{C_{70}})/2$ is in good qualitative agreement with the hypothesis of an efficient resonant energy transfer between both fullerene entities at room temperature.

10.3. Impact of Fullerene Composition Ratio on DIP/C₆₀:C₇₀ Solar Cells

The existence of a resonant energy transfer, promoting exciton transport between the two fullerene constituents in co-evaporated C₆₀:C₇₀ thin films at room temperature, can be considered a prerequisite for potential applications of C₆₀:C₇₀ blends as acceptor phases in organic photovoltaics. In this section, the focus is placed on the impact of a varying fullerene composition ratio on the resulting device characteristics of DIP/C₆₀:C₇₀ cells. For this purpose, in Figure 10.4 the *EQE* data of a set of representative devices is displayed.

Comparing the respective absorption coefficients in Figure 10.2 with the *EQE* data it becomes evident, that the *EQE* and with it the generated photocurrent, predominantly originates from the fullerene acceptor phase in plain DIP/C₆₀ reference bilayer cells, as expected from the considerations in Section 10.2. Solely a weak absorption shoulder at 550 nm can be assigned to the donor material DIP. For DIP/C₇₀ bilayer cells, the *EQE* is distinctly increased over the entire absorption range, yielding a maximum *EQE* of 50 % at 500 nm, exceeding that of 30 % obtained for DIP/C₆₀ bilayer cells. This increase is attributed to the overall higher absorption of C₇₀ in comparison to the buckminsterfullerene C₆₀. In accordance with the optical data shown in Figure 10.2 the *EQE* is slightly red-shifted for DIP/C₇₀ cells in comparison to DIP/C₆₀, resulting in a steep onset at 700 nm.

Verifying the impact of the mixed acceptor phase on the photovoltaic behavior, the C₆₀:C₇₀ fullerene acceptor composition was systematically changed. For solar cells based on a C₆₀:C₇₀ acceptor mixing ratio of 3:1, the *EQE* is intermediate to that of the respective bilayer reference devices. Upon increasing the C₇₀ content in the fullerene acceptor layer, the *EQE* is successively enhanced and finally adopts the shape of DIP/C₇₀ reference devices, as can be rationalized for

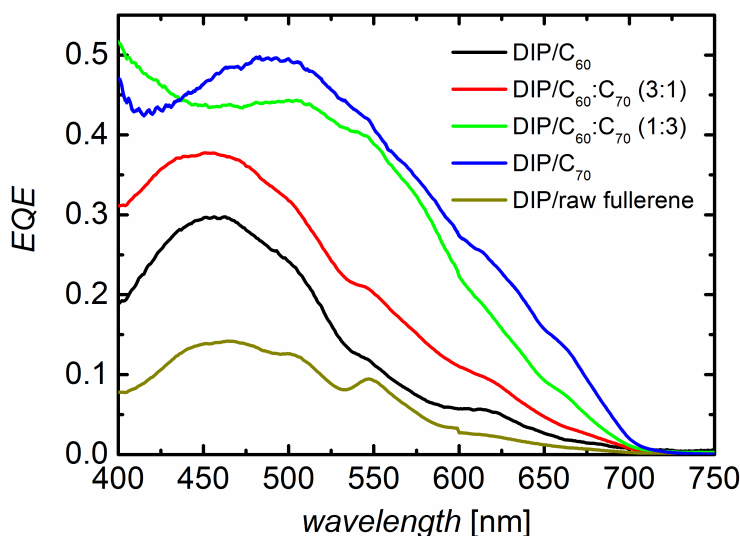


Figure 10.4.: External quantum efficiencies of representative DIP/C₆₀:C₇₀ organic photovoltaic cells, comprising different fullerene mixing ratios of the acceptor phase. Additionally, the *EQE* of a DIP/raw fullerene solar cell is displayed.

the solar cells based on a C₆₀:C₇₀ ratio of 1:3. Despite the non-identical energy levels of the neat fullerene entities reported in literature, no enhanced trapping or recombination losses are observed for solar cells based on mixed C₆₀:C₇₀ acceptor phases.

For photovoltaic cells comprising a raw fullerene acceptor layer the *EQE* is drastically reduced over the entire spectral range in comparison to the DIP/C₆₀ reference devices, despite the fact, that the absorption of the raw fullerene mixture slightly exceeds that of pure C₆₀ (see Figure 10.2). As a result, for DIP/raw fullerene cells the maximum *EQE* of 14 % measured at 550 nm is reduced by more than 50 % in comparison to DIP/C₆₀ cells. This decrease has to be assigned to enhanced recombination losses caused by the presence of higher order fullerenes in the raw fullerene mixture. In comparison to DIP/C₆₀ bilayer cells, the DIP donor contribution to the *EQE* seems to be almost unaffected in DIP/raw fullerene devices, whereas the fullerene photocurrent contribution is distinctly reduced. This means that after dissociation of excitons generated in the DIP donor layer into free charge carriers, the transport of the resulting electrons within the fullerene phase to the electrodes seems not to be significantly restricted. Hence, it is concluded that mainly the excitonic transport in the fullerene phase is distinctly deteriorated. The HOMO energies of the higher order fullerenes C₇₆ and C₈₄ are reported to be shifted by 0.5 eV towards higher energies in comparison to C₆₀ and C₇₀, whereas the LUMO energies remain almost equal. [232, 233] Accordingly, due to the specific energy level positions of the respective individual acceptor constituents of the raw fullerene blend, electronic transport between the different fullerene entities seems possible, whereas, with regard to excitonic transport, higher order fullerenes may act as traps. Only 1 - 3 % of higher order fullerenes are present in the initial raw fullerene composite, yet a smaller amount is anticipated in the processed raw fullerene

thin film due to the higher sublimation temperature of these higher mass fullerenes (see Section 10.2). Nevertheless, even impurity concentrations of 10^{-6} - 10^{-5} in polyacene single crystals are reported to affect transport of excitons and charge carriers significantly. [234]

Finally the voltage-dependent $j(V)$ characteristics were measured under AM1.5G standard illumination conditions, in order to judge on the macroscopic device performance. The $j(V)$ characteristics are shown in Figure 10.5 and the deduced solar cell parameters are summarized in Figure 10.6.

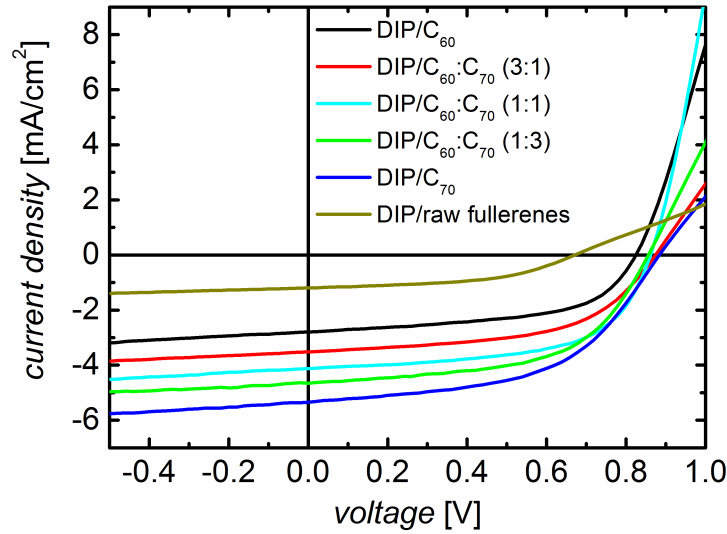


Figure 10.5.: $j(V)$ curves of DIP/C₆₀:C₇₀ solar cells employing various compositions of the fullerene acceptor blend. Moreover, the DIP/raw fullerene $j(V)$ characteristics are shown for comparison.

For DIP/C₆₀ bilayer solar cells a short circuit current density of 2.8 mA/cm² is obtained. A defined correlation between the C₇₀ content in the fullerene phase and j_{sc} can be confirmed, yielding a linear enhancement of the short circuit current density with increasing C₇₀ fraction. This outcome is in qualitative agreement with the *EQE* data shown above. Finally, for DIP/C₇₀ bilayer cells the short circuit current density is increased by 90% to 5.2 mA/cm². Remarkably, this value is very close to the expected j_{sc} increase of 80%, solely anticipated by weighting the absorption coefficients with the layer thicknesses of the absorber materials and the solar spectrum (see Section 10.2). The linear enhancement of j_{sc} as a function of C₇₀ content confirms that no significant increase of recombination losses occurs in the co-evaporated fullerene acceptor phases over the entire composition range under study. This outcome is corroborated by the results obtained for the fill factor. Consistently high values between 53% and 60% are obtained for this quantity, as illustrated in Figure 10.6. The slight variation of the fill factor as a function of the fullerene composition ratio is attributed to a change in the series resistance (see Table 10.1). The series resistance of a solar cell is determined under open circuit conditions and the parallel resistance under short circuit conditions. The series resistance of organic photovoltaic

cells is a complex quantity and factors determining R_s were discussed in more detail in Section 9.1. In this study, the change of the series resistance for the different solar cell configurations is mainly associated with the utilization of the PEDOT:PSS hole transport layer. The work function of PEDOT:PSS is very sensitive to the residual water content and with it, to the exact preparation conditions (see Section 4.2). Since the hydrophilic PEDOT:PSS layer is spin-cast under ambient conditions, the residual water content may vary. Therefore, a certain variation of the hole injection barrier at the PEDOT:PSS/DIP interface is considered to affect the series resistance of the solar cells and thereby, the fill factor. [115] As illustrated in Table 10.1 the parallel resistance of all DIP/C₆₀:C₇₀ photovoltaic devices is conformably high, reflecting the similar morphology for the different fullerene composition ratios, as evinced in Section 10.2.

solar cell configuration	FF [%]	R_s [Ωcm^2]	R_p [Ωcm^2]
DIP/C ₆₀	56	36	1200
DIP/C ₆₀ :C ₇₀ (3:1)	55	50	1300
DIP/C ₆₀ :C ₇₀ (1:1)	60	24	1300
DIP/C ₆₀ :C ₇₀ (1:3)	57	36	1100
DIP/C ₇₀	52	49	1000
DIP/raw fullerene	49	168	2000

Table 10.1.: Fill factors FF , series and parallel resistances, R_s and R_p of DIP/C₆₀:C₇₀ and DIP/raw fullerene solar cells.

As discussed in detail in Section 7.5, the open-circuit voltage is associated with the energy difference between the quasi Fermi-level splitting of the donor and acceptor material upon photo-doping. [97] Frontier energy levels of C₆₀ and C₇₀ are reported to be very similar hence, the almost unaffected V_{oc} values are in good agreement with this model and with literature. [97, 175, 227]

The increase of the power conversion efficiency as a function of C₇₀ content in the mixed fullerene phase originates primarily from the enhanced short circuit current density. For neat bilayer solar cells based on DIP/C₇₀, the power conversion efficiency is increased to 2.4 % in comparison to 1.3 % for DIP/C₆₀ bilayer cells.

For the chosen ratios of C₆₀:C₇₀ fullerene composition, the formation of bi-continuous interpenetrating networks composed of the two fullerenes between the D/A interface and the top-electrode cannot be fully excluded. Such bi-continuous interpenetrating networks are schematically indicated by the green and red line for the DIP/C₆₀:C₇₀ (1:1) solar cell in Figure 10.7. In order to analyze possible effects by such a structure, a different device design was compared. Instead of a stochastically grown fullerene acceptor phase formed upon co-evaporation of both constituents, an alternating stacked architecture was intentionally prepared by subsequently depositing neat fullerene layers on top of each other. The device designs are also shown in Figure 10.7. According to the thin film structural studies in Section 10.2, by this approach an interpenetrating network reaching from the D/A heterointerface to the Ag-electrode can be suppressed, allowing for an evaluation of the electronic transport compatibility of both fullerenes at room temperature. For the stacked architecture, the neat fullerene layer thicknesses were adjusted to 17.5

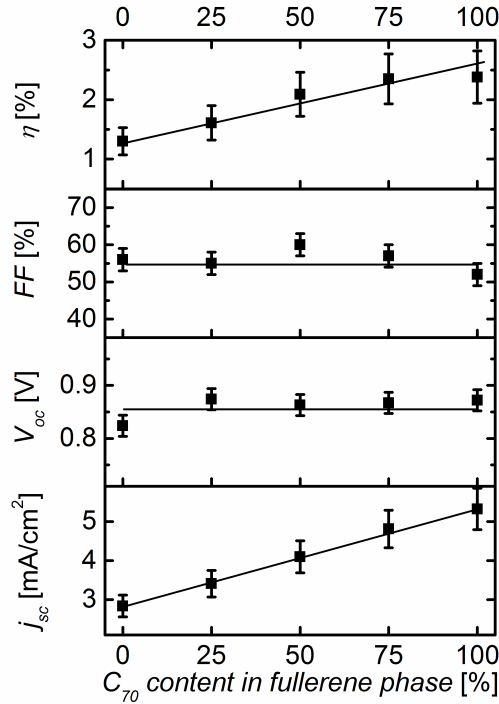


Figure 10.6.: Solar cell parameters of DIP/ C_{60} : C_{70} photovoltaic bilayer devices as function of the relative C_{70} fullerene content in the acceptor phase. Solid lines represent guides to the eye.

nm each, thus resembling the total fullerene layer thickness in the stochastically processed reference solar cells. Both potential layouts DIP/ C_{60} / C_{70} and DIP/ C_{70} / C_{60} were evaluated and compared to DIP/ C_{60} : C_{70} cells. The corresponding $j(V)$ characteristics are displayed in Figure 10.7. Apparently, for the different device architectures, no significant discrepancy in the photovoltaic parameters is observed. This finding illustrates and confirms the experimental proof of general electronic and excitonic compatibility of C_{60} and C_{70} at room temperature. Solely a minor difference in the $j(V)$ characteristics is observed around V_{oc} , yielding increased series resistances in case of the stacked layer designs ($R_s = 67 \Omega\text{cm}^2$ for DIP/ C_{60} / C_{70} and $R_s = 42 \Omega\text{cm}^2$ for DIP/ C_{70} / C_{60}) in comparison to the stochastically processed reference solar cells ($R_s = 24 \Omega\text{cm}^2$). This increase in R_s may be associated with the possible variation of the hole injection barrier at the PEDOT:PSS/DIP interface due to the sensitivity of the polymeric hole conduction layer on the processing conditions (*vide supra*), but may also indicate a slightly deteriorated transport across the fullerene/fullerene interface.

Finally, as shown in Figure 10.5, for DIP/raw fullerene photovoltaic devices all solar cell parameters are distinctly reduced in comparison to solar cells comprised of purified fullerenes C_{60} and C_{70} . The short circuit current density is significantly diminished by 60 % to 1.2 mA/cm² in comparison to neat DIP/ C_{60} bilayer devices despite the fact, that the overall absorption is increased in DIP/raw fullerene heterostructures (see Section 10.2). In the $j(V)$ curve a pronounced S-shape around V_{oc} occurs, resulting in a high series resistance of 168 Ωcm^2 and a fill factor

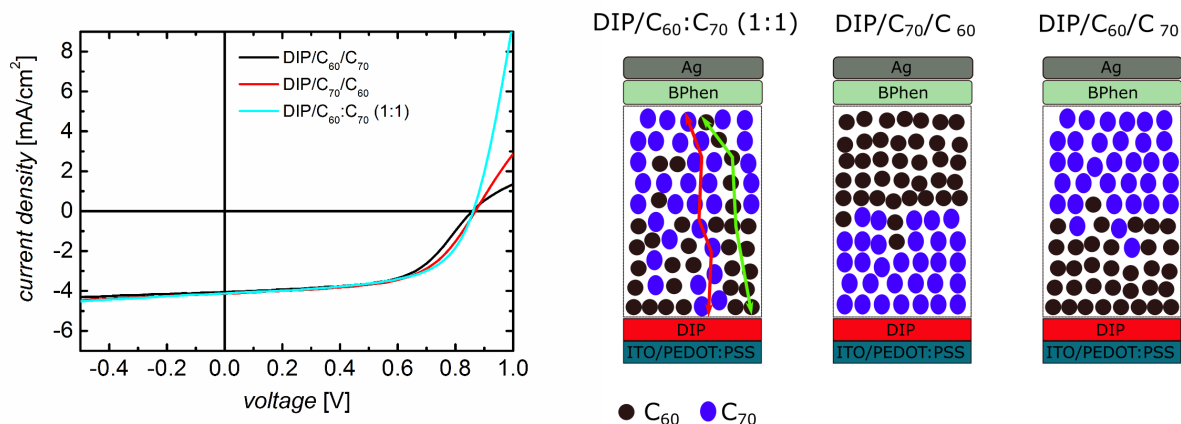


Figure 10.7.: $j(V)$ characteristics of deterministically stacked and stochastically co-evaporated photovoltaic devices. The corresponding device architectures are displayed on the right. The red and green line in the DIP/C₆₀:C₇₀ (1:1) structure indicate a possible path in the interpenetrating network between the D/A interface and the top-electrode composed of either fullerene. By employing a stacked architecture, the formation of such interpenetrating networks is prevented.

of only 49 %. These findings are in good agreement with the *EQE* data and clearly indicate, that transport of photo-generated excitons is hindered in those photovoltaic devices. Besides, V_{oc} is decreased to 0.66 V, indicating the increased recombination due to the enhanced exciton trapping.

Conclusion

In order to evaluate the need for highly purified fullerenes in organic photovoltaics, the impact of a varying mixing ratio of co-evaporated fullerenes on the photo-physical characteristics of DIP/C₆₀:C₇₀ photovoltaic cells was analyzed. A linear increase of j_{sc} as a function of C₇₀ content was attributed to the enhanced absorption of the latter, yielding a short circuit current density of 5.2 mA/cm² for DIP/C₇₀ bilayer cells. This enhancement with respect to DIP/C₆₀ solar cells was in almost perfect agreement with the anticipated photocurrent increase by weighting the absorption coefficients with the layer thickness of the photo-active materials and the solar spectrum. The linear increase of j_{sc} upon increasing C₇₀ content over the entire composition range, together with the observation of an almost unaffected fill factor, gave evidence for compatible electronic transport properties of both acceptor constituents under standard illumination conditions at room temperature. Aiming to verify this hypothesis, a different solar cell architecture was applied by evaporating both fullerenes on top of each other. The trilayer configurations DIP/C₆₀/C₇₀ and DIP/C₇₀/C₆₀ were tested with respect to their photovoltaic behavior. As no significant variations of the photovoltaic properties were detectable in comparison to DIP/C₆₀:C₇₀ solar cells, the latter being comprised of a stochastically mixed fullerene blend, these results give evidence for the excitonic and electronic compatibility of both fullerenes at

room temperature. Therefore, the utilization of highly purified C₆₀ might be reconsidered since prevalent synthesis procedures yield C₇₀ as the most abundant impurity in C₆₀. Instead, from an economical point of view, C₆₀ and C₇₀ fullerene mixtures should be used containing a high content of the latter but only a minor amount of higher order fullerenes. Solar cells based on DIP/raw fullerenes showed a distinctly deteriorated device performance, which was assigned in particular, to increased exciton recombination losses. These losses are associated with energetic trap states, introduced by traces of the higher order fullerenes in the raw blends. Therefore, the exclusion of such higher mass fullerenes by suitable refinement techniques remains imperative for potential high performance opto-electronic device applications.

11. Summary

It was the scope of this work to gain a deeper understanding of the correlation between interface energetics of molecular semiconductors in planar organic solar cells and the corresponding optoelectronic characteristics. For this aim, different approaches were followed. At first, a direct variation of donor/acceptor (D/A) interface energetics of bilayer cells was achieved by utilizing systematically modified donor compounds. This change could be correlated to the macroscopic device performance. At second, the impact of interface energetics was illustrated, employing a more extended device architecture. By introducing a thin interlayer between a planar D/A heterojunction, an energetic staircase was established. Exciton dissociation in such devices could be linked to the cascade energy level alignment of the photo-active materials. Finally, two different fullerene molecules C_{60} and C_{70} were employed in co-evaporated acceptor phases. The expected discrepancy in their electronic structure was related to the transport properties of the corresponding organic photovoltaic cells (OPVCs). The fullerenes are created simultaneously in common synthesis procedures. Next to the photo-physical relevance, the study was carried-out to judge on the necessity of separating the components from each other by purification which constitutes the cost-determining step in the total production costs. This Chapter summarizes the key results of this thesis.

Impact of Gradual Fluorination on the Properties of $F_n\text{ZnPc}/C_{60}$ Bilayer OPVCs

The energy differences between the frontier orbitals of donor and acceptor materials drive the separation of photo-generated excitons into free charge carriers. Moreover, the energy difference between the highest occupied molecular orbital (HOMO) of the donor and the lowest unoccupied molecular orbital (LUMO) of the acceptor is associated with the open circuit voltage V_{oc} . To gain detailed insight into these correlations, tailoring of energy levels by chemical modification of one of the photo-active materials provides a potential approach. Following this strategy, the effect of successive fluorination on the photo-physical properties of fluorinated zinc phthalocyanine $F_n\text{ZnPc}$ thin films and $F_n\text{ZnPc}/C_{60}$ ($n = 0, 4, 8, 16$) planar bilayer solar cells was analyzed. [175]

As was confirmed by ultraviolet photoelectron spectroscopy (UPS) measurements, frontier orbital energies are successively shifted towards lower energies upon increasing fluorination. The HOMO energy of the perfluorinated homologue $F_{16}\text{ZnPc}$ is lowered by 1.7 eV with respect to the

vacuum level in comparison to ZnPc. Complex electronic effects were observed upon deposition of the C₆₀ phase. For heterostructures based on ZnPc/C₆₀ and F₄ZnPc/C₆₀ Fermi-level pinning of the C₆₀ LUMO was evinced and concomitantly, the formation of an effective interface dipole of 0.6 eV in case of ZnPc/C₆₀ bilayers was ascertained by a shift of the secondary electron cut-off. Hence, the assumption of a vacuum level matching at such organic heterojunctions is not generally valid. This means, a combination of energy levels from literature can only be considered as a rough estimate, requiring detailed PES measurements for a comprehensive understanding of the actual electronic structure of D/A interfaces. Importantly, the existence or absence of Fermi-level pinning has crucial effects on the D/A interface energetics and thus, on the solar cell parameters and on the performance.

Comparison of external quantum efficiency (*EQE*) data revealed that in case of F₈ZnPc/C₆₀ the energetic offsets at the D/A interface are just in the range of the exciton binding energies therefore, causing a distinct limitation of exciton dissociation into free charge carriers. In contrast, efficient exciton dissociation could be demonstrated for ZnPc/C₆₀ and F₄ZnPc/C₆₀. In those bilayer cells, the relevant energetic offsets between the HOMO energies ΔE_{HOMO} and between the LUMO energies ΔE_{LUMO} at the D/A interface exceed the required exciton binding energies. For the solar cell based on F₁₆ZnPc/C₆₀ no energetic driving force for exciton splitting was discernable. Consistently, spectrally resolved PL measurements showed that the F₁₆ZnPc/C₆₀ interface is photo-inactive. Instead of exciton separation into free charge carriers, C₆₀ excitons are transferred to the phthalocyanine layer by a Förster resonant energy transfer. Nevertheless, a small but distinct photovoltaic response of both absorber materials could experimentally be confirmed by the *EQE* measurements. Therefore, a fundamentally different working mechanism was proposed, assuming excitons to be dissociated at the MoO₃/F₁₆ZnPc interface. [193] Moreover, the fullerene contribution to the photocurrent is substantially affected by a second exciton dissociation mechanism which was thoroughly investigated in the course of the transient absorption spectroscopy measurements (see below).

In comparison to ZnPc/C₆₀ reference cells, the $j(V)$ characterization yielded an increase of the open circuit voltage V_{oc} for F₄ZnPc and F₈ZnPc based devices by 30 % and 50 %, respectively. This increase was assigned to an increased effective band gap $E_{g,eff}$ and hence, to an enhanced quasi Fermi-level splitting at the D/A interface. [97, 100] The loss factor represents the energy difference between $E_{g,eff}$ and $e \cdot V_{oc}$. For F₈ZnPc/C₆₀ bilayer cells a loss factor of 0.8 eV was found, which is twice as high as for ZnPc/C₆₀ and F₄ZnPc/C₆₀ based devices. This observation was attributed to enhanced recombination taking place as a consequence of the insufficient energetic offsets at the F₈ZnPc/C₆₀ interface and counteracting exciton dissociation into free charge carriers. Finally, for F₁₆ZnPc/C₆₀ solar cells a V_{oc} of 0.41 V was obtained. In case of solar cells comprising such a photo-inactive interface, the work function difference of the electrodes is proven to determine V_{oc} .

Correlating D/A Interface Energetics of $F_n\text{ZnPc}/\text{C}_{60}$ with Electronic Dynamics

After correlating D/A interface energetics to macroscopic device characteristics of $F_n\text{ZnPc}/\text{C}_{60}$ ($n = 0, 4, 8, 16$) bilayer solar cells, the static picture was complemented by involving electronic dynamics, accessed via ultrafast transient absorption spectroscopy (TAS). Upon excitation of the fullerene phase at a pump wavelength of 480 nm, broad excited state absorption (ESA) bands centered at 1050 nm were detected for $F_n\text{ZnPc}/\text{C}_{60}$ heterostructures and a C_{60} reference thin film, which could be assigned to C_{60}^- anions. For all samples, dissociation of excitons into free charge carriers was proven to occur on an ultrafast time scale within 150 fs.

A discernable impact of D/A interface energetics on the amplitude of the excited state absorption signal was confirmed yielding a higher population of electrons in the C_{60} phase in case that ΔE_{HOMO} exceeds the exciton binding energy $E_{bind\text{C}_{60}}$. Accordingly, these changes were in particular attributed to reduced recombination of C_{60} excitons. These findings qualitatively concur with the fullerene contribution in the *EQE* data of the bilayer solar cells. Autoionization and subsequent dissociation of CT excitons into free charge carriers were demonstrated to contribute to these ESA signals. The charge generation process intrinsic to the fullerene is expected to take place throughout the C_{60} layer in all samples. Comparison of the ESA signals of the plain C_{60} reference thin film and the $F_8\text{ZnPc}/\text{C}_{60}$ and the $F_{16}\text{ZnPc}/\text{C}_{60}$ heterojunctions revealed, that this charge carrier generation mechanism predominantly determines the fullerene *EQE* contribution in the corresponding bilayer cells. Assuming a similar autoionization contribution to the *EQE* in all bilayer devices enables to judge on the additional impact on the photocurrent generation by the respective exciton dissociating D/A heterojunction. Accordingly, for $\text{ZnPc}/\text{C}_{60}$ ($F_4\text{ZnPc}/\text{C}_{60}$) bilayer solar cells, approximately 60 % (75 %) of the generated photocurrent is caused by charge carrier generation at the D/A interface and 40 % (25 %) originates by exciton splitting within the fullerene phase as a consequence of autoionization.

Importantly, subsequent to exciton dissociation into free charge carriers, recombination dynamics are unaffected by the D/A interface energetics on the investigated time scale of up to 500 ps, illustrating that non-geminate recombination at the D/A interface is not the dominant process which limits the device performance. Instead, recombination of free charge carriers is presumed to occur uniformly throughout the acceptor layer. ESA decay dynamics could be fitted by a biexponential function with the related time constants $\tau_1 = 3.8 \pm 0.5$ ps and $\tau_2 = 37 \pm 10$ ps. According to a first rough estimation of the charge carrier diffusion lengths, the former decay constant can be tentatively attributed to recombination at homogeneously distributed electronic trap states within the band gap of C_{60} , whereas the latter is assigned to recombination at the C_{60} /air boundary.

Energy Cascades as a New Concept to Improve Charge Carrier Generation in OPV

Next to affecting D/A interface energetics directly by chemical modification of an absorber material, aiming for manipulating quasi Fermi-level splitting and exciton dissociation alike, another conceptual approach was evaluated in this thesis, highlighting the crucial role of energy level alignment for the opto-electronic characteristics of organic photovoltaic cells. By the insertion of thin interfacial layers between planar donor/acceptor heterointerfaces, energetic cascades were established. For that purpose energy levels of the interfacial layers are required to be intermediate to those of the donor and acceptor material. As a result, such energetic staircases are associated with improved exciton dissociation into free charge carriers. This generic concept was illustrated by two different trilayer material combinations.

Low molecular weight diketopyrrolopyrroles (D1 - D3) were intentionally synthesized, differing in the electron deficiency of their terminal aryl units. As a consequence, a defined variation of their frontier orbital energies was achieved, i.e. energy levels are shifted by 160 meV towards lower energies for D3 with respect to D1. Taking advantage of the energy level variation, these materials were employed in combination with the acceptor C_{60} in cascade OPVCs. Establishing cascade energy level alignment by utilizing a donor compound and a suitable derivative thereof was reported for the first time. [136] By introducing a sub-monolayer of D3 at the D1/ C_{60} interface, an increase of the short-circuit current density j_{sc} by 80 % to 2.5 mA/cm² could be achieved with respect to plain D1/ C_{60} bilayer cells. *EQE* measurements disclosed that this enhancement is associated with an increase, in particular, of the fullerene photocurrent contribution. After photo-generation of excitons in C_{60} , these excitons can diffuse to the D3/ C_{60} interface to form bound CT states. Due to the particular energy level alignment, the adjacent D1 interface is assumed to destabilize these CT states and thereby, facilitate the generation of free charge carriers. Moreover, the improved dissociation mechanism may be supported by delocalization of the holes via a wave function spread-out across the D1/D3 interface into the D1 donor phase. For thicker interfacial layers, the gain in j_{sc} decreased. In case the interlayer was comprised of several monolayers, the second interface can be considered separated on molecular length scales. Hence, the energetic staircase is limited in facilitating exciton dissociation.

The concept of energy cascades was also applied to the high performance material combination DBP/ C_{70} . Due to the feasibility of tailoring energy levels by gradual fluorination of zinc phthalocyanine (*vide supra*), an energetic staircase could be implemented by the choice of F_8ZnPc as interlayer material. [175] As a consequence of employing a sub-monolayer of the fluorinated zinc phthalocyanine in DBP/ F_8ZnPc / C_{70} cascade cells, solar cell parameters were distinctly improved. The best results were obtained for an intermediate layer thickness of 5 Å, yielding a power conversion efficiency of 3.7 % compared to 2.2 % for the reference DBP/ C_{70} bilayer cell. Concerning organic cascade cells with thin interfacial dissociation layers, this outcome is among the best results reported in literature. [92, 93]

These results demonstrate the crucial role of interface energetics at organic/organic heterointerfaces for OPVCs. Next to scientific relevance, these findings are also of great significance with respect to technical applications. By implementing a single additional processing step, recombination losses can be specifically targeted in planar heterojunction OPVCs, thus improving their overall performance.

Excitonic and Electronic Compatibility of Mixed C₆₀:C₇₀ Acceptor Layers

In standard fullerene synthesis procedures, C₆₀ and C₇₀ are generated simultaneously at a 3:1 ratio including additionally 1 - 3 % of higher mass fullerenes in raw blends. The total material costs of the individual compounds are determined by the subsequent purification steps, i.e. by the separation of the constituents from each other. Since energy levels of both, C₆₀ and C₇₀ are reported almost identical, the necessity of purification from a cost-efficient point of view was under investigation. [18]

To this end, the effect of a varying C₆₀:C₇₀ acceptor mixing ratio on the performance of DIP/C₆₀:C₇₀ planar organic solar cells was analyzed. Device parameters, such as V_{oc} and FF , remained almost constant as a function of the C₇₀ content in co-evaporated fullerene phases. In contrast, the $j(V)$ characteristics showed a linear increase of j_{sc} , which was attributed to the higher absorption of C₇₀ in comparison to C₆₀. The presence of a Förster-type transfer allows for efficient energy transport between both fullerene components within C₆₀:C₇₀ blends at room temperature, as was confirmed by complementary spectrally resolved PL measurements.

Aiming to exclude the occurrence of interlaced C₆₀ and C₇₀ networks bridging donor material and the cathode in cells comprising a blended fullerene acceptor phase, a stacked acceptor C₆₀/C₇₀ design of identical thickness was chosen. Comparison of solar cell characteristics showed no significant discrepancy for the different device architectures, giving experimental proof for the excitonic and electronic compatibility of both fullerene compounds at room temperature.

Owing to the different sublimation temperatures related to their respective molecular masses, purification of fullerenes by e. g. gradient sublimation yields C₇₀ as the most abundant “impurity” of C₆₀. Hence, in terms of cost considerations, instead of highly purified C₆₀ acceptor layers, a C₆₀:C₇₀ fullerene mixture ought to be targeted. Concerning device performance this mixture should be comprised of a high content of the latter, because of its superior absorption. Additionally, DIP/raw fullerene solar cells were tested for the purpose of specifying the effect of higher order fullerenes on the device performance. All solar cell parameters were significantly reduced in these devices, which was attributed to increased excitonic recombination losses due to trap states introduced by the higher mass fullerenes within the blend. Accordingly, an exclusion of these higher mass fullerenes is still imperative for high performance applications of C₆₀ and C₇₀ in organic electronics.

Final Remarks

In this thesis the impact of interface energetics in planar organic solar cells on the corresponding opto-electronic device characteristics was under investigation. Versatile possibilities, in particular the use of energetically tailored donor molecules or the implementation of energetic staircases by introducing thin interfacial layers between the respective D/A heterostructure were demonstrated aiming to systematically change the interface energetics and thus, the performance of the functional units. Fundamental processes such as the quasi Fermi-level splitting at the D/A interface, the dissociation of CT excitons into free charge carriers and their associated recombination dynamics could be correlated with the frontier orbital energies at the D/A junction. Thereby, these studies provide a deeper understanding of complex photo-physical effects occurring on microscopic length scales and allow further optimization of opto-electronic devices based on small molecule semiconductors.

12. Zusammenfassung

Es war das Ziel dieser Arbeit, ein tieferes Verständnis der Beziehung zwischen der Energetik molekularer Halbleitergrenzflächen in planaren, organischen Solarzellen und den daraus resultierenden opto-elektronischen Bauteileigenschaften zu gewinnen. Zu diesem Zweck wurden verschiedene Ansätze verfolgt. Zum einen wurde eine Veränderung der Donator/Akzeptor (D/A) Grenzflächenenergetik in Bilagen-Solarzellen durch die Verwendung verschieden fluorierter Donatorverbindungen erreicht. Zum anderen wurde der Einfluss der Grenzflächenenergetik auf die photo-physikalischen Prozesse anhand einer geänderten Bauteilarchitektur aufgezeigt. Durch das Einbringen einer dünnen Schicht an der D/A Heterogrenzfläche wurde eine energetische Kaskade realisiert. In diesen Solarzellen konnte die Exzitonendissoziation mit der Anpassung der Kaskaden-Energieniveaus der molekularen Halbleiter in Verbindung gebracht werden. Abschließend wurden zwei unterschiedliche Fullerenmoleküle in ko-verdampften Akzeptorphasen eingesetzt. Der vermeintliche Unterschied in ihrer elektronischen Struktur wurde anhand der Transporteigenschaften der organischen photovoltaischen Zellen analysiert. In herkömmlichen Syntheseansätzen werden die beiden Fullerene gleichzeitig gebildet. Neben der photo-physikalischen Relevanz wurde die Studie durchgeführt, um die Notwendigkeit einer Trennung der beiden Verbindungen für das Leistungsverhalten opto-elektronischer Bauteile zu beurteilen, da dieser Aufreinigungsschritt der Kosten-bestimmende Prozess bei den gesamten Materialkosten darstellt. Dieses Kapitel fasst die wichtigsten Resultate dieser Arbeit zusammen.

Der Einfluss sukzessiver Fluorierung auf die Eigenschaften von $F_n\text{ZnPc}/\text{C}_{60}$ Bilagen-Solarzellen

Die Energiedifferenz der jeweiligen Molekülorbitale an der D/A Grenzfläche organischer photovoltaischer Zellen (OPVZs) ermöglicht die Dissoziation der Exzitonen in freie Ladungsträger. Zudem wird die Energiedifferenz zwischen dem höchsten besetzten Molekülorbital (Englisch: *highest occupied molecular orbital*, HOMO) des Donators und dem niedrigsten unbesetzten Molekülorbital (Englisch: *lowest unoccupied molecular orbital*, LUMO) des Akzeptors mit der offenen Klemmspannung (Englisch: *open circuit voltage*, V_{oc}) in Verbindung gebracht. Um Einsicht in diese Beziehungen zu erlangen, ist die gezielte Beeinflussung der Energieniveaus mittels chemischer Modifikation eines der molekularen Halbleitermaterialien eine vielversprechende Strategie. Diesem Ansatz folgend wurde der Einfluss einer sukzessiven Fluorierung auf die photo-

physikalischen Eigenschaften von $F_n\text{ZnPc}$ Dünnschichten und $F_n\text{ZnPc}/\text{C}_{60}$ ($n = 0, 4, 8, 16$) Bilagen-Solarzellen untersucht.

Wie mittels Ultraviolettphotoelektronenspektroskopie-Messungen (UPS) gezeigt werden konnte, werden infolge zunehmender Fluorierung die Molekülorbitale stufenweise zu niedrigeren Energien verschoben. Im Vergleich zu ZnPc ist das HOMO des perfluorierten Phthalocyanins $F_{16}\text{ZnPc}$ mit Referenz zum Vakuumniveau um 1,7 eV zu niedrigeren Energien verschoben. Bei anschließender Abscheidung der C_{60} Phase wurden komplexe elektronische Effekte beobachtet. So konnte für die Heterostrukturen, basierend auf $\text{ZnPc}/\text{C}_{60}$ und $F_4\text{ZnPc}/\text{C}_{60}$, ein Fermi-Niveau Pinning des C_{60} LUMOs nachgewiesen werden. Gleichzeitig wurde die Ausbildung eines effektiven Grenzflächen-dipols im Fall von $\text{ZnPc}/\text{C}_{60}$ beobachtet, der anhand der Verschiebung der Sekundärelektronen-Kante zu 0,6 eV bestimmt werden konnte. Daher ist die Annahme eines gemeinsamen, energetisch angepassten Vakuumniveaus an derartigen Organik/Organik-Grenzflächen im Allgemeinen nicht gerechtfertigt. Dies wiederum bedeutet, dass eine Kombination von Energieniveaus verschiedener Materialien nach ihren jeweiligen Literaturwerten nur eine grobe Abschätzung darstellen kann. Für eine tatsächliche Erfassung der elektronischen Struktur am D/A Übergang sind daher Photoelektronenspektroskopie-Studien unabdingbar. Die Existenz beziehungsweise das Ausbleiben des Fermi-Niveau Pinnings haben maßgeblichen Einfluss auf die Grenzflächenenergetik und damit auf die Leistungsdaten der entsprechenden Solarzellen.

Im Fall der $F_8\text{ZnPc}/\text{C}_{60}$ Solarzelle liegen die energetischen Abstände der jeweiligen HOMO und LUMO Energien im Bereich der Exzitonenbindungsenergien. Dies hat zur Folge, dass die Exzitonendissoziation in freie Ladungsträger limitiert ist, wie in den entsprechenden Messungen der externen Quanteneffizienz (EQE) gezeigt werden konnte. Im Gegensatz dazu, konnte eine effiziente Trennung der Exzitonen für die Solarzellen auf Basis von $\text{ZnPc}/\text{C}_{60}$ und $F_4\text{ZnPc}/\text{C}_{60}$ nachgewiesen werden. In diesen Bilagen-Zellen übersteigen die relevanten energetischen Abstände zwischen den HOMO Niveaus ΔE_{HOMO} und den LUMO Niveaus ΔE_{LUMO} an der D/A Grenzfläche die jeweiligen Exzitonenbindungsenergien. Für die Solarzelle auf Basis von $F_{16}\text{ZnPc}/\text{C}_{60}$ ist keine energetische Triebkraft für die Trennung der photo-generierten Exzitonen vorhanden. Spektral aufgelöste Photolumineszenz (PL) Messungen haben gezeigt, dass die $F_{16}\text{ZnPc}/\text{C}_{60}$ Grenzfläche photo-inaktiv ist, das heißt, dass eine Exzitonendissoziation in freie Ladungsträger an dieser Grenzfläche nicht stattfindet. Nichtsdestotrotz konnte in den EQE Messungen eine schwache, aber dennoch nachweisbare photovoltaische Antwort detektiert werden. Daher wurde eine grundlegend verschiedene Funktionsweise dieser Solarzelle vorgeschlagen. Exzitonen, die in C_{60} generiert werden, können über einen Förster-Resonanzenergietransfer auf die $F_{16}\text{ZnPc}$ -Schicht übertragen werden. Im Anschluss daran ist aufgrund der beteiligten Energieniveaus eine Trennung dieser Exzitonen an der $\text{MoO}_3/\text{F}_{16}\text{ZnPc}$ Grenzfläche möglich. [193] Außerdem wird der Beitrag des Fullerenes zum Photostrom durch einen zweiten Mechanismus beeinflusst, wie im Zuge der transienten Absorptionsmessungen (siehe unten) gezeigt werden konnte.

Im Vergleich zu den $\text{ZnPc}/\text{C}_{60}$ Referenzsolarzellen ergab die $j(V)$ -Charakterisierung der $F_4\text{ZnPc}/\text{C}_{60}$ und $F_8\text{ZnPc}/\text{C}_{60}$ basierten Zellen eine Zunahme der offenen Klemmspannung um

30 % beziehungsweise 50 %. Diese Erhöhung wurde der größeren effektiven Bandlücke $E_{g,eff}$ zugeschrieben und damit einer Vergrößerung der quasi-Fermi-Niveau Aufspaltung an der D/A Grenzfläche. Die Verlustenergie, die sich aus der Differenz zwischen $E_{g,eff}$ und $e \cdot V_{oc}$ ergibt, wurde für die F_8ZnPc/C_{60} Bilagen-Zellen zu 0,8 eV ermittelt. Damit übersteigt diese jene der Solarzellen auf Basis von $ZnPc/C_{60}$ und F_4ZnPc/C_{60} um einen Faktor zwei. Dieses Ergebnis wurde erhöhten Rekombinationsverlusten zugesprochen, die infolge der unzureichenden energetischen Triebkraft an der D/A Grenzfläche entstehen. Für Solarzellen auf der Basis von $F_{16}ZnPc/C_{60}$ wurde eine offene Klemmspannung von 0,41 V ermittelt. In diesem Fall wird V_{oc} durch den Unterschied der Austrittsarbeiten der beiden Elektroden bestimmt.

Korrelation zwischen der D/A Grenzflächenenergetik und der elektronischen Dynamik

Nach der Betrachtung der makroskopischen Bauteileigenschaften von F_nZnPc/C_{60} ($n = 0, 4, 8, 16$) Bilagen-Solarzellen im Gleichgewichtszustand wurde das stationäre Bild durch dynamisch ablaufende elektronische Prozesse erweitert. Zugang zu diesen Prozessen wurde mittels der ultraschnellen transienten Absorptionsspektroskopie (TAS) erlangt. Infolge der Photo-Anregung der Fullerenphase mit einer Wellenlänge von 480 nm konnten breite Absorptionsbanden der angeregten Zustände (Englisch: *excited state absorption*, ESA) im Bereich von 1050 nm für alle F_nZnPc/C_{60} Heterostrukturen und eine C_{60} Referenz-Dünnschicht nachgewiesen werden. Diese Absorptionsbanden angeregter Zustände konnten C_{60}^- Anionen zugeordnet werden. Dabei findet die Dissoziation der Exzitonen in freie Ladungsträger auf einer ultraschnellen Zeitskala innerhalb von 150 fs statt.

Es konnte ein deutlicher Einfluss der D/A Grenzflächenenergetik auf die Amplitude des jeweiligen ESA Signals nachgewiesen werden. Für den Fall, dass ΔE_{HOMO} die Exzitonenbindungsenergie der C_{60} Exzitonen $E_{BindC_{60}}$ übersteigt, war eine größere Anzahl freier Elektronen in der C_{60} Lage festzustellen. Diese Resultate stimmen qualitativ mit dem Beitrag der Fullerenphase der jeweiligen Solarzellen in den *EQE* Messungen überein. Es konnte gezeigt werden, dass die Autoionisation und anschließende Dissoziation der Ladungstransfer (Englisch: *charge transfer*, CT) Exzitonen in freie Ladungsträger zur Ausbildung der ESA Signale beitragen. Dieser intrinsische Ladungsträgergenerationsprozess findet in allen Proben unabhängig von der Gegenwart eines trennenden D/A Heteroübergangs statt. Der Vergleich der ESA Signale der reinen C_{60} Dünnschicht mit denen der F_8ZnPc/C_{60} und der $F_{16}ZnPc/C_{60}$ Heterostrukturen verdeutlichte, dass dieser Ladungsträgergenerationsprozess den dominanten Beitrag der Fullerenphase zur *EQE* in den entsprechenden Bilagen-Solarzellen liefert. Unter der Annahme, dass die Ladungsträgergeneration infolge von Autoionisation in allen Bilagen-Solarzellen ähnlich stark ausgeprägt ist, kann der zusätzliche Beitrag durch die Exzitonen-trennenden D/A Heteroübergänge auf die *EQE* bei einer exemplarischen Wellenlänge von 480 nm abgeschätzt werden. Im Fall von $ZnPc/C_{60}$ (F_4ZnPc/C_{60}) Bilagen-Solarzellen werden etwa 60 % (75 %) des Photostroms durch

Ladungsträgergeneration am D/A Heteroübergang erzeugt und 40 % (25%) entstehen durch Exzitonentrennung als Folge von Autoionisation innerhalb der C₆₀ Schicht.

Im Anschluss an die Exzitonendissoziation in freie Ladungsträger ist die Rekombinationsdynamik für alle Proben auf der untersuchten Zeitskala von bis zu 500 ps unbeeinflusst von der D/A Grenzflächenenergetik. Dies verdeutlicht, dass nicht-geminale Rekombination an der D/A Grenzfläche nicht der limitierende Faktor für die Leistungsfähigkeit der untersuchten Heterostrukturen ist. Stattdessen ist davon auszugehen, dass die Rekombination freier Ladungsträger gleichmäßig über die Fullerschicht verteilt stattfindet. Die Dynamik des ESA Signals konnte mit einer biexponentiellen Funktion gefittet werden. Die zugehörigen Zeitkonstanten betragen $\tau_1 = 3.8 \pm 0,5$ ps und $\tau_2 = 37 \pm 10$ ps. Unter Berücksichtigung der damit einhergehenden Diffusionslängen konnte die τ_1 -Komponente Rekombinationsverlusten zugeordnet werden, die infolge elektronischer Fallenzuständen in der Bandlücke von C₆₀ vorliegen, entstehen. Die Zeitkonstante τ_2 hingegen wurde Verlustprozessen an der Grenzfläche C₆₀/Luft zugeschrieben.

Energie-Kaskaden als Konzept zur Verbesserung der Ladungsträgergeneration in OPVz

Neben dem Ansatz, die D/A Grenzflächenenergetik durch chemische Modifikation eines der Absorbermaterialien zu verändern, um sowohl die quasi-Fermi-Niveau Aufspaltung als auch die Exzitonendissoziation in freie Ladungsträger gezielt zu beeinflussen, wurde eine weitere konzeptionelle Vorgehensweise verfolgt, welche die entscheidende Rolle der Energieniveaulagen an der D/A Grenzfläche für die opto-elektronischen Eigenschaften organischer Solarzellen verdeutlicht. Durch das Einbringen einer Monolagen dicken Schicht zwischen der D/A Grenzfläche wurden so genannte Energie-Kaskaden erzeugt. Entscheidend für die Ausbildung einer solchen Energie-Kaskade ist, dass die Energieniveaus der Zwischenschicht zwischen jenen des Donators und des Akzeptors liegen. Im Vergleich zu Bilagen-Solarzellen werden Kaskadenzellen mit einer höheren Konzentration an Ladungsträgern infolge einer verbesserten Exzitonendissoziation in Verbindung gebracht. Dieses allgemeine Konzept wurde anhand zweier Materialkombinationen untersucht.

Diketopyrrolopyrrol-Pigmente (D1 - D3) mit geringer molekularer Masse wurden derart synthetisiert, dass sie sich in der Elektronenverteilung ihrer äußeren Arylgruppe unterscheiden. Infolgedessen konnte eine definierte Veränderung der Energieniveaus erreicht werden. So wurden im Vergleich zu D1 das HOMO und LUMO Niveau für D3 um 160 meV zu niedrigeren Energien verschoben. Die Abstufung der energetischen Positionen der Energieniveaus ausnutzend, wurden diese Diketopyrrolopyrrol-Pigmente in Kombination mit dem Elektronenakzeptor C₆₀ in Kaskadensolarzellen verwendet. Erstmals wurde in dieser Studie eine Energie-Kaskade realisiert, indem ein Donatormaterial und dessen Derivat verwendet wurden. [136] Im Vergleich zu D1/C₆₀ Referenzsolarzellen konnte durch das Einbringen einer Sub-Monolage aus D3 zwischen

die D1/C₆₀ Grenzfläche die Kurzschlussstromdichte (Englisch: *short circuit current density, j_{sc}*) um 80 % auf 2,5 mA/cm² gesteigert werden. *EQE* Messungen zeigten, dass der Zugewinn in der Photostromdichte insbesondere auf eine Steigerung des Beitrags durch die Fullerschicht zurückzuführen ist. In C₆₀ erzeugte Exzitonen können innerhalb ihrer Lebensdauer an die D3/C₆₀ Grenzfläche diffundieren und dort gebundene CT Zustände ausbilden. Aufgrund der speziellen Positionen ihrer Energieniveaus kann die D1 Grenzfläche, die sich in unmittelbarer Nähe befindet, diese CT Zustände destabilisieren und somit die Generation freier Ladungsträger verbessern. Für dickere Zwischenschichten geht der Zugewinn der Photostromdichte zurück. Im Falle, dass die D3 Zwischenschicht aus mehreren Monolagen besteht, können die aus dem D3/C₆₀ Kontakt gebildeten CT Zustände als räumlich getrennt von der D1 Grenzfläche angenommen werden. Daher ist die Wirkung der Energie-Kaskade begrenzt und kann die Exzitonendissoziation in freie Ladungsträger nicht mehr effektiv unterstützen.

Das Konzept der Energie-Kaskaden wurde anschließend auf die leistungsfähigere Materialkombination DBP/C₇₀ übertragen. Aufgrund der Möglichkeit die Energieniveaus der Zinkphthalocyanine gezielt durch Fluorierung zu verändern (siehe oben), konnte eine Energie-Kaskade verwirklicht werden, indem F₈ZnPc als Zwischenschicht gewählt wurde. [175] Bei Verwendung einer Zwischenschicht im Sub-Monolagen Bereich in DBP/F₈ZnPc/C₇₀ Kaskadenzellen konnten die Solarzellenparameter deutlich verbessert werden. Die besten Resultate wurden für eine Zwischenschichtdicke von 5 Å erzielt, für die der Wirkungsgrad im Vergleich zu DBP/C₇₀ Referenzzellen von 2,2 % auf 3,7 % gesteigert werden konnte. Für organische Kaskadenzellen, in denen dünne molekulare Zwischenschichten eingesetzt werden, sind diese Resultate unter den besten, die bisher in der Literatur berichtet wurden. [92,93]

Diese Ergebnisse zeigen deutlich, welche maßgebliche Rolle die Energetik an Organik/Organik-Grenzflächen für die Parameter und das Leistungsverhalten organischer photovoltaischer Zellen einnimmt. Neben dem wissenschaftlichen Interesse an den mikroskopischen Prozessen, sind diese Resultate auch von wesentlicher Relevanz für die technische Realisierung leistungsfähiger organischer Solarzellen. Durch die Einführung eines einzelnen, einfach zu implementierenden Prozessierungsschrittes, können Rekombinationsverluste in planaren organischen Solarzellen gezielt verringert und somit deren Leistungsfähigkeit erheblich verbessert werden.

Untersuchung der Transportkompatibilität gemischter C₆₀:C₇₀ Akzeptorschichten in OPVZs bei Raumtemperatur

Etablierte Fulleren-Synthesen ergeben eine Roh-Fullerenmischung bestehend aus C₆₀ und C₇₀ in einem Verhältnis von 3:1, sowie zusätzlich 1 - 3 % Fullerene höherer molekularer Masse. Die Gesamtmaterialekosten der einzelnen Verbindungen werden durch die Aufreinigung bestimmt, das heißt, durch die Trennung der einzelnen Komponenten voneinander. Da in UPS Messungen gezeigt werden konnte, dass die Energieniveaus von C₆₀ und C₇₀ nahezu identisch sind, wur-

de die Notwendigkeit einer Aufreinigung im Hinblick auf den Effekt auf die photovoltaischen Kenngrößen untersucht. [18]

Hierfür wurde der Einfluss eines unterschiedlichen $C_{60}:C_{70}$ Akzeptor-Mischungsverhältnisses auf die Leistungsdaten planarer DIP/ $C_{60}:C_{70}$ Solarzellen analysiert. Die Solarzellenparameter offene Klemmspannung V_{oc} und Füllfaktor FF erwiesen sich als nahezu unabhängig von dem jeweiligen C_{70} -Anteil in der ko-verdampften Fullerenphase. Im Gegensatz dazu zeigte die $j(V)$ -Charakterisierung einen linearen Anstieg von j_{sc} mit der C_{70} Konzentration. Dieser Anstieg wurde der höheren Absorption von C_{70} im Vergleich zu C_{60} zugeordnet. Wie durch komplementäre, spektral aufgelöste PL Messungen verdeutlicht werden konnte, ermöglicht ein resonanter Energietransfer einen effizienten Transport der Anregungsenergie zwischen den beiden Fullerenen bei Raumtemperatur.

Um den Einfluss interpenetrierender Netzwerke aus C_{60} und C_{70} in ko-verdampften Fullerenphasen zu unterdrücken, welche das Donormaterial direkt mit der Kathode verbinden können, wurde die Akzeptorphase bei identischer Gesamtschichtdicke als C_{60}/C_{70} Schichtstapel aufgebracht. Der Vergleich der Solarzellenparameter zeigte keinen signifikanten Unterschied für die verschiedenen Bauteilarchitekturen, wodurch der experimentelle Nachweis einer exzitonischen und elektronischen Kompatibilität zwischen den beiden Fullerenen bei Raumtemperatur erbracht wurde.

Aus den unterschiedlichen molekularen Massen der jeweiligen Fullerene resultieren verschiedene Sublimationstemperaturen. Die Aufreinigung einer Roh-Fullerenmischung mittels Gradientensublimation ergibt C_{70} als häufigste „Verunreinigung“ von C_{60} . Unter Kostengesichtspunkten sollte daher anstelle von hochaufgereinigtem C_{60} eine $C_{60}:C_{70}$ Akzeptormischung angestrebt werden. Im Hinblick auf die Solarzeleigenschaften sollte diese Mischung aufgrund der höheren Absorption einen möglichst großen Anteil an C_{70} aufweisen.

Zusätzlich wurden Solarzellen auf Basis von DIP und der Roh-Fullerenmischung hergestellt und opto-elektronisch untersucht, um den Einfluss von Fullerenen höherer molekularer Masse auf die Bauteileigenschaften zu analysieren. Alle Solarzellenparameter zeigten sich deutlich verschlechtert. Dieses Verhalten wurde erhöhten exzitonischen Rekombinationsverlusten zugeordnet, die sich infolge von zusätzlichen Fallenzuständen ergeben. Diese Fallenzustände werden durch die Fullerene höherer molekularer Masse aufgrund deren energetischer Lage innerhalb der C_{60} bzw. C_{70} Bandlücke im Bauteil erzeugt. Daher ist eine Separation dieser Fulleren-Komponenten für die Anwendung von C_{60} und C_{70} als Akzeptoren in organischen, elektronischen Bauteilen mit hoher Leistungsfähigkeit unabdingbar,

Abschließende Bemerkungen

In dieser Arbeit wurde der Einfluss der Grenzflächenenergetik zwischen den molekularen Halbleiterschichten planarer Solarzellen auf die opto-elektronischen Eigenschaften der Bauteile unter-

sucht. Vielseitige Möglichkeiten wurden aufgezeigt, um die Grenzflächenenergetik systematisch zu variieren, wie zum Beispiel die Verwendung chemisch modifizierter, energetisch maßgeschneiderter Donatormoleküle, oder die Implementierung eines neuen Bauteilkonzepts, bei dem Energiekaskaden durch das Einbringen dünner Zwischenschichten an der jeweiligen D/A Grenzfläche realisiert wurden. Grundlegende Prozesse, wie die quasi-Fermi-Niveau Aufspaltung an der D/A Grenzfläche, die Trennung von CT Exzitonen in freie Ladungsträger und deren dynamisches Rekombinationsverhalten konnten somit gezielt untersucht und mit der Grenzflächenenergetik korreliert werden. Damit haben diese Studien zum grundlegenden Verständnis komplexer, auf molekularer Ebene ablaufender, photo-physikalischer Effekte beigetragen und liefern wichtige Erkenntnisse für die zukünftige Leistungsoptimierung molekularer opto-elektronischer Funktionseinheiten.

List of Figures

2.1. Illustration of the delocalized π -electron system of benzene and corresponding energy level diagram.	6
2.2. Energy diagram of an isolated molecule and a molecular crystal.	7
2.3. Description of electronic transitions in a Jablonski diagram.	8
2.4. Schematic explanation of the Franck-Condon principle.	9
2.5. Depiction of different types of excitons.	11
2.6. Illustration of hopping transport in a Gaussian density of states.	18
3.1. Energy diagram of a planar bilayer solar cell.	20
3.2. Processes occurring during photoconversion in a planar bilayer cell.	22
3.3. Demonstration of important parameters to be derived from $j(V)$ characteristics.	25
4.1. Illustration of the ligand configuration of F_nZnPc s ($n = 0, 4, 8, 16$).	32
4.2. Structure of the diketopyrrolopyrrole derivatives D1 - D3.	33
4.3. Structure of the donor compound DIP.	34
4.4. Structure of the donor material DBP.	35
4.5. Structure of the fullerene acceptors C_{60} and C_{70}	36
4.6. Structure of the exciton blocking material BPhen.	36
5.1. Schematic architecture of a planar bilayer cell.	39
5.2. Schematic depiction of the vacuum chamber.	40
6.1. Working principle of TAS and schematic transient spectrum.	45
6.2. Demonstration of the TAS setup.	47
6.3. Relevant energy levels of the sample and spectrometer for UPS measurements.	48
7.1. $j(V)$ characteristics of F_nZn/C_{60} solar cells.	54
7.2. Solar cell parameters of F_nZnPc/C_{60} photovoltaic devices.	55
7.3. Absorption coefficients and PL spectra of F_nZnPc thin films.	57
7.4. X-ray diffraction spectra of F_nZnPc thin films.	59
7.5. Lattice spacings and crystallite heights of F_nZnPc thin films.	60
7.6. Valence band and work function spectra of the $ZnPc/C_{60}$ heterojunction.	62
7.7. Band schemes of F_nZnPc/C_{60} heterojunctions.	63
7.8. HOMO energies of F_nZnPc s at the D/A interface.	64
7.9. <i>EQE</i> of F_nZnPc/C_{60} solar cells and energetic offsets at the D/A interfaces.	65

7.10. Spectrally resolved PL of ITO/MoO ₃ /F _n ZnPc/C ₆₀ heterostructures and associated bilayer cell working principles.	66
8.1. TA spectra of F _n ZnPc/C ₆₀ heterostructures and a C ₆₀ thin film.	72
8.2. Temporal rise of ESA signals of F _n ZnPc/C ₆₀ heterostructures and a C ₆₀ thin film.	73
8.3. TA spectra of F _n ZnPc/C ₆₀ heterostructures and of a C ₆₀ thin film at different time delays.	74
8.4. Biexponential fits of the ESA signals at 1050 nm of F _n ZnPc/C ₆₀ heterostructures and a C ₆₀ thin film.	75
8.5. TA spectra of ZnPc/C ₆₀ for different pump wavelength and fits of the transients.	76
8.6. Charge carrier generation mechanisms for C ₆₀ in F _n ZnPc/C ₆₀ bilayers.	80
9.1. Summary of the energy levels of D1, D2, D3 and C ₆₀	84
9.2. XRD spectra of cascade and bilayer solar cells.	85
9.3. $j(V)$ characteristics of D1/D3/C ₆₀ cascade solar cells and bilayer reference cells.	87
9.4. Normalized photovoltaic parameters of D1/D3/C ₆₀ cascade solar cells.	88
9.5. Absorption spectra of a D1/D3/C ₆₀ cascade cell and reference bilayer cells.	89
9.6. Series and parallel resistances of D1/D3/C ₆₀ cascade solar cells and D1/C ₆₀ OPVCs.	90
9.7. EQE of D1/D3/C ₆₀ cascade cells and reference bilayer cells.	91
9.8. Normalized EQE peaks at different wavelength and ratio of EQE peaks at 585 nm and 635 nm in D1/D3/C ₆₀ cascade cells.	92
9.9. Illustration of the energy level alignment and exciton dissociation mechanisms in cascade solar cells as a function of interlayer thickness.	93
9.10. Spectrally resolved PL of D1/D3/C ₆₀ cascade cells and D1/C ₆₀ bilayer cells.	94
9.11. EQE of D1/D2/C ₆₀ and D1/D3/C ₆₀ cascade cells and D1/C ₆₀ bilayer cells.	96
9.12. $j(V)$ characteristics of D1/D2/C ₆₀ and D1/D3/C ₆₀ cascade cells and D1/C ₆₀ bilayer cells.	97
9.13. Expected energy level alignment of DBP/F ₈ ZnPc/C ₇₀ cascade cells.	98
9.14. $j(V)$ characteristics of DBP/F ₈ ZnPc/C ₇₀ cascade cells and DBP/C ₇₀ cells.	99
9.15. Normalized photovoltaic parameters of DBP/F ₈ ZnPc/C ₇₀ cascade cells.	100
9.16. EQE of DBP/F ₈ ZnPc/C ₇₀ cascade cells and DBP/C ₇₀ devices.	101
9.17. Normalized EQE peak at 450 nm excitation for DBP/F ₈ ZnPc/C ₇₀ cascade cells	103
10.1. AFM images of DIP and DIP/C ₆₀ :C ₇₀ heterostructures.	107
10.2. Absorption coefficients of DIP, C ₆₀ , C ₇₀ and the raw fullerene mixture.	108
10.3. Spectrally resolved PL of C ₆₀ , C ₇₀ and C ₆₀ :C ₇₀ thin films.	110
10.4. EQE of representative DIP/C ₆₀ :C ₇₀ organic photovoltaic cells.	112
10.5. $j(V)$ characteristics of DIP/C ₆₀ :C ₇₀ solar cells.	113
10.6. Solar cell parameters of DIP/C ₆₀ :C ₇₀ cells as a function of the fullerene composition.	115
10.7. $j(V)$ characteristics of deterministically stacked and co-evaporated cells.	116

List of Tables

7.1. Series and parallel resistances of $F_n\text{ZnPc}/C_{60}$ solar cells.	56
7.2. Effective band gap, open circuit voltage, and loss term for $F_n\text{ZnPc}/C_{60}$ bilayer cells.	68
8.1. Time constants and amplitudes of biexponential fits of $F_n\text{ZnPc}/C_{60}$ heterostructures and the C_{60} thin film.	76
8.2. Fit parameters for different pump wavelength for the ZnPc/C_{60} heterostructure.	77
9.1. Photovoltaic parameters for $D1/D2/C_{60}$ and $D1/D3/C_{60}$ cascade solar cells and $D1/C_{60}$ bilayer devices.	97
10.1. Fill factors FF , series and parallel resistances, R_s and R_p of $DIP/C_{60}:C_{70}$ and DIP/raw fullerene solar cells.	114

Bibliography

- [1] C. Chiang, C. Fincher, Y. Park, A. Heeger, H. Shirakawa, E. Louis, S. Gau, and A. MacDiarmid. Electrical conductivity in doped polyacetylene. *Phys. Rev. Lett.*, 39:1098, 1977.
- [2] L. Chua, J. Zaumseil, J. Chang, E. Ou, P. Ho, H. Sirringhaus, and R. Friend. General observation of n-type field-effect behaviour in organic semiconductors. *Nature*, 434:194, 2005.
- [3] R. Chesterfield, J. Mc Keen, C. Newman, P. Ewbank, D. Silva Filho, J. Brédas, L. Miller, K. Mann, and C. Frisbie. Organic thin film transistors based on n-alkyl perylene diimides: Charge transport kinetics as a function of gate voltage and temperature. *J. Phys. Chem. B*, 108:19281, 2004.
- [4] K. Cnops, G. Zango, J. Genoe, P. Heremans, M. Martinez-Diaz, T. Torres, and D. Cheyns. Energy level tuning of non-fullerene acceptors in organic solar cells. *J. Am. Chem. Soc.*, 137:8991, 2015.
- [5] Heliatek. [http://www.heliatek.com/de/presse/pressemitteilungen/details/heliatek-erreicht-neuen-organischen-photovoltaik-weltrekord-mit-einer-effizienz-von-13.2](http://www.heliatek.com/de/presse/pressemitteilungen/details/heliatek-erreicht-neuen-organischen-photovoltaik-weltrekord-mit-einer-effizienz-von-13.2-%) %, 08.02.2016.
- [6] W. Wong and C. Ho. Functional metallophosphors for effective charge carrier injection/transport: New robust OLED materials with emerging applications. *J. Mater. Chem.*, 19:4457, 2009.
- [7] A. Chwang, M. Rothman, S. Mao, R. Hewitt, M. Weaver, J. Silvernail, K. Rajan, M. Hack, J. Brown, X. Chu, L. Moro, T. Krajewski, and N. Rutherford. Thin film encapsulated flexible organic electroluminescent displays. *Appl. Phys. Lett.*, 83:413, 2003.
- [8] Samsung. <http://www.samsung.com/de/consumer/mobile-devices/smartphones/galaxy-s/galaxy-s7/>, 01.09.2016.
- [9] S. Forrest. The path to ubiquitous and low-cost organic electronic appliances on plastic. *Nature*, 428:911, 2004.
- [10] N. Mc Keown. *Phthalocyanine Materials: Synthesis, Structure and Function (Chemistry of Solid State Materials)*. The Press Syndicate of the University of Cambridge, Cambridge, 1998.

- [11] H. Brinkmann, C. Kelting, S. Makarov, O. Tsaryova, G. Schnurpfeil, D. Wöhrle, and D. Schlettwein. Fluorinated phthalocyanines as molecular semiconductor thin films. *Phys. stat. sol. (a)*, 205:409, 2008.
- [12] H. Hoppe and N. Sariciftci. Organic solar cells: An overview. *J. Mater. Res.*, 19:1924, 2004.
- [13] K. Mazziio and C. Luscombe. The future of organic photovoltaics. *Chem. Soc. Rev.*, 44:78, 2015.
- [14] M. Green, K. Emery, Y. Hishikawa, W. Warta, and E. Dunlop. Solar cell efficiency tables (version 47). *Prog. Photovolt. Res. Appl.*, 24:3, 2016.
- [15] M. Schwoerer and H. Wolf. *Organic Molecular Crystals*. Wiley-VCH, Weinheim, 2007.
- [16] D. Schlettwein, K. Hesse, H. Tada, S. Mashiko, U. Storm, and J. Binder. Ordered growth of substituted phthalocyanine thin films: Hexadecafluorophthalocyaninatozinc on alkali halide (100) and microstructured Si surfaces. *Chem. Mater.*, 12:989, 2000.
- [17] U. Weiler. *Silizium-Farbstoff-Hybridssysteme für die Photovoltaik: Präparation und Eigenschaften*. Ph.D. thesis, University of Darmstadt, 2005.
- [18] M. Dresselhaus, G. Dresselhaus, and P. Eklund. *Science of Fullerenes and Carbon Nanotubes*. Academic Press, San Diego, 1996.
- [19] W. Brütting. *Physics of Organic Semiconductors*. Wiley-VCH, Weinheim, 2005.
- [20] M Hart, L. Craine, D. Hart, and C. Hadad. *Organische Chemie*. Wiley-VCH, Weinheim, 2007.
- [21] K. Vollhardt and N. Schore. *Organische Chemie*. Wiley-VCH, Weinheim, 2000.
- [22] M. Pope and C. Swenberg. *Electronic Processes in Organic Crystals and Polymers*. Oxford University Press, New York, 1999.
- [23] J. Simon und J.-J. André. *Molecular Semiconductors Photoelectrical Properties and Solar Cells*. Springer, Berlin, Heidelberg, New York, Tokyo, 1985.
- [24] H. Ibach and H. Lüth. *Festkörperphysik*. Springer, Berlin, Heidelberg, New York, Tokyo, 2009.
- [25] A. Jablonski. Efficiency of anti-Stokes fluorescence in dyes. *Nature*, 131:839, 1933.
- [26] J. Birks. *Photophysics of Aromatic Molecules*. Wiley-Interscience, Weinheim, 1970.
- [27] J. Franck and E. Dymond. Elementary processes of photochemical reactions. *Trans. Faraday Soc.*, 21:536, 1926.
- [28] E. Condon. A theory of intensity distribution in band systems. *Phys. Rev.*, 28:1182, 1926.

- [29] H. Haken and H. Wolf. *Molekülphysik und Quantenchemie*. Springer, Berlin, Heidelberg, New York, Tokyo, 2003.
- [30] A. Steindamm. *Exzitonische Verlustmechanismen in Organischen Bilagen-Solarzellen*. Ph.D. thesis, University of Würzburg, 2015.
- [31] M. Kasha. Characterization of electronic transitions in complex molecules. *Discuss. Faraday Soc.*, 9:14, 1950.
- [32] D. Mc Quarrie and J. Simon. *Physical Chemistry, a Molecular Approach*. University Science Books, Herndon, 1997.
- [33] H. Yersin and W. Finkenzeller. *Highly Efficient OLEDs with Phosphorescent Materials*. Wiley-VCH, Weinheim, 2008.
- [34] G. Bassani and V. Agranovich. *Electronic Excitations in Organic Based Nanostructures*. Elsevier Science, Amsterdam, Oxford, 2003.
- [35] H. Wannier. The structure of electronic excitation levels in insulating crystals. *Phys. Rev.*, 52:191, 1937.
- [36] N. Mott. Conduction in polar crystals. II. The conduction band and ultra-violet absorption of alkali-halide crystals. *Trans. Faraday Soc.*, 34:500, 1938.
- [37] C. Deibel, D. Mack, J. Gorenflot, A. Schöll, S. Krause, F. Reinert, D. Rauh, and V. Dyakonov. Energetics of excited states in the conjugated polymer poly(3-hexylthiophene). *Phys. Rev. B*, 81:085202, 2010.
- [38] M. Knuifer. Exciton binding energies in organic semiconductors. *Appl. Phys. A Mater. Sci. Process*, 77:623, 2003.
- [39] L. Gisslén and R. Scholz. Crystallochromy of perylene pigments: Interference between frenkel excitons and charge-transfer states. *Phys. Rev. B*, 80:115309, 2009.
- [40] T. Seko, K. Ogura, Y. Kawakami, H. Sugino, H. Toyotama, and J. Tanaka. Excimer emission of anthracene, perylene, coronene and pyrene microcrystals dispersed in water. *Chem. Phys. Lett.*, 291:438, 1998.
- [41] U. Heinemeyer, R. Scholz, L. Gisslón, M. Alonso, J. Ossó, M. Garriga, A. Hinderhofer, M. Kytka, S. Kowarik, A. Gerlach, and F. Schreiber. Exciton-phonon coupling in diindenoperylene thin films. *Phys. Rev. B*, 78:210, 2008.
- [42] P. Lane, P. Cunningham, J. Melinger, O. Esenturk, and E. Heilweil. Hot photocarrier dynamics in organic solar cells. *Nat. Commun.*, 6:DOI: 10.1038/ncomms8558, 2015.
- [43] T. Clarke and J. Durrant. Charge photogeneration in organic solar cells. *Chem. Rev.*, 110:6736, 2010.

- [44] V. Agranovich and G. Bassani. *Thin Films and Nanostructures. Electronic Excitations in Organic Based Nanostructures*. Elsevier, Amsterdam, Oxford, 2003.
- [45] P. Peumans, A. Yakimov, and S. Forrest. Small molecular weight organic thin-film photodetectors and solar cells. *J. Appl. Phys.*, 93:3693, 2003.
- [46] S. Menke and R. Holmes. Exciton diffusion in organic photovoltaic cells. *Energy Environ. Sci.*, 7:499, 2014.
- [47] T. Förster. Zwischenmolekulare Energiewanderung und Fluoreszenz. *Ann. Phys.*, 2:55, 1948.
- [48] B. Forster. 10th Spiers memorial lecture. Transfer mechanisms of electronic excitation. 10:7, 1959.
- [49] R. Lunt, N. Giebink, A. Belak, J. Benziger, and S. Forrest. Exciton diffusion lengths of organic semiconductor thin films measured by spectrally resolved photoluminescence quenching. *J. Appl. Phys.*, 105:053711, 2009.
- [50] K. Feron, W. Belcher, C. Fell, and P. Dastoor. Organic solar cells: Understanding the role of Förster resonance energy transfer. *Int. J. Mol. Sci.*, 13:17019, 2012.
- [51] S. Scully and M. Mc Gehee. Effects of optical interference and energy transfer on exciton diffusion length measurements in organic semiconductors. *J. Appl. Phys.*, 100:034907, 2006.
- [52] S. Scully, P. Armstrong, C. Edder, J. Fréchet, and M. Mc Gehee. Long-range resonant energy transfer for enhanced exciton harvesting for organic solar cells. *Adv. Mat.*, 19:2961, 2007.
- [53] G. Scholes. Long-range resonance energy transfer in molecular systems. *Annu. Rev. Phys. Chem.*, 54:57, 2003.
- [54] D. Dexter. A theory of sensitized luminescence in solids. *J. Chem. Phys.*, 21:836, 1953.
- [55] A. Fahrenbruch and R. Bube. *Fundamentals of Solar Cells. Photovoltaic Solar Energy Conversion*. Academic, New York, 1983.
- [56] B. Gregg and M. Hanna. Comparing organic to inorganic photovoltaic cells: Theory, experiment, and simulation. *J. Appl. Phys.*, 93:3605, 2003.
- [57] Y. Cheng, R. Silbey, D. da Silva Filho, J. Calbert, J. Cornil, and J. Brédas. Three-dimensional band structure and bandlike mobility in oligoacene single crystals: A theoretical investigation. *J. Chem. Phys.*, 118:3764, 2003.
- [58] C. Tang. Two-layer organic photovoltaic cell. *Appl. Phys. Lett.*, 48:183, 1986.

- [59] M. Jaiswal and R. Menon. Polymer electronic materials: A review of charge transport. *Polym. Int.*, 55:1371, 2006.
- [60] H. Bässler. Charge transport in disordered organic photoconductors. *phys. stat. sol. (b)*, 175:15, 1993.
- [61] R. Winter, M. Hammer, C. Deibel, and J. Pflaum. Improvement of the poly-3-hexylthiophene transistor performance using small molecule contact functionalization. *Appl. Phys. Lett.*, 95:263313, 2009.
- [62] D. Braun. Electronic injection and conduction processes for polymer devices. *J. Poly. Sci. B*, 41:2622, 2003.
- [63] H. Bässler and A. Köhler. Charge transport in organic semiconductors. *Top. Curr. Chem.*, 312:1, 2012.
- [64] A. Miller and E. Abrahams. Impurity conduction at low concentrations. *Phys. Rev.*, 120:745, 1960.
- [65] G. Schnönherr, R. Eiermann, and H. Bässler. Dispersive exciton transport in a hopping system with Gaussian energy distribution. *Chem. Phys.*, 52:287, 1980.
- [66] W. Pasveer, J. Cottaar, C. Tanase, R. Coehoorn, P. Bobbert, P. Blom, D. de Leeuw, and M. Michels. Unified description of charge-carrier mobilities in disordered semiconducting polymers. *Phys. Rev. Lett.*, 94:206601, 2005.
- [67] S. Tuladhar, M. Sims, J. Kirkpatrick, R. Maher, A. Chatten, D. Bradley, J. Nelson, P. Etchegoin, C. Nielsen, P. Massiot, W. George, and J. Steinke. Influence of alkyl chain length on charge transport in symmetrically substituted poly(2,5-dialkoxy-p-phenylenevinylene) polymers. *Phys. Rev. B*, 79:035201, 2009.
- [68] O. Rubel, S. Baranovskii, P. Thomas, and S. Yamasaki. Concentration dependence of the hopping mobility in disordered organic solids. *Phys. Rev. B*, 69:014206, 2004.
- [69] D. Monroe. Hopping in exponential band tails. *Phys. Rev. Lett.*, 54:146, 1985.
- [70] S. Baranovskii, H. Cordes, F. Hensel, and G. Leising. Charge carrier transport in disordered organic solids. *Phys. Rev. B*, 62:7934, 2000.
- [71] V. Arkhipov, E. Emelianova, and G. Adriaenssens. Effective transport energy versus the energy of most probable jumps in disordered hopping systems. *Phys. Rev. B*, 64:125125, 2001.
- [72] A. Wagenpfahl. *Numerical Simulations on Limitations and Optimization Strategies of Organic Solar Cells*. Ph.D. thesis, University of Würzburg, 2013.

- [73] R. Coehoorn, W. Pasveer, P. Bobbert, and M. Michels. Charge carrier concentration dependence of the hopping mobility in organic materials with Gaussian disorder. *Phys. Rev. B*, 72:155206, 2005.
- [74] D. Hoesterey and G. Letson. The trapping of photocarriers in anthracene by anthraquinone, anthrone and naphthacene. *J. Phys. Chem. Solids*, 24:1609, 1963.
- [75] A. Ghosh and T. Feng. Merocyanine organic solar cells. *J. Appl. Phys.*, 49:5982, 1978.
- [76] J. You, L. Dou, K. Yoshimura, T. Kato, K. Ohya, T. Moriarty, K. Emery, C. Chen, J. Gao, G. Li, and Y. Yang. A polymer tandem solar cell with 10.6 % power conversion efficiency. *Nat. Commun.*, 5:1446, 2013.
- [77] D. Veldman, S. Meskers, and R. Janssen. The energy of charge transfer states in electron donor-acceptor blends: Insight into the energy losses in organic solar cells. *Adv. Funct. Mater.*, 19:1939, 2009.
- [78] C. Brabec, G. Zerza, G. Cerullo, S. De Silvestri, S. Luzzati, J. Hummelen, and S. Sariciftci. Tracing photoinduced electron transfer process in conjugated polymer/fullerene bulk heterojunctions in real time. *Chem. Phys. Lett.*, 340:232, 2001.
- [79] H. Ohkita, S. Cook, Y. Astuti, W. Duffy, S. Tierney, W. Zhang, M. Heeney, I. Mc Culloch, J. Nelson, D. Bradley, and J. Durrant. Charge carrier formation in polythiophene/fullerene blend films studied by transient absorption spectroscopy. *J. Am. Chem. Soc.*, 130:3030, 2008.
- [80] J. Nelson. Polymer:fullerene bulk-heterojunction solar cells. *Mater. Today*, 14:462, 2011.
- [81] L. Onsager. Initial recombination of ions. *Phys. Rev.*, 54:554, 1938.
- [82] M. Hosoya, H. Oooka, H. Nakao, T. Gotanda, S. Mori, N. Shida, R. Hayase, Y. Nakano, and M. Saito. Organic thin film photovoltaic modules. *PA Journal Proceedings, 93rd Annual Meeting of The Chemical Society of Japan*, page 21, 2013.
- [83] M. Hiramoto, H. Fujiwara, and M. Yokoyama. Three-layered organic solar cell with a photoactive interlayer of codeposited pigments. *Appl. Phys. Lett.*, 58:1062, 1991.
- [84] J. Halls, C. Walsh, N. Greenham, E. Marseglia, R. Friend S. Moratti, and A. Holmes. Efficient photodiodes from interpenetrating polymer networks. *Nature*, 376:498, 1995.
- [85] G. Yu, J. Gao, J. Hummelen, F. Wudl, and A. Heeger. Polymer photovoltaic cells: Enhanced efficiencies via a network of internal donor-acceptor heterojunctions. *Science*, 270:1789, 1995.
- [86] M. Scharber and N. Sariciftci. Efficiency of bulk-heterojunction organic solar cells. *Prog. Polym. Sci.*, 38:1929, 2013.

- [87] B. Lassiter, C. Kyle Renshaw, and S. Forrest. Understanding tandem organic photovoltaic cell performance. *J. Appl. Phys.*, 113:214505, 2013.
- [88] M. Riede, C. Uhrich, J. Widmer, R. Timmreck, D. Wynands, G. Schwartz, W. Gnehr, D. Hildebrandt, A. Weiss, J. Hwang, S. Sundarraj, P. Erk, M. Pfeiffer, and K. Leo. Efficient organic tandem solar cells based on small molecules. *Adv. Funct. Mater.*, 21:3019, 2011.
- [89] C. Schlenker, V. Barlier, S. Chin, M. Whited, R. Mc Anally, S. Forrest, and M. Thompson. Cascade organic solar cells. *Chem. Mater.*, 23:4132, 2011.
- [90] O. Griffith and S. Forrest. Exciton management in organic photovoltaic multidonor energy cascades. *Nano Lett.*, 14:2353, 2014.
- [91] A. Barito, M. Sykes, D. Bilby, J. Amonoo, Y. Jin, S. Morris, P. Green, J. Kim, and M. Shtein. Recovering lost excitons in organic photovoltaics using a transparent dissociation layer. *J. Appl. Phys.*, 113:203110., 2013.
- [92] Z. Tan, K. Johnson, Y. Vaynzof, A. Bakulin, L. Chua, P. Ho, and R. Friend. Suppressing recombination in polymer photovoltaic devices via energy-level cascades. *Adv. Mater.*, 25:4131, 2013.
- [93] T. Heidel, D. Hochbaum, J. Sussman, V. Singh, M. Bahlke, I. Hiromi, J. Lee, and M. Baldo. Reducing recombination losses in planar organic photovoltaic cells using multiple step charge separation. *J. Appl. Phys.*, 109:104502, 2011.
- [94] B. Rand, J. Genoe, P. Heremans, and J. Poortmans. Solar cells utilizing small molecular weight organic semiconductors. *Photovolt: Res Appl.*, 15:659, 2007.
- [95] B. Qi and J. Wang. Fill factor in organic solar cells. *Phys. Chem. Chem. Phys.*, 15:8972, 2013.
- [96] D. Cheyons, J. Poortmans, P. Heremans, C. Deibel, S. Verlaak, B. Rand, and J. Genoe. Analytical model for the open-circuit voltage and its associated resistance in organic planar heterojunction solar cells. *Phys. Rev. B*, 77:165332, 2008.
- [97] K. Vandewal, K. Tvingstedt, A. Gadisa, O. Inganäs, and J. Manca. Relating the open circuit voltage to interface molecular properties of donor:acceptor bulk-heterojunction solar cells. *Phys. Rev. B*, 81:125204, 2010.
- [98] U. Hörmann, J. Kraus, M. Gruber, C. Schuhmair, T. Linderl, S. Grob, S. Kapfinger, K. Klein, M. Stutzman, H. Krenner, and W. Brütting. Quantification of energy losses in organic solar cells from temperature-dependent device characteristics. *Phys. Rev. B*, 88:235307, 2013.
- [99] A. Wilke, J. Endres, U. Hörmann, J. Niederhausen, R. Schlesinger, J. Frisch, P. Amsalem, J. Wagner, M. Gruber, A. Opitz, A. Vollmer, W. Brütting, A. Kahn, and N. Koch. Corre-

- lation between interface energetics and open circuit voltage in organic photovoltaic cells. *Appl. Phys. Lett.*, 101:233301, 2012.
- [100] J. Widmer, M. Tietze, K. Leo, and M. Riede. Open-circuit voltage and effective gap of organic solar cells. *Adv. Funct. Mater.*, 23:5814, 2013.
- [101] B. Han, L. Yu, K. Hevesi, G. Gensterblum, P. Rudolf, J. Pireaux, P. Thiry, R. Caudano, P. Lambin, and A. Lucas. Electronic transitions and excitations in solid C₇₀ studied by EELS and XPS C-1s satellite structures. *Phys. Rev. B.*, 51:7179, 1995.
- [102] A. Antony, M. Nisha, R. Manoj, and M. Jayaraj. Influence of target to substrate spacing on the properties of ITO thin films. *Appl. Surf. Sci.*, 225:294, 2004.
- [103] X. Ding, L. Hung, L. Cheng, Z. Deng, X. Hou, C. Lee, and S. Lee. Modification of the hole injection barrier in organic light-emitting devices studied by ultraviolet photoelectron spectroscopy. *Appl. Phys. Lett.*, 76:2704, 2000.
- [104] W. Böge and W. Plafmann. *Vieweg Handbuch Elektrotechnik*. Vieweg und Teubner Verlag, Wiesbaden, 2007.
- [105] N. Greenwood and A. Earnshaw. *Chemie der Elemente*. Wiley-VCH, Weinheim, 1988.
- [106] M. Chelvayohan and C. Mee. Work function measurements on (100), (110) and (111) surfaces of silver. *J. Phys. C*, 15:2305, 1982.
- [107] H. Ishii, K. Sugiyama, E. Ito, and K. Seki. Energy level alignment and interfacial electronic structures at organic/metal and organic/organic interfaces. *Adv. Mater.*, 11:605, 1999.
- [108] A. Wagenpfahl. S-shaped current-voltage characteristics of organic solar devices. *Phys. Rev. B*, 82:115306, 2010.
- [109] J. Meyer, S. Hamwi, M. Kröger, W. Kowalsky, T. Riedl, and A. Kahn. Transition metal oxides for organic electronics: Energetics, device physics and applications. *Adv. Mater.*, 24:5408, 2012.
- [110] J. Huang, P. Miller, J. Wilson, A. de Mello, J. de Mello, and D. Bradley. Investigation of the effects of doping and post-deposition treatments on the conductivity, morphology, and work function of poly(3,4-ethylenedioxythiophene)/poly(styrene sulfonate) films. *Adv. Funct. Mater.*, 15:290, 2005.
- [111] H. Peisert, M. Knupfer, F. Zhang, A. Petr, L. Dunsch, and J. Fink. The interface between phthalocyanines and PEDOT:PSS: Evidence of charge transfer and doping. *Surf. Sci.*, 566:554, 2004.
- [112] C. Chu, S. Li, C. Chen, V. Shrotriya, and Y. Yang. High-performance organic thin film transistors with metal oxide/metal bilayer electrode. *Appl. Phys. Lett.*, 87:193508, 2005.

- [113] L. Chen, Z. Hong, G. Li, and Y. Yang. Recent progress in polymer solar cells: Manipulation of polymer:fullerene morphology and the formation of efficient inverted polymer solar cells. *Adv. Mater.*, 21:1434, 2009.
- [114] J. Meyer, S. Hamwi, T. Bülow, H. Johannes, T. Riedl, and W. Kowalsky. Highly efficient simplified organic light emitting diodes. *Appl. Phys. Lett.*, 91:113506, 2007.
- [115] J. Wagner, M. Gruber, A. Wilke, Y. Tanaka, K. Topczak, A. Steindamm, U. Hörmann, A. Opitz, Y. Nakayama, H. Ishii, J. Pflaum, N. Koch, and W. Brütting. Identification of different origins for S-shaped current voltage characteristics in planar heterojunction organic solar cells. *J. Appl. Phys.*, 111:054509, 2012.
- [116] F. Moser and A. Thomas. *The Phthalocyanines*. CRC Press, Boca Raton, 1983.
- [117] C. Leznoff and A. Lever. *Phthalocyanines: Properties and Applications*. VCH Publishers Inc., New York, 1989.
- [118] M. Liao and S. Scheiner. Electronic structure and bonding in metal phthalocyanines, metal = Fe, Co, Ni, Cu, Zn, Mg. *J. Chem. Phys.*, 114:9780, 2001.
- [119] A. Davidson. The effect of the metal atom on the absorption spectra of phthalocyanine films. *J. Chem. Phys.*, 77:168, 1982.
- [120] X. Zhang and H. Xu. Influence of halogenation and aggregation on photosensitizing properties of zinc phthalocyanine (ZnPc). *J. Chem. Soc., Faraday Trans.*, 89:3347, 1989.
- [121] G. Löbbert. *Phthalocyanines*. Wiley-VCH, Weinheim, 2002.
- [122] J. Choi, S. Kim, C. Yoon, and J. Kim. Synthesis and characterization of thermally stable dyes with improved optical properties for dye-based lcd color filters. *New J. Chem.*, 36:812, 2012.
- [123] Y. Wang, J. Holden, A. Rao, W. Lee, X. Bi, S. Ren, G. Lehman, G. Hager, and E. Eklund. Interband dielectric function of C₆₀ and M₆C₆₀ (M = K, Rb, Cs). *Phys. Rev. B.*, 45:14396, 1992.
- [124] Y. Terao, H. Sasabe, and C. Adachi. Correlation of hole mobility, exciton diffusion length, and solar cell characteristics in phthalocyanine/fullerene organic solar cells. *Appl. Phys. Lett.*, 90:103515, 2007.
- [125] Z. Bao, A. Lovinger, and J. Brown. New air-stable n-channel organic thin film transistors. *J. Am. Chem. Soc.*, 120:207, 1998.
- [126] I. Bruder, J. Schöneboom, R. Dinnebier, A. Ojala, S. Schäfer, R. Sens, P. Erk, and J. Weis. What determines the performance of metal phthalocyanines (MPc, M = Zn, Cu, Ni, Fe) in organic heterojunction solar cells? A combined experimental and theoretical investigation. *Org. Electron.*, 11:377, 2010.

- [127] H. Mao, R. Wang, H. Huang, Y. Wang, X. Gao, S. Bao, A. Wee, and W. Chen. Tuning of C₆₀ energy levels using orientation-controlled phthalocyanine films. *J. Appl. Phys.*, 108:108, 2010.
- [128] M. Cook and I. Chambrier. *The Porphyrin Handbook*. Academic, San Diego, 2003.
- [129] T. Mayer, U. Weiler, C. Kelting, D. Schlettwein, S. Makarov, D. Wöhrle, O. Abdallah, M. Kunst, and W. Jaegermann. Silicon organic pigment material hybrids for photovoltaic application. *Sol. Energy Mater. Sol. Cells*, 91:1873, 2007.
- [130] D. Farnum, G. Mehta, G. Moore, and F. Siegel. Attempted Reformatsky reaction of benzonitrile. 1,4-diketo-3,6-diphenylpyrrolo[3,4-c]pyrrole. A lactam analogue of pentalene. *Tetrahedron Lett.*, 29:2549, 1974.
- [131] S. Qu and H. Tian. Diketopyrrolopyrrole (DPP)-based materials for organic photovoltaics. *Chem. Commun.*, 48:3039, 2012.
- [132] B. Walker, C. Kim, and T. Nguyen. Small molecule solution-processed bulk-heterojunction solar cells. *Chem. Mater.*, 23:470, 2011.
- [133] A. Iqbal, L. Cassar, A. Rochat, J. Pfenniger, and O. Wallquist. New heterocyclic pigments. *Coat. Technol.*, 60:37, 1988.
- [134] T. Beyerlein, B. Tieke, F. Lenger, and W. Brütting. New photoluminescent conjugated polymers with 1,4-dioxo-3,6-diphenylpyrrolo[3,4-c]pyrrole (DPP) and 1,4-phenylene units in the main chain. *Synth. Met.*, 130:115, 2002.
- [135] M. Wienk, M. Turbiez, J. Gilot, and R. Janssen. Narrow-bandgap diketopyrrolopyrrole polymer solar cells: The effect of processing on the performance. *Adv. Mater.*, 20:2556, 2008.
- [136] C. Mueller, M. Brendel, P. Ruckdeschel, J. Pflaum, and M. Thelakkat. Diketopyrrolopyrroles with a distinct energy level cascade for efficient charge carrier generation in organic solar cells. *Adv. Energy Mater.*, 5:1500914, 2015.
- [137] M. Münch. *Strukturelle Beeinflussung der Elektrischen Transporteigenschaften Dünner Organischer Schichten*. Ph.D. thesis, University of Stuttgart, 2001.
- [138] S. Sellner, A. Gerlach, F. Schreiber, M. Kelsch, N. Kasper, H. Dosch, S. Meyer, J. Pflaum, M. Fischer, and B. Gompf. Strongly enhanced thermal stability of crystalline organic thin films induced by aluminum oxide capping layers. *Adv. Mat.*, 16:1750, 2004.
- [139] A. Dürr. *Growth and Structure of DIP Thin-Films and Au-Contacts on DIP Thin-Films*. Ph.D. thesis, University of Stuttgart, 2002.

- [140] S. Kowarik, A. Gerlach, S. Sellner, L. Cavalcanti, O. Konovalov, and F. Schreiber. Real-time X-ray diffraction measurements of structural dynamics and polymorphism in diindenoperylene growth. *Appl. Phys. A.*, 95:233, 2009.
- [141] A. Dürr, F. Schreiber, M. Münch, N. Karl, B. Krause, V. Kruppa, and H. Dosch. High structural order in thin films of the organic semiconductor diindenoperylene. *Appl. Phys. Lett.*, 81:2276, 2002.
- [142] A. Dürr, N. Koch, M. Kelsch, A. Rühm, J. Ghijsen, R. Johnson, J.-J. Pireaux, J. Schwartz, F. Schreiber, H. Dosch, and A. Kahn. Interplay between morphology, structure, and electronic properties at diindenoperylene-gold interfaces. *Phys. Rev. B*, 68:1, 2003.
- [143] D. Kurrle and J. Pflaum. Exciton diffusion length in the organic semiconductor diindenoperylene. *Appl. Phys. Lett.*, 92:133306, 2008.
- [144] S. Rim and P. Peumans. The effects of optical interference on exciton diffusion length measurements using photocurrent spectroscopy. *J. Appl. Phys.*, 103:124515, 2008.
- [145] A. Tripathi and J. Pflaum. Correlation between ambipolar transport and structural phase transition in diindenoperylene single crystals. *Appl. Phys. Lett.*, 89:082103, 2006.
- [146] D. Yokoyama, Z. Wang, Y. Pu, K. Kobayashi, J. Kido, and Z. Hong. High efficiency simple planar heterojunction organic thin-film photovoltaics with horizontally oriented amorphous donors. *Sol. Energy Mater. Sol. Cells*, 98:472, 2012.
- [147] K. Bergemann and S. Forrest. Measurement of exciton diffusion lengths in optically thin organic films. *Appl. Phys. Lett.*, 99:243303, 2011.
- [148] M. Hirade and C. Adachi. Small molecular organic photovoltaic cells with exciton blocking layer at anode interface for improved device performance. *Appl. Phys. Lett.*, 99:153302, 2011.
- [149] D. Fujishima, H. Kanno, T. Kinoshita, E. Maruyama, M. Tanaka, M. Shirakawa, and K. Shibata. Organic thin-film solar cell employing a novel electron-donor material. *Sol. Energy Mater. Sol. Cells*, 93:1029, 2009.
- [150] P. Heiney, J. Fischer, A. Mc Ghie, W. Romanow, A. Denenstein, J. Mc Cauley Jr., A. Smith, and D. Cox. Orientational ordering transition in solid C₆₀. *Phys. Rev. Lett.*, 66:2911, 1991.
- [151] W. Krätschmer, L. Lamb, K. Fostiropoulos, and D. Huffman. Solid C₆₀: A new form of carbon. *Nature*, 347:354, 1990.
- [152] J. Abrefah, D. Olander, M. Balooch, and W. Siekhaus. Vapor pressure of buckminsterfullerene. *Appl. Phys. Lett.*, 60:1313, 1992.

- [153] L. Pettersson, L. Roman, and O. Inganäs. Modeling photocurrent action spectra of photovoltaic devices based on organic thin films. *J. Appl. Phys.*, 86:487, 1999.
- [154] J. Wagner, M. Gruber, A. Wilke, Y. Tanaka, K. Topczak, A. Steindamm, U. Hörmann, A. Opitz, Y. Nakayama, H. Ishii, J. Pflaum, N. Koch, and W. Brütting. Identification of different origins for S-shaped current voltage characteristics in planar heterojunction organic solar cells. *J. Appl. Phys.*, 111:054509, 2012.
- [155] A. Rajagopal, I. Hill, and A. Kahn. Electronic properties of metal-organic interfaces with application to electroluminescent devices. *Molecular Crystals and Liquid Crystals Science and Technology. Section A. Molecular and Liquid Crystals*, 322:245, 1998.
- [156] M. Chan, C. Lee, S. Lai, M. Fung, F. Wong, H. Sun, K. Lau, and S. Lee. Efficient organic photovoltaic devices using a combination of exciton blocking layer and anodic buffer layer. *J. Appl. Phys.*, 100:094506, 2006.
- [157] A. Steindamm, M. Brendel, A. Topczak, and J. Pflaum. Thickness dependent effects of an intermediate molecular blocking layer on the optoelectronic characteristics of organic bilayer photovoltaic cells. *Appl. Phys. Lett.*, 11:143302, 2012.
- [158] C. Osterwald. Translation of device performance measurements to reference conditions. *Solar Cells*, 18:269, 1986.
- [159] M. Birkholz, P. Fewster, and C. Genzel. *Thin Film Analysis By X-Ray Scattering*. Wiley-VCH, Weinheim, 2006.
- [160] J. Als-Nielsen and D. Mc Morrow. *Elements of Modern X-ray Physics*. Wiley VCH, Weinheim, 2000.
- [161] P. Scherrer. Bestimmung der Größe und der Inneren Struktur von Kolloidteilchen Mittels Röntgenstrahlen. *Nachrichten von der Gesellschaft der Wissenschaften zu Göttingen, Mathematisch-Physikalische Klasse*, :98, 1918.
- [162] C. Binning, C. Quate, and C. Gerber. Atomic force microscope. *Phys. Rev. Lett.*, 56:930, 1986.
- [163] <http://gwyddion.net/>. 24.10.2016.
- [164] I. Minda. Photoinduced Charge Dynamics in Indoline-Dye Sensitised Solar Cells. Master thesis, University of Stellenbosch, 2014.
- [165] E. Riedle, M. Beutter, S. Lochbrunner, J. Piel, S. Schenkl, S. Spörlein, and W. Zinth. Generation of 10 to 50 fs pulses tunable through all of the visible and the NIR. *Appl. Phys. B*, 71:457, 2014.
- [166] S. Braun, W. Salaneck, and Mats Fahlman. Energy-level alignment at organic/metal and organic/organic interfaces. *Adv. Mater.*, 21:1450, 2009.

- [167] S. Hüfner. *Photoelectron Spectroscopy*. Springer, Berlin, Heidelberg, 1995.
- [168] R. Schlaf. Calibration of photoemission spectra and work function determination. <http://rsl.eng.usf.edu/Documents/Tutorials/TutorialsWorkFunction.pdf>, 12.07.2016.
- [169] F. Reinert and S. Hüfner. Photoemission spectroscopy: From early days to recent applications. *New J. Phys.*, 7:97, 2005.
- [170] J. Kraus. *Physics of Molecular Donor-Acceptor Solar Cells: Correlation Between Interface Morphology, Energetics and Device Performance*. Ph.D. thesis, University of Augsburg, 2013.
- [171] N. Koch. Organic electronic devices and their functional interfaces. *ChemPhysChem*, 8:1438, 2007.
- [172] N. Koch and A. Vollmer. Electrode-molecular semiconductor contacts: Work-function-dependent hole injection barriers versus Fermi-level pinning. *Appl. Phys. Lett.*, 89:162107, 2006.
- [173] S. Krause, M. Casu, A. Schöll, and E. Umbach. Determination of transport levels of organic semiconductors by UPS and IPS. *New J. Phys.*, 10:085001, 2008.
- [174] A. Opitz, J. Wagner, W. Brütting, I. Salzmann, N. Koch, J. Manara, J. Pflaum, A. Hinderhofer, and F. Schreiber. Charge separation at molecular donor-acceptor interfaces: Correlation between interface morphology and solar cell performance. *IEEE J. Sel. Top. Quant. El.*, 16:1707, 2010.
- [175] M. Brendel, S. Krause, A. Steindamm, A. Topczak, S. Sundarraaj, P. Erk, S. Höhla, N. Fruehauf, N. Koch, and J. Pflaum. The effect of gradual fluorination on the properties of F_n ZnPc thin films and F_n ZnPc/ C_{60} bilayer photovoltaic cells. *Adv. Funct. Mater.*, 25:1565, 2015.
- [176] J. Meiss, A. Merten, M. Hein, C. Schuenemann, S. Schäfer, M. Tietze, C. Uhrich, M. Pfeiffer, K. Leo, and M. Riede. Fluorinated zinc phthalocyanine as donor for efficient vacuum-deposited organic solar cells. *Adv. Funct. Mater.*, 22:405, 2012.
- [177] R. Murdey, N. Sato, and M. Bouvet. Frontier electronic structures in fluorinated copper phthalocyanine thin films studied using ultraviolet and inverse photoemission spectroscopies. *Mol. Cryst. Liq. Cryst.*, 455:211, 2006.
- [178] D. Zahn, G. Gavrila, and M. Gorgoi. The transport gap of organic semiconductors studied using the combination of direct and inverse photoemission. *Chem. Phys.*, 325:99, 2006.
- [179] A. Sánchez-Díaz, L. Burtone, M. Riede, and E. Palomares. Measurements of efficiency losses in blend and bilayer-type zinc phthalocyanine/ C_{60} high-vacuum-processed organic solar cells. *J. Phys. Chem. C*, 116:16384, 2012.

- [180] S. Karan and B. Mallik. Nanoflowers grown from phthalocyanine seeds: Organic nanorec-
tifiers. *J. Phys. Chem. C*, 112:2436, 2008.
- [181] M. Alonso, M. Garriga, J. Ossó, S. Sellner, and H. Dosch. Strong optical anisotropies of
F₁₆CuPc thin films studied by spectroscopic ellipsometry. *J. Am. Chem. Soc.*, 128:15052,
2006.
- [182] D. de Oteyza, E. Barrena, J. Ossó, S. Sellner, and H. Dosch. Thickness-dependent struc-
tural transitions in fluorinated copper-phthalocyanine (F₁₆CuPc) films. *J. Am. Chem.
Soc.*, 128:15052, 2006.
- [183] A. Ogunsipe, D. Maree, and T. Nyokong. Solvent effects on the photochemical and fluo-
rescence properties of zinc phthalocyanine derivatives. *J. Mol. Struct.*, 650:131, 2003.
- [184] *Private communication to Cambridge Crystallographic Data Center (CCDC reference code
CUPOCY14)*. P. Erk.
- [185] A. Opitz, B. Ecker, J. Wagner, A. Hinderhofer, F. Schreiber, J. Manara, J. Pflaum, and
W. Brütting. Mixed crystalline films of co-evaporated hydrogen- and fluorine-terminated
phthalocyanines and their application in photovoltaic devices. *Org. Electron.*, 10:1259,
2009.
- [186] A. Opitz, J. Wagner, W. Brütting, A. Hinderhofer, and F. Schreiber. Molecular semicon-
ductor blends: Microstructure, charge carrier transport, and application in photovoltaic
cells. *Phys. Status Solidi A*, 12:2683, 2009.
- [187] D. de Oteyza, E. Barrena, J. Ossó, H. Dosch, S. Meyer, and J. Pflaum. Controlled
enhancement of the electron field-effect mobility of F₁₆CuPc thin-film transistors by use
of functionalized SiO₂ substrates. *Appl. Phys. Lett.*, 87:183504, 2005.
- [188] J. Ossó, F. Schreiber, M. Alonso, M. Garriga, E. Barrena, and H. Dosch. Structure,
morphology, and optical properties of thin films of F₁₆CuPc grown on silicon dioxide. *Org.
Electron.*, 5:135, 2004.
- [189] L. Siebbeles, A. Huijser, and T. Savenije. Effects of molecular organization on exciton
diffusion in thin films of bioinspired light-harvesting molecules. *J. Mater. Chem*, 19:6067,
2009.
- [190] A. Topczak, T. Roller, B. Engels, W. Brütting, and J. Pflaum. Nonthermally activated
exciton transport in crystalline organic semiconductor thin films. *Phys. Rev. B*, 89:201203,
2014.
- [191] A. Kahn, N. Koch, and W. Gao. Electronic structure and electrical properties of interfaces
between metals and conjugated molecular films. *J. Polym. Sci. B*, 41:2529, 2003.

- [192] M. Golden, M. Knupfer, J. Fink, J. Armbruster, T. Cummins, H. Romberg, M. Roth, M. Sing, M. Schmidt, and E. Sohmen. The electronic structure of fullerenes and fullerene compounds from high-energy spectroscopy. *Condens. Matter*, 7:8219, 1995.
- [193] T. Zhang, J. Huang, F. He, L. Chen, G. Niu, J. Pan, and Q. Song. The effect of built-in field on the interface exciton recombination and dissociation in n-n type organic solar cells. *Sol. Energy Mater. Sol. Cells*, 112:73, 2013.
- [194] Q. Song, H. Yang, Y. Gang, C. Gong, and C. Li. Evidence of harvesting electricity by exciton recombination in an n-n type solar cell. *J. Am. Chem. Soc.*, 132:4554, 2010.
- [195] A. Chang, Y. Chen, H. Lin, L. Lin, K. Wong, and R. Schaller. Charge carrier dynamics of vapor-deposited small-molecule/fullerene organic solar cells. *J. Am. Chem. Soc.*, 135:8790, 2013.
- [196] D. Dick, X. Wei, S. Jeglinski, R. Benner, Z. Vardeny, D. Moses, V. Srdanov, and F. Wudl. Transient spectroscopy of excitons and polarons in C₆₀ films from femtoseconds to milliseconds. *Phys. Rev. Lett.*, 73:2760, 1994.
- [197] O. Ito. Photoinduced electron transfer of fullerenes (C₆₀ and C₇₀) studied by transient absorption measurements in near-IR. *Res. Chem. Intermed.*, 23:389, 1997.
- [198] A. Bakulin, J. Hummelen, M. Pshenichnikov, and P. Lossdrecht. Ultrafast hole-transfer dynamics in polymer/PCBM bulk-heterojunctions. *Adv. Funct. Mater.*, 20:1653, 2010.
- [199] S. Cook, R. Katoh, and A. Furube. Ultrafast studies of charge generation in PCBM:P3HT blend films following excitation of the fullerene PCBM. *J. Phys. Chem. C*, 113:2547, 2009.
- [200] S. Kazaoui, N. Minami, Y. Tanabe, H. Byrne, A. Eilmes, and P. Petelenz. Comprehensive analysis of intermolecular charge-transfer excited states in C₆₀ and C₇₀ films. *Phys. Rev. B*, 58:7689, 1998.
- [201] P. Lane, P. Cunningham, J. Melinger, and E. Heilweil. Hot photocarrier dynamics in organic solar cells measured by transient absorption and time-resolved terahertz spectroscopy. *Proc. of SPIE*, 9184:97840G–2, 2014.
- [202] A. Köhler, D. dos Santos, D. Beljonne, Z. Shuai, J. Brédas, A. Holmes, A. Kraus, K. Müllen, and R. Friend. Charge separation in localized and delocalized electronic states in polymeric semiconductors. *Nature*, 392:903, 1998.
- [203] P. Lane, P. Cunningham, J. Melinger, and G. Kushto. Photoexcitation dynamics in films of C₆₀ and Zn phthalocyanine with a layered nanostructure. *Phys. Rev. Lett.*, 108:077402, 2012.
- [204] G. Burkhard, E. Hoke, Z. Beiley, and M. McGehee. Free carrier generation in fullerene acceptors and its effect on polymer photovoltaics. *J. Phys. Chem. C*, 116:26674, 2012.

- [205] W. Jeong, Y. Lee, H. Shim, T. Kim, S. Kim, and J. Kim. Photoconductivity of C₆₀ as an origin of bias-dependent photocurrent in organic photovoltaics. *Adv. Funct. Mater.*, 22:3089, 2012.
- [206] S. Suttty, G. Williams, and H. Aziz. Role of the donor material and the donor acceptor mixing ratio in increasing the efficiency of Schottky-junction organic solar cells. *Org. Electron.*, 14:2392, 2013.
- [207] A. Palai, S. Mishra, A. Kumar, R. Srivastava, M. Kamalasanan, and M. Patri. Synthesis and characterization of red-emitting poly(aryleneethynylene)s based on 2,5-bis(2-ethylhexyl)-3,6-di(thiophen-2-yl)pyrrolo[3,4-c]pyrrole-1,4(2h,5h)-dione (DPP). *Macromol. Chem. Phys.*, 211:1043, 2010.
- [208] W. Tress, A. Petrich, M. Hummert, M. Hein, K. Leo, and M. Riede. Imbalanced mobilities causing S-shaped IV curves in planar heterojunction organic solar cells. *Appl. Phys. Lett.*, 98:063301, 2011.
- [209] C. Schwarz, H. Büssler, I. Bauer, J. Koenen, E. Preis, U. Scherf, and A. Köhler. Does conjugation help exciton dissociation? A study on poly(p-phenylene)s in planar heterojunctions with C₆₀ or TNF. *Adv. Mater.*, 24:922, 2012.
- [210] X. Zhu, Q. Yang, and M. Muntwiler. Charge-transfer excitons at organic semiconductor surfaces and interfaces. *Acc. Chem. Res.*, 42:1779, 2009.
- [211] N. Sariciftci. Role of buckminsterfullerene, C₆₀, in organic photoelectric devices. *Prog. Quantum Electron.*, 19:131, 1995.
- [212] S. Grob, M. Gruber, A. Bartynski, U. Hörmann, T. Linderl, M. Thompson, and W. Brütting. Amorphous vs. crystalline exciton blocking layers at the anode interface in planar and planar-mixed heterojunction organic solar cells. *Appl. Phys. Lett.*, 104:213304, 2014.
- [213] Y. Zhou, T. Taima, T. Kuwabara, and K. Takahashi. Efficient small-molecule photovoltaic cells using a crystalline diindenoperylene film as a nanostructured template. *Adv. Mater.*, 25:6069, 2013.
- [214] P. Groppe. Photovoltaische Dünnschichtzellen auf Basis der Organischen Halbleitermaterialien Tetraphenyldibenzoperiflanthen (DBP) und Fulleren C₇₀. Bachelor thesis, University of Würzburg, 2015.
- [215] A. Barito, M. Sykes, B. Huang, D. Bilby, B. Frieberg, J. Kim, P. Green, and M. Shtein. Universal design principles for cascade heterojunction solar cells with high fill factors and internal quantum efficiencies approaching 100 %. *Adv. Energy Mater.*, 4:1400216, 2014.
- [216] T. Schmalz, W. Seitz, D. Klein, and G. Hite. Elemental carbon cages. *J. Am. Chem. Soc.*, 110:1113, 1988.

- [217] H. Kroto, J. Heath, S. O'Brien, R. Curl, and R. Smalley. C_{60} : Buckminsterfullerene. *Nature*, 329:529, 1987.
- [218] K. Tohji, A. Paul, L. Moro, R. Malhotra, D. Lorents, and R. Ruoff. Selective and high-yield synthesis of higher fullerenes. *J. Phys. Chem.*, 99:17785, 1995.
- [219] S. Saito and A. Oshiyama. Electronic and geometric structures of C_{70} . *Phys. Rev. B.*, 44:11532, 1991.
- [220] C. Li, H. Yip, and A. Jen. Functional fullerenes for organic photovoltaics. *J. Mater. Chem.*, 22:4161, 2012.
- [221] J. Sakai, T. Taima, T. Yamanari, and K. Saito. Annealing effect in the sexithiophene: C_{70} small molecule bulk-heterojunction organic photovoltaic cells. *Sol. Energy Mater. Sol. Cells*, 93:1149, 2009.
- [222] X. Xi, W. Li, J. Wub, J. Ji, Z. Shi, and G. Li. A comparative study on the performances of small molecule organic solar cells based on CuPc/ C_{60} and CuPc/ C_{70} . *Sol. Energy Mater. Sol. Cells*, 94:2435, 2010.
- [223] R. Pandey, A. Gunawan, K. Mkhoyan, and R. Holmes. Efficient organic photovoltaic cells based on nanocrystalline mixtures of boron subphthalocyanine chloride and C_{60} . *Adv. Func. Mater.*, 22:617, 2012.
- [224] R. Pandey, Y. Zou, and R. Holmes. Efficient, bulk heterojunction organic photovoltaic cells based on boron subphthalocyanine chloride- C_{70} . *Appl. Phys. Lett.*, 101:033308, 2012.
- [225] J. Subbiah, P. Beaujuge, K. Choudhury, and S. Ellinger. Combined effects of MoO_3 interlayer and PC $_{70}$ BM on polymer photovoltaic device performance. *Org. Electron.*, 11:955, 2010.
- [226] L. Popescu. *Fullerene Based Organic Solar Cells*. Ph.D. thesis, University of Groningen, 2008.
- [227] J. Weaver. Electronic structures of C_{60} , C_{70} and the fullerenes: Photoemission and inverse photoemission studies. *J. Phys. Chem. Solids*, 53:1433., 1992.
- [228] A. Sperlich. *Electron Paramagnetic Resonance Spectroscopy of Conjugated Polymers and Fullerenes for Organic Photovoltaics*. Ph.D. thesis, University of Würzburg, 2013.
- [229] J. Venables, G. Spiller, and M. Hanbücken. Nucleation and growth of thin films. *Rep. Prog. Phys.*, 47:399, 1984.
- [230] E. Negri, G. Orlandi, and E. Zerbetto. The infrared and raman active vibrational frequencies of C_{60} hexaanion. *Chem. Phys. Lett.*, 196:303, 1992.
- [231] W. Pickett, I. Ehrenreich, and E. Spaepen. *Solid State Physics*. Academic Press, New York, 1994.

- [232] D. Poirier, J. Weaver, K. Kikuchi, and Y. Achiba. Electronic structure of C_{84} and K_xC_{84} : Comparison to C_{60} and graphite. *Zeitschrift für Physik D, Atoms, Molecules and Clusters*, 26:79, 1993.
- [233] S. Hino, K. Matsumoto, S. Hasegawa, H. Inokuchi, T. Morikawa, T. Takahashi, K. Seki, K. Kikuchi, S. Suzuki, I. Ikemoto, and Y. Achiba. Ultraviolet photoelectron spectra of C_{76} and K_xC_{76} . *Chem. Phys. Lett.*, 197:38, 1992.
- [234] J. Pflaum, J. Niemax, and A. Tripathi. Chemical and structural effects on the electronic transport in organic single crystals. *Chem. Phys.*, 325:152, 2006.

Publication List

1. A. Steindamm, M. Brendel, A. Topczak, and J. Pflaum. Thickness dependent effects of an intermediate molecular blocking layer on the optoelectronic characteristics of organic bilayer photovoltaic cells. *Appl. Phys. Lett.*, 11:143302, 2012.
2. M. Brendel, S. Krause, A. Steindamm, A. Topczak, S. Sundarraj, P. Erk, S. Höhla, N. Fruehauf, N. Koch, and J. Pflaum. The effect of gradual fluorination on the properties of F_nZnPc thin films and F_nZnPc/C_{60} bilayer photovoltaic cells. *Adv. Funct. Mater.*, 25:1565, 2015.
3. C. Mueller, M. Brendel, P. Ruckdeschel, J. Pflaum, and M. Thelakkat. Diketopyrrolopyrroles with a distinct energy level cascade for efficient charge carrier generation in organic solar cells. *Adv. Energy Mater.*, 5:1500914, 2015.

LEBENS LAUF
Michael Brendel
Kiefernweg 15, 97854 Steinfeld
Telefon: +49157/87009316
E-Mail: michael.brendel@physik.uni-wuerzburg.de

Persönliche Daten

geboren am 21.07.1986 in Lohr a. Main
ledig

Promotion

Seit 01/2012 **Promotion an der Graduate School of Science and Technology**
Julius-Maximilians-Universität Würzburg
Thema der Promotion: *Correlation between Interface Energetics of Molecular Semiconductors and Opto-Electronic Properties of Planar Organic Solar Cells*

Studium

10/2009 - 11/2011 **Masterstudium der Technologie der Funktionswerkstoffe**
Abschluss mit der Note sehr gut (1,5)
Julius-Maximilians-Universität Würzburg
Thema der Masterarbeit: *Photovoltaische Zellen basierend auf Diindenoperylen als Donator-Material*

10/2006 - 10/2009 **Bachelorstudium der Technologie der Funktionswerkstoffe**
Abschluss mit der Note gut (2,2)
Julius-Maximilians-Universität Würzburg

Schulbildung

06/2006 **Abitur**
Abschluss mit der Note gut (2,0)
Franz-Ludwig von Erthal Gymnasium Lohr a. Main

Ort, Datum

Unterschrift

Affidavit

I hereby confirm that my thesis entitled “Correlation between Interface Energetics of Molecular Semiconductors and Opto-Electronic Properties of Planar Organic Solar Cells” is the result of my own work. I did not receive any help or support from commercial consultants. All sources and / or materials applied are listed and specified in the thesis.

Furthermore, I confirm that this thesis has not yet been submitted as part of another examination process neither in identical nor in similar form.

Place, Date

Signature

Eidesstattliche Erklärung

Hiermit erkläre ich an Eides statt, die Dissertation “Der Zusammenhang zwischen der Energetik molekularer Halbleitergrenzflächen und den opto-elektronischen Eigenschaften planarer organischer Solarzellen” eigenständig, d.h. insbesondere selbständig und ohne Hilfe eines kommerziellen Promotionsberaters, angefertigt und keine anderen als die von mir angegebenen Quellen und Hilfsmittel verwendet zu haben.

Ich erkläre außerdem, dass die Dissertation weder in gleicher noch in ähnlicher Form bereits in einem anderen Prüfungsverfahren vorgelegen hat.

Ort, Datum

Unterschrift

Danksagung

Ich möchte mich bei allen bedanken, die mich bei meiner Arbeit unterstützt und zum Gelingen der Promotion beigetragen haben.

- Insbesondere danke ich meinem Doktorvater Prof. Dr. Jens Pflaum für die Möglichkeit, die Promotion in seiner Arbeitsgruppe durchführen zu können. Vielen Dank für die sehr interessante Aufgabenstellung und den Gestaltungsfreiraum der eigenen Forschung. Durch die sehr gute Betreuung und die zahlreichen Diskussionen habe ich viel lernen können.
- Außerdem geht mein Dank an Prof. Dr. Matthias Bode und Prof. Dr. Bernd Engels für die Übernahme der Betreuung im Advisory Committee. Danke für die Diskussionen und Anregungen während der zahlreichen Treffen.
- Prof. Dr. Heinrich Schwoerer danke ich für die herzliche Aufnahme in seine Arbeitsgruppe am Laser Research Institute der Universität Stellenbosch in Südafrika während des DAAD Stipendiums. Für die Hilfe bei den transienten Absorptionsmessungen möchte ich besonders Essraa Ahmed, Iulia Minda und Xavier von Stein danken. Die Zeit in Stellenbosch wird mir wissenschaftlich und privat immer in bester Erinnerung bleiben.
- Außerdem möchte ich mich bei unseren Kooperationspartnern bedanken. Prof. Dr. Mukundan Thelakkat und Dr. Christian Müller von der Universität Bayreuth danke ich für die tolle Zusammenarbeit im Rahmen des “Solar Technologies Go Hybrid”-Projekts. Des Weiteren gilt mein Dank den Kooperationspartnern des DFG Schwerpunktprogrammes SPP1355. Besonders ist hierbei Prof. Dr. Wolfgang Brütting, Dr. Mark Gruber und Dr. Ulrich Hörmann von der Universität Augsburg, Prof. Dr. Norbert Koch und Dr. Stefan Krause von der Humboldt-Universität Berlin zu nennen. Außerdem bedanke ich mich bei den Kollegen von BASF Dr. Sudhakar Sundarraj und Dr. Peter Erk für die Bereitstellung der Materialien und die Diskussion der wissenschaftlichen Ergebnisse. Zudem bedanke ich mich bei Steffen Höhla und Stephan Hirschmann von der Universität Stuttgart für die Herstellung der ITO-Substrate und die Materialaufreinigung.
- Vielen Dank an alle Mitarbeiter der experimentellen Physik VI und insbesondere an meine Arbeitsgruppe. Es war immer eine tolle und angenehme Arbeitsatmosphäre. Vor allem möchte ich Dr. Andreas Steindamm erwähnen, der mir mit zahlreichen Diskussionen und der Unterstützung im Labor schon während meiner Masterarbeit zur Seite stand.

- Ein herzliches Danke für die gute Zusammenarbeit geht auch an die von mir betreuten Master- und Bachelorstudenten Florian Staub, Johannes Mahr, Jana Wulf und Philipp Groppe.
- Vielen Dank an Diep Phan, die gute Seele der EP VI, für die Hilfe bei der Bürokratie.
- Herzlichen Dank an meine Freundin Melissa Lange für die Unterstützung und das Verständnis, das du mir in dieser Zeit entgegen gebracht hast.
- Schließlich danke ich meinen Eltern Renate und Franz Brendel und meinem Onkel Walter Eck für ihre Unterstützung. Ihr hattet immer ein offenes Ohr und habt mir bei so vielem geholfen.